CHEMISTRY AND APPLICATIONS OF A FEW TAILOR-MADE METAL-ORGANIC MATERIALS

Thesis Submitted to AcSIR for the Award of the Degree of
DOCTOR OF PHILOSOPHY
in Chemical Sciences

By

RAHUL DEV MUKHOPADHYAY

Registration No: 10CC11J39004

Under the guidance of

Prof. A. AJAYAGHOSH

CSIR-NATIONAL INSTITUTE FOR INTERDISCIPLINARY SCIENCE AND TECHNOLOGY (CSIR-NIIST)
THIRUVANANTHAPURAM-695 019, KERALA, INDIA

April, 2017

Dedicated to

My Beloved Maa & Baba

DECLARATION

I hereby declare that the matter embodied in the thesis entitled: "**Chemistry and Applications of a Few Tailor-Made Metal-Organic Materials**" is the result of the investigations carried out by me at the Photosciences and Photonics Section, Chemical Sciences and Technology Division, CSIR-National Institute for Interdisciplinary Science and Technology (CSIR-NIIST), Thiruvananthapuram, under the supervision of Prof. A. Ajayaghosh and the same has not been submitted elsewhere for any other degree.

In keeping with the general practice of reporting scientific observations, due acknowledgement has been made wherever the work described is based on the findings of other investigators.

Rahul Dev Mukhopadhyay

राष्ट्रीय अंतर्विषयी विज्ञान तथा प्रौद्योगिकी संस्थान
वैज्ञानिक तथा औद्योगिक अनुसंधान परिषद्
इंडस्ट्रियल इस्टेट पी.ओ., पाप्पनंकोड, तिरुवनंतपुरम, भारत–695 019
CSIR-NATIONAL INSTITUTE FOR INTERDISCIPLINARY SCIENCE & TECHNOLOGY (CSIR-NIIST)
Council of Scientific & Industrial Research
Industrial Estate P.O., Pappanamcode, Thiruvananthapuram, India-695 019
डॉ. ए. अजयघोष एफएनए, एफटीडब्ल्यूएएस
निदेशक
Dr. A. Ajayaghosh FNA, FTWAS
Director

April 03, 2017

CERTIFICATE

This is to certify that the work incorporated in this Ph.D. thesis entitled ***"Chemistry and Applications of a Few Tailor-Made Metal-Organic Materials"*** *submitted by* ***Mr. Rahul Dev Mukhopadhyay*** *to Academy of Scientific and Innovative Research (AcSIR) in fulfilment of the requirements for the award of the* ***Degree of Doctor of Philosophy in Chemical Sciences*** *embodies original research work under my supervision. I further certify that this work has not been submitted to any other University or Institution in part or full for the award of any degree or diploma. Research material obtained from other sources has been duly acknowledged in the thesis. Any text, illustration, table etc., used in the thesis from other sources, have been duly cited and acknowledged.*

Rahul Dev Mukhopadhyay

A. Ajayaghosh
(Supervisor)

ACKNOWLEDGEMENTS

It is with great pleasure that I extend my deep sense of gratitude to Prof. A. Ajayaghosh, my thesis supervisor, for suggesting the research problem, for his valuable guidance, support, encouragement and scientific freedom of thought and action, leading to the successful completion of this work.

I would like to express my gratitude to Prof. M. V. George for being a huge inspirational figure for budding chemists like me at CSIR-NIIST.

I thank Dr. Suresh Das and Dr. Gangan Pratap, former Directors of CSIR- NIIST, Trivandrum, for providing me the necessary facilities for carrying out this work.

My sincere thanks are also due to:

- *Dr. K. R. Gopidas, Dr. D. Ramaiah, Dr. Joshy Joseph, Dr. Narayanan Unni, Dr. K. Yoosaf, Dr. C. Vijayakumar, Dr. B. Deb and Dr. V. Karunakaran, present and former scientists of the Photosciences and Photonics, Chemical Sciences and Technology Division, for their help and support.*
- *Dr. Mangalam S. Nair and Dr. R. Luxmi Varma, former and present AcSIR co-ordinators.*
- *Dr. D. Ramaiah, Dr. K. R. Gopidas, Dr. S. Annanthakumar my DAC members.*
- *Dr. Tapas Kumar Maji, Dr. A. Hazra from JNCASR, Bangalore and Dr. Rahul Bannerjee, from CSIR-NCL, Pune for gas adsorption studies and valuable discussions.*
- *Dr. Prabha D. Nair of SCTIMST, Trivandrum for contact angle studies.*
- *Dr. Rajesh Simhadri of College of Engineering, Trivandrum for the high-speed camera recording.*
- *Dr. V. K. Praveen and Dr. Sreejith Shankar for fruitful discussions.*
- *Dr. Anesh Gopal and Dr. K.K. Kartha and other former members of the Photosciences and Photonics Group for their guidance, support and advice.*

- *Mr. G. Tarafdar, Mr. Pradeep P.S. and Ms. Ameena Almas K. N. for helping me in experiments.*
- *All present and former members of 'The AG Group' and other members of Photosciences and Photonics Section, for their help and cooperation.*
- *Special thanks to Mr. Samrat Ghosh, Ms. Divya Susan Philips and Mr. Gourab Das for their help.*
- *Dr. J. D. Sudha for supporting and helping me in every possible way during my stay at CSIR-NIIST.*
- *Mr. Robert Philip and Mr. J. S. Kiran for their general help and support.*
- *Mr. C. K. Chandrakanth and Mr. M. R. Chandran for SEM analysis and Mr. Kiran M. for TEM analysis.*
- *Mrs. M. Saumini, Mr. Adarsh, Mr. P. Preethanuj and Mr. T. Arun for NMR and Mrs. S. Viji for mass spectral analyses.*
- *All my teachers for their encouragement at different stages of my academic career.*
- *Council of Scientific and Industrial Research (CSIR) and Department of Science and Technology (DST), Government of India for financial assistance.*

I am deeply and forever indebted to my parents, my in-laws, my sister, my niece and my very beautiful wife for their constant source of love, confidence and support. Finally I would like to remember my brother-in-law, for encouraging me to pursue my research career by taking excellent care of my old parents while I was miles away from home. Today, wherever he is he must be feeling very proud about me. I thank him for his blessings.

Rahul Dev Mukhopadhyay

CONTENTS

List of Abbreviations

ADA	(*E*)-Azobenzene-4,4'-dicarboxylic acid
An	Aniline
APS	Ammonium persulphate
Azo	Azobenzene
AzPBA	(*E*)-4,4’-(diazene-1,2-diyl)bis(4,1-phenylene)bis(oxy)dibutanoic acid
AzSA	(*E*)-2-hydroxy-5-(phenyldiazenyl)benzoic Acid
BA	2,5-bis(dodecycloxy)terephthalaldehyde
BET	Brunauer–Emmett–Teller
BFDH	Bravais, Friedel, Donnay and Harker
Boc	*tert*-butyloxycarbonyl
c	Concentration
CA	Contact angle
CAH	Contact angle hysteresis
calcd	Calculated
CD	Cyclodextrin
cm	Centimeter
CoI_h	Columnar hexagonal
CORF	Carbon monoxide releasing framework
CPG	Coordination polymer gel
°C	Degree Celsius
DEF	Diethyl formamide
D_{max}	Deformation maximum
DMF	Dimethyl formamide
DMSO	Dimethyl sulfoxide
DMSO-d_6	Deuterated dimethyl sulfoxide
DNA	Deoxyribonucleic acid
DPA	Diphenylalanine
DS	Diazonium salt

DSB	Distyrylbenzene
E/*Z*	Entgegen (German: opposite) / zusammen (German: together)
EDXS	Energy-dispersive X-ray Spectroscopy
Eq.	Equation
equiv.	Equivalent
ESI	Electrospray ionization
et al.	*Et allii/alia*
EtOH	Ethanol
F	Force
FAB	Fast atom bombardment
FeBTC	Ferric (1,3,5-benzenetricarboxylic acid)
FESEM	Field emission scanning electron microscopy
FFT	Fast Fourier transform
FT-IR	Fourier transform infrared
g	gram
G′	Storage modulus
G″	Loss modulus
GCMC	Grand canonical Monte Carlo
GPa	Gigapascal
h	Hour
HqPBA	4,4'-(1,4-phenylenebis(oxy))dibutanoic acid
HRMS	High resolution mass spectrometry
HRTEM	High resolution transmission electron microscopy
Hz	Hertz
ICD	Induced circular dichroism
ICP	Infinite coordination polymer
IFFT	Inverse fast Fourier transform
IR	Infrared
IRFeBTC	Irradiated ferric (1,3,5-benzenetricarboxylic acid)

IUPAC	International Union of Pure and Applied Chemistry
J	Coupling constant
JCPDS	Joint committee on powder diffraction standards
K	Kelvin
kHz	Kilo Hertz
kV	Kilovolts
kWh	Kilowatt-hour
L	Liter
M	Molar
m	Meter
max	maximum
m.p.	Melting point
M^+	Molecular ion peak
mdeg	Millidegree
MeOH	Methanol
mg	Milligram
Mg-CP	Magnesium coordination polymer
Mg-CP⊃α-CD	Magnesium coordination polymer encapsulating alpha cyclodextrin
Mg-CP⊃β-CD	Magnesium coordination polymer encapsulating beta cyclodextrin
Mg-CP⊃γ-CD	Magnesium coordination polymer encapsulating gamma cyclodextrin
β-CD⊃Na-AdCA	Beta cyclodextrin encapsulating sodium salt of adamantane carboxylic acid
MHz	Mega Hertz
MIL	Materials of Institute Lavoisier
min	Minutes
mL	Milliliter
mm	Millimeter
mM	Millimolar
mmol	Millimoles

MOF	Metal-organic framework
MOG	Metal-organic gel
mol	Mole
MOM	Metal-organic material
MOP	Metal-organic polyhedra
ms	Millisecond
NLC	Nonlinear compressibility
NLDFT	Non-local density functional theory
nm	Nanometer
nM	Nanomolar
$N \cdot m^{-1}$	Newton per meter
NMP	*N*-methyl pyrrolidone
NMR	Nuclear magnetic resonance
Olz	Osalazine
PCN	Porous coordination network
PCP	Porous coordination polymer
PEG	Polyethylene glycol
pH	Hydrogen ion concentration at logarithmic scale
PNBA	*p*-Nitrobenzoic acid
PNIPAM	poly(*N*-isopropylacrylamide)
ppm	Parts per million
rpm	Rotations per minute
rt	Room temperature
s	Second
SA	Sliding angle
SAED	Selected area electron diffraction
SAXS	Small angle x-ray scattering
$S\ cm^{-1}$	Siemens per centimeter
SEM	Scanning electron microscopy
SURMOF	Surface mounted metal-organic framework

T	Temperature
TEM	Transmission electron microscopy
TEMED	Tetramethylethylenediamine
TGA	Thermogravimetric analysis
TMS	Tetramethylsilane
U	Impact velocity
UiO	Universitetet i Oslo
USA	United States of America
UV	Ultraviolet
v	Volume
Vis	Visible
W	Watt
WAXD	Wide angle x-ray diffraction
WAXS	Wide angle x-ray scattering
XRD	X-ray diffraction
Zn-CP	Zinc coordination polymer
α	Alpha
β	Beta
α-CD	Alpha cyclodextrin
β-CD	Beta cyclodextrin
β_{max}	Spreading factor maximum
δ	Chemical shift
γ	Gamma
γ-CD	Gamma cyclodextrin
λ	Wavelength
µg	Microgram
µm	Micrometer
µM	Micromolar
µN	Micro Newton

μ_s	Coefficient of static friction
θ	Theta
ξ_{max}	Dimensionless height factor maximum
0-D	Zero dimensional
1-D	One dimensional
2-D	Two dimensional
3-D	Three dimensional

PREFACE

Isaac Asimov once commented about research, *"The most exciting phrase to hear in science, the one that heralds new discoveries, is not Eureka! (I've found it!), but that's funny"*. I am perhaps one of those researchers, who although likes his share of eureka moment, but at the same time, doesn't like to overlook any interesting yet uncommon observation. Before you, therefore lies a thesis, containing results and inferences from some of those designed experiments and serendipitous observations that I was able to obtain during my doctoral research at CSIR-NIIST.

When I joined the Ajayaghosh group in 2010, one of the ongoing research projects in the group was to develop stimuli-responsive supramolecular assemblies, especially those which respond to light.[1] I was therefore entrusted upon to develop porous stimuli responsive metal-organic materials, considering the importance of the emerging area of metal-organic frameworks (MOFs). Till then, very few reports on photoresponsive metal-organic materials were rarely present in the scientific literature. But by the end of 2011, there was a sudden upsurge in the area of photoresponsive MOFs and to our surprise, different research groups came up with interesting ideas, to develop smart porous photoresponsive materials. Although we were not at a vantage point to comment on this research area, we took it as a challenge to understand and study the approaches adopted by various groups and highlighted the area with a big heart to the scientific community.[2]

As a result, we reconstructed our research problem and were involved in the design of photoresponsive coordination polymer gels to study the isomerization property of azobenzene in a soft gel scaffold rather than in a rigid crystalline framework. A gel is

usually expected to possess a fibrillar network structure, but the gel in our case showed a sheet like morphology that assembled to form microscopic flower like structures. In order to capture the fibrillar morphology of the gel as well as to understand the gelation mechanism, we decided to conduct a time-dependent morphological analysis. Much to our surprise, we were able to unravel a kinetically controlled, aggregation induced crystal growth pathway in these materials. We were further able to tune this growth process using light by inducing a pre-synthetic isomerization of the photoresponsive ligand. The gel obtained in the presence of light irradiation possessed a different morphology, comprising of micrometer-sized six armed stars. Not only the morphology, but also the properties of these two gel materials were affected by the photoirradiation process. The materials once formed were not affected by light.[3]

In our further quest to develop a stimuli-responsive platform for programmable release or capture of guest molecules, we were able to design a thermoresponsive coordination polymer platform with specifically controlled host-guest interactions. The system reported was multi-stimuli responsive and the host-guest interactions could be efficiently controlled using chemicals as well. Moreover, we found that the systems reported so far respond either in solution or in the solid phase. The coordination polymer that we were able to develop was solution processable and therefore could be modulated both in solution as well as in the quasi-solid state when incorporated inside a hydrogel matrix. It could also be utilized for the chemical decoding of otherwise very difficult to identify, optically transparent organic molecules.[4]

Out of the several things, that we had learnt so far in the field of metal-organic materials, their tunable crystal growth process and easy to fabricate nano-meso-micro scale morphological structures attracted us the most. We hypothesized that, if a surface can be functionalized with an ordered arrangement of such structures, perhaps superhydrophobic surfaces with dual scale rough features perhaps can be fabricated. We found out that a nanoscale coordination polymer, functionalized over an alumina substrate, behaves like the superhydrophobic surface of a lotus leaf with a very high water contact angle. Usually, the properties of an organic ligand are transferred to a 3-D space, when it is converted to a coordination polymer. We therefore thought of investigating the hydrophobic nature of a surface, functionalized with the organic ligand. To our surprise, the ligand surface showed hydrophobicity as well as water droplet pinning effect, much like the petals of rose. We thereby combined these biomimicking observations to utilize water as a lubricant between two surfaces in contact. We believe that this proof of concept research can be exploited in future to develop slippery iceless skating arenas and save huge amount of energy required for the refrigeration of ice.[5]

Overall, I believe that the present thesis should provide the readers with substantial insights, on the research on stimuli-responsive (light, heat, moisture) metal-organic materials. Herein, we have incorporated studies and explored properties that are not conventionally performed or observed for these materials. The concepts reported herein, are represented in a simplistic manner and the chemistry exploited makes use of simple observations made in our lab. Finally, I must admit that it would have been impossible to write this thesis, without the help, support and guidance of my research supervisor Prof.

Ajayaghosh and many others who helped me during the research activities and writing. I hope, researchers not only from the chemistry background, but also from other fields of science, who love exploring crazy scientific ideas, will enjoy reading it.

References

1. Supramolecular Gels and Functional Materials Research in India. K. K. Kartha, **R. D. Mukhopadhyay** and A. Ajayaghosh, *Chimia*, 2013, **67**, 51.
2. Photoresponsive Metal-Organic Materials: Exploiting the Azobenzene Switch. **R. D. Mukhopadhyay**, V. K. Praveen and A. Ajayaghosh, *Mater. Horiz.*, 2014, **1**, 572.
3. Light Driven Mesoscale Assembly of a Coordination Polymeric Gelator into Flowers and Stars with Distinct Properties. **R. D. Mukhopadhyay**, V. K. Praveen, A. Hazra, T. K. Maji and A. Ajayaghosh, *Chem. Sci.*, 2015, **6**, 6583.
4. Rose Petal and Lotus Leaf Inspired Two-in-One Approach to Energy-Efficient Mechanical Motion. **R. D. Mukhopadhyay**, B. Vedanarayan and A. Ajayaghosh, (*manuscript in preparation*).
5. Precise Control of Host-Guest Interactions by a Coordination Polymeric Gelator. **R. D. Mukhopadhyay**, G. Das and A. Ajayaghosh, (*manuscript in preparation*).

Chapter 1

Stimuli-Responsive Metal-Organic Materials: Recent Developments

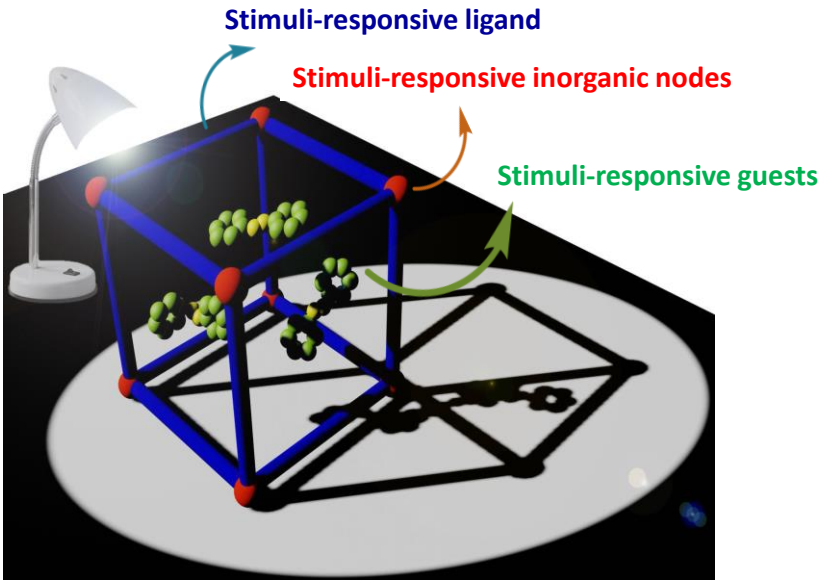

1.1. Abstract

Chemists have always been inspired to design materials that are smart enough to respond towards an external stimulus, in a predictable and controllable manner. Lately, this chemistry has also made a mark in the emerging area of metal–organic materials (MOMs). If one can regulate the properties of porous hybrid materials with various external stimuli such as light, heat, pressure and chemicals, their scope of applications can further be expanded. This field is turning out to be highly promising and gradually progressing from nano to mesoscopic size domains. However, one needs significant in-depth research to deliver materials that are truly smart and

practically viable. In this introductory chapter, an overview on the recent developments in the area of stimuli-responsive MOMs has been presented. A special emphasis has been laid on MOMs that respond to light. This includes various strategies to selectively capture or release guest molecules via photoisomerization and cycloaddition reactions inside a metal-organic matrix. According to the reports discussed herein, the azobenzene based ligands have been identified as promising candidates for the design of photoresponsive MOMs. Nevertheless, these specifically designed MOMs, can be exploited beyond photochemical structural transformations and host-guest chemistry. The design principles aiming at such applications are finally presented as the objectives of the present thesis.

1.2. Introduction

The advent of MOMs can be considered as a watershed moment in the field of functional supramolecular chemistry. MOMs can be broadly classified as crystalline, zero-dimensional (0-D), metallo-supramolecular architectures comprising of metal-organic polyhedra (MOP), 1-D nanowires, 2-D nanosheets or as polymeric networks such as Infinite Coordination Polymers (ICPs), Porous Coordination Polymers (PCPs), Porous Coordination Networks (PCNs), Metal-Organic Frameworks (MOFs) etc. (Figure 1.1).[1] Amorphous analogues of MOMs are often referred to as metal-organic gels (MOGs) or coordination polymer gels (CPGs).[2]

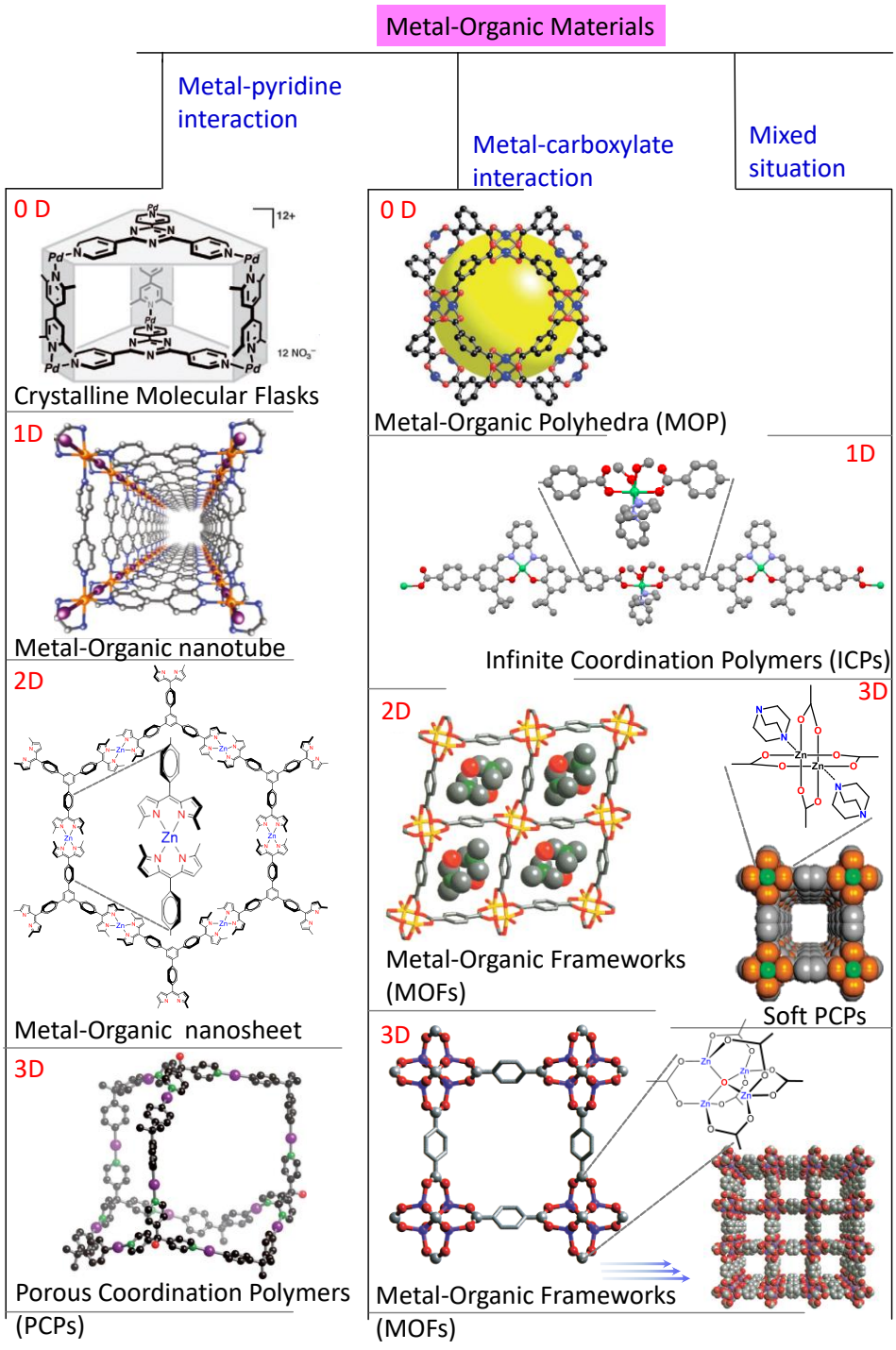

Figure 1.1. Different kinds of MOMs based on the linkages between inorganic clusters and organic joints. Illustrative examples involving pyridine and carboxylate-based ligands and their combination are demonstrated. The structure in each case can be further classified as discrete 0-D in nature or periodically extended in 1-, 2- or 3-D structures.

The first reported coordination polymer is perhaps Prussian Blue which was synthesized by German painter and colour maker Diesbach in 1704.[3] However, the use of an organic ligand to generate a coordination polymer, dates back to late 1950's, when Saito and co-workers reported crystals of complexes obtained from nitriles of aliphatic dibasic acids and Cu(I).[4] MOMs have therefore existed since long, but this research field caught special attention only in the late 1990's owing to the pioneering works of Yaghi (who coined the term MOFs),[5] Kitagawa (who coined the term PCPs)[6] and many others who consequently explored this rich arena of chemistry.[1] According to Yaghi, MOFs should be understood as MOMs built by strong covalent bonds between an inorganic cluster and an organic ligand and not as a subset of coordination polymers, formed from weak coordination linkages.[7] However, according to the International Union of Pure and Applied Chemistry (IUPAC) recommendations 2013, "coordination polymer" is the most general term. A subset of coordination polymers is often referred to as coordination networks and MOFs are considered as a further subset of coordination networks.[8] These materials are generally formed from the interaction of metal ions with an organic molecule containing a ligating functionality such as cyanide, pyridyl, phosphate, carboxylate etc. Out of these, pyridyl or carboxylate linkers are most commonly used, although mixed situations comprising of both kind of metal-ligand linkages may occur in several cases. In spite of the fact that we encounter several names and architectures (0-D, 1-D, 2-D and 3-D) in the scientific literature, we may consider all these

materials under a single category of MOMs (Figure 1.1). In 1998, based on their porous nature, Kitagawa and co-workers classified MOMs into three generations (Figure 1.2a).[9] The porosity of the first generation MOMs collapses on removal of guest molecules and this transformation is irreversible in nature. The second generation MOMs exhibit a robust framework structure and hence permanent porosity. The third generation structures, by virtue of their flexibility, exhibit dynamic porosity and can reversibly respond to both chemical as well as physical stimuli. Therefore, it has been a long held aspiration for material chemists to design and synthesize such hybrid materials that respond to various stimuli leading to the 3rd generation of hybrid porous structures. These multicomponent structures laid the foundation for stimuli-responsive MOMs.

1.3. Strategies for Designing a Stimuli-Responsive MOM

An ideal stimuli-responsive MOM responds to a single or multiple stimuli in a predictable manner. On application of a particular stimulus, the structural changes in the MOMs results in detectable response in terms of their inherent physical or chemical properties. For reasons related to the reusability of the MOMs, these changes should be reversible and the pristine structure of the MOMs should be regenerated on withdrawing the stimulus or by the application of an antagonistic stimulus.[10] Stimuli-responsive MOMs can be categorized into two groups, depending upon the nature of the applied stimulus.

- If a MOM responds to chemical species such as molecules, ions etc. or under some specific chemical environment such as pH, redox etc., it can be referred to as a chemical stimuli-responsive MOM.

- Similarly, MOMs responding to physical stimuli such as pressure, heat, light etc., can be considered as physical stimuli-responsive MOMs.

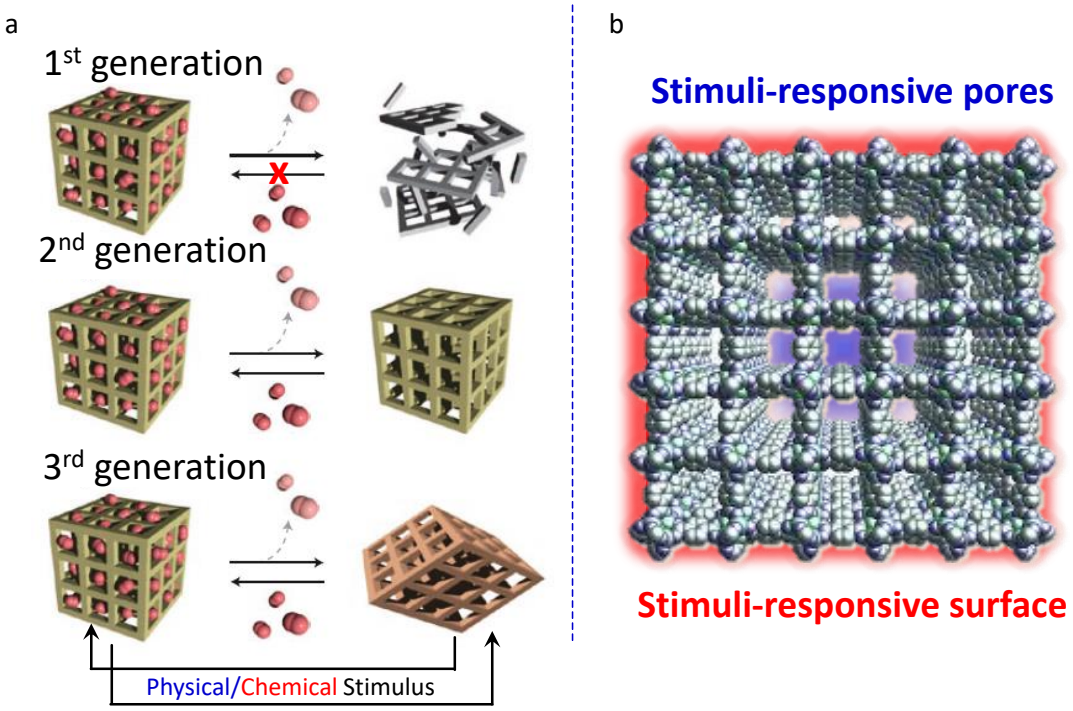

Figure 1.2. (a) Classification of PCPs proposed by Kitagawa and co-workers. (b) Stimuli-responsive sites in a MOM. Red halo represents the bulk surface while the blue halo represents the pores of the MOM.

The design principles of a stimuli-responsive MOM should involve a prior consideration of the pros and cons of any applied stimulus as well as the intended application. For applications such as drug delivery that involves biological systems, a

non-invasive external stimulus like light is preferred. In such cases, light of higher wavelength (infrared region) is desirable due to its better penetration power and minimal scattering effects. Systems responding towards chemical stimuli should be highly selective and immune towards any other competing stimuli present in the system. In most cases, a reaction-based approach is exploited. A chemical interaction with a dynamic nature is, in principle, preferred to obtain a reversible and cyclic response. A MOM can be made stimuli-responsive by making use of three different strategies *i.e.* via incorporation of a stimuli-responsive organic ligand, a stimuli-responsive guest molecule, or an inorganic cluster responding towards a particular stimulus (see Graphical Abstract). In this regard, it is observed in most cases that, according to the functionalization, the chemical/physical stimulus can either affect the nanoporous network of a MOM or act on its bulk surface (Figure 1.2b). An ideal stimuli-responsive MOM needs to meet the following criteria:

- The stimuli-responsive motif remains stable during the course of synthesis of the MOM.

- The motif retains its stimuli-responsive nature even inside the metal-organic matrix.

- The response should not be localized but occur in larger length scales, enabling easy detection by general characterization techniques.

- The structure of the MOM should remain intact even after the application of a particular stimulus.

Therefore, based on the aforementioned classification of MOMs, we would like to segregate our discussion into two major sections, initially dealing with chemical stimuli-responsive MOMs and later with physical stimuli-responsive MOMs.

1.4. Chemical Stimuli-Responsive MOMs

Changes in pH and redox environment have been widely used as chemical stimuli for responsive MOMs.[10] However, we would like to focus on MOMs that undergo changes in their shape/structure or behavior in presence of a specific chemical species (gas, competing guests or solvent molecules).

Kitagawa and co-workers have developed soft PCP based chemosensors that can decode different molecular guests, *i.e.* these PCPs can detect and differentiate aromatic guests from one another with a corresponding fluorescence readout (Figure 1.3a and 1.3b).[11] The decoding host was synthesized by embedding naphthalenediimide into the scaffold of an interpenetrated PCP network. Due to the flexible structural dynamics, an intense turn-on emission was observed when a class of aromatic compounds was incorporated inside the framework. The resulting luminescence output depended on the chemical substitution of the aromatic guest (Figure 1.3c). Such structural variations in a flexible porous coordination polymer has been further utilized for the detection of CO_2 by incorporating fluorescent guest

molecules within the PCP network (Figure 1.3d).[12] The adsorption of CO_2 induced a structural transformation in the host at a specific threshold pressure, which in turn resulted in conformational variations of the guest, distyrylbenzene (DSB). This interaction subsequently led to a change in fluorescence of DSB. Different fluorescence response from gases having similar physicochemical properties (CO_2 and acetylene) was reported in this work. Later, Chen *et al.* have reported a blue colored Co^{II} based MOF that can reversibly transform to red in presence of coordinative molecules such as H_2O and NH_3 (Figure 1.4a).[13] The colorimetric response was accompanied with the corresponding changes in the coordination environment around the metal centers, which led to a transformation in the framework topology and gate opening effect. Yaghi and Stoddart have developed a γ–cyclodextrin-based MOF that selectively adsorbs CO_2 at low pressures, involving reversible carbon fixation and decomposition via carbonate formation.[14] This binding and decomposition events could be visually identified by the color changes of a zwitterionic azobenzene-based pH indicator (methyl red) that was incorporated within the pores. The color of the MOF turned red on adsorption of CO_2. When the source of CO_2 was removed, the crystals reverted back to yellow (Figure 1.4b). This process could be repeated multiple times without any noticeable fatigue.

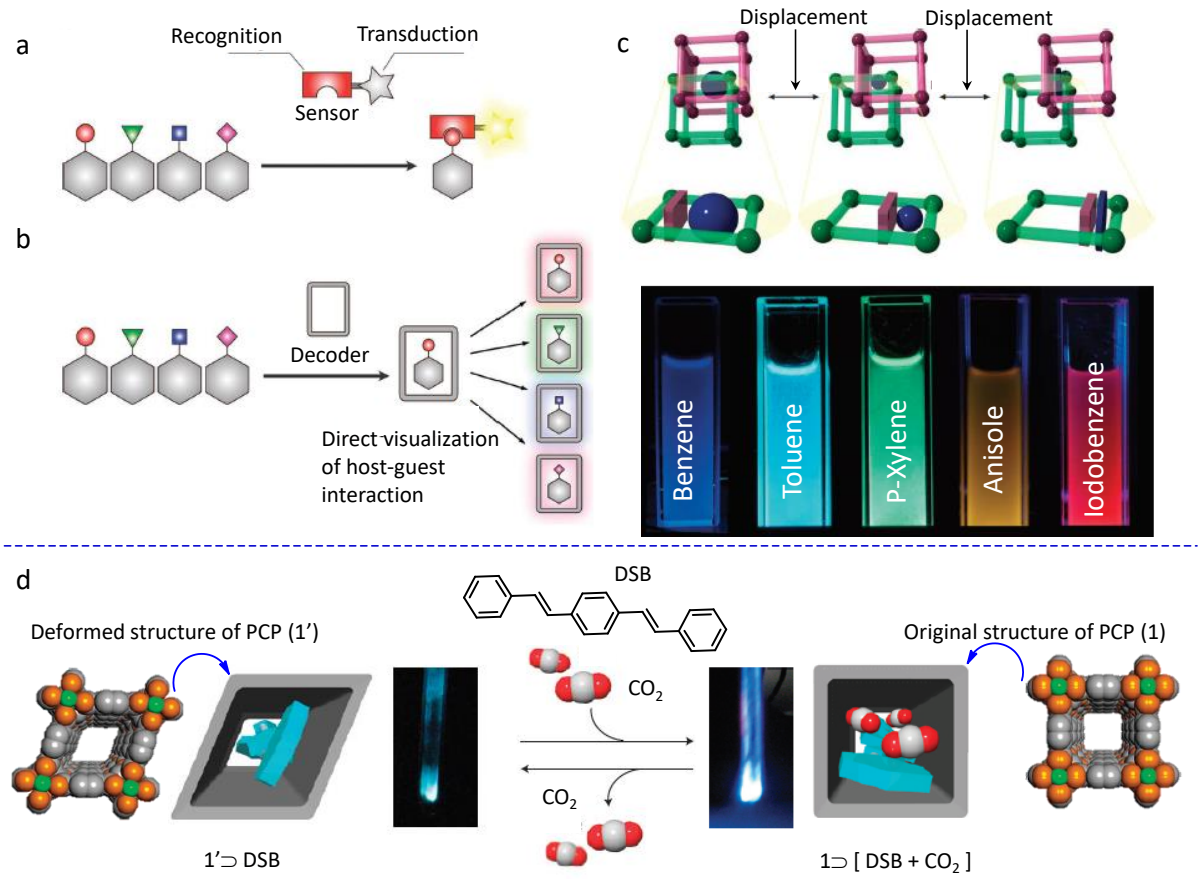

Figure 1.3. Schematic representation of the conventional protocol for (a) molecular sensing and (b) molecular decoding. (c) Guest induced changes in dimensions of PCP pores and the corresponding photograph showing luminescence of the flexible, molecular decoding PCP suspended in each organic solvent after excitation at 365 nm. (d) CO_2 adsorption induced structural changes in PCP facilitating the conformational changes in DSB (molecular structure represented) and the associated fluorescence response. The original and deformed PCP structures are denoted as 1 and 1' respectively. Photographs of the composite PCPs in two different states were taken at 195 K under ultraviolet irradiation (excitation at 366 nm).[11,12]

Moreover, chemical stimuli acting on the surface of MOMs can also be utilized for a variety of applications. For instance, Kitagawa and co-workers have shown that

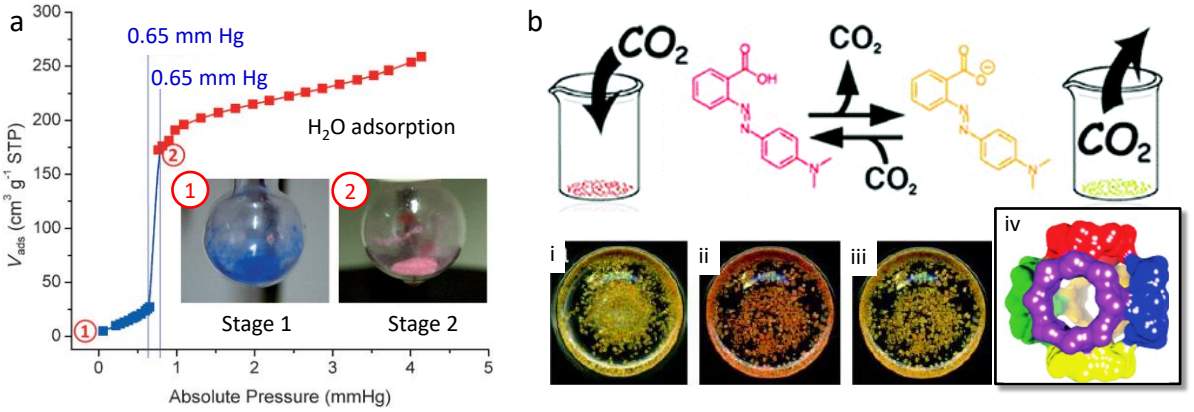

Figure 1.4. (a) Structural transformation of a MOM from its blue (1) to red (2) form during water adsorption. (b) Schematic representation and photographs of as prepared γ–cyclodextrin-based MOF encapsulating a pH indicator, methyl red (i), after CO_2 adsorption (ii) and desorption (iii). Structure of the γ–cyclodextrin-based MOF (iv).[13,14]

a combination of MOF and a self-assembling peptide diphenylalanine (DPA) can be exploited to develop an autonomous motor system (Figure 1.5a).[15] The motor works via a two-step mechanism. In the first step, addition of a framework leaching agent such as sodium ethylenediaminetetraacetate leads to the partial destruction of the MOF structure at the crystal surface. This favors the release of trapped DPA molecules into water and their self-assembly at the water/MOF interface generates a large surface tension gradient, resulting in a strong Marangoni effect and stronger propulsion. Later, Ikezoe *et al.* have demonstrated that the same effect can be reproduced without the decomposition of the MOF and can be further utilized for the generation of electrical power.[16] Similarly, chemical stimuli acting on the bulk surface of the MOMs have been exploited for the controlled release of entrapped guest

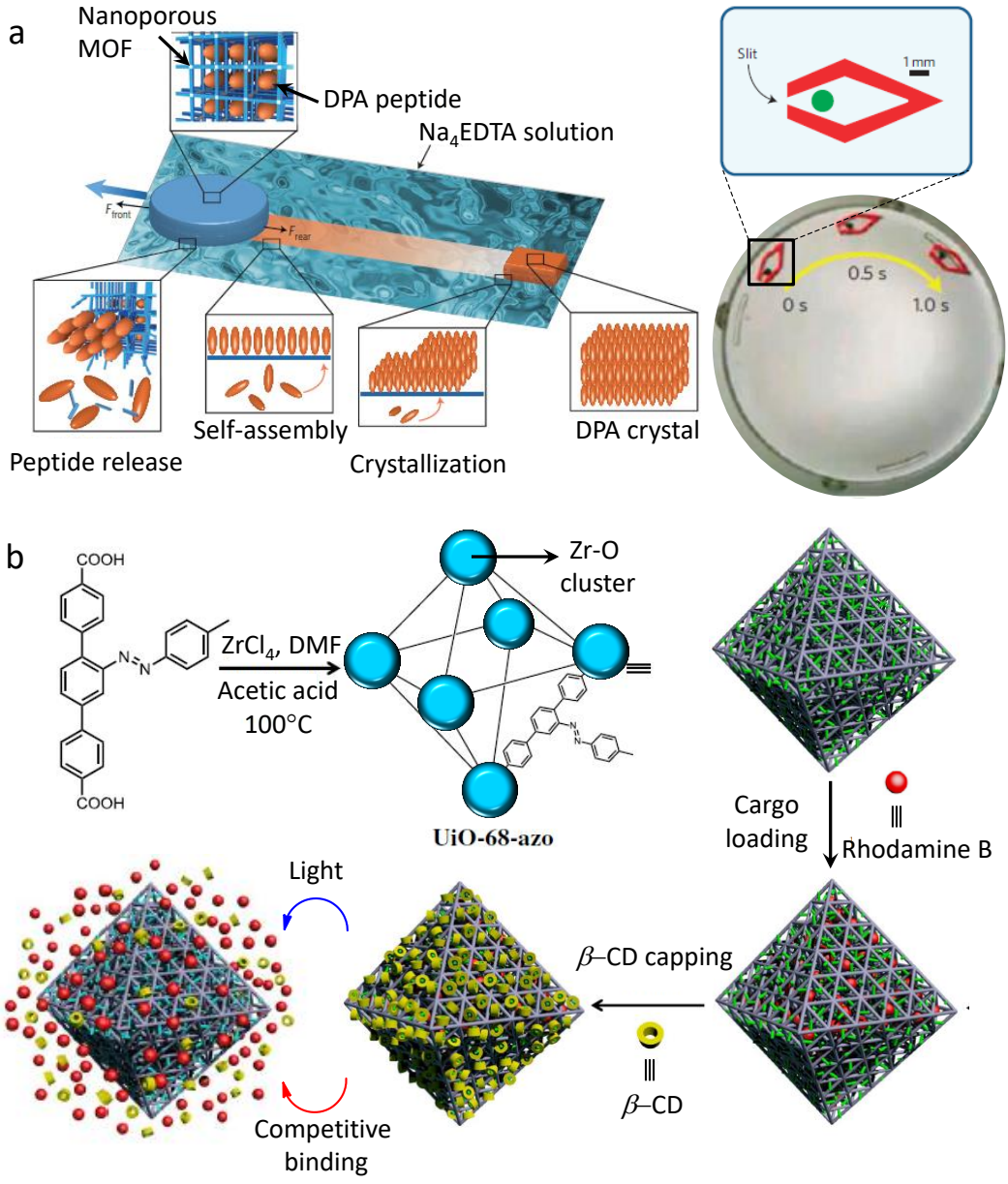

Figure 1.5. (a) Schematic representation of chemical stimuli-responsive mechanical motion of a MOF pellet making use of Marangoni effect. Photograph showing actual movement of an added mass (see inset). (b) Synthetic scheme for a MOF with its bulk surface modified using β–CD. The MOF can release its incorporated guests (Rhodamine B) in presence of either light or a competing chemical stimuli.[15,17]

molecules. Meng *et al.* have reported an azobenzene functionalized zirconium MOF loaded with an organic dye (Rhodamine B).[17] Further capping with β-cyclodextrin, forms a host-guest complex with the azobenzene stalks protruding from the surface of the MOF and prevents the release of the trapped guest molecules. Such structures can release guest molecules in the presence of a chemical stimulus (competing guest molecules) (Figure 1.5b).

1.5. Physical Stimuli-Responsive MOMs

In this section, MOMs which respond to physical stimuli such as pressure, heat and light shall be discussed. Our major focus will be on light, which is considered as the champion physical stimulus and has a great potential because of its noninvasiveness, abundance and easy availability from a renewable energy source such as the sun.

1.5.1. Pressure-Responsive or Stress-Responsive MOMs

When MOMs are subjected to high pressure, it often results in compression, amorphization or phase transitions (Figure 1.6a).[18-20] However, these pressure induced structural transformations are not necessarily reversible.[21-23] Interestingly, abnormal stress induced deformations are observed in some MOMs. Negative linear compressibility (NLC) is an example of linear elastic phenomena induced by pressure in MOMs.[24] When pressure is applied, the unit cell of a MOM is expected to undergo compression along all the three crystallographic axes. However, in certain cases a

decrease in two of the cell parameters and an increase in the third is observed. This compression induced anisotropic shrinkage behavior is referred to as NLC.

Tzeng and co-workers have reported the combined effect of pressure and moisture in determining the phase transition between two zinc based coordination polymers (Figure 1.6b).[25] One of the polymers with water molecules coordinated to zinc ions (**CP-1**) was strongly emissive, with an emission maximum at ~495 nm, while the other coordination polymer (**CP-2**) devoid of any coordinated water molecules was found to be poorly emissive. Authors were able to convert **CP-2** to the **CP-1** via mechanical grinding in the presence of water. Simple heating of **CP-1** transformed it back to **CP-2**. Ross and co-workers have reported the effect of pressure (0–4.7 GPa) on the photoluminescence properties and crystal structure of a terbium-adipate based MOM.[26] Within this pressure range, the MOM undergoes three phase transitions that leads to changes in the number of symmetry independent Tb^{3+} sites in the crystal lattice, thereby altering its $^5D_4$-$^7F_5$ emission profile.

Mito and co-workers have demonstrated pressure induced structural transformations and magnetic property modulation of three types of bimetallic MOM magnets, namely $Mn^{II}Cr^{III}$ (ferrimagnet), $Ni^{II}Cr^{III}$ (ferromagnet) and $Ni^{II}Fe^{III}$ (ferromagnet) (Figure 1.6c).[27] The work highlights two significant facts: (a) the pressure induced shrinking of the bridging structure and a concomitant increase in the antiferromagnetic contribution results in a positive impact on ferrimagnets and a

negative impact on ferromagnets and (b) high responsivity and reversibility of the frameworks are directly related to their strength and spatial margin.

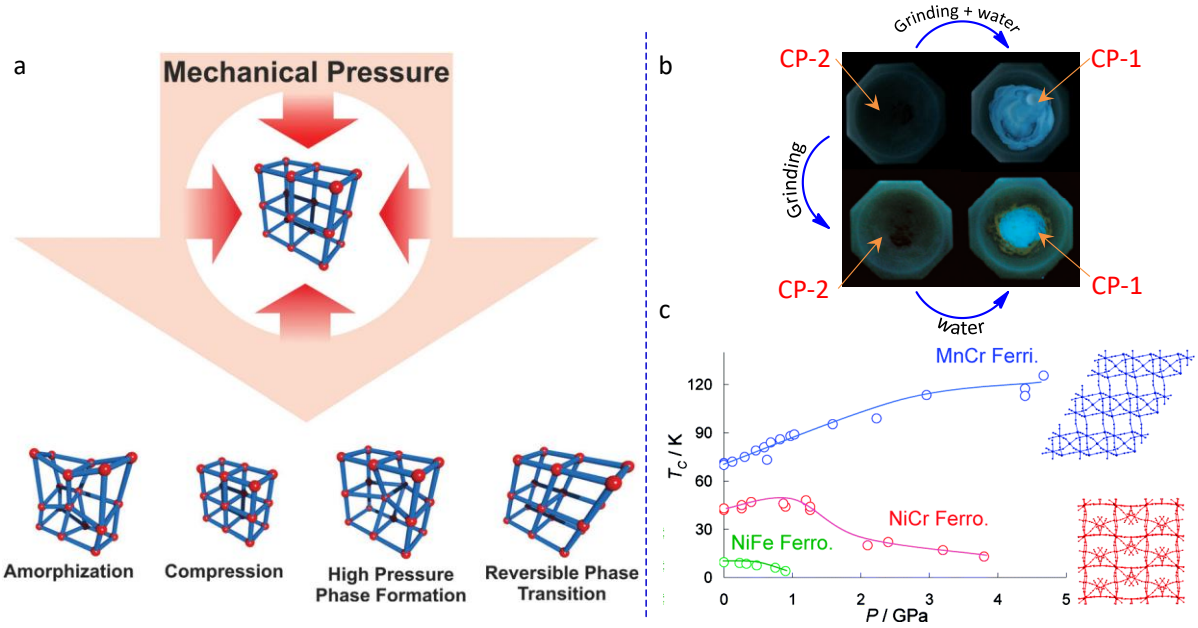

Figure 1.6. (a) Possible modes of structural transformations a MOM can undergo, upon application of a mechanical pressure. (b) Moisture dependent mechanochemical behavior, tuning the luminescent properties of a MOM. (c) Changes in magnetic properties of MOMs induced by pressure.[25,27,28]

1.5.2. Thermoresponsive MOMs

Although heat is considered to be energy expensive, it has been immensely exploited as a physical stimulus in MOMs that exhibit reversible changes in their lattice parameters in response to the changes in temperature.[28] Henke and Fischer have reported a MOM with dangling side chains that in the as-synthesized state possessed a framework with large pores entrapping solvent molecules. Upon activation, the pores

shrunk and became narrow (Figure 1.7a).[29] When the temperature was further raised to 493 K, the increase in the thermal mobility of the linker side chains resulted in swelling of the MOM, leading to larger pores.

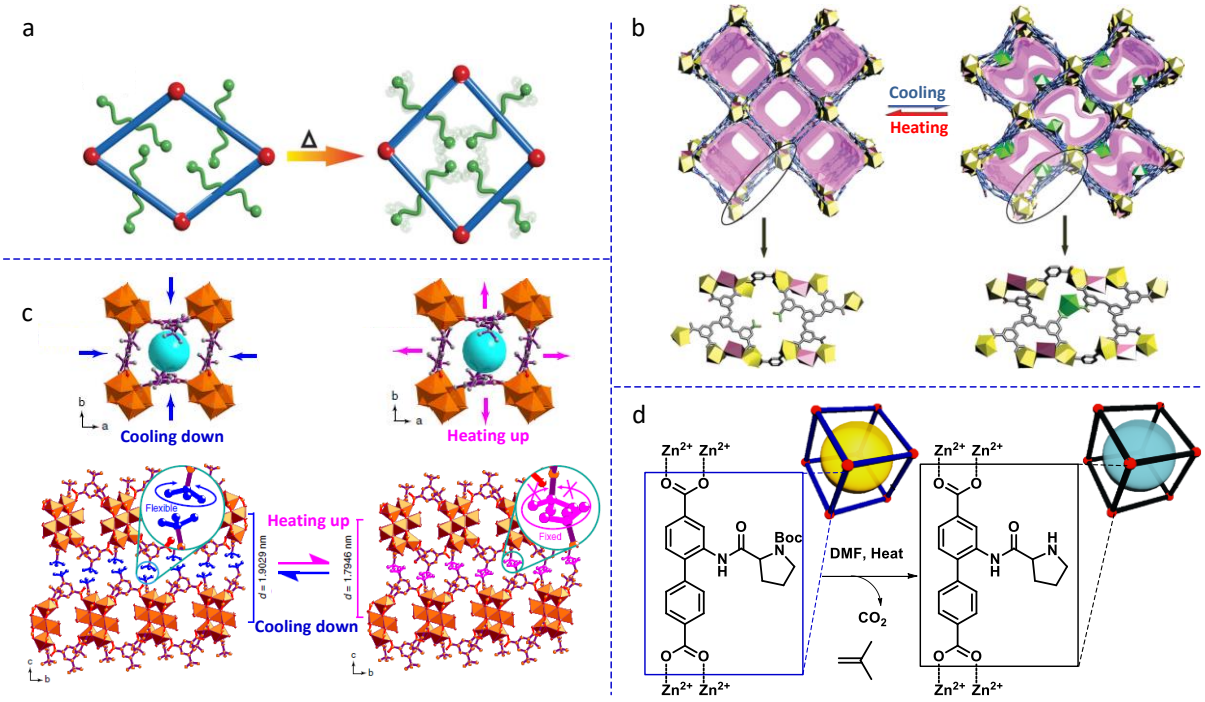

Figure 1.7. (a) Thermoresponsive swelling of pores in a MOM. (b) Pore modification in a MOM in response to temperature, with concomitant release/capture of free intrinsic Eu^{3+} ions. (c) Changing of interlayer distance and in the crystallographic *ab* plane of a 2-D MOM due to the shrinkage (heating) and expansion (cooling) of the framework. (d) Post-synthetic thermoresponsive chemical modulation in a MOM.[28,30,31]

Zhang and co-workers have reported temperature-controlled reversible single-crystal to single-crystal transformation in a MOM, resulting in specific capture/release of free intrinsic Eu^{3+} ions (Figure 1.7b).[30] At room temperature, the MOM contains free carboxylate groups bordering the 1-D square channels containing free Eu^{3+} ions.

Upon lowering the temperature, the carboxylate-hooks spontaneously captures the free intrinsic Eu^{3+} ions, leading to the distortion of the 1-D square channels. In another report, Zhao and co-workers have reported molecular sieve membranes based on 2-D MOMs for effective gas separation. These membranes were found to be thermally switchable with good reversibility, thanks to the molecular level flexibility of its metal-organic components (Figure 1.7c).[31]

Temperature has also been used as a stimulus to perturb the proton conductivity of MOMs. Kitagawa and Shimizu groups have independently demonstrated high temperature induced proton conductivity in MOMs under anhydrous conditions. While the former reported a maximum proton conductivity of 2.2×10^{-5} S cm^{-1} at 120 °C,[32] the latter reported a value almost a magnitude higher (5×10^{-4} S cm^{-1}) at 150 °C.[33] Ghosh and co-workers have also demonstrated similar temperature dependent proton conductivity (1×10^{-4} S cm^{-1} at 150 °C) under anhydrous conditions. The MOM also showed high degree of proton conductivity in presence of water vapor.[34]

Apart from imparting changes in the porous architecture, thermal treatment can also alter the molecular composition of the MOM. For example, organic linkers containing amine groups protected by bulky *tert*-butylcarbamate (Boc) group can be deprotected by heating to higher temperatures (Figure 1.7d).[35-36] This kind of thermal post-synthetic modification of MOM may alter its degree of interpenetration and pore functionalization.

1.5.3. Photoresponsive MOMs

Unlike pressure and heat, light is a cheap as well as non-invasive stimulus, which can instantly be focused at a precise location and controlled by the use of different wavelengths and intensity. Photoresponsive smart materials have therefore attracted great attention of the scientific community over the past several years. Out of several photoresponsive systems, the chemistry of azobenzenes and diarylethenes has been widely explored in the area of MOMs, which will be discussed in the forthcoming sections.

1.5.3.1. Photochemistry of Diarylethene-derived MOMs

Diarylethenes appended with heterocyclic aryl groups are considered as an important class of molecules because of their ability to undergo fatigue resistant photochromic transformation between their open ring (generally colorless) and closed ring (generally colored) isomers (Figure 1.8a). Moreover, these transformations are thermally irreversible.[37] This kind of photoinduced cyclization or ring-opening in solution and in solid state (single crystal to single crystal) has been reported in a few MOMs. Clever and co-workers have investigated MOM cages composed of dithienylethene and demonstrated the reversible interconversion between a structurally flexible open form and a rigid closed form, respectively with UV and

visible light.[38] These structural changes were also accompanied by a change in the affinity of the cage towards an anionic guest, $[B_{12}F_{12}]^{2-}$(Figure 1.8b).

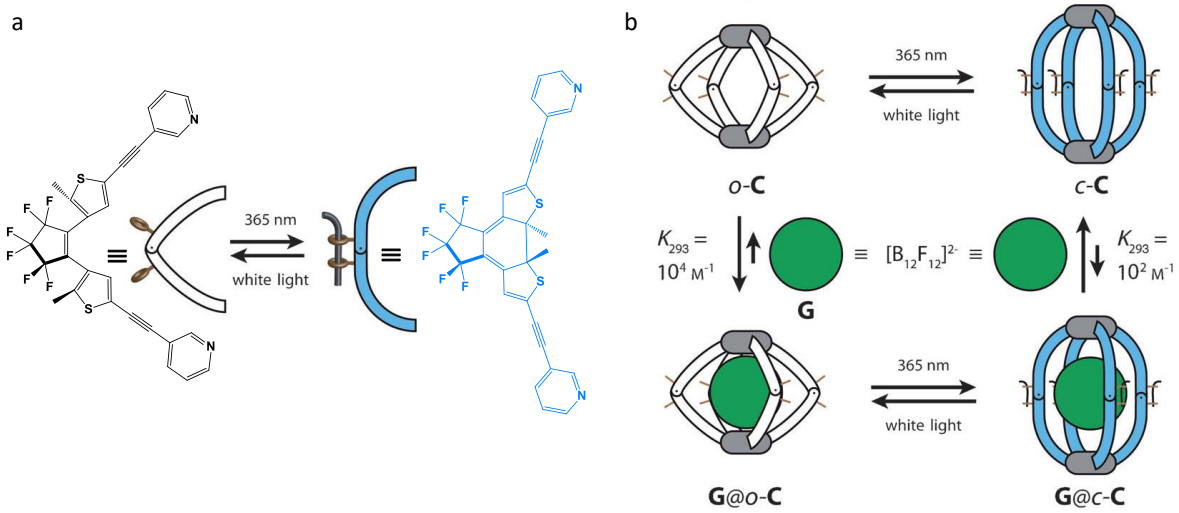

Figure 1.8. Schematic and structural representation of (a) photoinduced cyclization/ring opening of a diarylethene-based ligand and (b) in a 0-D MOM, showing the corresponding capture and release of an anionic guest $[B_{12}F_{12}]^{2-}$.[38]

Grzybowski and co-workers utilized this chemistry after imprinting micropatterns of a diarylethene dye into the crystals of a MOM and these modified crystals were used for monitoring environmental changes caused by light exposure.[39] Luo *et al.* have used a photosensitive diarylethene ligand to construct a photochromic MOM. Low energy CO_2 capture and release was demonstrated with a record high desorption capacity under irradiation conditions (Figure 1.9a).[40] A general perception might be that, such changes are more feasible in soft hybrid materials like supramolecular gels. In a quest to answer this question, Zhang and co-workers incorporated a photochromic dithienylethene moiety as a linker in a metal-organic gel

exhibiting thermoreversible sol-gel transition.[41] The gel was also found to respond towards water, anions as well as light, and reversible photochromism was observed (Figure 1.9b).

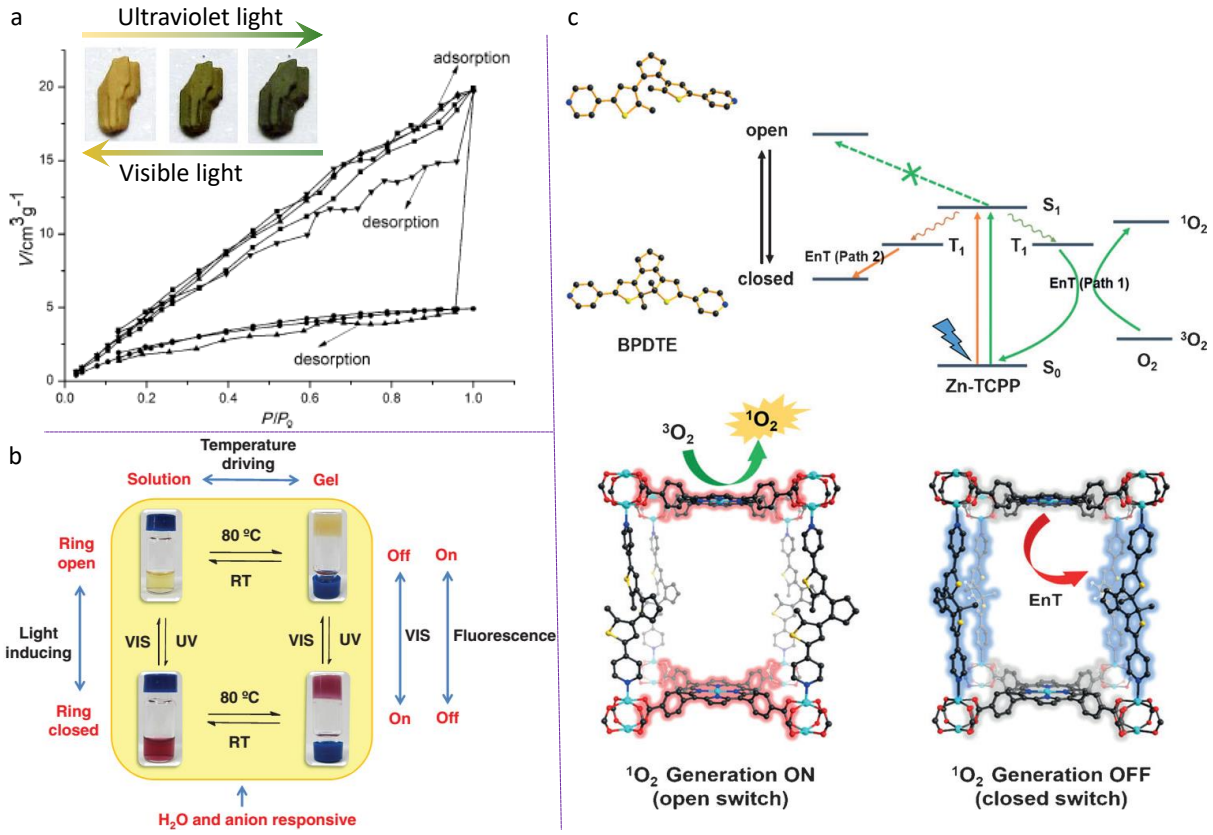

Figure 1.9. (a) Photoinduced changes in CO_2 adsorption and desorption isotherms in a diarylethene-based MOF. Photographs showing the photochromic changes in the MOF crystal upon exposure to UV and visible light. (b) A diarylethene-based metal-organic gel that responds to multiple stimuli like light, heat, anions and water. (c) Photoinduced tuning of energy transfer pathways between open and closed forms in a diarylethene-based MOF to control singlet oxygen generation.[40,41,43]

Shustova and co-workers have shown that the open and closed forms of a diarylethene ligand having different absorption properties can provide different pathways for energy transfer to porphyrins in a mixed ligand MOF.[42] Later, Zhou and

co-workers extended these findings and demonstrated that, porphyrins being a well-known photosensitizer, such MOFs can exhibit photochemical control over singlet oxygen ($^1O_2$) generation (Figure 1.9c).[43-44]

1.5.3.2. Photochemistry of Azobenzene-derived MOMs

The chemistry of photoinduced *cis-trans* isomerization is essentially nature inspired, since it is well-understood and investigated with regard to the phenomenon of vision. Such a change in molecular orientation, as in *cis-trans* isomerization, leads to larger structural changes and is not expected to occur in the rigid crystalline state. Azobenzenes can exist in either *trans* or *cis* conformation. Azobenzene photochemistry may be one of the most widely studied *cis-trans* isomerization in synthetic systems.[45-47] The *cis-trans* isomerization can occur via the irradiation of light of appropriate wavelength, in presence of mechanical stress or electrostatic stimulation. Azobenzene exhibits remarkable photostability and negligible photodecomposition even after prolonged irradiation. The large change in the size, shape and polarity of the molecule associated with *trans* to *cis* photoisomerization, has been extensively used to design a variety of smart materials when integrated into polymers, elastomers, liquid crystals, etc. Incorporation of azobenzene in various self-assembled soft materials like supramolecular and polymeric gels has facilitated the reversible modulation of their functional properties.[48-49]

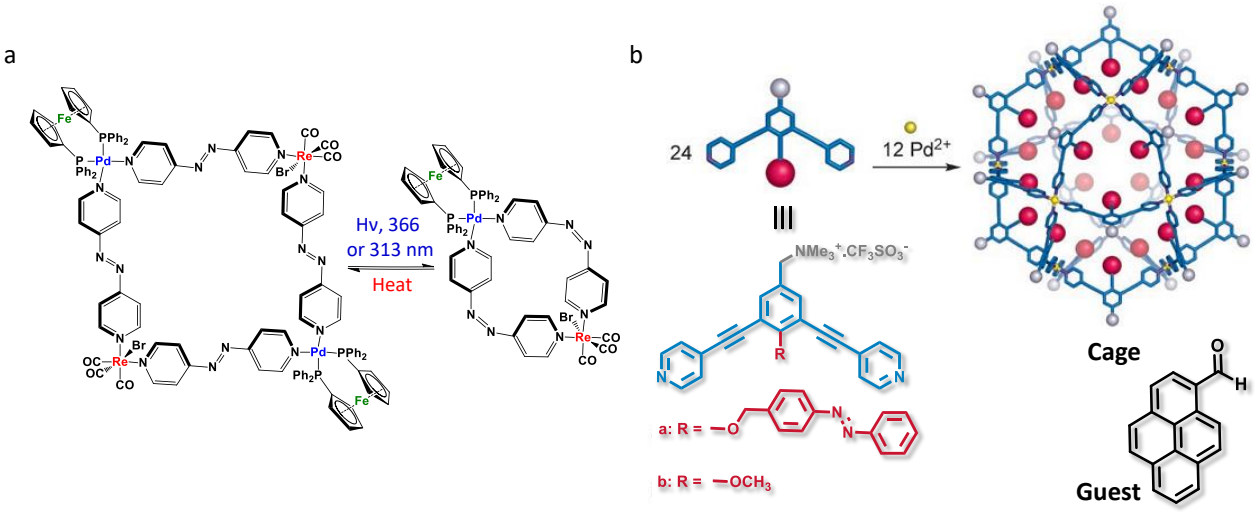

Figure 1.10. (a) *E*/*Z* isomerization of azobenzenes within 0-D MOMs, leading to an interconversion between tetranuclear to dinuclear Pd-Re metallo-supramolecular squares. (b) Schematic and structural representation of the azobenzene functionalized $M_{12}L_{24}$ spherical complex and the chemical structure of the guest used in the study.[77]

While efficient photoisomerization of azobenzene has been shown to facilitate drastic changes in properties, partial isomerization can also be advantageous for the controlled property modulation as demonstrated with the Ostwald type ripening of organic nanodots to 1-D supramolecular rods and chopping of gel fibers.[50-51] Another interesting report pertaining to partial isomerization of an azobenzene moiety is the thermally assisted photonic inversion of supramolecular handedness in π-systems.[52] Similarly, *E*/*Z* isomerization of azobenzenes has been used for photonically switching the properties of MOMs.

Lees and co-workers have synthesized a series of Pd-Re as well as Pd tetranuclear squares bridged by photoresponsive linkages. Irradiation of these squares with ultra violet (UV) light led to the formation of the corresponding dinuclear

squares which subsequently reconverted to the tetranuclear squares on thermal treatment (Figure 1.10a).[53] The Pt-Re squares did not exhibit such transformations, instead a photo-triggered disassembly of the metallo-squares was observed and all processes were influenced by the lability of the metal centres. In 2007, Fujita and co-workers reported a photoresponsive cationic spherical metallo-supramolecular cage complex composed of 24 pyridine based bent bridging ligands and 12 metal ion centres.[54] The ligand was designed in such a way that the azobenzene functionality attached to the concave side of the bridging ligand always project towards the core of the spherical complex, making it hydrophobic in nature (Figure 1.10b). In 1:1 CH_3CN/H_2O, a hydrophobic probe, 1-pyrenecarboxaldehyde was incorporated within the pores of the cage. Upon UV light irradiation, the interior of cage became less hydrophobic as *cis*-azobenzene is more polar than *trans*-azobenzene, resulting in a weaker interaction between the cage and the guest thereby driving the guest out of the host cavity. Later in 2010, Clever *et al.* demonstrated the visible light triggered photoisomerization and release of *cis*-4,4′-azobenzene bis-sulfonate guest from a metal-organic cage. The MOM was composed of four rigid, bent bis-monodentate pyridyl ligands and two Pd(II) ions.[55] These cages were functionalized with polyethylene glycol (PEG) chains. When less soluble cages (without the glycol chains) were used, photoisomerization of the guest followed by its release from the cage cavity caused immediate crystallization via cross-linking of the individual cages. It was also observed that even excess *cis*-isomer can promote such crystallization

(without the need of any photoisomerization), although the morphology of the crystals (oval shaped) differed from that obtained via photoisomerization (square shaped).

Although a number of 0-D azobenzene-based MOMs were reported, the isomerization of azobenzenes as direct linkers in the structural backbone of rigid polymeric MOMs, has always been a challenging task. However, Stock and co-workers, were able to show that a covalently linked azobenzene moiety dangling in the MOF pore walls retained its inherent isomerization ability.[56] Soon after this, the same group extended this chemistry to a large number of frameworks and also via post-synthetic modifications, whereby successful photoisomerization of azobenzene moieties was demonstrated in the synthesized MOFs.[57-59] Subsequently, Zhou and co-workers utilized this chemistry to reversibly alter CO_2 uptake via photochemical and thermal treatment of an azobenzene appended MOF (Figure 1.11a).[60] A structural envelope generated from the powder X-ray diffraction data showed an increase in electron density around the Zn_4O clusters in the UV irradiated materials (*cis*-state) than in the heat treated (*trans*-state) ones, justifying why CO_2 molecules faced a difficulty in approaching the metal clusters, the main sites for CO_2 adsorption. The interpenetrated nature induced steric restrictions in these MOFs and a delayed change of gas adsorption properties limited the photochemical applications of these MOMs.

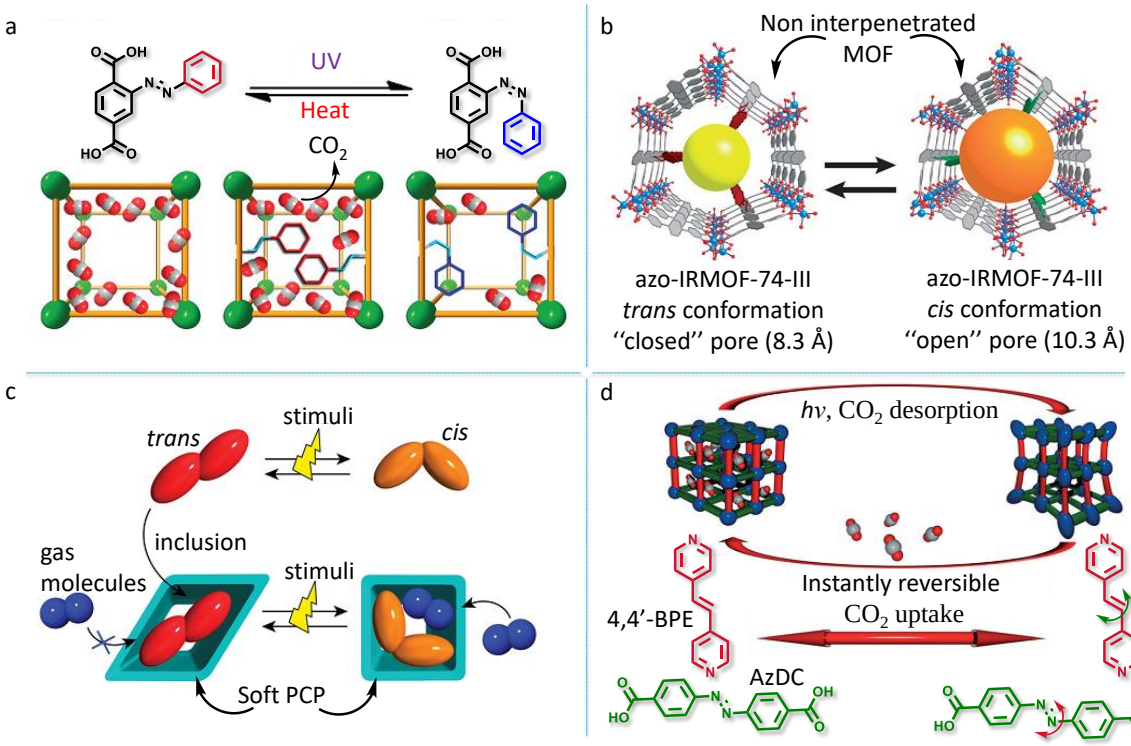

Figure 1.11. Schematic representation of (a) reversible alteration of CO_2 uptake in a MOF with an azobenzene appendage, (b) a non-interpenetrated MOF with an azobenzene appendage that can encapsulate a luminescent dye as a guest, (c) photoinduced structural changes of an azobenzene guest in a soft PCP host, affecting its gas adsorption behavior and (d) dynamic photoswitching in a MOF containing azobenzene-4,4'-dicarboxylate (AzDC) and *trans*-1,2-bis(4-pyridyl)ethylene (4,4'-BPE) ligands capable of low energy CO_2 uptake and release.[77]

Yaghi and co-workers, therefore, tried to address this challenge using a MOM having an azobenzene appendage.[61] In this MOF-74 based structure, the magnesium clusters and organic ligands stack in a linear fashion, leading to the formation of large, non-interpenetrated 1-D hexagonal pores (Figure 1.11b). Spectroscopic studies revealed that an encapsulated luminescent dye was not released under ambient conditions. The release of the dye from the pores was triggered only upon irradiation

of the MOF at the isosbestic point in the absorption spectrum of the ligand during photoisomerization, inducing a wagging motion of the azobenzene appendages via a two way *cis–trans* isomerization. In another strategy, Kitagawa and co-workers reported the isomerization of azobenzene as a guest within the pores of a flexible MOM.[62] The isomerization yield was found to be higher than that in the previous reports, probably due to the comparatively less steric constraints around the azobenzene guests (Figure 1.11c). The photoisomerization of azobenzene triggered a remarkable structural transformation of the host MOM framework. The MOM with azobenzene in the *trans*-state did not adsorb N_2 due to the close contact between the host framework and the encapsulated azobenzene molecules that caused pore blockage. Upon UV irradiation, the formed *cis*-azobenzene molecules caused the expansion of the framework to a tetragonal form with an 8.3–fold increase in N_2 adsorption. In this work, light induced photoisomerization of azobenzene was utilized to trigger guest (N_2) capture rather than release, via light induced host to guest structural transformation. Such isomerization also depends on the close packing of the guest molecules within the MOM pores.[63] A MOF prepared by Hill *et al.* exhibited low energy photoresponsive behavior, where a dynamic bending of the azobenzene core was observed; although on a local scale (Figure 1.11d).[64] During adsorption experiments, this photoresponsive behavior was exploited to trigger the uptake and release of CO_2 in real time. On exposure to UV light, 64% of the adsorbed CO_2 was

instantaneously released and this was achieved using broadband radiation, much like concentrated solar sources.

Perhaps, the next bigger challenge is to control such stimuli responsive behavior at the mesoscopic dimensions, to construct devices out of functional materials for real world applications.[65] Unearthing unprecedented properties from MOMs by exploiting chemistry at the mesoscale level is therefore no exception.[66,67] In this context, photoswitching and cargo release in a dual reservoir and valve layered, surface mounted metal–organic framework (SURMOF) can be considered promising (Figure 1.12a).[68] Quartz crystal microbalance experiments proved that the release of the guest molecule could be optically triggered. Synthesis of such intelligent two component systems is possible by allowing the growth of a second layer of photoresponsive MOF over a SURMOF via liquid phase epitaxy. MOFs having such interfaces between two distinct mesoscale crystal boundaries can be of great significance in near future. Recently, control on the solubility and guest inclusion properties of a MOP (0-D MOM) using light has been reported (Figure 1.12b).[69] A MOP with azobenzene appendages pointing outside the polyhedral nanospace favors π–π interactions with an adjacent MOP, leading to aggregation and formation of an insoluble precipitate. The mesoscopic pockets created in between the MOPs are suitable for inclusion of comparatively large guest molecules like methylene blue.

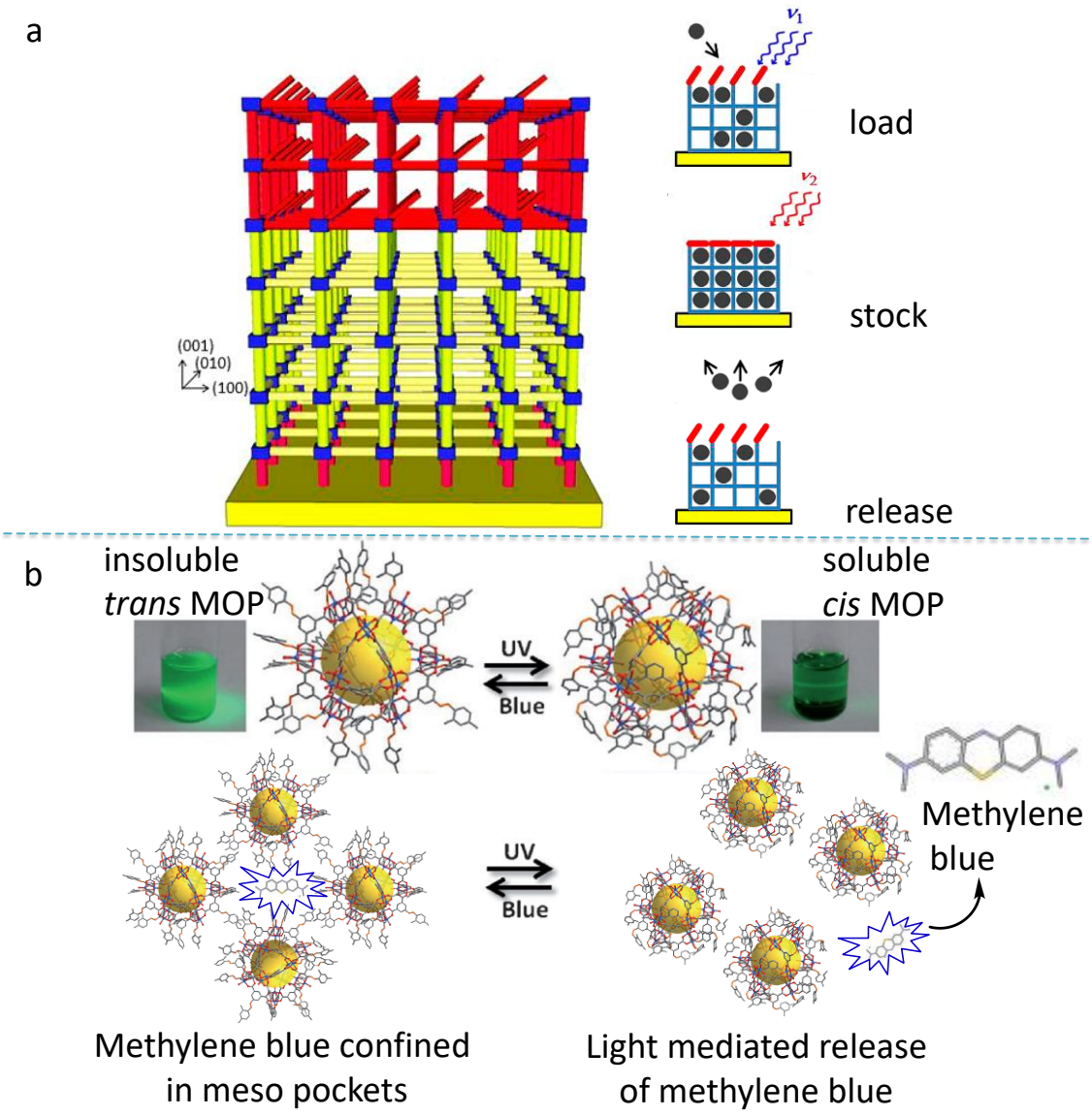

Figure 1.12. Photoisomerization at a MOM surface. (a) Schematic representation of light mediated cargo capture, storage and release in a two component SURMOF. (b) Photo controlled solubility variation and cargo (methylene blue) release from mesoscopic pockets in a MOP.[77]

Upon irradiation with UV light, the *trans*-azobenzene appendages isomerize to the *cis*-state, thereby disfavoring π–π interactions, leading to the disaggregation and hence an increase in solubility. In addition to this, *cis*-azobenzene, due to its higher

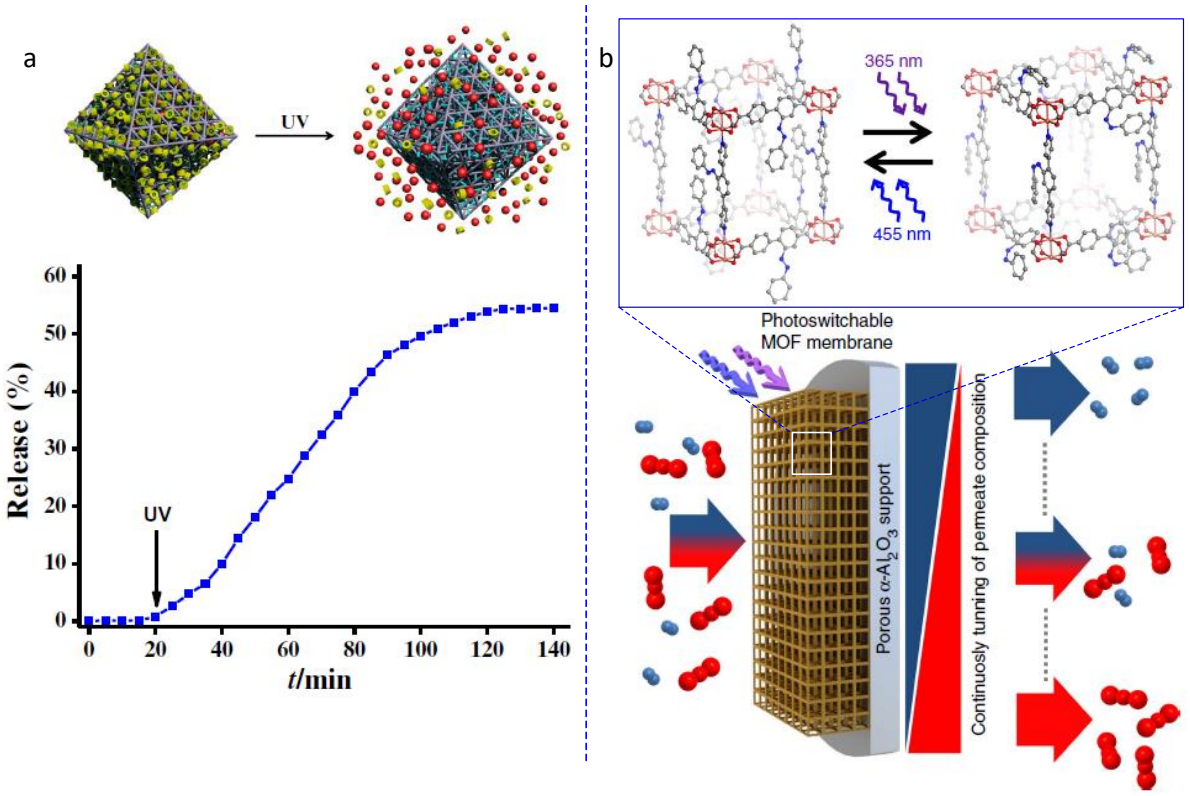

Figure 1.13. (a) Photoinduced guest release in a β–CD modified MOF. Photoinduced release profile of encapsulated dye (rhodamine B). (b) Schematic illustration of a photoswitchable MOF membrane with tunable molecular selectivity. Left-hand side of the membrane shows the molecular feed mixture depicted in red and blue. The permeate composition on the right-hand side of the membrane can be continuously tuned by photoirradiation. The structure of the MOM and the associated photochemical changes are represented along with.[17,70]

dipole moment facilitates the solubility of the MOP in polar solvents. This disaggregation process is accompanied by simultaneous release of the trapped methylene blue molecules. Both guest capture as well as precipitation can be reversibly triggered using blue light as the antagonistic optical stimulus and the whole process can be repeated for several cycles. Therefore, via proper surface functionalization, the guest release profiles of a MOM can be greatly tuned. For

example, in the MOM prepared by Meng *et al.* as described in section 1.4., the surface functionalization with *β*–CD not only allows the guest release in presence of chemical stimuli, but also in presence of light (Figure 1.5b).[17] UV light induces *trans* to *cis* isomerization of the azobenzene stalks over the MOF surface favoring the release of both *β*–CD and the encapsulated rhodamine B molecules (Figure 1.13a). Very recently, Wang *et al.* have reported photo-tunable molecular separation using azobenzene based MOF membranes. By controlling the irradiation times or by simultaneous UV and visible light irradiation, authors were able to control the *cis*-*trans* ratio. This affects the membrane permeability and hence the separation factor to a large extent and could be continuously fine-tuned (Figure 1.13b).[70]

Despite the reports on reversible photoisomerization mentioned above, there are two major drawbacks that limit the practical application of azobenzenes in biological systems and in the field of materials. The major disadvantage is the requirement of UV light to induce the $E \rightarrow Z$ isomerization via $\pi \rightarrow \pi^*$ excitation. UV irradiation is known to be invasive and potentially interfering with biological samples, thereby destroying the specimen. The typically incomplete reverse $Z \rightarrow E$ photoisomerization, induced by irradiating in the visible region can be considered as another potential problem. In most of the azobenzene derivatives the $n \rightarrow \pi^*$ absorption bands of both *E*- and *Z*-isomers mostly overlap with each other (Figure 1.14a and 1.14b).

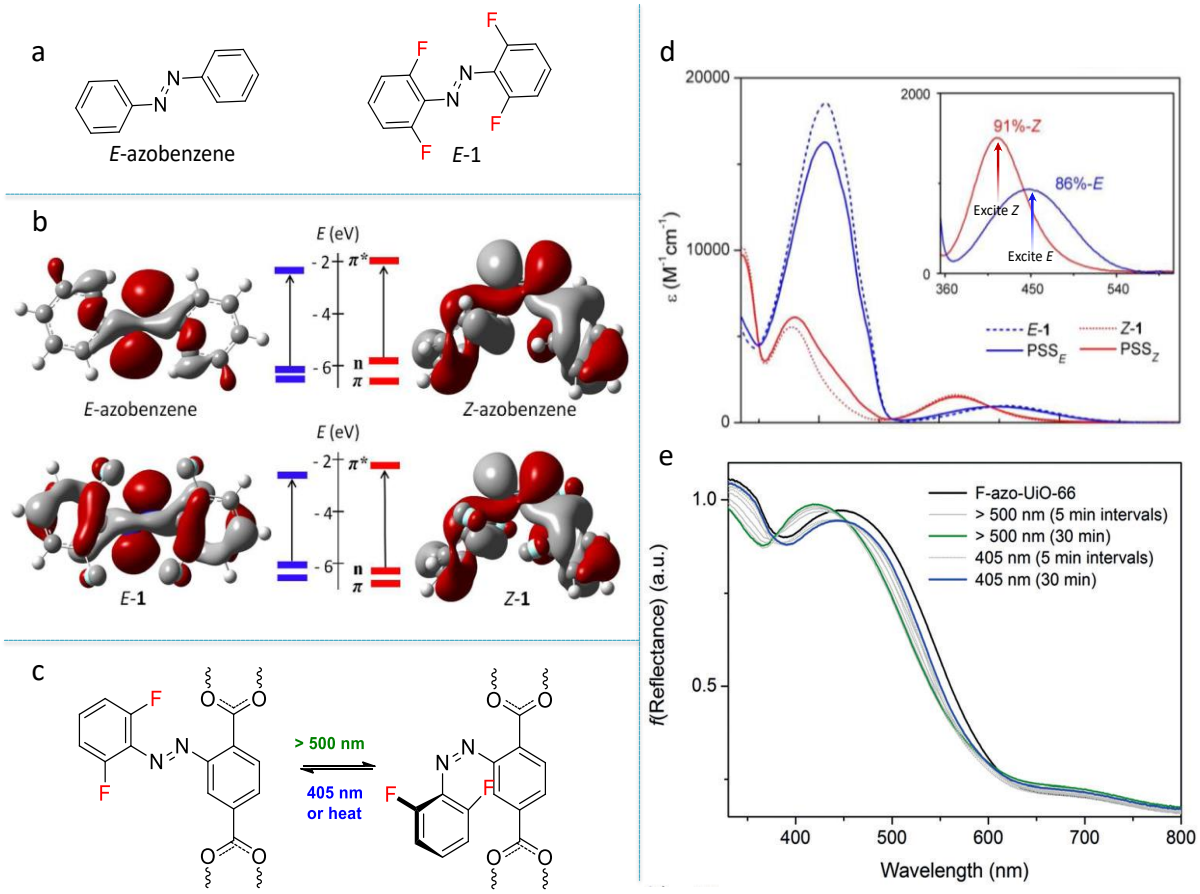

Figure 1.14. (a) Molecular structure of *trans*-azobenzene (*E*) and *trans*-*o*-tetrafluoraoazobenzene (*E*-1). (b) Energy level diagram of the π, *n*, and π^* orbitals of azobenzene and *o*-tetrafluoraoazobenzene in *trans* (*E* and *E*-1) and *cis* (*Z* and *Z*-1) states respectively. (c) Two way photoisomerization with visible light in a MOF with *o*-difluoraoazobenzene appendage. Photoinduced changes in the UV-vis spectra of fluorinated azobenzene derivatives in (d) solution state where PSS represents photostationary state and (e) in the MOF (F-azo-Uio-66).[71,75]

Therefore, while exciting the *Z* isomer with visible light leads to *E*→*Z* isomerization in both directions, as a result *E* rich photostationary states are deprived after back-switching. These limitations can be circumvented by separating the $n\rightarrow\pi^*$ bands of *E*- and *Z*-isomers by clever modification of the azobenzene chromophore.[71-74] Thus, in principle, very high to complete *E*/*Z* photoconversions can be achieved

using visible light, that can in turn be used to isomerize each isomer selectively if the separation between the two $n \rightarrow \pi^*$ bands is large enough. Such a separation of the $n \rightarrow \pi^*$ bands of *E*- and *Z*- isomers of azobenzenes was achieved by incorporating fluorine atoms ortho to the azo moiety (Figure 1.14a and 1.14b). Castellanos *et al.* incorporated *o*-difluoroazobenzene photoswitches as pendant groups in aluminium and zirconium based MOMs (Figure 1.14c).[75] Both the organic ligand as well as the MOM (F-azo-Uio-66) showed reversible photoresponse towards blue and green light (Figure 1.14d and 1.14e). In another report, Lyndon *et al.* demonstrated visible light triggered capture and release of CO_2 molecules by a nanocomposite of MOMs, formed via adsorption of a visible light responsive azobenzene dye (methyl red) on to its external surface.[76]

The introduction of stimuli-responsive functionalities within MOMs to develop smart porous materials has therefore been a tedious, but interesting research odyssey. In this chapter, we have tried to highlight the major milestones and challenges in the field of stimuli-responsive MOMs.[77] Inspired by the extent of available knowledge and the promising applications, we planned to explore the possibilities of designing stimuli-responsive MOMs with unprecedented properties, spatiotemporal control and applications, leading to novel multifunctional materials. With a huge library of already reported MOMs and much more to be discovered, controllable and non-invasive stimuli-responsiveness is envisioned to open up fascinating research in the field of porous materials with real world applications.

1.6. Objectives of the Present Investigation

Azobenzene photochemistry has been successfully applied in the design of polymers, elastomers and liquid crystal based smart materials. However, from **Chapter 1**, one can understand that the exploitation of azobenzene photochemistry in MOMs is limited to the development of porous materials, capable of capturing and/or releasing guest molecules, assisted by photoirradiation. Therefore, the utilization of azobenzene-based MOMs for other significant and scientifically relevant applications needs to be specifically addressed to:

- investigate the self-assembly pathways of porous materials by the application of physical stimulus such as light.
- develop host-guest systems with controllable and programmable, step-wise release and encapsulation profiles of guest molecules.
- fabricate functional (such as bioinspired superhydrophobic) surfaces composed of azobenzene based MOMs, having nano-meso scale rough morphological features. For instance, light controlled variation of hydrophobicity of such surfaces can be an added advantage.

One of the fundamental problems that scientists are trying to understand is, how complex structural forms evolve from simple precursors in both living as well as non-living systems. It is believed that molecular building blocks are transformed into complex architectures through the mesoscopic space, with the aid of assembly

processes induced by chemical and physical forces.[65,78] Having a clear balance between molecular aggregation and crystallization, one can create a number of functional hybrid superstructured materials exhibiting exceptional properties, via self-assembly at the mesoscale level.[79] From a chemist's view point, natural evolution of mesoscopic objects is via a combination of chemical synthesis, molecular self-assembly (supramolecular chemistry) and co-ordination chemistry (the very basis of metal-organic materials chemistry) in soft scaffolds, triggered by physical forces such as heat, magnetic fields and light. Therefore, in **Chapter 2**, we have combined the MOM and gel chemistry to create photoresponsive structures to understand the effect of light on the kinetic pathways of mesoscopic structural evolution in synthetic molecular systems. We demonstrate that, light induced photoisomerization of an azobenzene based ligand can restrict the crystal growth process of a MOM via coordination modulation. This modulation leads to soft viscoelastic materials having different morphologies (flowers and stars) and properties (porosity and viscoelasticity). It may further be noted that post-synthetic photoisomerization is not observed in any of the materials due to the rigid nature of the framework.[80]

Our next approach was to generate solution processable MOMs for the controlled stimuli-responsive release of guest (cyclodextrin) molecules. Herein, we synthesized a water soluble MOM, composed of an azobenzene-based ligand tethered with a chiral metal oxide chain on one side. The azobenzene ligands act as suitable binding sites for cyclodextrin molcules. These multicomponent systems can reversibly

encapsulate and release cyclodextrins in response to a physical stimulus such as heat and chemical stimulus such as competitive guest molecules. The release and capture profiles can be specifically controlled and programmed using the thermodynamic advantages of a system in equilibrium. Such controllable stimuli-responsive reversible guest encapsulation and release is demonstrated in **Chapter 3** using optical characterization techniques such as induced circular dichroism spectroscopy.

Since MOMs can form various nano-meso-microscopically structured morphological features, we thought of fabricating superhydrophobic surfaces with MOMs. It was observed that in presence of water as an external stimulus, our MOM functionalized surface behaved like a lotus leaf showcasing slippery hydrophobicity, while the organic ligand displayed sticky hydrophobicity just like the rose petals. Negligible photoisomerization was observed for the prepared MOMs, in the solid state and therefore light controlled superhydrophobicity was not achieved. However, by combining these two aforementioned biomimetic observations, we were able to explore frictionless mechanical motion of small objects, using water as a lubricant in **Chapter 4**. The concept that we tried to explore at the laboratory scale may open up avenues for the construction of iceless skating arenas in the future. This can save huge amount of energy that is spent on the refrigeration of ice.

The present thesis, therefore, presents a systematic investigation on the synthesis and properties of a few tailor-made MOMs. Herein, the formation of various

nano to mesoscale architectures of these MOMs and their stimuli-responsive properties are investigated and reported in detail.

1.7. References

1. J. J. Perry IV, J. A. Perman and M. J. Zaworotko, *Chem. Soc. Rev.*, 2009, **38**, 1400.
2. J. Zhang and C.-Y. Su, *Coord. Chem. Rev.*, 2013, **257**, 1373.
3. A. Kraft, *Bull. Hist. Chem.*, 2008, **33**, 61.
4. Y. Kinoshita, I. Matsubara, T. Higuchi and Y. Saito, *Bull. Chem. Soc. Jpn.*, 1959, **32**, 1221.
5. H. Li, M. Eddaoudi, M. O'Keeffe and O. M. Yaghi, *Nature*, 1999, **402**, 276.
6. M. Kondo, T. Yoshitomi, K. Seki, H. Matsuzaka and S. Kitagawa, *Angew. Chem., Int. Ed.*, 1997, **36**, 1725.
7. D. J. Tranchemontagne, J. L. Mendoza-Corte´s, M. O'Keeffe and O. M. Yaghi, *Chem. Soc. Rev.*, 2009, **38**, 1257.
8. S. R. Batten, N. R. Champness, X. -M. Chen, J. G. -Martinez, S. Kitagawa, L. Öhrström, M. O'Keeffe, M. P. Suh and J. Reedijk, *Pure Appl. Chem.*, 2013, **85**, 1715.
9. S. Kitagawa and M. Kondo, *Bull. Chem. Soc. Jpn.*, 1998, **71**, 1739.
10. S. S. Nagarkar, A. V. Desai and S. K. Ghosh, *Chem. Asian J.*, 2014, **49**, 2358.
11. Y. Takashima, V. M. Martinez, S. Furukawa, M. Kondo, S. Shimomura, H. Uehara, M. Nakahama, K. Sugimoto and S. Kitagawa, *Nat. Commun.*, 2011, **2**, 168.
12. N. Yanai, K. Kitayama, Y. Hijikata, H. Sato, R. Matsuda, Y. Kubota, M. Takata, M. Mizuno, T. Uemura and S. Kitagawa, *Nat. Mater.*, 2011, **10**, 787.
13. Q. Chen, Z. Chang, W. -C. Song, H. Song, H. -B. Song, T. -L. Hu and X. -H. Bu, *Angew. Chem., Int. Ed.*, 2013, **52**, 11550.

14. J. J. Gassensmith, H. Furukawa, R. A. Smaldone, R. S. Forgan, Y. Y. Botros, O. M. Yaghi and J. F. Stoddart, *J. Am. Chem. Soc.*, 2011, **133**, 15312.
15. Y. Ikezoe, G. Washino, T. Uemura, S. Kitagawa and H. Matsui, *Nat. Mater.*, 2012, **11**, 1081.
16. Y. Ikezoe, J. Fang, T. L. Wasik, T. Uemura, Y. Zheng, S. Kitagawa and H. Matsui, *Adv. Mater.*, 2015, **27**, 288.
17. X. Meng, B. Gui, D. Yuan, M. Zeller and C. Wang, *Sci. Adv.*, 2016, **2**, e1600480.
18. K. W. Chapman, D. F. Sava, G. J. Halder, P. J. Chupas and T. M. Nenoff, *J. Am. Chem. Soc.*, 2011, **133**, 18583.
19. K. W. Chapman, G. J. Halder and P. J. Chupas, *J. Am. Chem. Soc.*, 2009, **131**, 17546.
20. S. A. Moggach, T. D. Bennett and A. K. Cheetham, *Angew. Chem., Int. Ed.*, 2009, **48**, 7087.
21. K. W. Chapman, G. J. Halder and P. J. Chupas, *J. Am. Chem. Soc.*, 2008, **130**, 10524.
22. W. Li, M. R. Probert, M. Kosa, T.D. Bennett, A. Thirumurugan, R. P. Burwood, M. Parinello, J. A. K. Howard and A. K. Cheetham, *J. Am. Chem. Soc.*, 2012, **134**, 11940.
23. K. J. Gagnon, C. M. Beavers and A. Clearfield, *J. Am. Chem. Soc.*, 2013, **135**, 1252.
24. A. L. Goodwin, D. A. Keen and M. G. Tucker, *Proc. Natl. Acad. Sci. U. S. A.*, 2008, **105**, 18708.
25. B.-C. Tzeng, T.-Y. Chang and H.-S. Sheu, *Chem. Eur. J.*, 2010, **16**, 9990.
26. E. C. Spencer, J. Zhao, N. L. Ross, M. B. Andrews, R. G. Surbella and C. L. Cahill, *J. Solid State Chem.*, 2013, **202**, 99.
27. M. Ohba, W. Kaneko, S. Kitagawa, T. Maeda and M. Mito, *J. Am. Chem. Soc.*, 2008, **113**, 4475.

28. A. Schneemann, V. Bon, I. Schwedler, I. Senkovska, S. Kaskel and R. A. Fischer, *Chem. Soc. Rev.*, 2014, **43**, 6062.
29. S. Henke, A. Schneemann and R. A. Fischer, *Adv. Funct. Mater.*, 2013, **23**, 5990.
30. M. Zhu , X.-Z. Song , S.-Y. Song , S.-N. Zhao , X. Meng , L.-L. Wu ,C. Wang , and H.-J. Zhang, *Adv. Sci.*, 2015, **2**, 1500012.
31. X. Wang, C. Chi, K. Zhang, Y. Qian, K. M. Gupta, Z. Kang, J. Jiang and D. Zhao, *Nat. Commun.*, 2017, **8**, 14460.
32. S. Bureekaew, S. Horike, M. Higuchi, M. Mizuno, T. Kawamura, D. Tanaka, Yanai and S. Kitagawa, *Nat. Mater.*, 2009, **8**, 831.
33. J. A. Hurd, R. Vaidhyanathan, V. Thangadurai, C. I. Ratcliffe, I. L. Moudrakovski and G. K. H. Shimizu, *Nat. Chem.*, 2009, **1**, 705.
34. S. S. Nagarkar, S. M. Unni, A. Sharma, S. Kurungot and S. K. Ghosh, *Angew. Chem. Int. Ed.*, 2014, **53**, 2638.
35. R. K. Deshpande, J. L. Minnaar and S. G. Telfer, *Angew. Chem., Int. Ed.*, 2010, **49**, 4598.
36. D. J. Lun, G. I. N. Waterhouse and S. G. Telfer, *J. Am. Chem. Soc.*, 2011, **133**, 5806.
37. H. Tian and S. Yang, *Chem. Soc. Rev.*, 2004, **33**, 85.
38. M. Han, R. Michel, B. He, Y.-S. Chen, D. Stalke, M. John and G. H. Clever, *Angew. Chem., Int. Ed.*, 2013, **52**, 1319.
39. S. Han, Y. Wei, C. Valente, R. Forgan, J. Gassensmith, R. Smaldone, H. Nakanishi, A. Coskun, J. F. Stoddart and B. Grzybowski, *Angew. Chem., Int. Ed.*, 2011, **50**, 276.
40. F. Luo, C. B. Fan, M. B. Luo, X. L.Wu, Y. Zhu, S. Z. Pu, W.-Y. Xu and G.-C. Guo, *Angew. Chem., Int. Ed.*, 2014, **53**, 9298.
41. S. C. Wei, M. Pan, K. Li, S. Wang, J. Zhang and C. Y. Su, *Adv. Mater.*, 2014, **26**, 2072.

42. D. E. Williams, J. A. Rietman, J. M. Maier, R. Tan, A. B. Greytak, M. D. Smith, J. A. Krause and N. B. Shustova, *J. Am. Chem. Soc.*, 2014, **136**, 11886.
43. J. Park, D. Feng, S.Yuan and H.-C. Zhou, *Angew. Chem., Int. Ed.*, 2015, **54**, 430.
44. J. Park, Q. Jiang, D. Feng and H.-C. Zhou, *Angew. Chem., Int. Ed.*, 2016, **55**, 7188.
45. *Smart Light-Responsive Materials: Azobenzene-Containing Polymers and Liquid Crystals* Y. Zhao and T. Ikeda, Eds. John Wiley & Sons, Inc., Hoboken, New Jersey, 2009.
46. S. Yagai and A. Kitamura, *Chem. Soc. Rev.*, 2008, **37**, 1520.
47. M.-M. Russew and S. Hecht, *Adv. Mater.*, 2010, **22**, 3348.
48. S. S. Babu, V. K. Praveen and A. Ajayaghosh, *Chem. Rev.*, 2014, **114**, 1973.
49. A. Harada, Y. Takashima and M. Nakahata, *Acc. Chem. Res.*, 2014, **47**, 2128.
50. S. Mahesh, A. Gopal, R. Thirumalai and A. Ajayaghosh, *J. Am. Chem. Soc.*, 2012, **134**, 7227.
51. R. Rajaganesh, A. Gopal, T. M. Das and A. Ajayaghosh, *Org. Lett.*, 2012, **14**, 748.
52. A. Gopal, M. Hifsudheen, S. Furumi, M. Takeuchi and A. Ajayaghosh, *Angew. Chem., Int. Ed.*, 2012, **51**, 10505.
53. S.-S. Sun, J. A. Anspach and A. J. Lees, *Inorg. Chem.*, 2002, **41**, 1862.
54. T. Murase, S. Sato and M. Fujita, *Angew. Chem., Int. Ed.*, 2007, **46**, 5133.
55. G. H. Clever, S. Tashiro and M. Shionoya, *J. Am. Chem. Soc.*, 2010, **132**, 9973.
56. A. Modrow, D. Zarqarani and R. Herges, N. Stock, *Dalton Trans.*, 2011, **40**, 4217.
57. S. Bernt, M. Feyand, A. Modrow, J. Wack, J. Senker and N. Stock, *Eur. J. Inorg. Chem,*, 2011, 5378.
58. A. Modrow, D. Zarqarani, R. Herges and N. Stock, *Dalton Trans.*, 2012, **41**, 8690.

59. A. Modrow, M. Feyand, D. Zarqarani, R. Herges and N. Stock, *Z. Anorg. Allg. Chem.*, 2012, 2138.
60. J. Park, D. Yuan, K. T. Pham, J.-R. Li, A. Yakovenko and H.-C. Zhou, *J. Am. Chem. Soc.*, 2012, **134**, 99.
61. J. W. Brown, B. L. Henderson, M. D. Kiesz, A. C. Whalley, W. Morris, S. Grunder, H. Deng, H. Furukawa, J. I. Zink, J. F. Stoddart and O. M. Yaghi, *Chem. Sci.*, 2013, **4**, 2858.
62. N. Yanai, T. Uemura, M. Inoue, R. Matsuda, T. Fukushima, M. Tsujimoto, S. Isoda and S. Kitagawa, *J. Am. Chem. Soc.*, 2012, **134**, 4501.
63. D. Hermann, H. Emerich, R. Lepski, D. Schaniel and U. Ruschewitz, *Inorg. Chem.*, 2013, **52**, 2744.
64. R. Lyndon, K. Konstas, B. P. Ladewig, P. D. Southon, C. J. Kepert and M. R. Hill, *Angew. Chem., Int. Ed.*, 2013, **52**, 3695.
65. R. F. Service, *Science*, 2012, **335**, 1167.
66. J. Reboul, S. Furukawa, N. Horike, M. Tsotsalas, K. Hirai, H. Uehara, M. Kondo, N. Louvain, O. Sakata and S. Kitagawa, *Nat. Mater.*, 2012, **11**, 717.
67. Y. Sakata, S. Furukawa, M. Kondo, K. Hirai, N. Horike, Y. Takashima, H. Uehara, N. Louvain, M. Meilikhov, T. Tsuruoka, S. Isoda, W. Kosaka, O. Sakata and S. Kitagawa, *Science*, 2013, **339**, 193.
68. L. Heinke, M. Cakici, M. Dommaschk, S. Grosjean, R. Herges, S. Bräse and C. Wöll, *ACS Nano*, 2014, **8**, 1463.
69. J. Park, L.-B. Sun, Y.-P. Chen, Z. Perry and H.-C. Zhou, *Angew. Chem., Int. Ed.*, 2014, **53**, 5842.
70. Z. Wang, A. Knebel, S. Grosjean, D. Wagner, S. Bräse, C. Wöll, J. Caro and L. Heinke, *Nat. Commun.*, 2016, **7**, 13872.
71. D. Bléger, J. Schwarz, A. M. Brouwer and S. Hecht, *J. Am. Chem. Soc.*, 2012, **134**, 20597.

72. O. S. Bushuyev, A. Tomberg, T. Friščić and C. J. Barrett, *J. Am. Chem. Soc.*, 2013, **135**, 12556.
73. S. Samanta, A. A. Beharry, O. Sadovski, T. M. McCormick, A. Babalhavaeji, V. Tropepe and G. A. Woolley, *J. Am. Chem. Soc.*, 2013, **135**, 9777.
74. M. J. Hansen, M. M. Lerch, W.Szymanski and B. L. Feringa, *Angew. Chem., Int. Ed.*, 2016, **55**, 13514.
75. S. Castellanos, A. Goulet-Hanssens, F. Zhao, A. Dikhtiarenko, A. Pustovarenko, S. Hecht, J. Gascon, F. Kapteijn and D. Bléger, *Chem. Eur. J.*, 2016, **22**, 746.
76. R. Lyndon, K. Konstas, A. W. Thornton, A. J. Seeber, B. P. Ladewig and M. R. Hill, *Chem. Mater.*, 2015, **27**, 7882.
77. R. D. Mukhopadhyay, V. K. Praveen and A. Ajayaghosh, *Mater. Horiz.*, 2014, **1**, 572.
78. M. Nakatsuji, *Biomater. Sci.*, 2013, **1**, 9.
79. H. Cölfen and S. Mann, *Angew. Chem., Int. Ed.*, 2003, **42**, 2350.
80. R. D. Mukhopadhyay, V. K. Praveen, A. Hazra, T. K. Maji and A. Ajayaghosh, *Chem. Sci.*, 2015, **6**, 6583.

Chapter 2

Light Driven Mesoscale Assembly of a Coordination Polymeric Gelator into Flowers and Stars with Distinct Properties

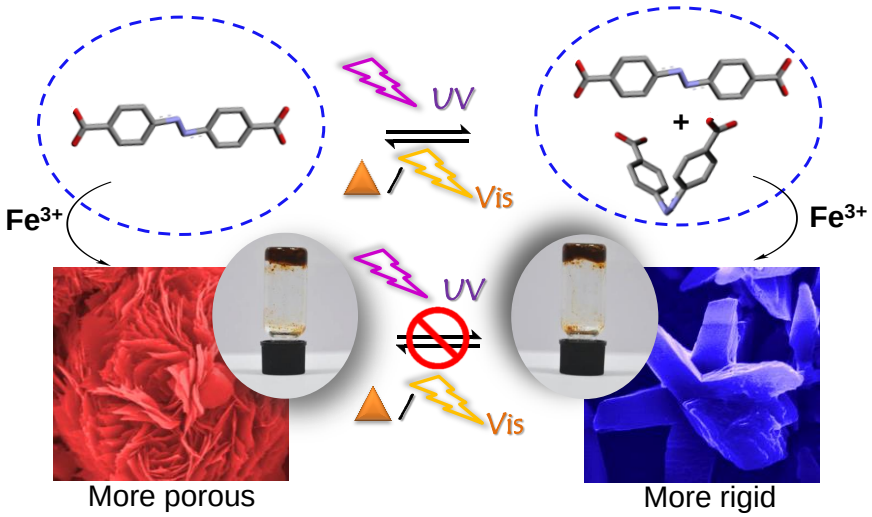

2.1. Abstract

*Control over the self-assembly process of porous metal-organic materials at the mesoscopic domain, with an external stimulus, often leads to unprecedented polymorphism and properties. Herein, we demonstrate how light can be used as a powerful tool to intervene the kinetically controlled mesoscale self-assembly of a coordination polymeric gelator. Light ($\lambda_{bandpass}$ = 350 nm) induced coordination modulation via photoisomerization (~37.5 %) of an azobenzene-based dicarboxylate linker (**ADA**) followed by aggregation mediated crystal growth resulted in two*

distinct morphological forms (flowers and stars) that showed subtle difference in their physical properties. Scanning electron microscopic (SEM) investigation indicated a diffusion limited kinetic self-assembly process in these colloidal coordination polymeric gel (CPG) particles. This process probably coupled with the formation of multiple structure-directing inorganic building blocks due to strong interactions between Fe(III) and carboxylate linkers, resulted in the formation of a number of morphological forms. With time, flower and star like structures evolved respectively from trans ***(CPG1)*** *and a mixture of trans-cis isomers (****CPG2****) obtained after irradiation. The molecular level packing of the gel material was confirmed from the reconstructed high-resolution transmission electron microscopic (HRTEM) images. Moreover, it was found that the two gels differed in their viscoelastic behavior and porosity.*

2.2. Introduction

Mesoscopic science is broadly defined as the space between nanoscopic (atoms, molecules and assemblies up to a few nanometres in size) and the macroscopic (hierarchical assemblies, a few micrometres in size or more) domains. The evolution of mesoscopic materials is controlled by chemical and physical processes, wherein atoms and molecules interact through physical forces, guided by thermodynamic and kinetic phenomena. Molecular self-assembly is a key nucleation point for mesoscopic evolution of functional materials and occupies a unique space in the field of

'nanoarchitectonics',[1-4] which is a novel conceptual idea for the construction of functional materials via control over reactions or assembly of molecules, making use of different physical stimuli.[3] In recent years, metal–organic frameworks (MOFs) or porous coordination polymers (PCPs),[5-8] known for their highly crystalline porous nature and ubiquitous applications, have been receiving attention in the field of nanoarchitectonics.

Kitagawa and co-workers have extensively published on the control of MOF/PCP self-assembly in the mesoscopic domain to explore the opportunities to integrate novel functions into these materials, without changing their crystal structures. In 2009, the group demonstrated a coordination modulation method using monobasic acetic acid molecules as capping reagents to perturb the framework extension of PCPs (Figure 2.1a).[9] The reaction rate and crystal morphology was mainly determined by the competitive interaction between the coordination mode used to construct the framework and the acetate–copper interaction. This process favours anisotropic one-dimensional fusion of the cubic nanocrystals, indicating an oriented attachment mechanism to form nanorod like structures (Figure 2.1b). The growth process of nanocubes was a consequence of aggregation-mediated crystal growth. The growth of nanorods in the [001] direction was mainly favoured by the selective coordination modulation on the [100] surfaces of the nanocubes. Moreover, it was observed that the coordination modulation method can produce highly

crystalline and porous nanorods as compared to that of bulk crystals obtained using the conventional solvothermal method (Figure 2.1c).

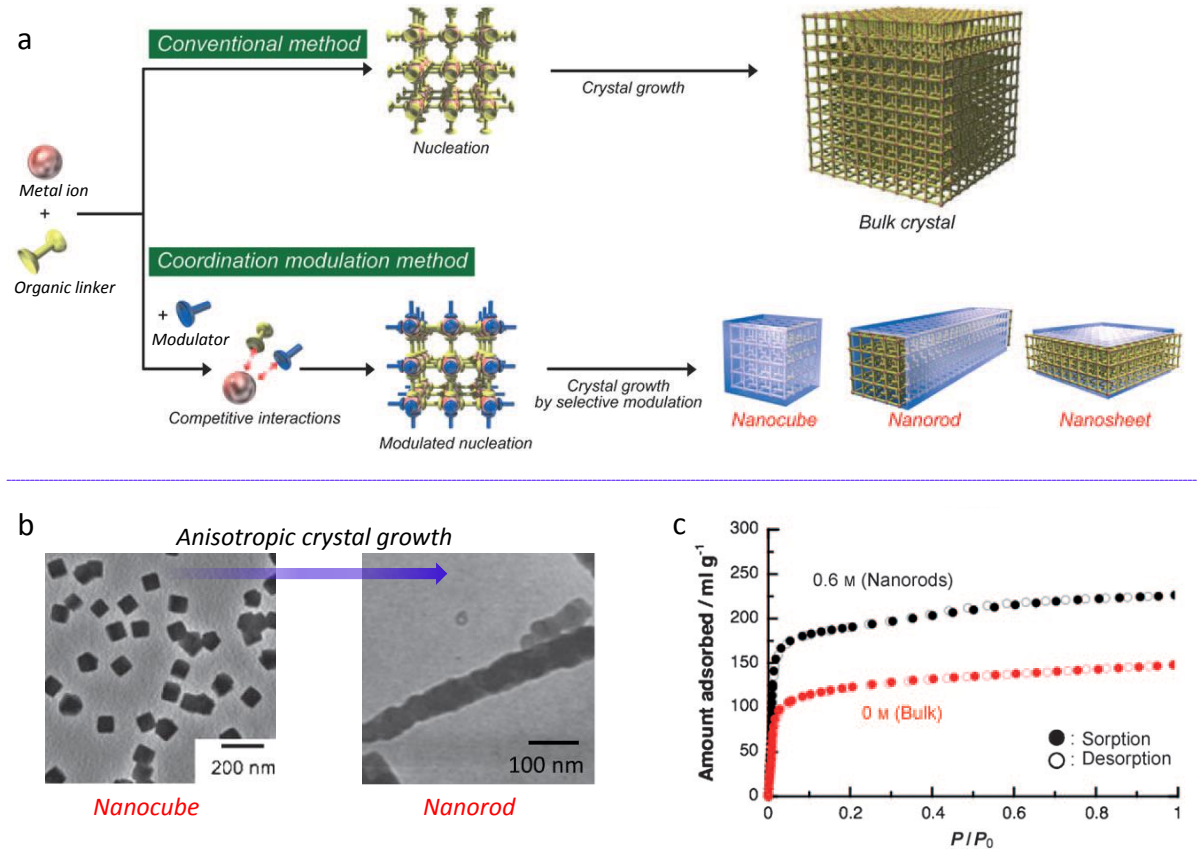

Figure 2.1. (a) Schematic representation of the coordination modulation process in the synthesis of Cu-acetate MOF. (b) TEM images showing anisotropic growth of the crystals from nanocubes to nanorods at the mesoscopic size-domain. (c) Carbon dioxide adsorption isotherm at 195 K for bulk powder and nanorod PCP samples prepared via coordination modulation.[9]

Third generation elastic porous coordination polymers are known to change their structure in response to molecular encapsulation. The original structure is however recovered, once the guest has been removed from the nanoporous cavities (see Chapter 1, Figure 1.2a). Utilizing the process of coordination modulation,

Kitagawa and co-workers demonstrated crystal downsizing of a PCP, $[Cu_2(dicarboxylate)_2(amine)]_n$, in the mesoscopic domain (Figure 2.2a), thereby influencing its structural flexibility and inducing a molecular scale shape-memory effect in the coordination framework (Figure 2.2b).[10] Shape-memory materials alter their morphological appearance in response to an external stimulus, hold on to their new temporary shape, even after the removal of the stimulus and return to their original morphological state when another external stimulus is applied. In mesoscale PCPs exhibiting a molecular shape-memory effect, the original nanopore was deformed to a temporary shape under the action of an adsorption stress. The temporary shape of the nanopore was maintained even after the desorption process. The original shape was restored only upon thermal treatment (Figure 2.2c and 2.2d).

Kitagawa *et al.* have shown that spatial organization of PCP crystals results in higher-order mesoscopic structures.[11] This kind of mesoscopic modulation of PCP growth is important in separation systems, heterogeneous catalysis, in ion/electron transport and photonic devices. Inspired by geological pseudomorphic mineral replacement events, the authors demonstrated how the nucleation site of PCP crystal growth could be spatially controlled, leading to the fabrication of mesoscopic architecture, in both two and three dimensions (Figure2.3a). The method may be interpreted as the morphological replacement of a shaped sacrificial metal oxide substrate with an analogous PCP architecture. From time dependent field-emission scanning electron microscopy (FESEM) analysis, it was observed that the fine

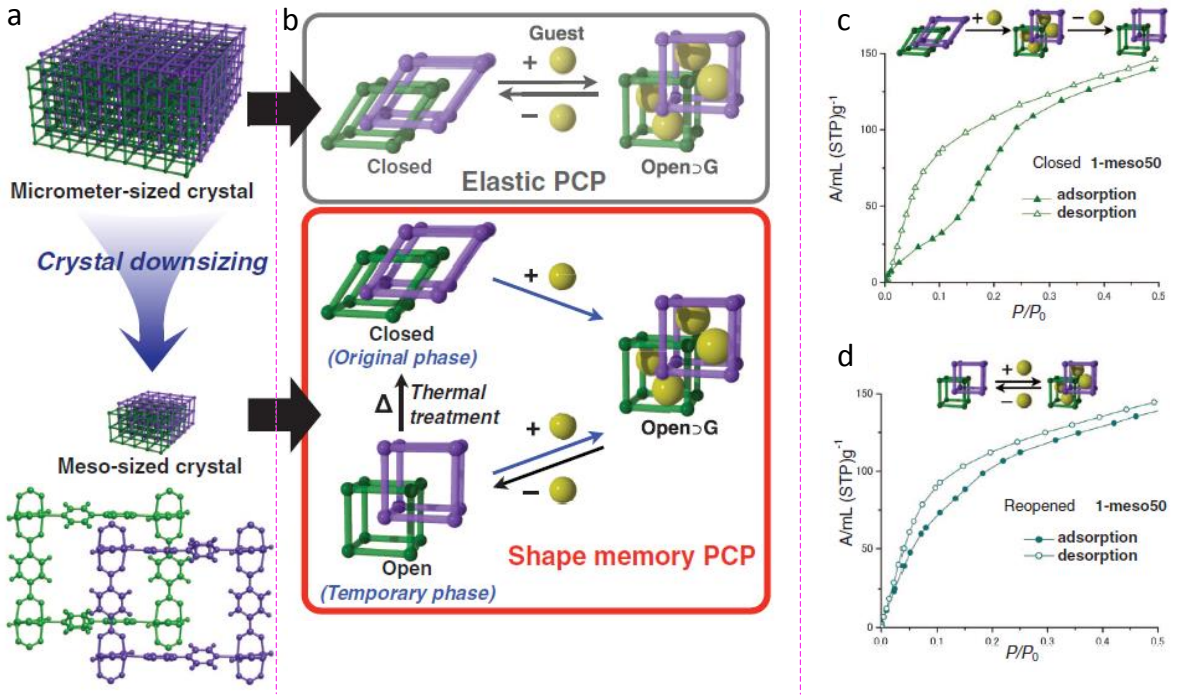

Figure 2.2. (a) Schematic representation of crystal downsizing to obtain meso-sized crystal in $[Cu_2(dicarboxylate)_2(amine)]_n$, having a doubly interpenetrated crystal structure. (b) Schematic representation of comparative structural changes observed in an elastic bulk PCP and in a meso-sized PCP showing shape memory effect. (c) Methanol adsorption isotherm at 303 K for shape memory PCP for the first cycle of adsorption-desorption process showing gate opening behavior and (d) absence of structural changes in the second cycle of adsorption-desorption process.[10]

morphological details of periodic alumina inverse opal structures were preserved by using such a method (Figure 2.3b). The metal oxide substrate acts both as a source for metal ions as well as an 'architecture-directing' agent. The method was also utilized to obtain alumina aerogels with hierarchical porosity. The hydrophobic micropores of the PCP along with the mesopores/macropores inherited from the parent alumina aerogel network synergistically enhanced the selectivity and mass transfer for water-ethanol separation.

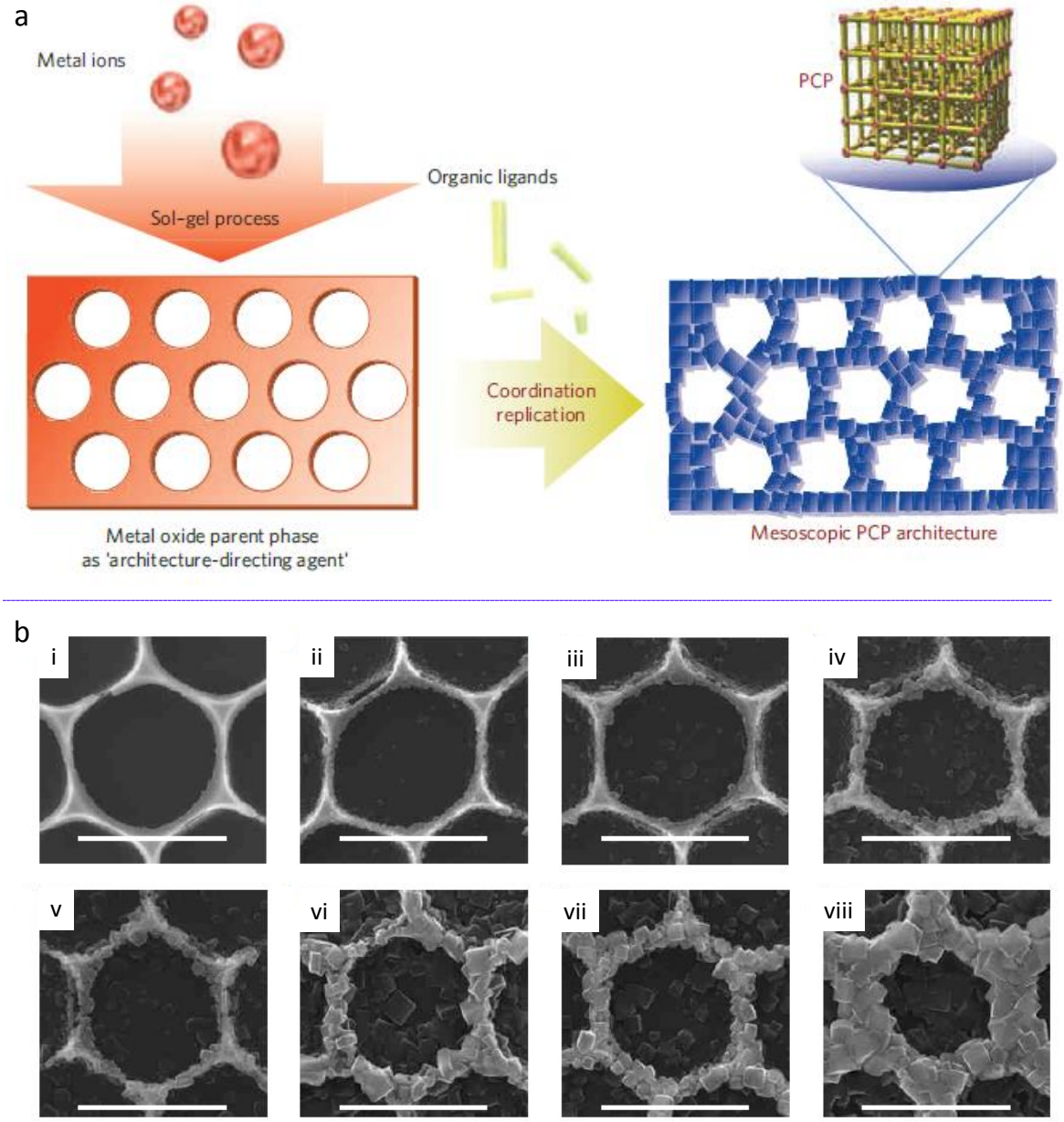

Figure 2.3. (a) Concept of coordination replication and formation of mesoscopic architectures inspired by pseudomorphic mineral replacement events. (b) FESEM images of alumina substrate with periodic inverse opal structures obtained after 0 s (i), 1 s (ii), 4 s (iii), 6 s (iv), 10 s (v), 20 s (vi), 40 s (vii) and 60 s (vii) of replication process. Scale bars, 1 μm.[11]

While wide range of applications are envisaged for MOFs and PCPs, reversible control on the porosity and gas adsorption properties of such materials remains a challenging task. Therefore, an innovative approach in tuning the properties of MOFs or PCPs is of paramount importance. Such considerations encourage chemists to explore the possibility of light sensitive metal–organic systems.[12-13] In this context, azobenzene, a widely explored photoswitch,[14-17] has been utilised recently by a number of research groups to design photoresponsive crystalline porous materials.[18-24] However, photoisomerization of directly linked azobenzene moieties in a rigid coordination framework is often found to be difficult.[18] Therefore, an alternate approach is required to explore the utility of *cis–trans* photoisomerization of azobenzene moieties in a metal–organic coordination framework. Unlike rigid crystalline MOFs or PCPs, amorphous organogels are an entirely different class of soft material, possessing a flexible supramolecular network.[25-35] Gels are known to provide an excellent medium to create a dynamic environment, ideal for crystal growth process via defect rectification during reversible self-assembly.[36-37] A gel medium is also a clever option to create hierarchical mesoscopic structures having complex forms.[38] While there are several reports on photoresponsive gels,[16,39] reports on photoresponsive microporous coordination polymeric gels are rare.[40] Moreover, a deeper understanding of the structural evolution of MOFs and PCPs at the mesoscopic scale under the influence of light is, as yet, unknown. This is rather surprising while

considering the importance of mesoscopic structures in the field of materials science.[41-42]

Herein, we combine the chemistry of metal–organic materials and gels to create photoresponsive structures, to understand the effect of light on the kinetic pathways of mesoscopic structural evolution in synthetic molecular systems and study their properties. For this purpose, we designed a photoresponsive coordination polymeric gelator, which forms a gel having a flower-like morphology. Interestingly, pre-synthetic photoirradiation of the gelator resulted in star-shaped morphology with distinct rheological and gas adsorption properties. Our experience with supramolecular gels[31] encouraged us to exploit the Materials of Institute Lavoisier (MIL) family of coordination polymers, many of which are known for instantaneous gelation of the reaction mixture.[43-47] Since the structural rigidity of MOFs and PCPs do not facilitate post-synthetic photoisomerization of azobenzene on larger length scales,[21] we hypothesized that if a pre-synthetic isomerization is carried out, the *cis*-form of azobenzene should, in principle, get locked in the rigid matrix of the hybrid material, thereby leading to self-assembled forms with different properties.

2.3. Results and Discussion

2.3.1. Synthesis of Organic Linker ADA

Azobenzene-4,4'-dicarboxylic acid (**ADA**) was synthesized from *p*-Nitrobenzoic acid (**PNBA)** as shown in Scheme 1. The nitro group in **PNBA** was converted to the azo moiety, via oxidative coupling in presence of glucose and air, under alkaline conditions. The reaction was highly exothermic and care was taken to control the reaction temperature around 50 °C. The obtained disodium salt of **ADA** was soluble in water and was therefore slowly acidified with glacial acetic acid to obtain crude **ADA**. The overall yield of this reaction was 62%.

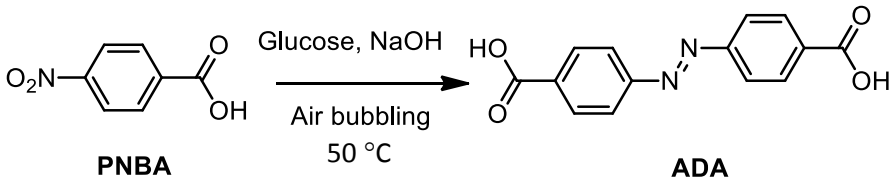

Scheme 1. Reagents and conditions for the synthesis of **ADA** from **PNBA**.

2.3.2. Synthesis and Characterization of Coordination Polymer Gel (CPG)

In a typical experiment, a gently warmed mixture of the azobenzene-4,4'-dicarboxylic acid (**ADA**, 10 mg, 0.037 mmol) and triethylamine (10.5 μL, 0.075 mmol) in dimethyl sulfoxide (DMSO, 0.25 mL) was added to an equimolar quantity of $Fe(NO_3)_3 \cdot 9H_2O$ (15 mg, 0.037 mmol) in same volume of DMSO, leading to immediate gelation (Fig. 2.4). Gelation was observed in polar solvents such as DMSO

and dimethyl formamide (DMF) at a critical gelator concentration (CGC) of 20 mg mL^{-1} (c = 7.4 x 10^{-2} M) with respect to **ADA** and was found to be highly sensitive towards mechanical disturbance.[28] However, the gel was not thermally reversible in nature by virtue of its coordination network. This gel primarily composed of *trans*-**ADA** isomers was termed **CPG1**. The involvement of metal–ligand coordination responsible for such gelation was confirmed from Fourier-transform infrared (FT-IR)

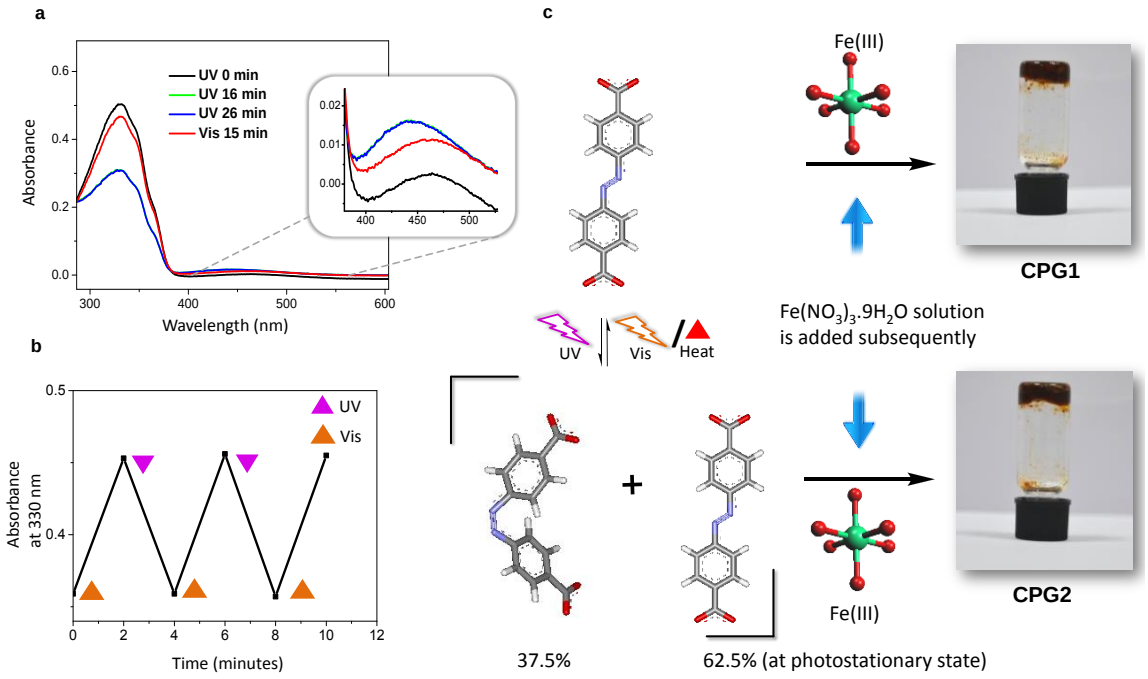

Figure 2.4. (a) Absorption spectra of the **ADA** solution in DMSO (1.85 × 10^{-5} M) before and after irradiation with ultraviolet (UV) and visible (vis) light. Inset shows the zoomed in region of 379-527 nm corresponding to the *n*-*π** transition band of *cis*-azobenzene. (b) Reversibility of photoisomerization, shown for 3 cycles. (c) Schematic representation of synthesis of **CPG1** and **CPG2** (corresponding gel images are shown). *Trans* and *cis* isomers of **ADA** (Carbon – grey; Nitrogen – blue; Oxygen – red; Hydrogen – white) and probable structure of inorganic octahedra (Iron –orange; Oxygen – red) are also shown.

spectroscopic studies (Fig. 2.5a).[48-49] The intense IR band at 1688 cm^{-1}, corresponding to asymmetric carbonyl stretching frequency of the free acid **ADA**, diminished with considerable broadening in the case of coordination polymeric gel (**CPG1**), with the appearance of a new band at 1413 cm^{-1}, corresponding to the symmetric stretching frequency.[49] Deconvolution of the broad band at ~1700 cm^{-1} suggests that the separation between the asymmetric and symmetric carbonyl stretching frequency increases in **CPG1** when compared to **ADA**, as evidenced from the higher wavenumber peak contributions at 1700, 1717 and 1731 cm^{-1}. This observation primarily suggests the presence of unidentate coordination in **CPG1**, although the presence of bidentate binding modes cannot be completely ruled out, as indicated by the peak contribution at 1671 cm^{-1} (Fig. 2.5b).[48]

In order to check the photoresponsive nature, we irradiated the gel sample with UV light. However, the gel remained intact and did not show any spectroscopic changes even after hours of photo irradiation (Fig. 2.6a). Therefore, we thought of exploring the effect of the photoisomerization of **ADA** before the preparation of the gel. The absorption spectrum of **ADA** in DMSO (c = 1.85 x 10^{-5} M), showed two bands with maxima at 330 and 440 nm, corresponding to $\pi \rightarrow \pi^*$ and $n \rightarrow \pi^*$ transitions, respectively. Photoisomerization studies revealed that the molecule reaches a photostationary state within 16 min, where ~ 37.5% of the molecules are present in the *cis*-form (Fig. 2.4a) upon irradiating with UV light ($\lambda_{bandpass}$ = 350 nm).

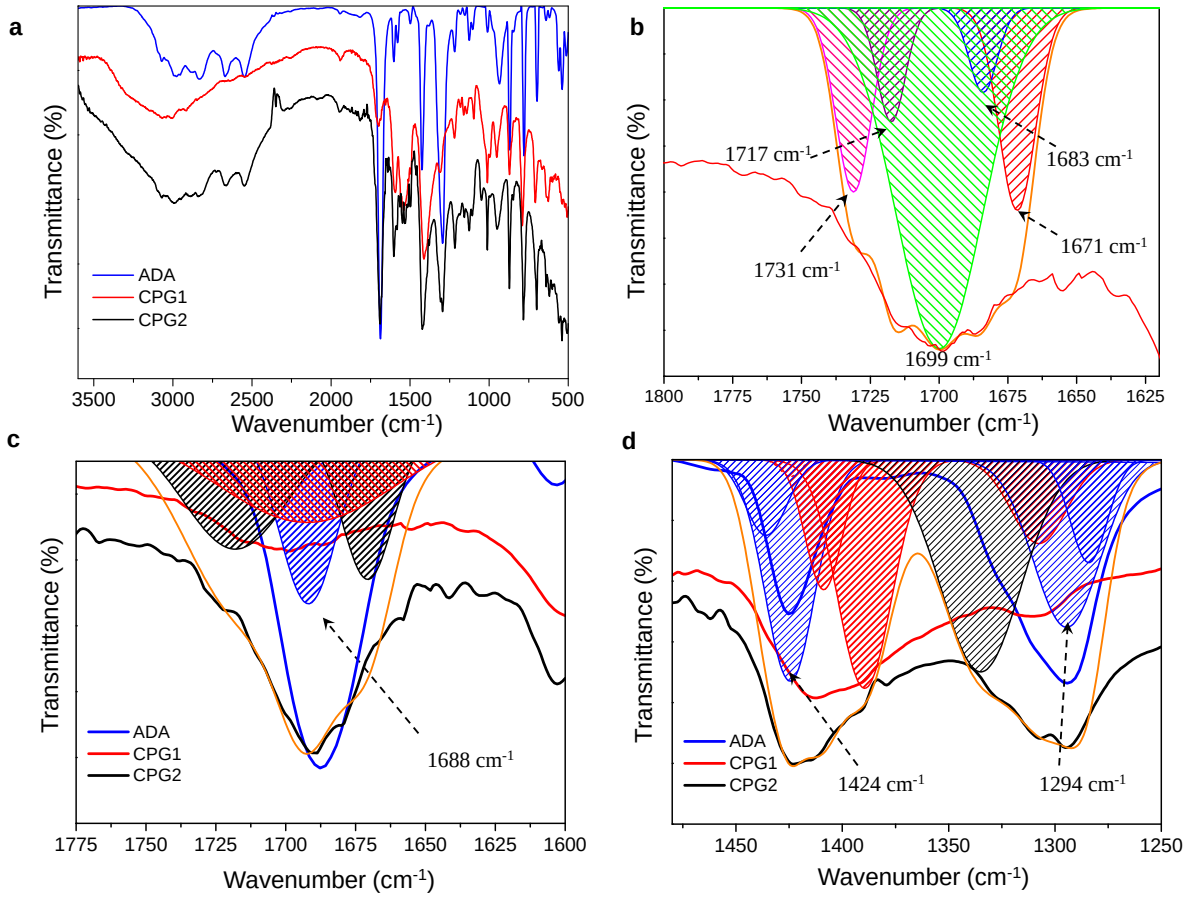

Figure 2.5. (a) FT-IR spectra of **ADA**, **CPG1** and **CPG2**. (b) Deconvolution of the broad asymmetric stretching frequency (~1700 cm^{-1}) band of **CPG1** (shown in red). (c and d) Deconvolution of FT-IR spectra of **CPG2**, in the range (c, 1775-1600 cm^{-1}) and (d, 1480-1250 cm^{-1}) shows the presence of both **ADA** as well as **CPG1** peaks in **CPG2**. The shaded plots in all the above cases represent the functions obtained from the deconvolution of **CPG1** and **CPG2** spectra. The additive deconvoluted plot is represented by orange lines in both cases.

The photoisomerization of the azobenzene core was clearly reversible with respect to UV and visible light ($\lambda_{bandpass}$ = 350 and 420 nm) and was also reproducible over several repeated cycles (Fig. 2.4b). Thus, when a solution of **ADA** and triethylamine in DMSO (20 mg mL^{-1}) was irradiated with UV light ($\lambda_{bandpass}$ = 350

nm) for about 4 h (to confirm that maximum conversion has taken place) and then a solution of $Fe(NO_3)_3 \bullet 9H_2O$ in DMSO was added to it, the mixture slowly turned into a gelatinous material, which was kept under UV light ($\lambda_{bandpass}$ = 350 nm) for about an hour and then analyzed. This gel primarily composed of a mixture of *trans* and *cis* isomers of **ADA** is termed as **CPG2** (Fig. 2.4c). **CPG2** was also found to be highly photostable and did not show any spectroscopic change on irradiation with visible light ($\lambda_{bandpass}$ = 420 nm) (Fig. 2.6b).

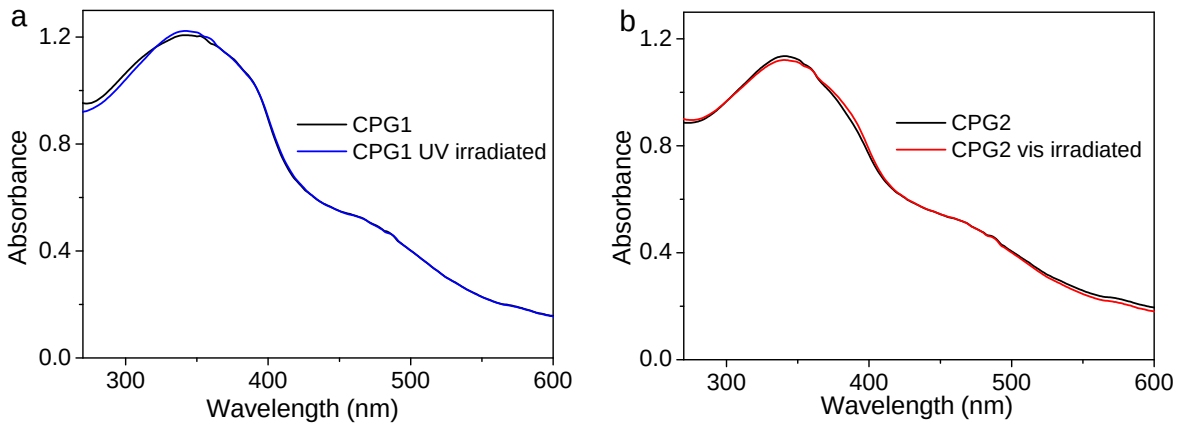

Figure 2.6. Absorption spectra of (a) **CPG1** and (b) **CPG2** before and after UV (350 nm) and visible light (420 nm) irradiation respectively. Experiments were repeated after 1 h of irradiation in each case.

2.3.3. Morphological Analysis of CPG1

Scanning electron microscopic (SEM) analysis of the **CPG1** revealed the formation of macroscopic sheets (Fig. 2.7). Furthermore, these sheets have a tendency to stack one above the other to form various metastable superstructures (Fig. 2.7a). Detailed morphological analysis of the gel sample by SEM showed the formation of the

coordination polymeric gel through an evolutionary morphogenesis as reported previously in the case of certain infinite coordination polymers.[50-53]

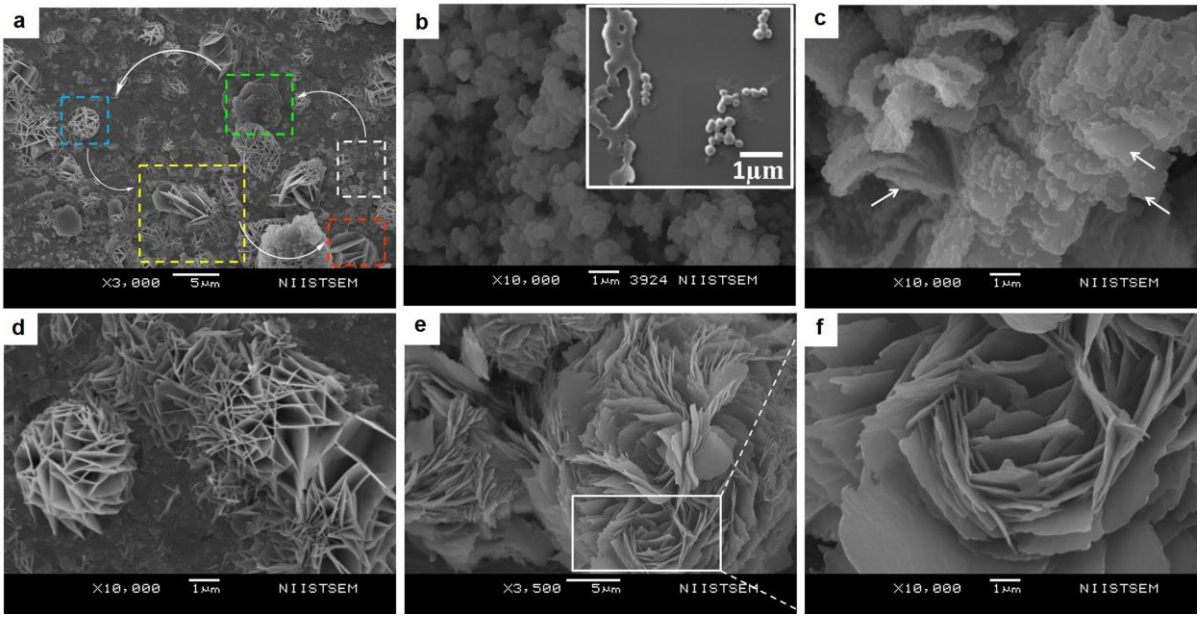

Figure 2.7. SEM analysis of **CPG1**. (a) Different morphological forms of **CPG1** captured in one frame. Platelets (white box), rough sheets (green box), cabbage (blue box), large smooth sheets (yellow box) and flower (red box). (b-f) Time dependent SEM analysis of **CPG1**. (b) Nanoscale **CPG1** platelets formed immediately, inset shows platelets undergoing fusion. (c,d) Images obtained after 5-6 h. (c) Gradual smoothening of rough sheets. Smoothened portions marked with arrows. (d) Formation of cabbage like structure. (e) Matured metal-organic flowers formed after 1 day. (f) Zoomed in view of the box marked in (e), showing nanoscale sheets (~ 25 nm thickness).

A time-dependent analysis of the gel formation mechanism indicates that, at the initial stages of development, globular seeds are formed (Fig. 2.7b) which agglomerated to form linear as well as branched aggregates that grew into two-dimensional (2-D) sheets. However, the surface of larger sheets initially had a rough topography, which got smoothened via a gradual process of annealing (Fig. 2.7c).

Folding of the smaller sheets led to a cabbage like structure (Fig. 2.7d) followed by the sideways stacking of the sheets, which ultimately resulted in metal–organic flowers (Fig. 2.7e). These micrometer sized flowers had nanoscale features in which the sheets were found to be approximately 25 nm thick (Fig. 2.7f).

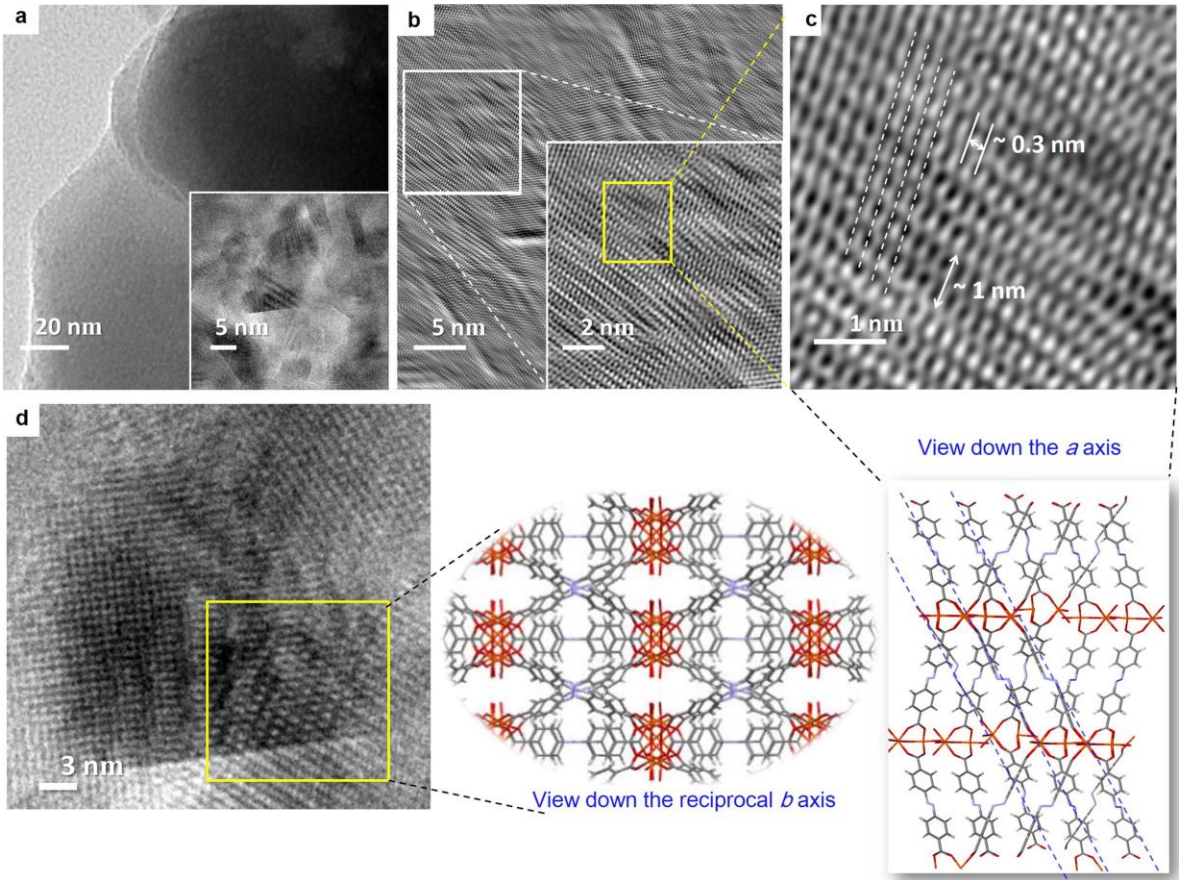

Figure 2.8. (a) TEM image of **CPG1** nanosheets. An HRTEM image of a nanosheet is shown in the inset. (b) IFFT reconstruction of the HR-TEM image shown as inset in (a). Zoomed in view of the marked box region is shown as inset. (c, d) Lattice planes corresponding to the molecular packing of the coordination polymeric chains observed from the reconstructed HR-TEM image. Crystal structure viewed down axis '*a*' and reciprocal cell axis '*b*' of PCN 243 are shown as a guide to the eye.[66]

Transmission electron microscopic (TEM) analysis of **CPG1** also confirmed a sheet like morphology (Fig. 2.8a). Lattice planes were clearly visible in the high-resolution transmission electron microscopy (HR-TEM) images, suggesting a highly ordered structure (Fig. 2.8a, inset).

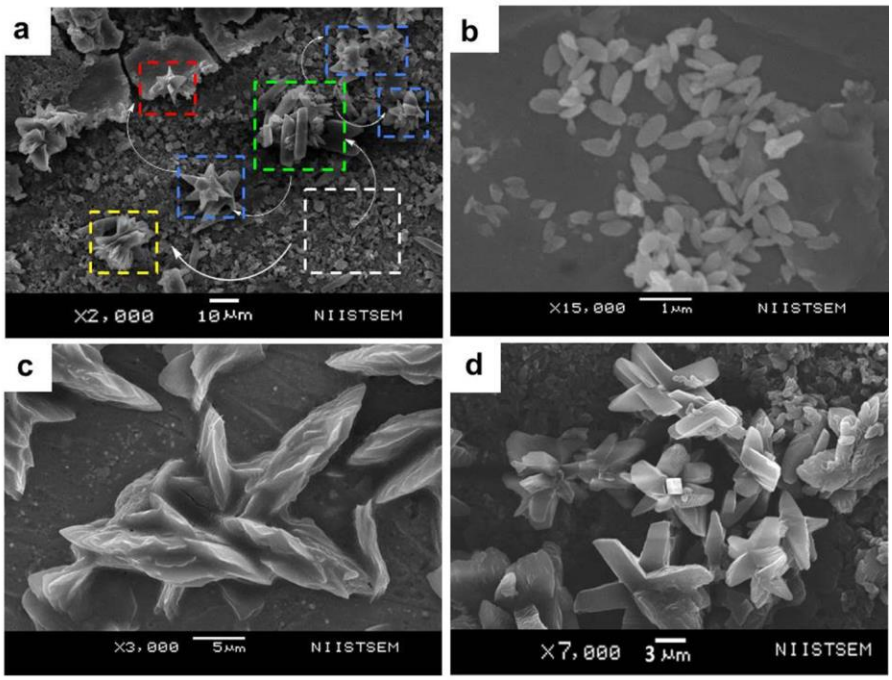

Figure 2.9. SEM analysis of **CPG2**. (a) Different morphological forms of **CPG2** captured in one frame. Leaves (white box), thick leaves (yellow box), tentacles (green box), stars in the formation (blue box), and crystalline stars (red box). (b-d) Time dependent SEM analysis of **CPG2**. (b) Nanoscale leaves of **CPG2** after immediate gelation. (c) Aggregation of nanoleaves after 1 h. (d) Crystalline metal–organic stars obtained after 1 day.

The morphology of the irradiated metal–organic gel (**CPG2**) was quite different (Fig. 2.9) from its non-irradiated counterpart, **CPG1** (Fig. 2.7). The morphology of **CPG2** comprised of six armed metal–organic stars. Akin to the

growth process of **CPG1**, **CPG2** also showed a gradually evolving process starting from small leaf-like seeds (Fig. 2.9b), which were about 400 nm in length and 200 nm in width. These kind of leaves were obtained by immediate mixing of the two primary components ($Fe3^{+}$ and **ADA**). After about 1h the leaves grew in size, most probably by aggregation induced mesoscale growth process to form thick leaves and tentacles (Fig. 2.9c). When we observed the morphology of the gel after aging the gel for a day we found that the tentacles had started fusing at a point and ultimately evolved into star-like superstructures that possessed well-defined facets as that of a crystal (Fig. 2.9d).

2.3.4. Analysis of Growth Process of CPG1 and CPG2

Although, in time-dependent experiments, we could mostly observe a particular morphology after a certain time interval, more than one morphological form were also found (Fig. 2.7a and 2.9a) at a few places in both the samples, which suggest that the growth process was not only time dependent but also depends on the local concentration of the initial components. Most of the formed intermediate structures might be controlled by kinetic processes rather than thermodynamic control and are therefore limited by diffusion.[54-56] At lower concentration of particles, the process of aggregation is controlled by diffusion leading to the formation of a patterned structure with random branching, whereas higher concentration leads to fast aggregation process leading to the formation of more compact structures. This process happens

due to the large surface to volume ratio and high collision frequency of the particles. The occurrence of several unreacted sites on the surface of the seeds due to fast nucleation process, results in further polymerization through coordination linkages and thereby fusion of the particles. With the gradual decrease in the concentration of the ligands and the metal ions, the nucleation of new particles is reduced and annealing of existing nuclei prevails much like the Ostwald ripening process.[15] Unlike a single step thermodynamically controlled pathway, a kinetically controlled crystal growth process usually takes place via a sequence of steps involving amorphous intermediates. Such transformations can be easily tuned by various chemical stimuli (additives), which influence the energy of activation of nucleation (n), growth (g) and phase transformation (t) processes.[57-58] Photoirradiation of *trans*-**ADA** molecules with UV light leads to the formation of energetically unstable *cis*-**ADA** isomer, which in combination with the unisomerized *trans*-**ADA** molecules can significantly influence the nucleation–growth–transformation processes. Therefore, a new kinetic pathway is followed, which is shown in a modified energy profile diagram, similar to that proposed previously by Mann and co-workers (Fig. 2.10).[57] In order to confirm this hypothesis, we carried out the synthesis of nanoscale **CPG1** and **CPG2** under thermodynamic conditions at a very low concentration where we were able to arrive at only nanoplatelets and leaves. The presence of nanoplatelets and leaves were confirmed from SEM and TEM analyses (Fig. 2.11).

According to the Bravais, Friedel, Donnay and Harker (BFDH) law, the morphology of a crystal is mainly determined by the slowest growing facet of the crystal.[59-60] The 2-D nucleus on a particular crystal facet determines the overall crystal morphology depending on the probabilities of growth or dissolution at a particular site. A crystal, in principle, should grow in a particular direction unless the energetics

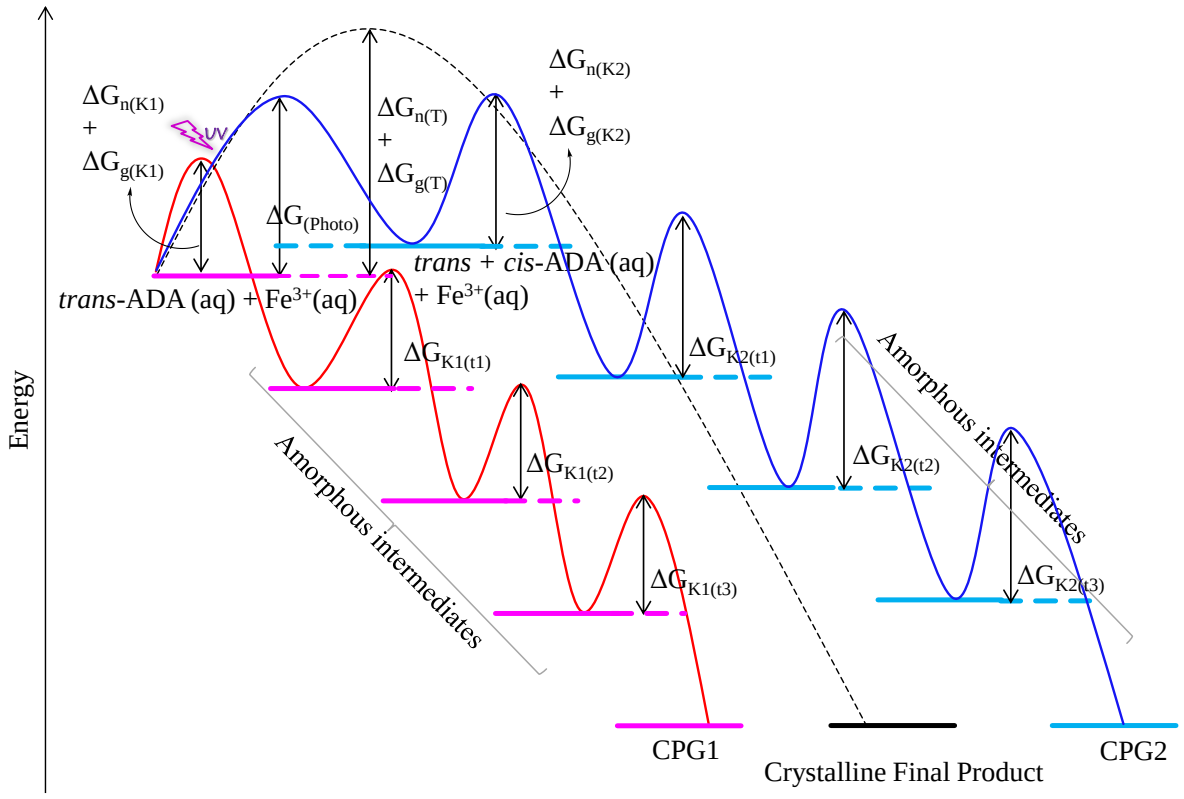

Figure 2.10. Energy profile showing the thermodynamic and kinetic pathways for crystal growth. Thermodynamic (T) pathway is a one step process while kinetic (K1 and K2) pathways pass through several amorphous intermediate stages before ending up with a crystalline final product. The sequence of transformations depends on the free energy of activation of nucleation (ΔG_n), growth (ΔG_g) and phase transformations (ΔG_t). In the case of photoirradiation at the beginning, there is an additional activation energy for photoisomerization (ΔG_{Photo}).

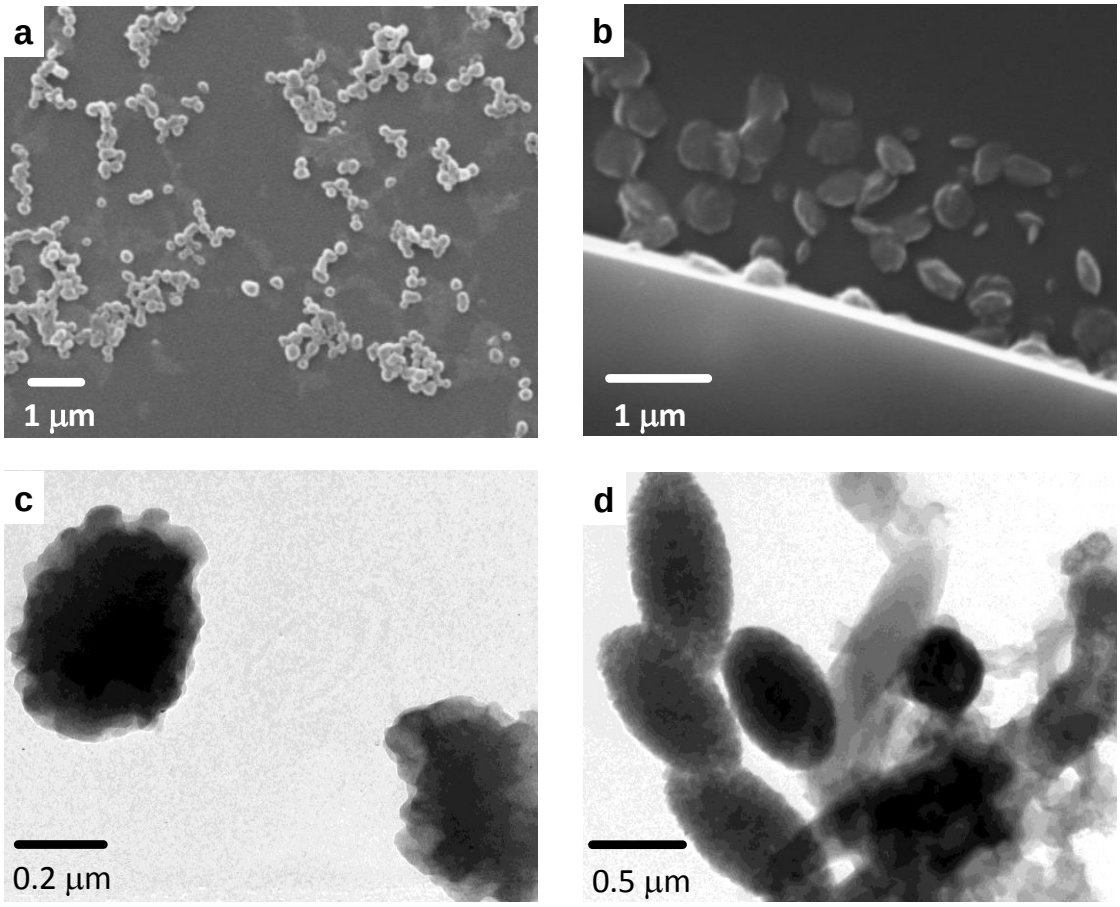

Figure 2.11. Nanoscale coordination polymeric gel particles obtained under thermodynamic conditions. SEM images of (a) nanoscale **CPG1** platelets, (b) nanoscale **CPG2** leaves. TEM images of (c) nanoscale **CPG1** platelets, (d) nanoscale **CPG2** leaves.

is changed along a particular facet. Now, taking a closer look at the formation mechanism (Fig. 2.12) for both **CPG1** and **CPG2**, one can assume that the transformation of platelets (for **CPG1**) to leaves (for **CPG2**) essentially occurs by a similar process of anisotropic crystal growth. At the photostationary state, ~ 37.5% of *cis*-**ADA** can trigger this anisotropic growth mechanism by varying the crystal growth rates along different facets. It is known that the *cis*-isomer of azobenzene can form

energetically less favorable self-assembled structures.[61] In case of a coordination driven self-assembly, the non-planar nature of *cis*-**ADA** can further hamper the chain growth process.

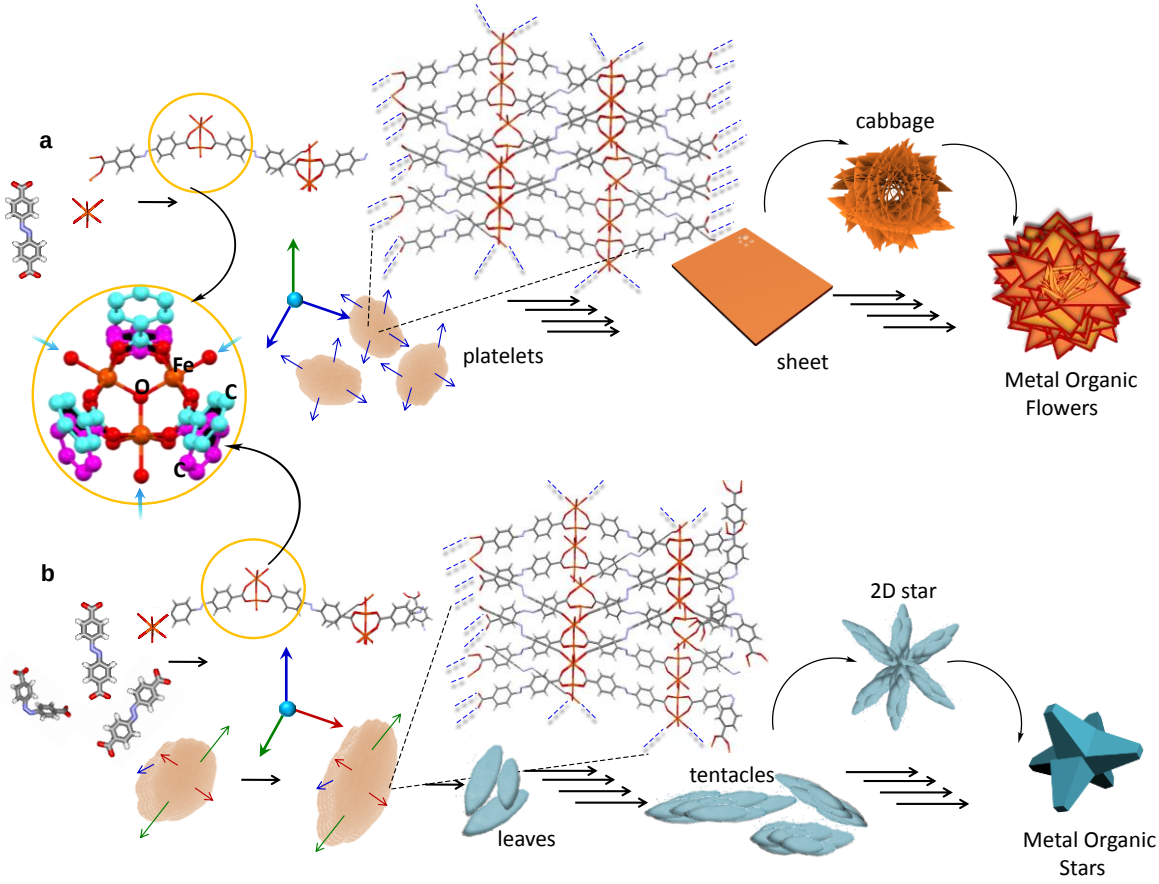

Figure 2.12. Proposed formation pathways of (a) flowers in **CPG1** and (b) stars in **CPG2**. Fusion of platelets in **CPG1** leads to the formation of 2-D sheets and finally the flowers. The anisotropic growth along different facets in **CPG2** leads to the formation of stars. Blue, green and red arrows represent the maximum, moderate and restricted rates of crystal growth. Blue broken lines indicate directions of polymeric extension. All short contacts are not shown to obtain visual clarity. The basic building block containing the Fe_3O cluster with coordinated solvent molecules (marked by sky blue arrow) and the first phenyl ring of **ADA** is represented in the yellow circle. **ADA** molecules projecting outside (cyan) and inside (magenta) the plane of paper are also represented.

The growth process stops because the geometry of the inorganic cluster brings *cis*-**ADA** closer to the coordination polymeric chain, where it remains in a sterically unfavorable position to undergo further reaction. Thus, *cis*-**ADA** can essentially act as a capping agent, which hinders the crystal growth along a particular facet. The presence of these capping agents is difficult to verify even experimentally, and therefore, the explanation of such process is essentially speculative, especially in the absence of a completely understood crystal growth mechanism.[9,62] It is hypothesized that the rate of crystal growth may range from moderate to maximum along different facets (Fig. 2.12b). This anisotropy arises only after smaller fragments (oligomers) of the coordination polymeric chain, containing *trans*-**ADA** (~ 62.5%) nucleate to form platelet like structures at the threshold of nanoscale. Transformation of platelets to leaves essentially takes place at the mesoscale followed by aggregation of preformed crystalline nanoleaves leading to the formation of microscopic superstructures. While trying to understand the growth process in these materials, it came to our notice that the morphology of colloidal hematite, a naturally occurring mineral, is also affected by similar aggregation mediated crystal growth process, showcasing several polymorphs ranging from platelets, ellipsoidal particles to stars. One can have a chemical control over the growth of different facets to facilitate such anisotropic crystal growth.[63-64] The same control has been achieved in the present case via photonic manipulation. A number of approaches towards engineering the self-assembly process of framework materials at the mesoscopic domain are known.[9-11] It

is important to note that in all these cases, a third component, for instance, a coordination modulator, surfactant or a template, was necessary to achieve such mesoscopic control over self-assembly. Whereas, in the present case, a certain fraction of the isomerized organic ligand is enough to bifurcate the bottom-up self-assembly process, while other *cis*-**ADA** molecules may get entrapped in the microporous structure.

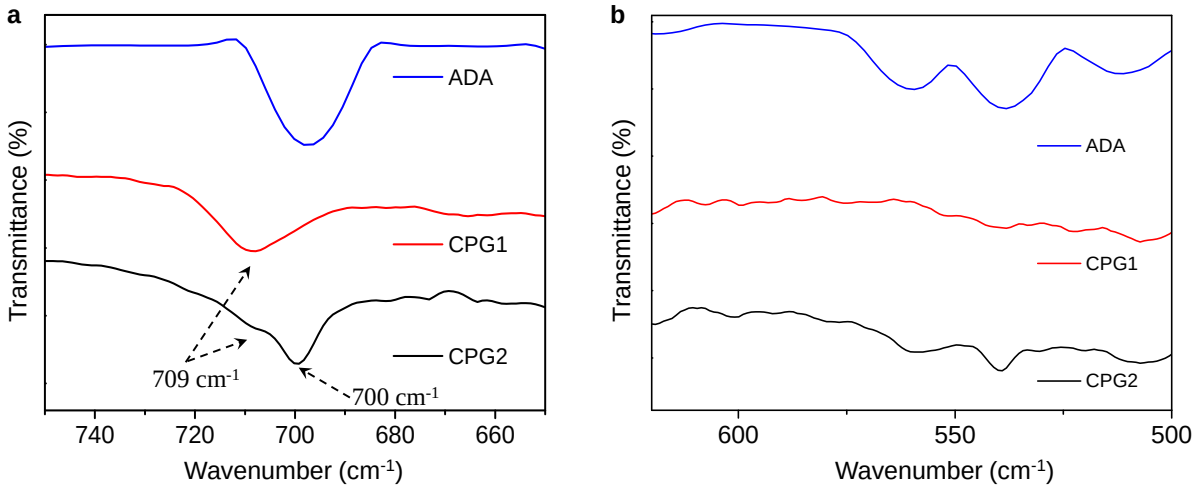

Figure 2.13. FT-IR spectra of **ADA**, **CPG1** and **CPG2**. (a) Zoomed in (750–650 cm^{-1}) view of the band at ~720 cm^{-1} confirms that *cis*-isomer of **ADA** is not present in **CPG2**. (b) Zoomed in view of the region (620–500 cm^{-1}). Absence of bands at ~560 cm^{-1} confirms that hematite phase is not present.

The *cis*-**ADA** molecules can gradually reconvert back to the thermodynamically more stable *trans*-**ADA**. The fact that *cis*-**ADA** reconverted to *trans*-**ADA** in **CPG2** was confirmed from the FT-IR studies, where no new peak at higher wavenumber region (~ 720 cm^{-1}) corresponding to *cis*-**ADA** was observed.[20] The peak corresponding to the *trans* isomer (700 cm^{-1}) in free **ADA** was shifted to

709 cm^{-1} in **CPG1** and observed as a shoulder in **CPG2** along with a prominent peak at 700 cm^{-1} corresponding to free *trans*-**ADA** (Fig. 2.13a). This was further confirmed from the deconvoluted FT-IR spectra of **CPG2**, where the peaks at 1688, 1424 and 1294 cm^{-1} corresponding to free **ADA**, which were absent in **CPG1**, were found to be present in **CPG2** (Fig. 2.5c and 2.5d). The results also indicate the shifting of the asymmetric stretching frequency of **ADA** towards the lower wavenumber region, basically indicating that the bidentate coordination modes become more prominent in **CPG2**.

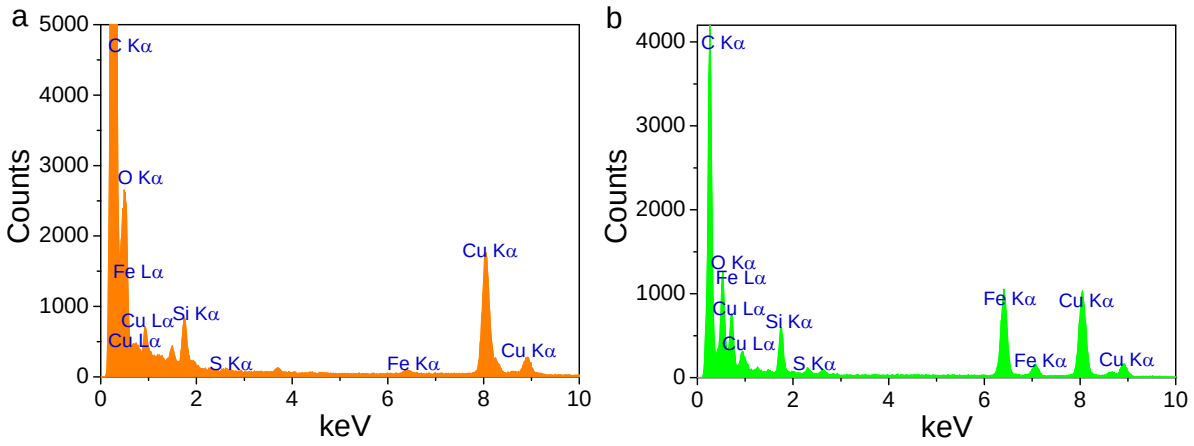

Figure 2.14. EDX analysis of (a) **CPG1** nanosheets and (b) **CPG2** nanoleaves observed in TEM analysis.

One of the problems of working with Fe(III) or Al(III) (hard acid) carboxylate (hard base) coordination polymers is the immediate formation of strong metal–ligand coordination, that does not allow defect rectification during the crystal growth process, leading towards precipitates or gels in most cases.[65-66] The *in situ* formation of multiple structure directing inorganic building blocks under kinetic conditions

often adds to this problem.[43,44,66] Therefore, the actual structure determination in the gel state, containing a mixture of polymorphic structures, is difficult to assign, even via computational simulation. However, we could derive some ideas from inverse fast Fourier transform (IFFT) reconstructed HR-TEM images, which showed the existence of coordination polymeric chains arranged in a parallel manner (Fig. 2.8b and 2.8c). This image matches with the recently reported crystal structure of PCN-243,[66] a MOF formed from **ADA** and an Fe(III) based inorganic cluster, when viewed along the *a*-axis. The distance between the polymeric chains roughly corresponds to 0.3 nm. Further, the presence of **ADA** (molecular length ~ 1.12 nm) in the polymeric chains can be corroborated from the slightly kinked structure of the azobenzene core. Similarly, the rhombic pores visualized in Fig. 2.8d can be compared with the same crystal structure, when viewed along the *b*-axis.

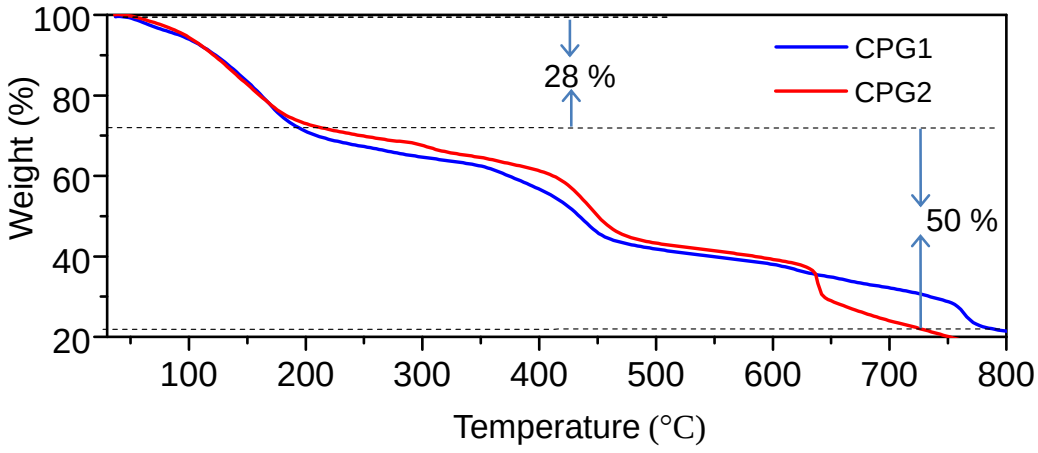

Figure 2.15. TGA plot of **CPG1** and **CPG2**.

Elemental analysis (**CPG1**: C, 40.39; H, 3.96; N, 6.19; S, 8.16 and **CPG2**: C, 41.56; H, 4.31; N, 6.16; S, 8.57), energy dispersive X-ray (EDX) analysis (Fig. 2.14) and thermogravimetric analysis (TGA) of the two forms (Fig. 2.15) showed similar composition, solvent weight loss and thermal decomposition pattern. The powder X-ray diffraction (XRD) pattern of the two forms **CPG1** and **CPG2** also did not show any considerable difference (Fig. 2.16a) pointing that both the morphological forms possess similar metal-linker connectivity. The simulated XRD pattern obtained from PCN-243 matches well with the observed pattern in **CPG1** and **CPG2** although the possibility of other amorphous phases cannot be completely ruled out, as evident from the presence of a broad peak (2θ =12–30°) in the XRD pattern of both the materials. However, the XRD peaks corresponding to a hematite (α-Fe_2O_3) phase with rhombohedral structure (*a*, *b* = 0.5 nm, *c* = 1.38 nm, JCPDS card no. 24-0072) is completely absent in either **CPG1** or **CPG2** (Fig. 2.16a). Also the FT-IR peaks corresponding to the lattice vibrations in α-Fe_2O_3 (~ 500–600 cm^{-1}) is absent in either case (Fig. 2.13b).[64] These data confirm that the observed unusual splitting of the growth process in our material was not affected by the pseudomorphic growth replication process over hematite or the presence of hematite phase as an impurity.[10] From the above investigations, we could conclude that the strong hard acid–hard base interactions result in fast unidentate coordination, and thereby gelation. With time, most of the amorphous intermediates are converted to more crystalline forms, which

show bidentate coordination modes. It is also observed that the presence of *cis*-**ADA** in the formation of **CPG2** basically slows down the crystallization process within the gel matrix resulting in more crystalline products.

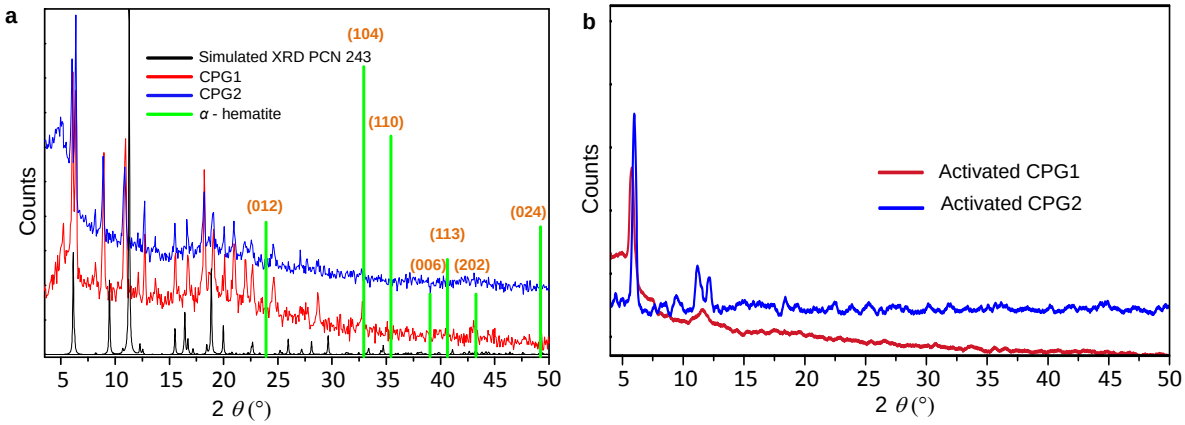

Figure 2.16. (a) XRD pattern of **CPG1** (red) and **CPG2** (blue). Simulated PXRD pattern of PCN-243 (black) and stick pattern of rhombohedral hematite (α-Fe_2O_3, JCPDS card No. 24-0072) phase (green) are also shown for a comparison. (b) XRD pattern of **CPG1** (dark red) and **CPG2** (blue) activated at 150 °C.

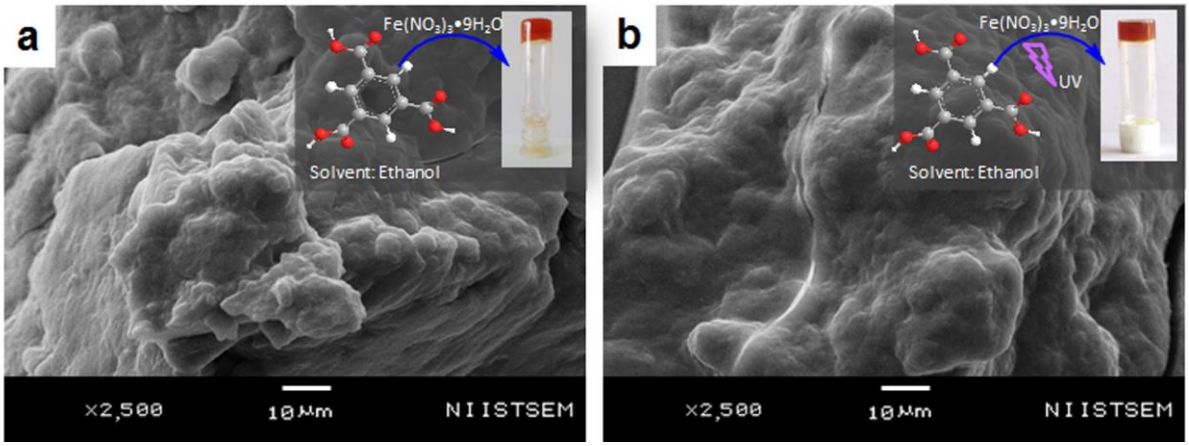

Figure 2.17. SEM images of (a) **FeBTC** gel and (b) **IRFeBTC** gel. Insets show the corresponding photographs of the gels along with the structure of the starting materials.

As a result, the presence of amorphous to highly crystalline species in the xerogel matrix makes the system highly heterogeneous for correlation of structure with properties. Further, in order to confirm that the mesoscopic change in the morphology is only due to the photoresponsive moiety and not due to formation of different inorganic clusters under UV light irradiation, a similar system derived from a non-photoisomerizable organic ligand, trimesic acid was subjected to UV light irradiation (Fig. 2.17). In this case, we could not observe any difference in the morphology between **FeBTC** and **IRFeBTC** gels, revealing that the inorganic cluster was not affected by any external physical stimulus such as light, unless it comes in contact with a photoresponsive organic material.

2.3.5. Comparative Mechanical Strength and Porosity Analysis of CPG1 and CPG2

Gel-like behavior of **CPG1** and **CPG2** was confirmed from rheological studies, where for both the materials, the value of elastic storage modulus (G′) was found to be invariant with the applied frequency and it also exceeded the value of elastic loss modulus (G″) by an order of magnitude. These studies also lead to the conclusion that in comparison to **CPG1**, **CPG2** has a greater storage modulus, and was more viscoelastic in nature (Fig. 2.18a and 2.18b). The XRD patterns of both the gels activated prior to gas adsorption studies when compared with that of the as-synthesized form indicate a lesser degree of transformation from the pristine

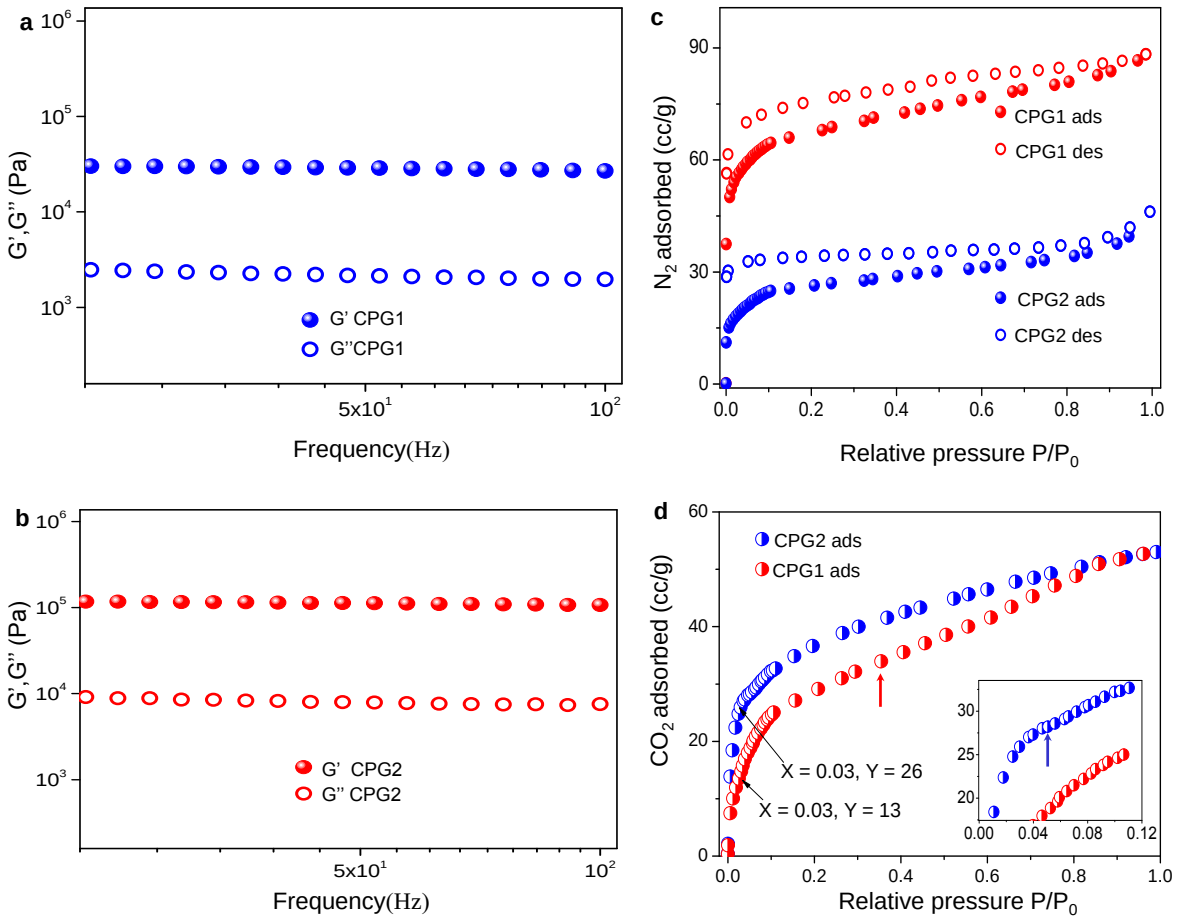

Figure 2.18. (a) Rheological behavior of **CPG1** and (b) **CPG2**. (c) N_2 adsorption (ads) and desorption (des) isotherms of **CPG1** and **CPG2** at 77 K. (d) CO_2 adsorption isotherms of **CPG1** and **CPG2** at 195 K. Inset shows the zoomed in low pressure region. Red and blue arrows indicate stepwise uptake of CO_2 in case of **CPG1** and **CPG2**, respectively.

crystalline form for activated **CPG2**, while activation of **CPG1** transformed it almost into an amorphous material (Fig. 2.16b). Thus, application of heat or stress led to a lesser change in structure in the case of **CPG2**, corroborating greater rigidity and ability to retain its parent structure as compared to **CPG1**. This rigidity may be

attributed to the compact packing of the molecular motifs in **CPG2** as compared to **CPG1**.

In order to have an idea about the porosity of the two materials, N_2 gas adsorption measurements were performed on both **CPG1** and **CPG2**. The adsorption isotherm obtained in both cases showed a typical type I behavior according to International Union of Pure and Applied Chemistry (IUPAC) classification, confirming the microporosity of the samples (Fig. 2.18c).[24,67] Significant hysteresis was observed in the process of desorption for both samples.

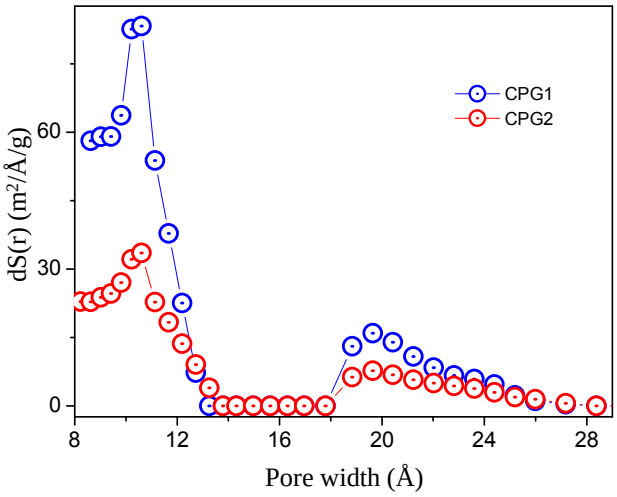

Figure 2.19. Comparative pore size distribution for **CPG1** and **CPG2**. Pore volume in **CPG1** and **CPG2** was calculated to be 0.127 and 0.062 cc/g, respectively.

The micropore dimensions calculated from the pore size distribution plot (10.2 Å) (Fig. 2.19) matches well with the length of **ADA**. The maximum amount of N_2 adsorbed at saturation pressure in the case of **CPG1** was found to be 88 mL g^{-1} and it possessed a Brunauer–Emmett–Teller (BET) surface area ~223 m^2 g^{-1}. In the case of

CPG2, maximum uptake was found to be 46 mL g^{-1} of the sample and the BET surface area was substantially decreased to ~ 90 $m^2 g^{-1}$ (Fig. 2.18c). The difference in gas adsorption properties has been compared with previous literature reports, where N_2 and CO_2 adsorption has been measured as a function of morphology or photoresponsive behavior, and the results indicate that the porosity difference obtained in our material is quite significant.[20,68] Apart from this, the surface area is higher when compared to previously reported xerogels and aerogels,[69-71] although aerogels obtained by supercritical CO_2 treatment are known to exhibit better porosity in most cases.[47] In the absence of a particular crystalline phase, the drop-off in N_2 gas uptake in **CPG2** may be ascribed to the loss in surface area due to downsizing of the coordination network combined with considerable amount of pore blocking due to the presence of encapsulated **ADA** molecules, as evidenced from the FT-IR studies. As a result, **CPG2** possesses lower available free volume due to considerable pore blocking. The presence of encapsulated **ADA** molecules, leading to a more close packed structure, supports the improvement in rheological behavior. However, the CO_2 adsorption isotherm (Fig. 2.18d) showed that at low partial pressure (0.03), **CPG2** adsorbs almost double the amount of CO_2 than **CPG1**. The comparatively high uptake of CO_2 at lower pressure can be assigned to the ability of **CPG2** to undergo spatial adjustments. Due to this probable structural changes, the lone pairs of electrons over nitrogen atoms are now directed towards the pores,[72] which can then act as potential sites for CO_2 adsorption (Fig. 2.18d, inset).[73] **CPG1** on the other hand shows

a broad second step in the adsorption isotherm at higher partial pressure (0.46) to finally match the total amount of adsorbed CO_2 found in the case of **CPG2**. This can be ascribed to the guest-induced second-order structural transformations taking place in **CPG1**.[10] At higher pressures; **CPG2** did not show any such change, indicating its densely packed rigid structure.

2.4. Conclusions

Results of this study point toward the conclusion that, irrespective of the presence of a photoresponsive group in **CPG1** or **CPG2**, light does not have a post-synthetic influence on its bulk structure. However, pre-synthetic photoisomerization of the precursor of the coordination polymer leads to morphologically different macroscopic structures. Time-dependent morphological investigations suggest that light-induced structural evolution nucleates at the molecular level, transforms at the mesoscopic level via controlled facetted crystal growth process, leading to different macroscopic morphological forms of **CPG1** and **CPG2** in the present case. Photoinduced coordination modulation can therefore be applied as a promising tool for 'nanoarchitectonics' to control the kinetic self-assembly of photoresponsive coordination polymers. It is further observed that the aforesaid synthetic strategy can have a profound influence on the properties of porous metal–organic materials. Such porous gels like **CPG2** with better rheological properties along with comparatively lower intake of N_2 and better CO_2 capture properties can easily replace the pore

blocking binder materials used in generating shaped bodies from MOFs for industrial applications.[74-75] Alternately, the generation of iron oxide nanoparticles from such gel templates would be of interest for further investigation.[76-77]

2.5. Experimental Section

2.5.1. Materials and Methods

Unless otherwise stated, all starting materials, reagents and dry solvents were purchased from commercial suppliers and used as received. Azobenzene-4,4'-dicarboxylic acid (**ADA**) was synthesized according to Scheme 1, based on a reported procedure.[78] Melting points were determined with MEL-Temp-II melting point apparatus and are uncorrected. ^{1}H (500 MHz) and ^{13}C (125 MHz) NMR experiments were performed on a Bruker Avance DPX spectrometer. Chemical shifts are reported in parts per million (ppm) using tetramethylsilane (TMS) (δ_H = 0 ppm) or the solvent residual signal (DMSO-d_6: δ_C = 39.50 ppm) as an internal reference. Elemental analyses were performed on a Perkin-Elmer Series 2 Elemental Analyzer 2400. IR spectra were obtained from a Perkin-Elmer Spectrum One FT-IR spectrometer using KBr (neat). Deconvolution of FT–IR spectra was performed using Fityk 0.9.8 software.[79] Thermogravimetric analysis (TGA) was carried out using TA instruments Q 50 and all samples were heated at 10 K/min under N_2 atmosphere. **CPG1** and **CPG2** were washed with DMSO for several times to remove the unreacted starting

materials. It was then dried in an oven, kept at 150 °C for 24 h, to obtain the xerogel powder which was used for further characterization.

2.5.2. Preparation of Azobenzene-4,4'-Dicarboxylic Acid (ADA)

PNBA (2 g, 7.4 mmol) and sodium hydroxide (6.7 g, 167.5 mmol) were dissolved in distilled water (30 mL) by heating in a water bath at 50 °C. To this solution, a solution of glucose (13.33 g, 74 mmol) dissolved in distilled water (20 mL) was added drop wise, maintaining the temperature of the water bath at 50 °C. The highly exothermic reaction resulted in the spontaneous formation of a dark brown solution. A stream of air was passed through this reaction mixture using a dropper connected to a 5 W air pump. The reaction mixture was kept in the water bath (50 °C) with constant bubbling of air for 4-5 h and then the chocolate brown precipitate was filtered off. The precipitate was dissolved in distilled water (100 mL) and later acidified by dropwise addition of glacial acetic acid (10 mL) resulting in a light pink precipitate. This precipitate was filtered and washed with water (500 mL) and then dried in an oven maintained at 70 °C to obtain **ADA** as a light pink powder in 62% yield. m.p. > 320^{o}C; FT-IR (KBr): ν_{max} = 2826(m), 1688(s), 1603(w), 1423(m), 1298(s), 933(m) cm^{-1}; ^{1}H NMR (500 MHz, DMSO-d_6, TMS, 25^{o}C): δ = 8.16 (d, 4H, Ar-H), 8.00 (d, 4H, Ar-H) ppm; ^{13}C NMR (125 MHz, DMSO-d_6, 25^{o}C): δ = 122.5, 130.3, 133.0, 153.8, 166.2 ppm; Elemental analysis: Calcd. for $C_{14}H_{10}N_2O_4$; C, 62.22; H, 3.73; N, 10.37. Found: C, 61.84; H, 3.60; N, 10.14.

2.5.3. Synthesis of Nanoscale CPG1

ADA (100 mg, 0.37 mmol), dissolved in dry DMSO (50 mL) was taken in a 250 mL amber colored round bottom flask. To this solution, triethyl amine (0.2 mL) was added and the flask was tightly sealed and kept in an oil bath maintained at 50 °C for 2 h to confirm that the majority of the molecules remain in the thermodynamically favorable *trans*-state. The temperature was then brought down to 40 °C and to this mixture, a solution of ferric nitrate nonahydrate (150 mg, 0.37 mmol) in dry DMSO (50 mL) was added and the mixture was left undisturbed for 6-7 h. The temperature was slowly brought down to room temperature and the colloidal precipitate was collected and purified by repeated cycles of washing with dry DMSO and centrifugation (at 2500 rpm). A speck of the material was further dispersed in DMSO or methanol via sonication (for 15 min) and then drop casting over freshly cleaved mica substrate or TEM grids for morphological analysis.

2.5.4. Synthesis of Nanoscale CPG2

ADA (100 mg, 0.37 mmol) dissolved in dry DMSO (50 mL) and triethyl amine (0.2 mL) was taken in a flat bottom quartz flask. The resulting solution was irradiated with 365 nm light using a Rayonet reactor for 4 h and to this solution, ferric nitrate nonahydrate (150 mg, 0.37 mmol) in dry DMSO (50 mL) was added and the mixture was left undisturbed for 6-7 h under UV light. Care was taken that continuous irradiation did not increase the temperature of the reaction mixture above 40 °C. The

material was purified via repeated cycles of washing and centrifugation (at 2500 rpm). A speck of the material was further dispersed in DMSO or methanol via sonication (for 15 min) and then drop casting over freshly cleaved mica substrate or TEM grids for morphological analysis.

2.5.5. Synthesis of Gels with Non-Photoresponsive Ligand

A solution of trimesic acid or 1,3,5-benzenetricarboxylic acid (BTC, 42 mg, 0.2 mmol) in ethanol (1 mL) was mixed with a solution of $Fe(NO_3)_3{\cdot}9H_2O$ (81 mg, 0.2 mmol) in ethanol (1 mL) in 2:3 volumetric ratio resulting in immediate formation of a gel (**FeBTC**).[47] For synthesis of irradiated gel (**IRFeBTC**), the ethanolic solution of BTC was irradiated with UV light ($\lambda_{band\ pass}$ = 350 nm) for 2 h prior to the addition of $Fe(NO_3)_3{\cdot}9H_2O$ in ethanol.

2.5.6. Experimental Techniques

2.5.6.1. Optical Measurements and Photoirradiation

Electronic absorption spectra were recorded on a Shimadzu UV-3600 scanning spectrophotometer using a 1 cm path length quartz cuvette. Solid-state absorption or reflection spectra were obtained using $BaSO_4$ as a standard. Photoirradiation was carried out using LOT-Oriel 200 W high pressure Hg Lamp utilizing $\lambda_{band\ pass}$ = 350 and 420 nm.

2.5.6.2. Scanning Electron Microscopy (SEM)

SEM images were obtained using a Zeiss EVO 18 cryo SEM Special Edn with variable pressure detector working at 20-30 kV. Time dependent SEM analysis was carried out by breaking the formed gel at different time intervals and dropcasting the same on freshly cleaved mica substrate. All the samples were coated with gold prior to examination.

2.5.6.3. Transmission Electron Microscopy (TEM)

Transmission electron microscopy (TEM) and high resolution TEM (HRTEM) were performed on a FEI, TECNAI 30 G2 S-TWIN microscope with an accelerating voltage of 100 and 300 kV, respectively. 1 mg of the xerogel samples of **CPG1** or **CPG2** (both purified and dried) were well dispersed in 5 mL methanol by ultra-sonication for 15 min and then drop casting on carbon coated copper grids. Images were obtained without staining. IFFT reconstruction of the HR-TEM images was done using a software programme, Digital Micrograph^{TM} (GATAN Inc.) following a reported procedure.[80] Initially, a fast Fourier transform (FFT) of the experimentally obtained image was taken, which was followed by appropriate mask filtering to remove the spatial frequency of the diffractogram. Finally, the IFFT gave rise to a reconstructed HR-TEM image.

2.5.6.4. Rheology Experiments

Rheological measurements were carried out in an Anton Paar Physical Modulated Compact Rheometre-150 Physica (Germany). A parallel plate sensor having a diameter 50 mm and a gap size of 0.1 mm was used. Measurements were carried out in dynamic oscillatory mode using strain amplitude of 1% in the frequency range 0.012-100 rad/sec.

2.5.6.5. BET Adsorption Studies

The BET adsorption isotherms for N_2 (at 77 K) and CO_2 (at 195 K) were performed on a QUANTACHROME QUADRASORB SI analyzer. About 100-125 mg of the xerogel samples (**CPG1** and **CPG2**) were placed in sample cells, then the samples were outgassed under high vacuum conditions at 423 K for 12 h in case of **CPG1** and for 16 h in the case of **CPG2** for N_2 adsorption and at 413 K for 10 h in case of **CPG1** and 373 K for 5 h in case of **CPG2** for CO_2 adsorption experiments. The adsorbate was taken in sample tubes and the change in pressure was monitored. The degree of adsorption was ascertained from the decrease in pressure at the equilibrium state. All operations were automatically performed and controlled by computers. Pore size distribution analysis was performed using the non-local density functional theory (NLDFT) equilibrium model.

2.6. References

1. M. Aono, *Sci. Technol. Adv. Mater.*, 2011, **12**, 040301.
2. K. Ariga, Q. Ji, J. P. Hill, Y. Bando and M. Aono, *NPG Asia Mater.*, 2014, **4**, e17.
3. K. Ariga, Q. Ji, W. Nakanishi, J. P. Hill and M. Aono, *Mater. Horiz.*, 2015, **2**, 406.
4. K. Ariga, Y. Yamauchi, G. Rydzek, Q. Ji, Y. Yonamine, K. C. -W. Wu and J. P. Hill, *Chem. Lett.* 2014, **43**, 36.
5. H. Li, M. Eddaoudi, M. O'Keeffe and O. M. Yaghi, *Nature*, 1999, **402**, 276.
6. H. Furukawa, K. E. Cordova, M. O'Keeffe and O. M. Yaghi, *Science*, 2013, **341**, 1230444.
7. M. Kondo, T. Yoshitomi, K. Seki, H. Matsuzaka and S. Kitagawa, *Angew. Chem., Int. Ed.*, 1997, **36**, 1725.
8. S. Kitagawa, R. Kitaura and S. Noro, *Angew. Chem., Int. Ed.*, 2004, **43**, 2334.
9. T. Tsuruoka, S. Furukawa, Y. Takashima, K. Yoshida, S. Isoda and S. Kitagawa, *Angew. Chem., Int. Ed.*, 2009, **48**, 4739.
10. Y. Sakata, S. Furukawa, M. Kondo, K. Hirai, N. Horike, Y. Takashima, H. Uehara, N. Louvain, M. Meilikhov, T. Tsuruoka, S. Isoda, W. Kosaka, O. Sakata and S. Kitagawa, *Science*, 2013, **339**, 193.
11. J. Reboul, S. Furukawa, N. Horike, M. Tsotsalas, K. Hirai, H. Uehara, M. Kondo, N. Louvain, O. Sakata and S. Kitagawa, *Nat. Mater.*, 2012, **11**, 717.
12. N. Kishi, M. Akita, M. Kamiya, S. Hayashi, H.-F. Hsu and M. Yoshizawa, *J. Am. Chem. Soc.*, 2013, **135**, 12976.
13. R. D. Mukhopadhyay, V. K. Praveen and A. Ajayaghosh, *Mater. Horiz.*, 2014, **1**, 572.
14. A. Gopal, M. Hifsudheen, S. Furumi, M. Takeuchi and A. Ajayaghosh, *Angew. Chem., Int. Ed.*, 2012, **51**, 10505.

15. S. Mahesh, A. Gopal, R. Thirumalai and A. Ajayaghosh, *J. Am. Chem. Soc.*, 2012, **134**, 7227.
16. R. Rajaganesh, A. Gopal, T. M. Das and A. Ajayaghosh, *Org. Lett.*, 2012, **14**, 748.
17. G. Abellán, E. Coronado, C. Martí-Gastaldo, A. Ribera, J. L. Jordá and H. García, *Adv. Mater.*, 2014, **26**, 4156.
18. A. Modrow, D. Zargarani, R. Herges and N. Stock, *Dalton Trans.*, 2011, **40**, 4217.
19. J. Park, D. Yuan, K. T. Pham, J. R. Li, A. Yakovenko and H. C. Zhou, *J. Am. Chem. Soc.*, 2012, **134**, 99.
20. N. Yanai, T. Uemura, M. Inoue, R. Matsuda, T. Fukushima, M. Tsujimoto, S. Isoda and S. Kitagawa, *J. Am. Chem. Soc.*, 2012, **134**, 4501.
21. R. Lyndon, K. Konstas, B. P. Ladewig, P. D. Southon, P. C. Kepert and M. R. Hill, *Angew. Chem., Int. Ed.*, 2013, **52**, 3695.
22. J. W. Brown, B. L. Henderson, M. D. Kiesz, A. C. Whalley, W. Morris, S. Grunder, H. Deng, H. Furukawa, J. I. Zink, J. F. Stoddart and O. M. Yaghi, *Chem. Sci.*, 2013, **4**, 2858.
23. L. Heinke, M. Cakici, M. Dommaschk, S. Grosjean, R. Herges, S. Brase and C. Woll, *ACS Nano*, 2014, **8**, 1463.
24. J. Park, L. B. Sun, Y. P. Chen, Z. Perry and H. C. Zhou, *Angew. Chem., Int. Ed.*, 2014, **53**, 5842.
25. S. Yagai and A. Kitamura, *Chem. Soc. Rev.*, 2008, **37**, 1520.
26. X. Yang, G. Zhang and D. Zhang, *J. Mater. Chem.*, 2012, **22**, 38.
27. P. Dastidar, *Chem. Soc. Rev.*, 2008, **37**, 2699.
28. H. A. Barnes, *J. Non-Newtonian Fluid Mech.*, 1997, **70**, 1.
29. M.-O. M. Piepenbrock, G. O. Llyod, N. Clarke and J. W. Steed, *Chem. Rev.*, 2010, **110**, 1960.

30. J. Zhang and C.-Y. Su, *Coord. Chem. Rev.*, 2013, **257**, 1373.
31. S. S. Babu, V. K. Praveen and A. Ajayaghosh, *Chem. Rev.*, 2014, **114**, 1973.
32. T. F. A. de Greef and E. W. Meijer, *Nature*, 2008, **453**, 171.
33. T. Aida, E. W. Meijer and S. I. Stupp, *Science*, 2012, **335**, 813.
34. S. Saha, G. Das, J. Thote and R. Banerjee, *J. Am. Chem. Soc.*, 2014, **136**, 14845.
35. H. B. Aiyappa, S. Saha, P. Wadge, R. Banerjee and S. Kurungot, *Chem. Sci.*, 2015, **6**, 603.
36. O. M. Yaghi, G. Li and H. Li, *Chem. Mater.*, 1997, **9**, 1074.
37. J. A. Foster, M.-O. M. Piepenbrock, G. O. Llyod, N. Clarke, J. K. Howard and J. W. Steed, *Nat. Chem.*, 2010, **2**, 1037.
38. K. J. C. van Bommel, A. Friggeri and S. Shinkai, *Angew. Chem., Int. Ed.*, 2003, **42**, 980.
39. H. Yamaguchi, Y. Kobayashi, R. Kobayashi, Y. Takashima, A. Hashidzume and A. Harada, *Nat. Commun.*, 2012, **3**, 603.
40. S. C. Wei, M. Pan, K. Li, S. Wang, J. Zhang and C. Y. Su, *Adv. Mater.*, 2014, **26**, 2072.
41. R. F. Service, *Science*, 2012, **335**, 1167.
42. M. Nakatsuji, *Biomater. Sci.*, 2013, **1**, 9.
43. C. Serre, F. Millange, S. Surble and G. Ferey, *Angew. Chem., Int. Ed.*, 2004, **43**, 6285.
44. T. R. Whitfield, X. Wang, L. Liu and A. J. Jacobson, *Solid State Sciences*, 2005, **7**, 1096.
45. J. Zhang and C.-Y. Su, *Coord. Chem. Rev.*, 2013, **257**, 1373.
46. Q. Wei and S. L. James, *Chem. Commun.*, 2005, 1555.
47. M. R. Lohe, M. Rose and S. Kaskel, *Chem. Commun.*, 2009, 6056.
48. G. B. Deacon and R. J. Phillips, *Coord. Chem. Rev.*, 1980, **33**, 227.
49. T. Ishiwata, Y. Furukawa, K. Sugikawa, K. Kokado and K. Sada, *J. Am. Chem. Soc.*, 2013, **135**, 5427.

50. M. Oh and C. A. Mirkin, *Nature*, 2005, **438**, 651.
51. S. Jung and M. Oh, *Angew. Chem., Int. Ed.*, 2008, **47**, 2049.
52. Y. M. Jeon, G. S. Armatas, D. Kim, M. G. Kanatzidis and C. A. Mirkin, *Small*, 2009, **5**, 46.
53. A. M. Spokoyny, D. Kim, A. Sumrein and C. A. Mirkin, *Chem. Soc. Rev.*, 2009, **38**, 1218.
54. T. Witten and L. Sander, *Phys. Rev. Lett.*, 1981, **47**, 1400.
55. J. Ge, J. Lei and R. N. Zare, *Nat. Nanotech.*, 2012, **7**, 428.
56. J. Zeng and Y. Xia, *Nat. Nanotech.*, 2012, **7**, 415.
57. H. Cölfen and S. Mann, *Angew. Chem., Int. Ed.*, 2003, **42**, 2350.
58. J.-L. Li and X.-Y. Liu, *Adv. Funct. Mater.*, 2010, **20**, 3196.
59. J. D. H. Donnay and D. Harker, *Am. Mineral.*, 1937, **22**, 446.
60. A. Umemura, S. Diring, S. Furukawa, H. Uehara, T. Tsuruoka and S. Kitagawa, *J. Am. Chem. Soc.*, 2011, **133**, 15506.
61. F. Rakotondradany, M. A. Whitehead, A. M. Lebuis and H. F. Sleiman, *Chem. – Eur. J.*, 2003, **9**, 4771.
62. W. Cho, H. J. Lee and M. Oh, *J. Am. Chem. Soc.*, 2008, **130**, 16943.
63. E. Matijević and P. Scheiner, *J. Colloid Interface Sci.*, 1978, **63**, 509.
64. M. Ocaña, M. P. Morales and C. J. Serna, *J. Colloid Interface Sci.*, 1995, **171**, 85.
65. L. Li, S. Xiang, S. Cao, J. Zhang, G. Ouyang, L. Chen and C. -Y. Su, *Nat. Commun.*, 2013, **4**, 1774.
66. D. Feng, K. Wang, Z. Wei, Y. P. Chen, C. M. Simon, R. K. Arvapally, R. L. Martin, M. Bosch, T. F. Liu, S. Fordham, D. Yuan, M. A. Omary, M. Haranczyk, B. Smit and H. C. Zhou, *Nat. Commun.*, 2014, **5**, 5723.
67. H. Sato, R. Matsuda, K. Sugimoto, M. Takata and S. Kitagawa, *Nat. Mater.*, 2010, **9**, 661.
68. H. J. Lee, W. Cho, S. Jung and M. Oh, *Adv. Mater.*, 2009, **21**, 674.

69. Y.-O. Liu, L. He, J. Zhang, X. Wang and C.-Y. Su, *Chem. Mater.*, 2009, **21**, 557.
70. J. Zhang, X. Wang, L. He, L. Chen, C. -Y. Su and S. L. James, *New J. Chem.*, 2009, **33**, 1070.
71. S. Samai and K. Biradha, *Chem. Mater.*, 2012, **24**, 1165.
72. Y. Takashima, V. M. Martinez, S. Furukawa, M. Kondo, S. Shimomura, H. Uehara, M. Nakahama, K. Sugimoto and S. Kitagawa, *Nat. Commun.*, 2011, **2**, 168.
73. C. M. Nagaraja, R. Haldar, T. K. Maji and C. N. R. Rao, *Cryst. Growth Des.*, 2012, **12**, 975.
74. A. U. Czaja, N. Trukhan and U. Müller, *Chem. Soc. Rev.*, 2009, **38**, 1284.
75. S. Mitchell, N. L. Michels, K. Kunze and J. Perez-Ramirez, *Nat. Chem.*, 2012, **4**, 825.
76. S. Alam, C. Anand, K. Ariga, T. Mori and A. Vinu, *Angew. Chem., Int. Ed.*, 2009, **48**, 7358.
77. W. Cho, S. Park and M. Oh, *Chem. Commun.*, 2011, **47**, 4138.
78. S. Ameerunisha and P. S. Zacharias, *J. Chem. Soc., Perkin Trans.*, 1995, **2**, 1679.
79. M. Wojdyr, *J. Appl. Cryst.*, 2010, **43**, 1126.
80. Y.-M. Kim, J.-M. Jeong, J.-G. Kim, Y.-J. Kim and Y. S. Lim, *J. Korean Phys. Soc.*, 2006, **48**, 250.

Chapter 3

Precise Control of Host-Guest Interactions in a Coordination Polymer Gel

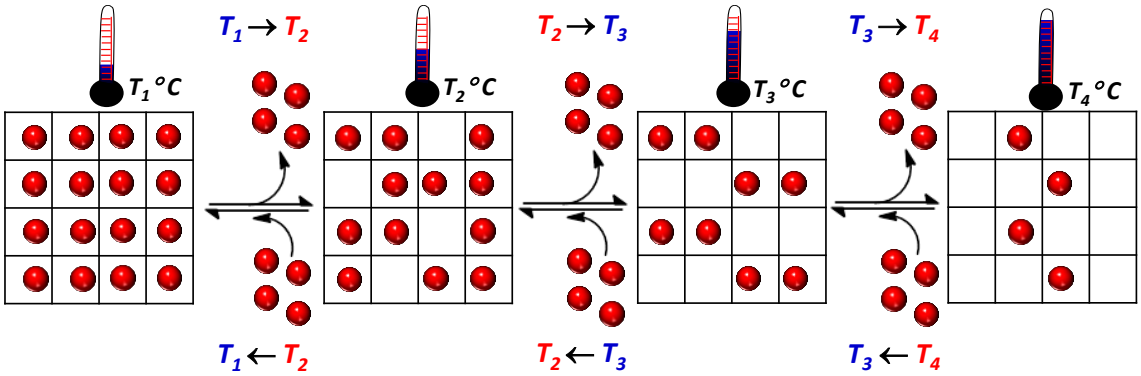

3.1. Abstract

*Having a precise control over host-guest interactions is a challenge in the design of smart supramolecular systems. While nature has the unique ability to precisely control multi-step biochemical processes, artificial host-guest systems rarely possess such command. This is further coupled with additional challenges to develop multi-stimuli responsive systems and to modulate their behavior under chemically competing environments. Herein, we have designed a coordination polymer with azobenzene appendages (**Mg-CP**), which act as suitable binding sites for cyclodextrin (**CD**) molecules. Exploiting the thermodynamic benefits of a system in equilibrium, we*

*have demonstrated stepwise and controllable delivery of cyclodextrins using both physical (temperature) and chemical (competitive guest molecules) stimuli. The system showcases different binding profiles towards different cyclodextrins and can, therefore, be utilized for their chemical decoding at molecular level. This host-guest system with tunable inclusion-release profiles manifests a prototype towards controlled drug delivery motifs, capable of stimuli-responsive release and encapsulation of drug molecules (cyclodextrins). The coordination polymeric host-guest system described herein has therefore been incorporated in a polymer hydrogel matrix replicating a drug delivery device for the controlled release of drug molecules (**α-CD**) in response to changes in temperature in a quasi-solid state.*

3.2. Introduction

Ever since the postulation of the lock and key concept by Emil Fischer in 1894,[1] a myriad of studies have been reported in the area of host–guest interactions, aiming at understanding the mechanism behind enzymatic action in biological systems. Most of the enzymatic processes, starting with the synthesis of peptides via translation, degradation of various metabolites, synthesis and hydrolysis of adenosine triphosphate, etc. proceed in a stepwise fashion and with absolute control.[2] While nature has the wisdom to explicitly fine tune and program such sophisticated interactions, it still remains a challenge to achieve such precision and control in artificial host-guest systems. Several of these native systems are precisely controlled

by external or internal stimuli, however designing such artificial stimuli-responsive systems remains a challenging task.[3] Due to its instant delivery at a specific location and control via different wavelengths and intensities, light is arguably the most attractive physical stimulus. While most of the photoresponsive systems use deleterious ultraviolet radiation, biochemical applications like drug delivery demand light of higher wavelength (infrared region) due to its better penetration depth, minimal scattering, and photothermal heating capacity.[4-7] Heat, on the other hand is not considered such a friendly stimulus, due to issues related to energy consumption and the resulting irreversible thermal changes that hamper the reusability of host-guest systems.[3,8] However, temperature can take advantage of the thermodynamic benefits of host-guest equilibrium and could further be exploited to demonstrate the formation (capture) or dissociation (release) of a host-guest complex in a stepwise manner.[9-10] Similar control can also be achieved in presence of chemical agents that are capable of inducing responsiveness in a host guest system by competing with already encapsulated guest molecules.[3]

Sada and co-workers have reported a zirconium-based MOF with its external surface modified with a polymer, poly(*N*-isopropylacrylamide) (PNIPAM).[11] This polymer is known to undergo a thermal, coil–globule phase transition, between its dissolved (temperature < 32 °C) and aggregated states (temperature > 32 °C). These changes can reversibly switch the guest release properties of the PNIPAM modified

MOFs between the low temperature ‘‘*open* (*ON*)’’ state, and the high temperature ‘‘*closed* (*OFF*)’’ state (Figure 3.1).

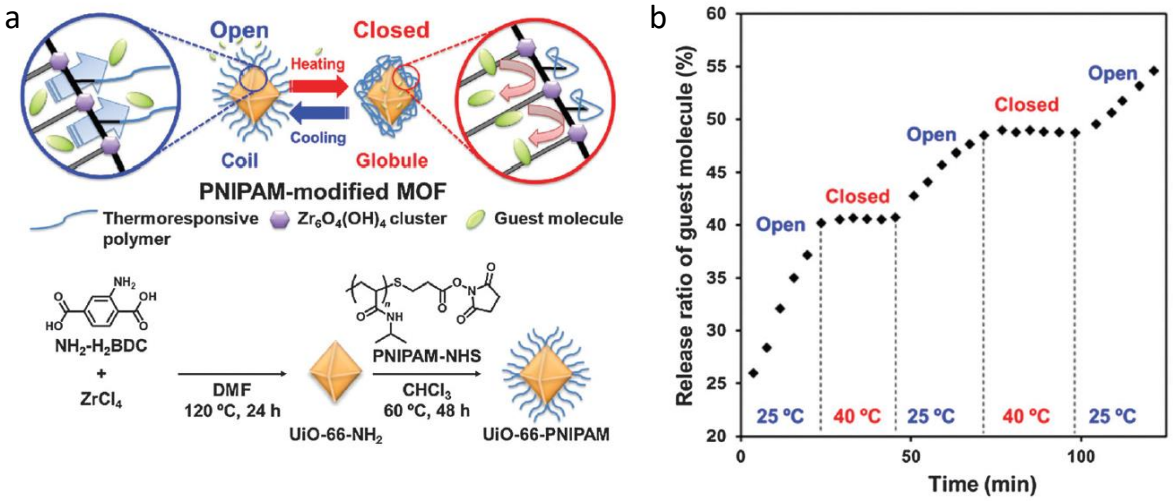

Figure 3.1. (a) Schematic representation of thermally controlled guest release using PNIPAM modified MOF (top), and synthetic scheme of the thermoresponsive MOF (bottom). (b) Temperature controlled stepwise release-and-halt profile of Resorufin by PNIPAM modified MOF in water. The release ratio was determined from the absorbance maximum of Resorufin at 572 nm.[11]

Meng *et al.* have reported the stepwise multi stimuli-responsive guest release from an azobenzene functionalized zirconium MOF (see Chapter 1, section 1.4).[12] The bulk surface of these MOFs with azobenzene appendages protruding outwards resulted in a host-guest complex with *β*-cyclodextrin (Figure 3.2a). Dissociation of this complex and hence the release of the guest molecules encapsulated inside the MOF was achieved via the simultaneous addition of a competitive binding agent, followed by its exposure to UV light. UV light induces a *cis-trans* isomerization of azobenzene that further changes the nanoporous environment, thereby forcing the residual guest molecules to escape (Figure 3.2b). Very recently, Kitagawa and co-

workers have reported the release of carbon monoxide from a highly robust manganese carbonyl complex embedded Zr(IV)-based metal–organic framework.[13]

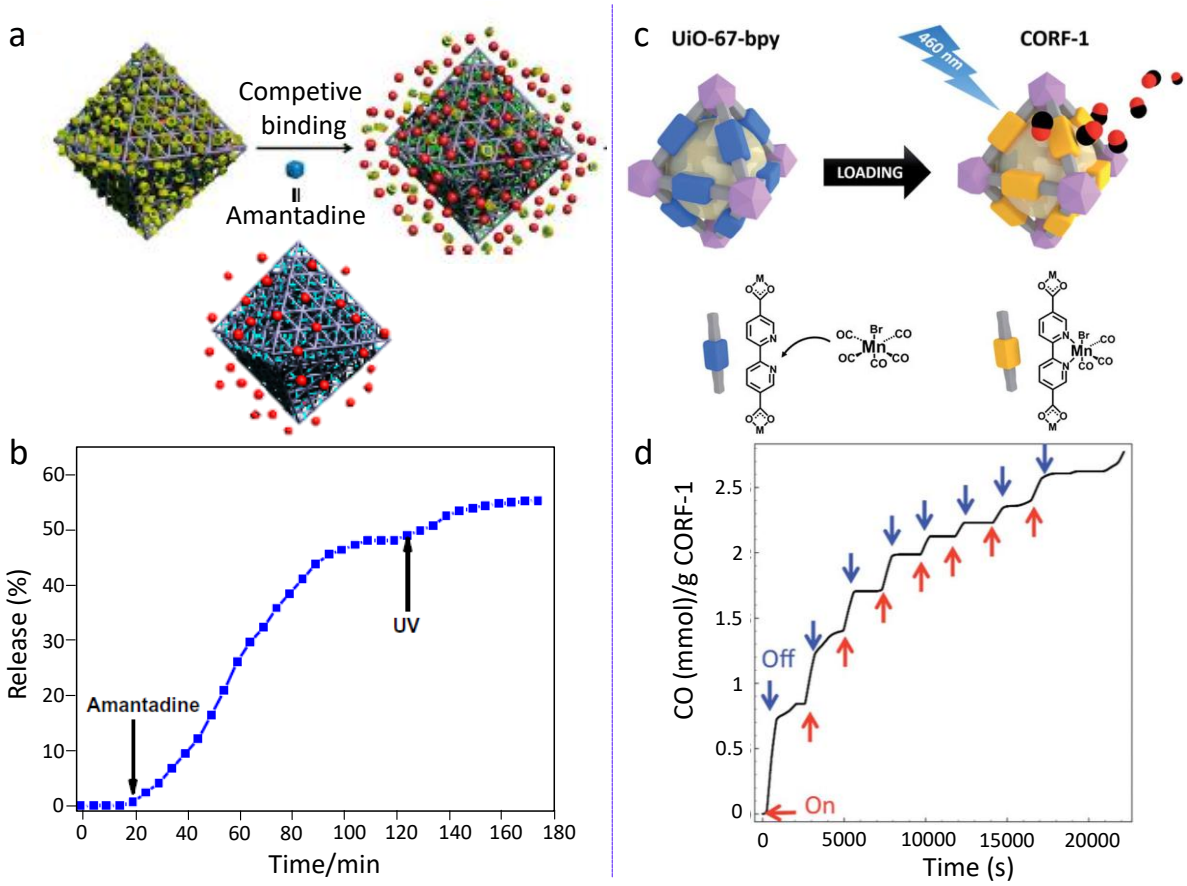

Figure 3.2. (a) Schematic representation of step-wise release of guest molecules by application of different stimuli. (b) Release profile of encapsulated guest (Rhodamine B) by the addition of amantadine followed by UV irradiation. (c) Schematic representation of loading of manganese carbonyl complex on Zr(IV)-MOF, resulting in **CORF-1** and the subsequent release of CO molecules from **CORF-1** upon photoirradiation. (d) Switchable release profile of CO from **CORF-1** upon intermittent photoirradiation of visible light (460 nm) from a 15 W source.[12,13]

This CO releasing framework (**CORF-1**) was found to be highly efficient and the stepwise release profile was controlled via multiple on-off switching using low

intensity visible light (460 nm, 15 W) (Figure 3.2c-d). In another report, Kahn and co-workers have reported pH and K^+ responsive DNA-functionalized MOFs (Figure 3.3a-c). Stepwise release of cargo entrapped within the MOF pores was demonstrated by adjusting the pH of the solution between 5.5 and 7.4 or by the alternative addition of K^+ that stabilizes the G-quadruplex and competing 18-crown-6-ether (K^+ binding agent) (Figure 3.3d-e).[14] From the above discussion it is clear that the whole process is limited to the stepwise release of guests only and no recapture is possible due to the irreversible nature of these systems. Also the amount of guest released is not consistent in each step. Herein, we discuss how the complexation as well as decomplexation of cyclodextrins with a coordination polymer gelator (**Mg-CP**) can be specifically controlled using heat and various competing chemical stimuli.

Cyclodextrins (CDs) consist of a cyclic chain of (α-1,4)-linked α-D-glucopyranose units and are produced during bacterial digestion of cellulose. Rather than being perfectly cylindrical, CDs have a truncated cone-like shape, with a hydrophobic interior cavity suitable for encapsulating hydrophobic guest molecules and a hydrophilic external surface leading to its water solubility.[15] CDs have therefore been widely exploited as hydrophobic drug delivery vehicles as well as in the design of functional supramolecular polymers.[16-17] Very recently, CDs have also been recognized as potent drug molecules for treating fatal neurodegenerative disorders like Niemann-Pick type C and as anti-obesity dietary fibers for flushing out fat from high cholesterol diets.[18-19] However, a suitable delivery system for easy, detectable

and controlled step-wise release of CDs in solution as well as in soft solid state devices is yet to be explored.

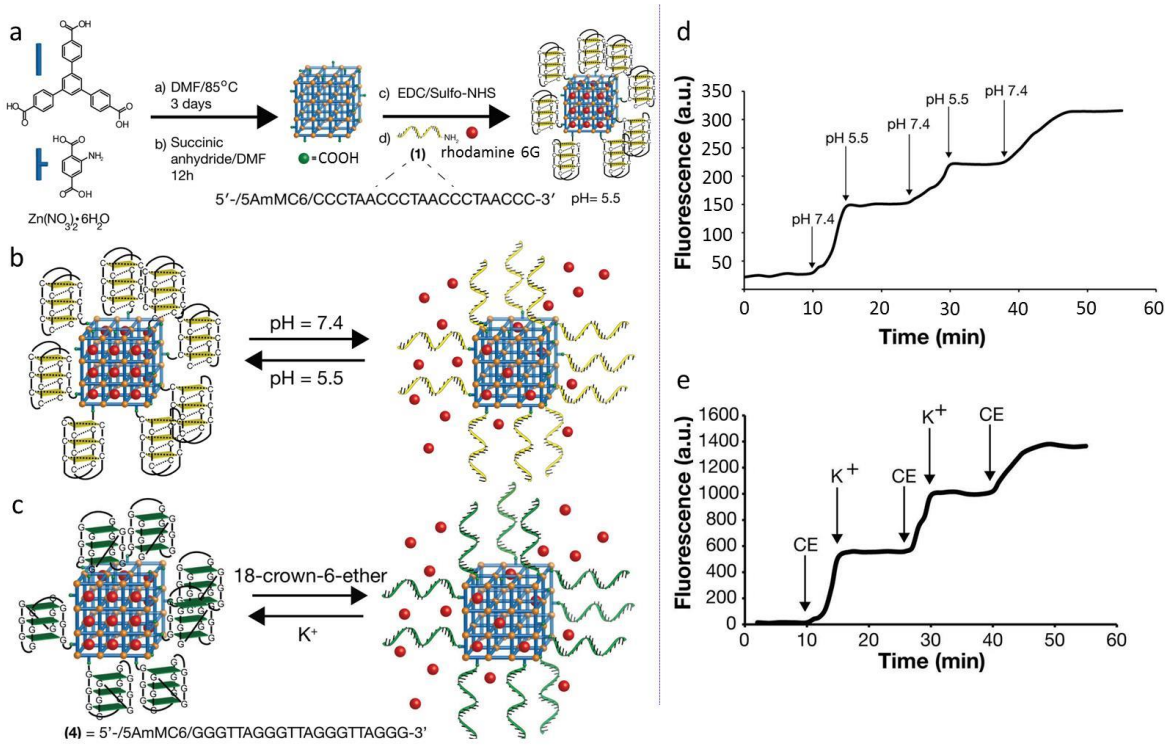

Figure 3.3. Schematic representation of (a) synthesis of a DNA modified MOF, (b) guest release from a pH responsive DNA modified MOF, and (c) guest release from a K^+ / 18-crown-6-ether responsive DNA modified MOF. (d) pH responsive and switchable *ON* (pH 7.4) - *OFF* (pH 5.5) release profile of guest molecules (Rhodamine 6G), in a stepwise manner as represented in (b). (e) Stepwise and switchable *ON* (18-crown-6-ether) - *OFF* (K^+) release of the guests from DNA modified MOFs, as represented in (c).[14]

Unlike other organic molecules CDs are optically transparent and their release and binding profiles cannot be identified using common spectroscopic techniques like absorption and fluorescence. Nevertheless, by virtue of their inherent chirality, CDs offer the possibility to follow their binding-release isotherms at a particular

temperature, via induced circular dichroism (ICD) spectroscopy.[20-21] However, this requires a functional platform, say a coordination polymer possessing accessible binding motifs. In this regard, several hydrophobic organic molecules like azobenzene, adamantane, bipyridine, etc. can act as suitable binding sites for cyclodextrins.[17] If such organic linkages can be organized over a linear inorganic secondary building unit (SBU), forming an one-dimensional (1-D) coordination polymer, the system may reversely accept and release CD molecules in solution upon the application of an appropriate stimulus. According to a report by Yaghi and co-workers, **MOF-74** based structure, composed of a chiral infinite rod-shaped magnesium or zinc oxide cluster and dioxidoterephthalate based organic linkers, forms a non-interpenetrated framework.[22] The ligand has a carboxylic acid motif with an *ortho*-positioned hydroxy group, as in salicylic acid. The observed structure can probably be restricted along the crystallographic *b* axis, if the organic strut contains the metal binding functionalities on one end. Such a design leads to a polymer brush-like structure, with the organic linkers organized along the infinite metal oxide chain as reported in the case of ICPs (Infinite Coordination Polymers) of calcium, manganese, cadmium, zirconium, lanthanides, etc.[23] With this idea in mind we prepared an organic ligand (**AzSA**) with a hydrophobic azobenzene core and metal binding salicylic acid moiety towards its one end.

3.3. Results and Discussion

3.3.1. Synthesis of the Organic Linker AzSA

Synthesis of (*E*)-2-hydroxy-5-(phenyldiazenyl)benzoic acid or salicylic acid derivative of azobenzene (**AzSA**) was carried out via the diazo coupling reaction between salicylic acid (**SA)** and aniline (**An**) as shown in Scheme 2. **An** was diazotized under acidic conditions in presence of sodium nitrite ($NaNO_2$) to obtain the corresponding diazonium salt (**DS**). The diazonium salt was then slowly added to an alkaline solution of **SA**, and the overall pH of the reaction mixture was maintained at 8-9. An ice bath was used to maintain the reaction temperature below 5 °C. Pure **AzSA** was obtained via recrystallization of the crude azo dye from an ethanol–water (1:3) mixture in 75% yield.

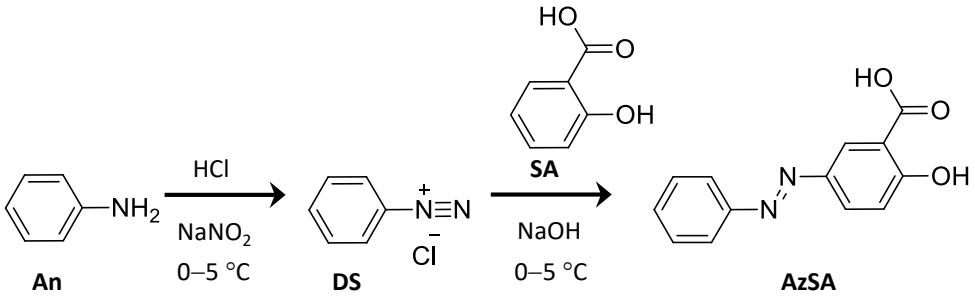

Scheme 2. Reagents and conditions for the synthesis of **AzSA**.

3.3.2. Synthesis and Characterization of the Coordination Polymer Gel (Mg-CP)

The magnesium based coordination polymer, **Mg-CP** was synthesized via a solvothermal reaction (Figure 3.4a) of azobenzene salicylic acid (**AzSA**) with $Mg(NO_3)_3{\cdot}6H_2O$ in high boiling solvents. The reaction in diethylformamide (DEF), specifically resulted in the formation of a coordination polymer gel (Figure 3.4b). The gel was found to be thermally irreversible and its non-linear rheological behavior was confirmed by the amplitude sweep studies (Figure 3.4c). The critical gelation concentration was found to be 4 mg mL^{-1} (Figure 3.4d). The xerogel obtained from **Mg-CP** was further characterized by Fourier transform infrared (FT-IR) and ^1H NMR spectroscopy. Coordination of the carboxylic acid and hydroxyl groups in **AzSA** to the MgO-based inorganic cluster was confirmed by the absence of the free O-H stretching band (2500-3300 cm^{-1}) in its FT-IR spectrum (Figure 3.5a). The unsymmetric nature of the bidentate bridging mode of coordination with additional bridging was corroborated by the difference between asymmetric and symmetric stretching frequencies of the carbonyl group that increased from 217 cm^{-1} in **AzSA** to 223 cm^{-1} in **Mg-CP** (Figure 3.5b).[24] Thermogravimetric analysis (TGA) confirmed the superior thermal stability of **Mg-CP** over the ligand **AzSA**. The thermal decomposition of the 1-D CP was found to start around 300°C, whereas the ligand (**AzSA**) started to decompose around 200°C.

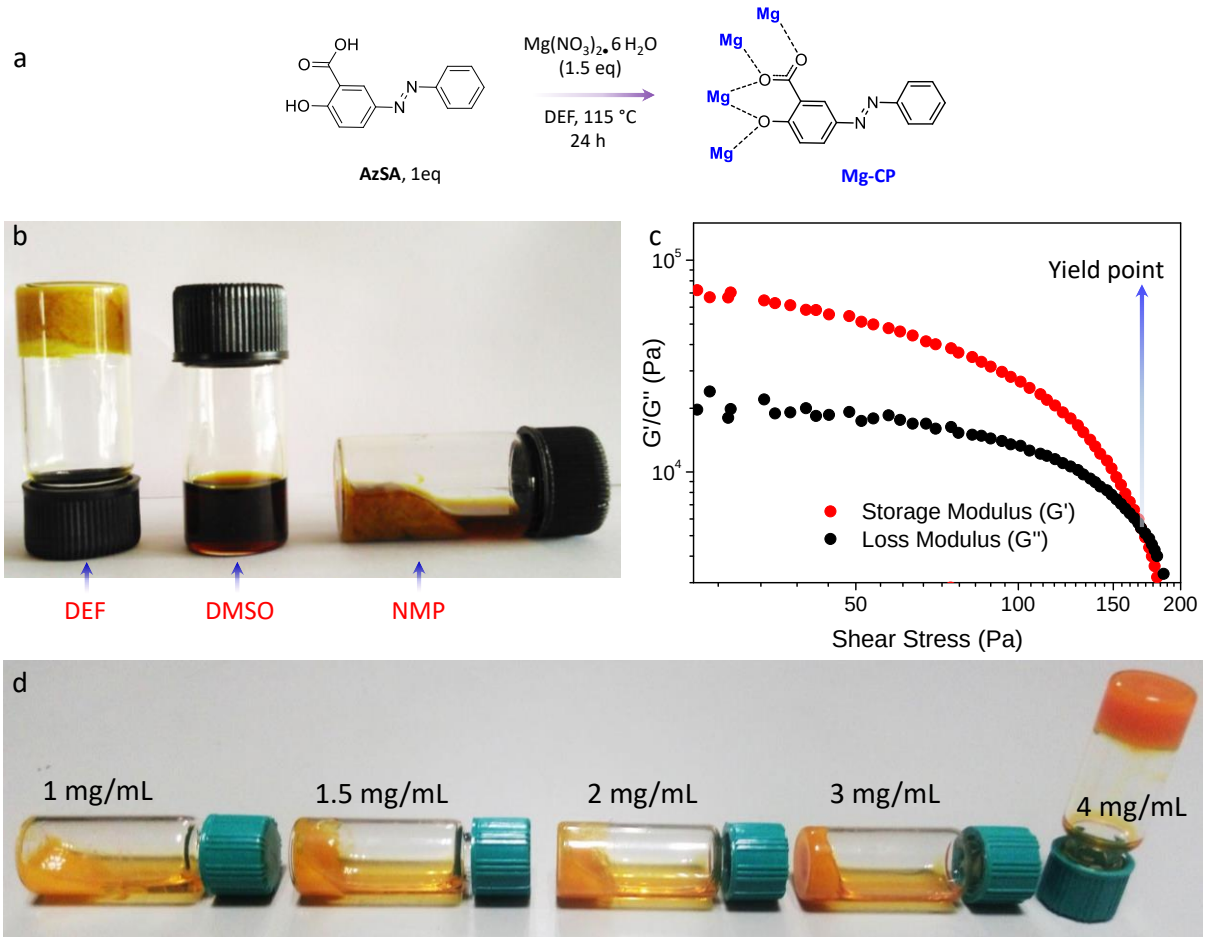

Figure 3.4. (a) Reagents and conditions for the synthesis of **Mg–CP** from **AzSA**. (b) Photographs of **Mg–CP** obtained using different solvents for its synthesis. A stable CP gel was obtained only in DEF. (c) Nonlinear rheological response (amplitude sweep) of **Mg–CP** gel. (d) Photographs showing formation of **Mg–CP** at the critical gelation concentration (4 mg mL^{-1}).

Moreover, a residual weight (42%) equivalent to the amount of Mg-O present in **Mg-CP** remained even above 700°C (Figure 3.5c). The phenolic –OH proton, which is otherwise exchangeable in CD_3OD can be visualized in the ^1H NMR spectrum of **AzSA** due to strong intramolecular hydrogen bonding. The absence of the phenolic -OH peak in the ^1H NMR spectrum of **Mg-CP** confirmed the coordination of

the ligand with Mg^{2+}. Broadening of the peaks in the aromatic region and the presence of coordinated DEF solvent molecules was also evident from the ^{1}H NMR spectrum of **Mg-CP** (Figure 3.5d).

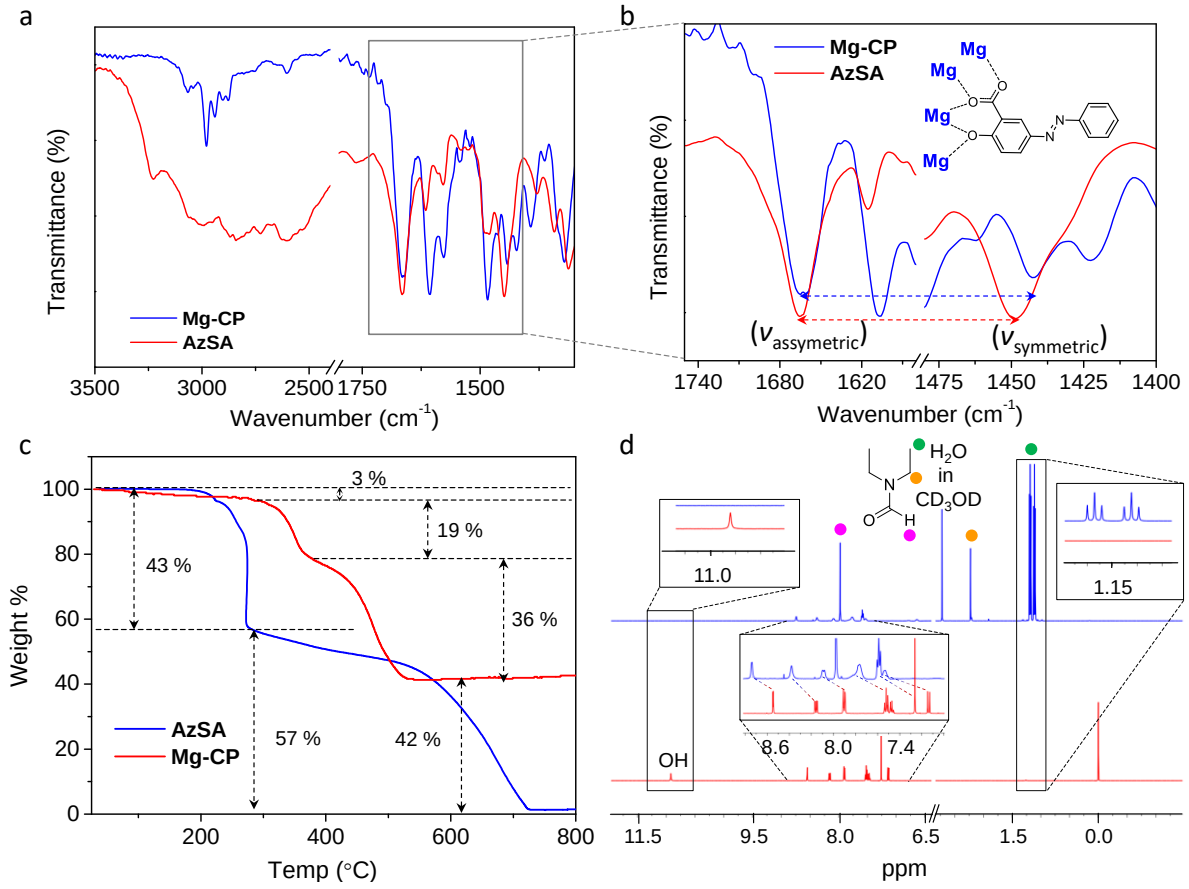

Figure 3.5. (a) FT-IR spectra of the organic ligand **AzSA** and the coordination polymer **Mg-CP** showing changes in the region corresponding to O–H stretching and the asymmetric and symmetric stretching frequencies of the carbonyl bond. (b) Expanded portion of the region (1750–1400 cm^{-1}), showing the differences in the asymmetric and symmetric stretching bands of the carbonyl bond. The structure represents the coordination modes of **AzSA** with Mg^{2+}. (c) Thermogravimetric analysis (TGA) of **Mg-CP** and **AzSA**. (d) ^{1}H NMR spectra of **Mg-CP** and **AzSA** (500 MHz, CD_3OD).

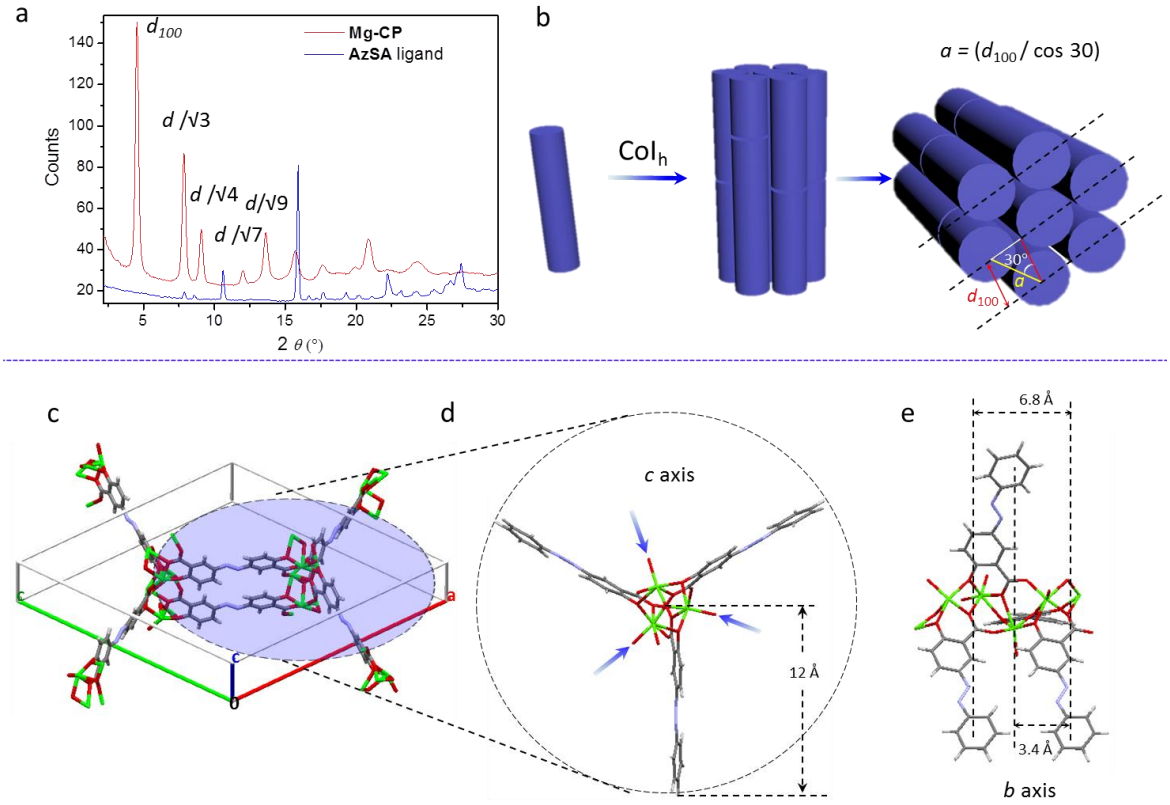

Figure 3.6. (a) WAXS analysis of **Mg-CP** and **AzSA**. (b) Schematic representation of columnar hexagonal (Col$_h$) packing of **Mg-CP** polymeric strands and calculation of the lattice parameter. (c) Crystal structure of osalazine-based MOF, **Zn_2(Olz)**.[26] Proposed structure and molecular dimensions of **Mg-CP** based on the structure of **Zn_2(Olz)**, viewed along (d) *c* axis (blue arrows represent coordinated solvent molecules) and (e) *b* axis. Crystal structure of **Zn_2(Olz)**, reproduced with permission from the original authors.

Wide-angle X-ray scattering (WAXS) analysis (Figure 3.6a) of the **Mg-CP** xerogel powder revealed intense diffraction peaks indicating a highly crystalline columnar hexagonal (Col$_h$) structure, with *d*-spacing ratios of *d*, *d*/√3, *d*/√4, *d*/√7, *d*/√9. **AzSA** did not show any such ordering. From the first diffraction peak of **Mg-CP** (d_{100} = 19.45 Å), the hexagonal lattice parameter *a*, was estimated to be 22.45 Å,

which in turn provides information about the diameter of the columnar stacks in **Mg-CP** xerogel powder (Figure 3.6b).[25] The diameter determined from XRD is in good agreement with the distance of ~24 Å, reported for Zn^{2+}-osalazine based MOF [**Zn_2(Olz)**], by Long and co-workers (Figure 3.6c and 3.6d) which is isostructural to its magnesium anlogue.[26] The distances between the parallel and antiparallel organic struts of **AzSA** were estimated to be 6.8 Å and 3.4 Å respectively, by comparing with the crystal structure of **Zn_2(Olz)** (Figure 3.6e).

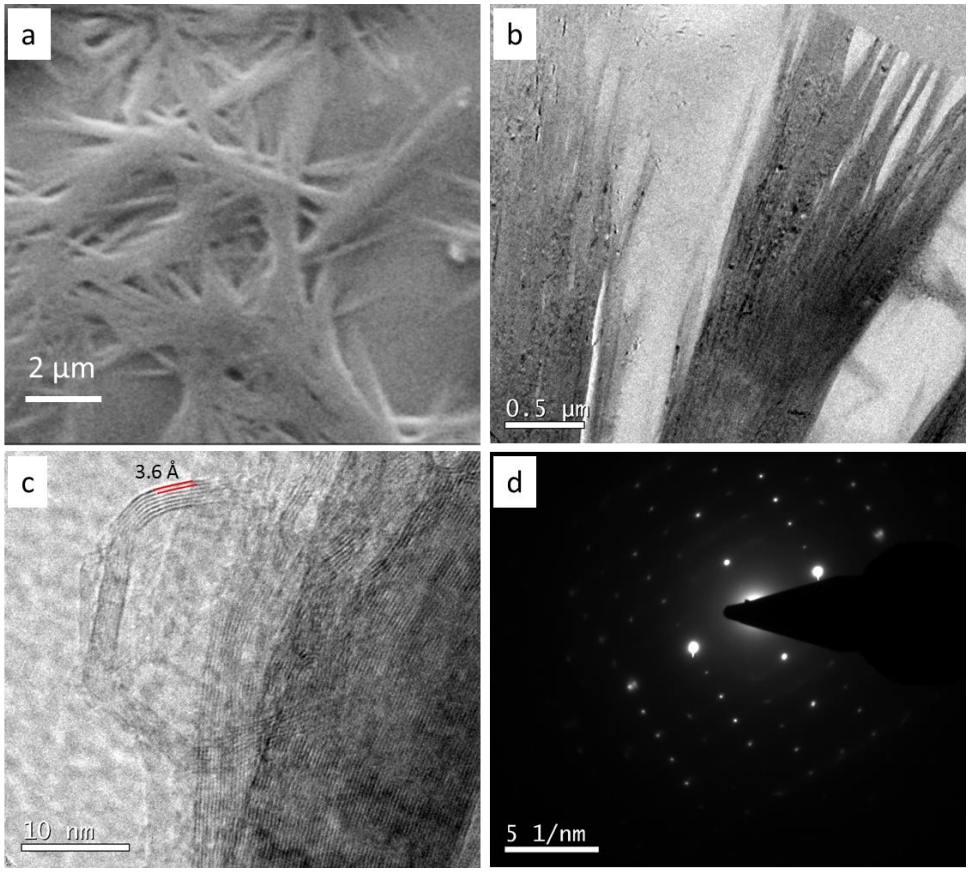

Figure 3.7. (a) SEM image of **Mg-CP** fibres. (b) Low and (c) high magnification TEM image of **Mg-CP** fibres obtained from methanol solution. (d) Single-crystalline SAED pattern obtained from agglomerates of **Mg-CP** fibres.

Electron microscopy (SEM and TEM) images revealed that the **Mg-CP** gel was composed of thin fibres (Figure 3.7a,b). TEM images of these fibres (Figure 3.7c), revealed the highly crystalline nature of a closely packed and ordered (d = 3.6 Å) structure corresponding to a columnar hexagonal lattice as looked along the b axis (Figures 3.6e). A SAED pattern corroborating the single crystalline nature was obtained from the larger agglomerates of **Mg-CP** fibres (Figure 3.7d).

3.3.3. Host-Guest Interaction Studies of AzSA and Mg-CP with Cyclodextrins

In order to estimate the effective concentration of **AzSA** in **Mg-CP**, we recorded the UV-Vis spectra of **AzSA** at varying concentrations (1.7×10^{-5} to 4.4×10^{-4} M) in ethanol and ethanol-water (maximum 4% ethanol) mixture. The absorbance at λ_{max} = 343 nm (ethanol) and 350 nm (ethanol-water) was plotted against the concentration of **AzSA** to obtain a calibration plot (Figure 3.8a). Since the normalized absorption spectrum of **AzSA,** in ethanol-water mixture, fairly matches the absorption spectrum of **Mg-CP** in water (Figure 3.8b), the calibration plot could be used to estimate the effective concentration of **AzSA** in **Mg-CP**. The host-guest interaction of the cyclodextrins with **Mg-CP** as well as its organic precursor **AzSA** was studied in solution state. The intrinsic chirality of cyclodextrins allowed us to monitor the binding interactions using a circular dichroism spectrophotometer. A positive induced circular dichroism (ICD) band at 355 nm corresponding to the π-π^* transition

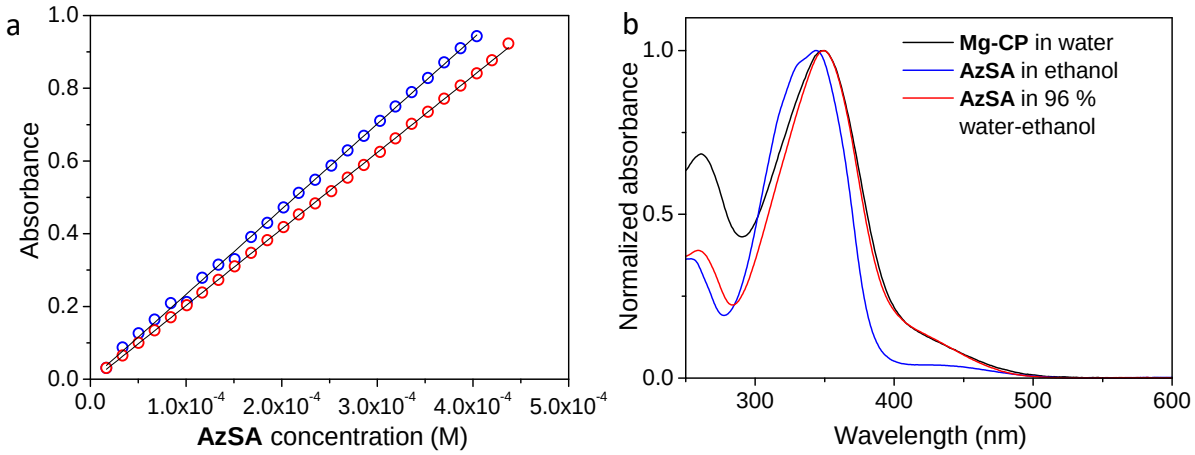

Figure 3.8. (a) Calibration plot for **AzSA** in ethanol (blue) and 4 % ethanol–water (red) obtained from concentration dependent UV-Vis absorption. Black lines indicate a linear fit to the observed data points. (b) Normalized absorption spectra of **AzSA** and **Mg-CP** in different aqueous solvents.

and a small negative band at 440 nm corresponding to *n*-π* transition (Figure 3.9a), clearly indicates the binding event of α-cyclodextrin (**α-CD**) with **Mg-CP** and **AzSA.** The hydrophobic azobenzene core resides inside the CD cavity with its electronic transition moment parallel to the CD axis.[27] The intensity of the ICD signals at 355 nm was found to be 2–fold higher for **Mg-CP** as compared to **AzSA** when titrated with 3.5 and 4.5 equivalents of **α-CD** respectively (Figure 3.9a). A detailed titration plot of the two systems shows that the ICD response was more consistent in case of **Mg-CP** as compared to **AzSA** (Figure 3.9b). In the case of **AzSA**, no selectivity in the binding profiles of **α, β** or **γ-CD** was observed (Figure 3.9c), whereas CD binding isotherms, clearly demonstrated the preferential binding of **α-CD** to **Mg-CP** followed by **β-CD** and **γ-CD** (Figure 3.9d). The ICD spectrum of **Mg-CP⊃β-CD** was similar to that of **Mg-CP⊃α-CD**, suggesting similar orientation of **AzSA** stalks inside the

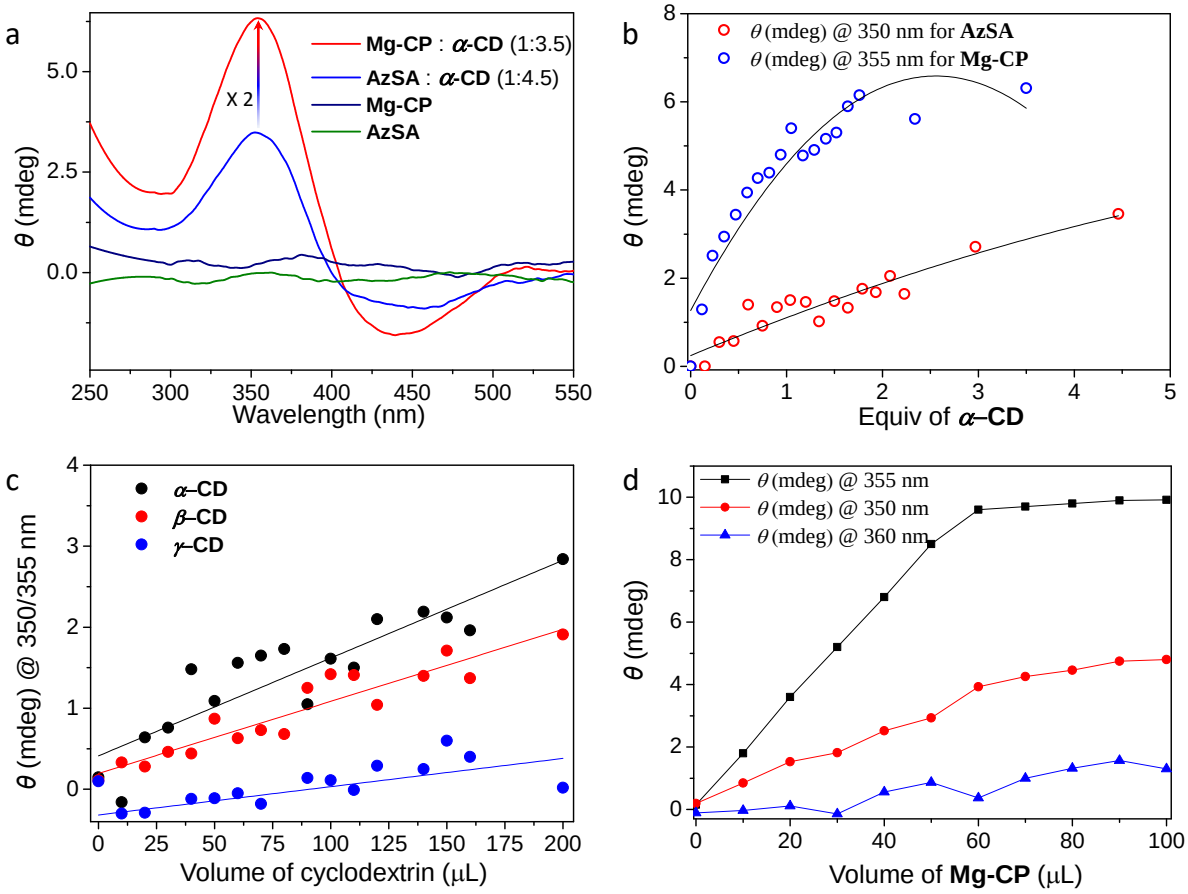

Figure 3.9. (a) ICD spectra of **AzSA** and **Mg-CP** and those obtained upon addition of with 4.5 and 3.5 equiv. of **α–CD** respectively. (b) Changes in the ICD signal (π–π^* transition band) of **AzSA** and **Mg-CP** at different concentration of **α–CD**. Black lines represents the corresponding non-linear fits to the observed data points. (c) Binding isotherms of **AzSA** with different cyclodextrins at 25 °C. Linear fit to the observed data points are also represented. (d) Binding isotherms of **Mg-CP** with different cyclodextrins, **α–CD** (black), **β–CD** (red) and **γ–CD** (blue) at 25 °C.

β-CD cavity. The interaction of **γ-CD** with **Mg-CP** and **AzSA** was found to be rather weak. The ICD spectrum of **Mg-CP⊃γ-CD** was recorded at a temperature below the room temperature (15℃) and consisted of a broad positive signal in the range 350-500 nm (Figure 3.10a).

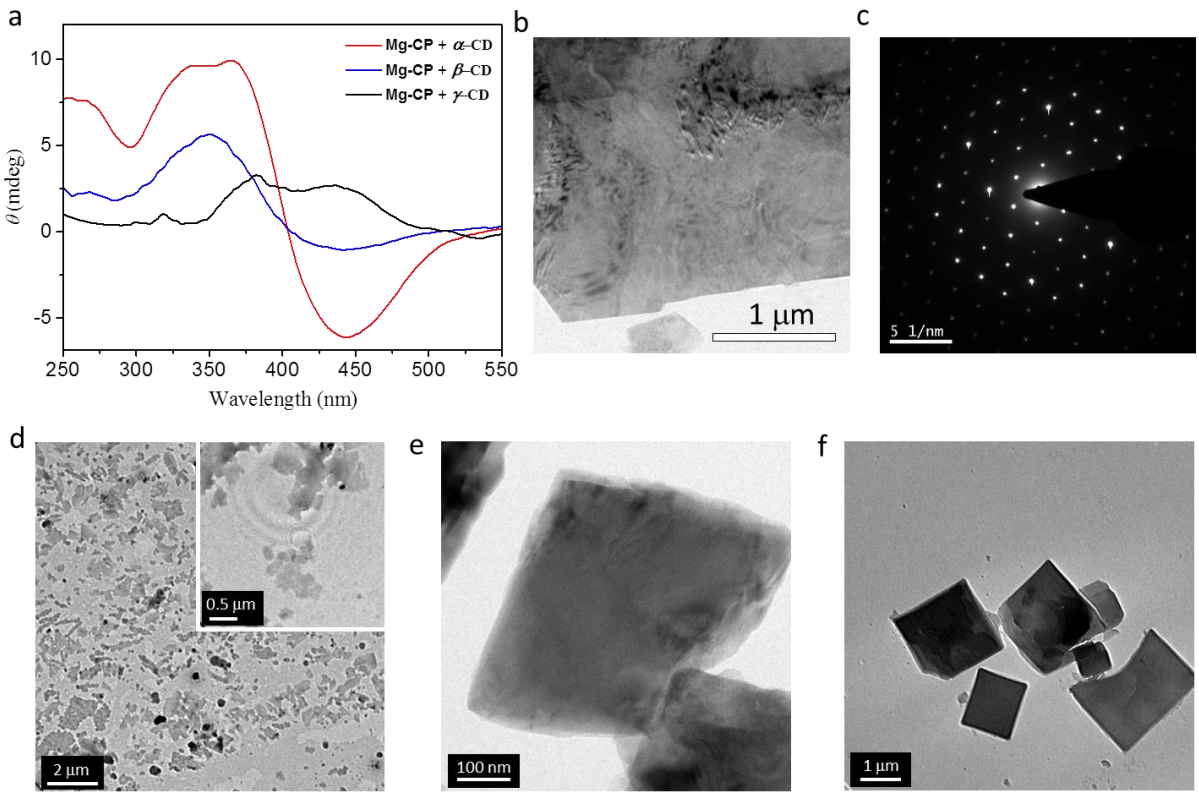

Figure 3.10. (a) ICD spectra of **Mg-CP** in presence of α, β and γ cyclodextrins. (b) TEM image of micro sheets obtained from an aqueous solution of **Mg-CP**. (c) SAED pattern confirming the single-crystalline nature of **Mg-CP** micro sheets. TEM image of **Mg-CP** sheets in presence of (d) **α–CD**; inset shows the zoomed-in image of the amorphous nanosheets, (e) **β–CD** and (f) **γ–CD**.

Mg-CP was found to form micrometer-sized single crystalline sheets (Figure 3.10b and 3.10c) in water which disintegrated into smaller nanoscale fragments upon addition of **α-CD** (Figure 3.10d). Upon interaction with **β-CD,** the sheets broke down into comparatively larger fragments (Figure 3.10e). **Mg-CP** on treatment with **γ-CD** lead to the formation of large cross linked supramolecular microstructures as evidenced by TEM analysis (Figure 3.10f). These structures were, however, found to be amorphous in nature.

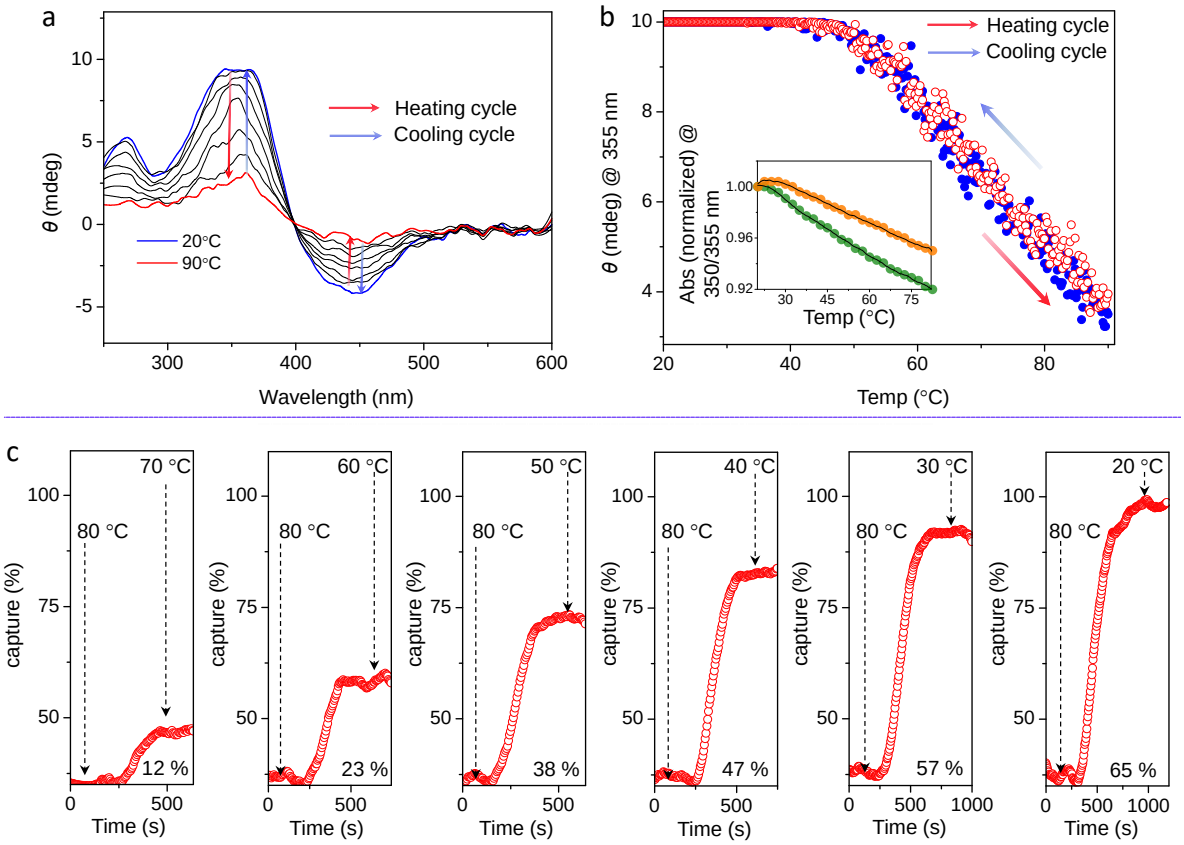

Figure 3.11. (a) Temperature dependent ICD spectra of **Mg-CP⊃α-CD**. (b) Changes in the intensity of the ICD band at 355 nm on heating (red) and cooling (blue) a solution of **Mg-CP⊃α-CD** in water from 20°C to 90°C. Inset shows the thermal degradation profile of **Mg-CP⊃α-CD** (orange) and **AzSA⊃α-CD** (green), obtained from UV-Vis absorption spectroscopy. (c) Temperature controlled quantitative capture of **α–CD** by an aqueous solution of **Mg-CP**.

On increasing the temperature of an aqueous solution of **α-CD** encapsulated **Mg-CP** (**Mg-CP⊃α-CD**) in the range 20–80°C, a steady decrease in the intensity of the ICD signal at 355 nm and 440 nm was observed. This decrease in intensity correlates to the thermal release of the **α-CD** from **Mg-CP** via temperature induced decomplexation (Figure 3.11a). The thermal release and capture profiles of **α-CD**

from **Mg-CP** followed identical pathways and no hysteresis was observed during heating or cooling cycles (Figure 3.11b). Similar results were obtained for the **α-CD** complex of **AzSA** (**AzSA⊃α-CD**). The thermal stability of both the inclusion complexes, was determined by monitoring the decrease in intensity of the absorption band at 350/355 nm with respect to the increase in temperature (inset, Figure 3.11b). The **α-CD** encapsulated complex of **Mg-CP** (**Mg-CP⊃α-CD**) was found to thermally more stable than the corresponding complex of **AzSA** (**AzSA⊃α-CD**) in agreement with our previous observations. **Mg-CP⊃α-CD** was therefore chosen as the model system for demonstrating temperature controlled capture and release of guest molecules (CDs) from the host network. By changing the temperature of **Mg-CP⊃α-CD** solution, the amount of **α-CD** captured or released could be quantitatively controlled. A temperature dependent capture profile is presented in Figure 3.11c.

3.3.4. Temperature Controlled Release of α–CD by Mg-CP

One of the prerequisites for a perfect host-guest system is to have an easily tunable and reversible binding or release profile in response to an applied stimulus. One of the most relevant properties of any ideal remotely controlled systems is to dodge the process of point capture or point release. For instance, a high dosage of a drug is often administered at an initial point of treatment and may be repeated at a later stage or the dosage may be lowered after several hours or days. This drug administration protocol is not economically viable and is not free from side effects. In order to address this

problem, scientists have tried to develop efficient methods for continuous and controlled drug delivery for prolonged time periods or throughout the whole course of the treatment.[28] Most of the stimuli-responsive drug delivery systems reported in literature does not show any capture or release of drug molecules in the absence of a stimulus. A gradual and continuous release or capture process starting at a particular point is generally observed, upon the application of a particular stimulus, which in most cases cannot be further delayed, controlled or reversed.[5]

It has not yet been demonstrated that the capture-release processes can be carried out in a stepwise and reversible manner, with specific control over the amount of guest molecules captured or released. However, by controlling the cooling rate from 15°C/min to 5°C/min, we demonstrated that the binding rates of **α-CD** to **Mg-CP** could be controlled from rapid to moderate to slow (Figure 3.12a). The system also showed reversible binding and release of **α-CD** from the polymer over several heating–cooling cycles (Figure 3.12b). In line with the conventions of a system in thermodynamic equilibrium, the equilibrium constant or the ratio of the **α-CD** encapsulated sites to that of the free sites present in **Mg-CP** and the amount of free **α-CD** molecules present in solution, remains constant at a particular temperature. The ratio of bound to free **α-CD** could also be kept constant for any desired duration. As a result, the ICD signal of **α-CD** encapsulated complex of **Mg-CP** (**Mg-CP$\supset\alpha$-CD**) remains constant at a particular temperature and this is an inherent property of this

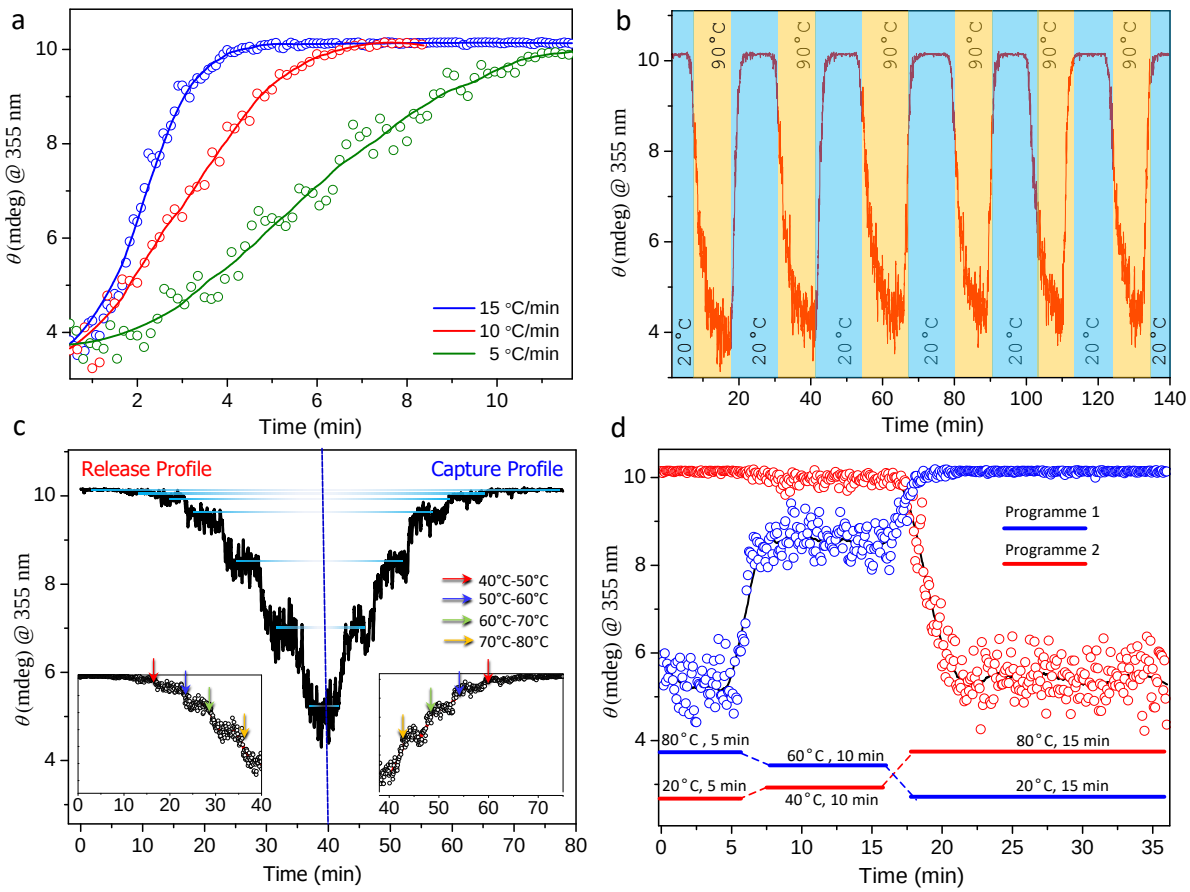

Figure 3.12. (a) Tunable binding of **α–CD** by **Mg-CP** obtained by variation of the cooling rate of solution from 15 to 5°C/min. Non-linear fit to the observed data points are also represented. (b) Thermally reversible binding (blue) and release (yellow) of **α–CD** by **Mg-CP**. (c) Step-wise release and capture of **α–CD** by **Mg-CP**. The insets show the magnified view of the release (left) and capture (right) profiles. The arrows represent the specific changes in the temperature. (d) Programmed release (red) and capture (blue) of **α–CD** from **Mg-CP**. Inset shows the schematic representation of the corresponding programmes employed.

host-guest complex. Therefore, by increasing or decreasing the temperature at regular intervals, a definite amount of **α-CD** can be released or captured by **Mg-CP** in a reversible and stepwise fashion (Figure 3.12c). This property also allowed the release

or capture of **α-CD** in different instalments by adjusting the temperature of the solution. This host-guest complex thus manifests itself to be programmable on an increasing or decreasing temperature scale and any desired release or capture profile may be obtained based on the programme set on the thermostat (Figure 3.12d).

3.3.5. Chemical–Stimuli Controlled Release of CDs by Mg-CP in Solution

Apart from being thermoregulated, the cyclodextrin binding-release profiles of **Mg-CP** can also be modulated by various chemical stimuli capable of competing with the azo appendages as guests for the CDs. For example, the sodium salt of adamantane carboxylic acid (**Na-AdCA**) due to its molecular dimensions matching the hydrophobic **β-CD** cavity (0.6 nm), has been exploited as an excellent guest for **β-CD**. Therefore, **β-CD** can be efficiently removed as a complex of **Na-AdCA** (**β-CD⊃Na-AdCA**) from a solution of **Mg-CP⊃ β-CD**, by adding an equivalent amount of the competitive guest. The free **Mg-CP** can now interact with an equivalent amount of **α-CD** to form a very stable host-guest complex (**Mg-CP⊃α-CD**) (Figure 3.13a). However, **α-CD** on the other hand, cannot accommodate **Na-AdCA** due to its relatively smaller lumen (0.47 nm). The addition of an equivalent amount of **Na-AdCA**, therefore does not tamper the ICD signal in this case. The whole process represents a chemical stimuli-responsive release and uptake of cyclodextrins by **Mg-CP**. Once **Mg-CP** forms a stable complex with **α-CD**, the system becomes

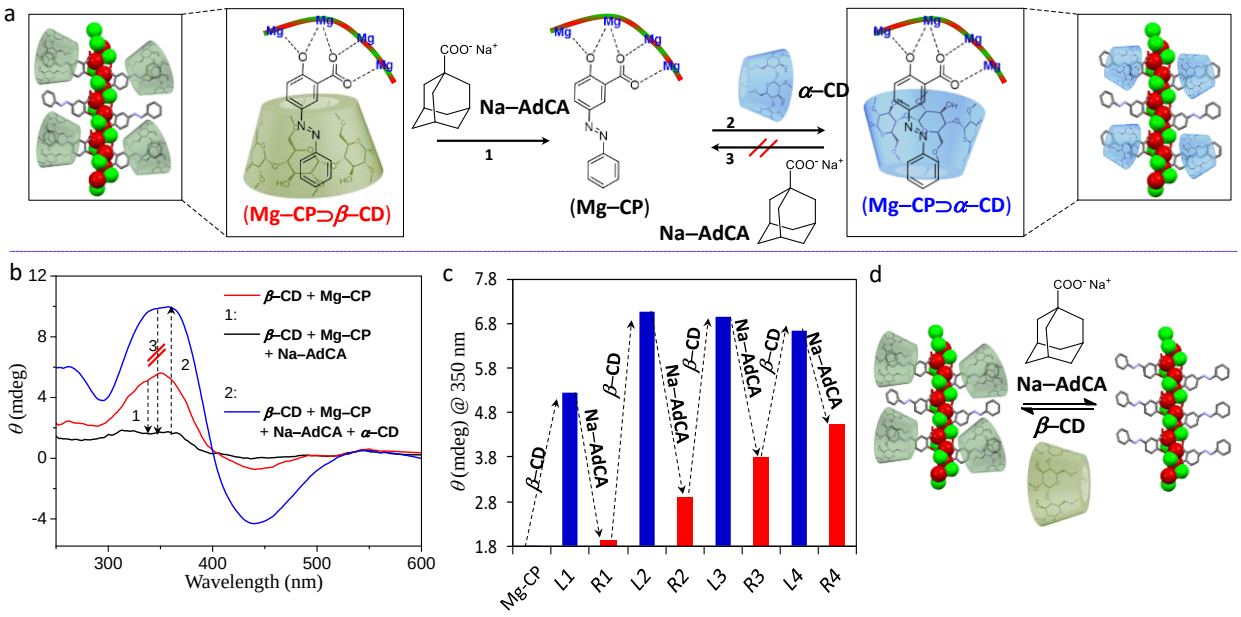

Figure 3.13. (a) Schematic representation of interaction of ***β*-CD** (green) with **Mg-CP** in presence of competing guest molecules like **Na-AdCA** and ***α*-CD** (blue). (b) Changes in the ICD spectra of **Mg-CP** in the presence of competing host-guest interactions (1-3) as represented in (a). (c) Loading of **Mg-CP** with ***β*-CD** (L, blue) and its release (R, red) by the successive addition of competitive guest **Na-AdCA** shown up to four cycles. (d) Schematic representation of loading-release process. Chiral polymeric Mg-O cluster represented in space filling model with magnesium (green) and oxygen (red) in all cases.

chemically irreversible (Figure 3.13b) but continues to be thermally reversible. Nevertheless, chemical reversibility can be achieved by adding a fresh feed of ***β*-CD** in place of ***α*-CD** to the free **Mg-CP**. This chemically stimulated uptake-release process was found to be reversible over several cycles, until the process succumbs to the poor solubility of ***β*-CD** in water (Figure 3.13c). Since it has been established earlier that the affinity of **Mg-CP** towards different cyclodextrins follows the order ***α*-CD** > ***β*-CD** > ***γ*-CD** (Figure 3.9d), we thought it worth to investigate the competitive interaction involving different CDs. It was observed that, with time, a solution of

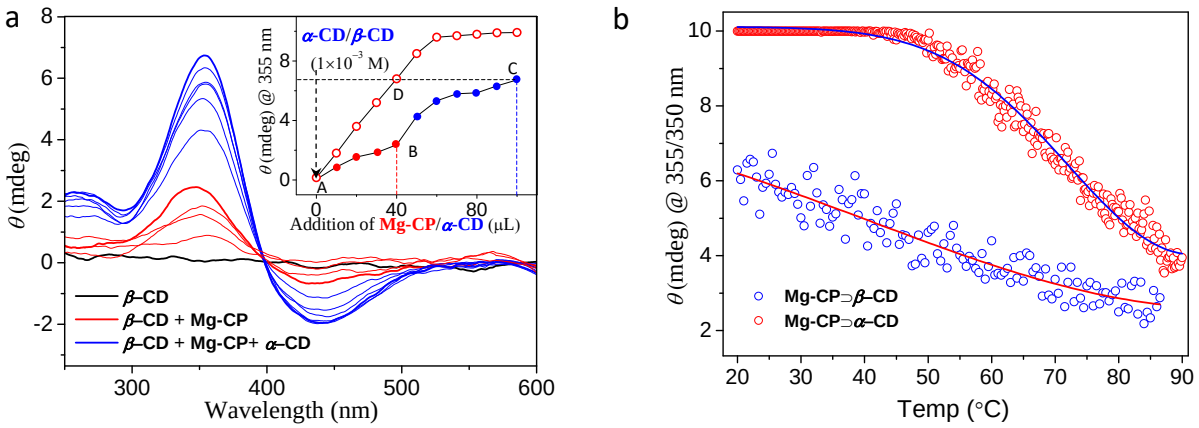

Figure 3.14. (a) Changes in the ICD spectra on replacing ***β*-CD** from **Mg-CP** with ***α*-CD**. Inset shows the changes in the ICD band (355 nm) on addition of **Mg-CP** (red) followed by ***α*-CD** (blue) to a solution of ***β*-CD**. Addition of **Mg-CP** (red, unfilled) to a solution of ***α*-CD** at the same concentration is shown for reference. (b) Thermal dissociation profiles of **Mg-CP⊃*α*–CD** (red) and **Mg-CP⊃*β*–CD** (blue). Non-linear curve fits for the data points are represented in red (**Mg-CP⊃*β*–CD**) and blue (**Mg-CP⊃*α*–CD**).

***β*-CD** encapsulated complex of **Mg-CP** can be slowly modified to an all ***α*-CD** exchanged **Mg-CP**. The experiment was carried out by adding aliquots of **Mg-CP** to a solution of ***β*-CD** (point A, Figure 3.14a) until an excess of ***β*-CD** was present (point B, Figure 3.14a), and no vacant sites was available in **Mg-CP** for the encapsulation of ***α*-CD**. The gradual increase in the ICD signal upon addition of ***α*-CD**, confirmed that the ***β*-CD** was gradually replaced with ***α*-CD** and slowly released into the solution. This process continued until all the ***β*-CD** in the complex was replaced and the binding sites of **Mg-CP** were saturated with ***α*-CD** (point C, Figure 3.14a). The ICD signal of the resulting complex matched with that obtained by the complete saturation

of **Mg-CP** (40 μL) with **α-CD** at exactly the same concentrations (point D, Figure 3.14a).

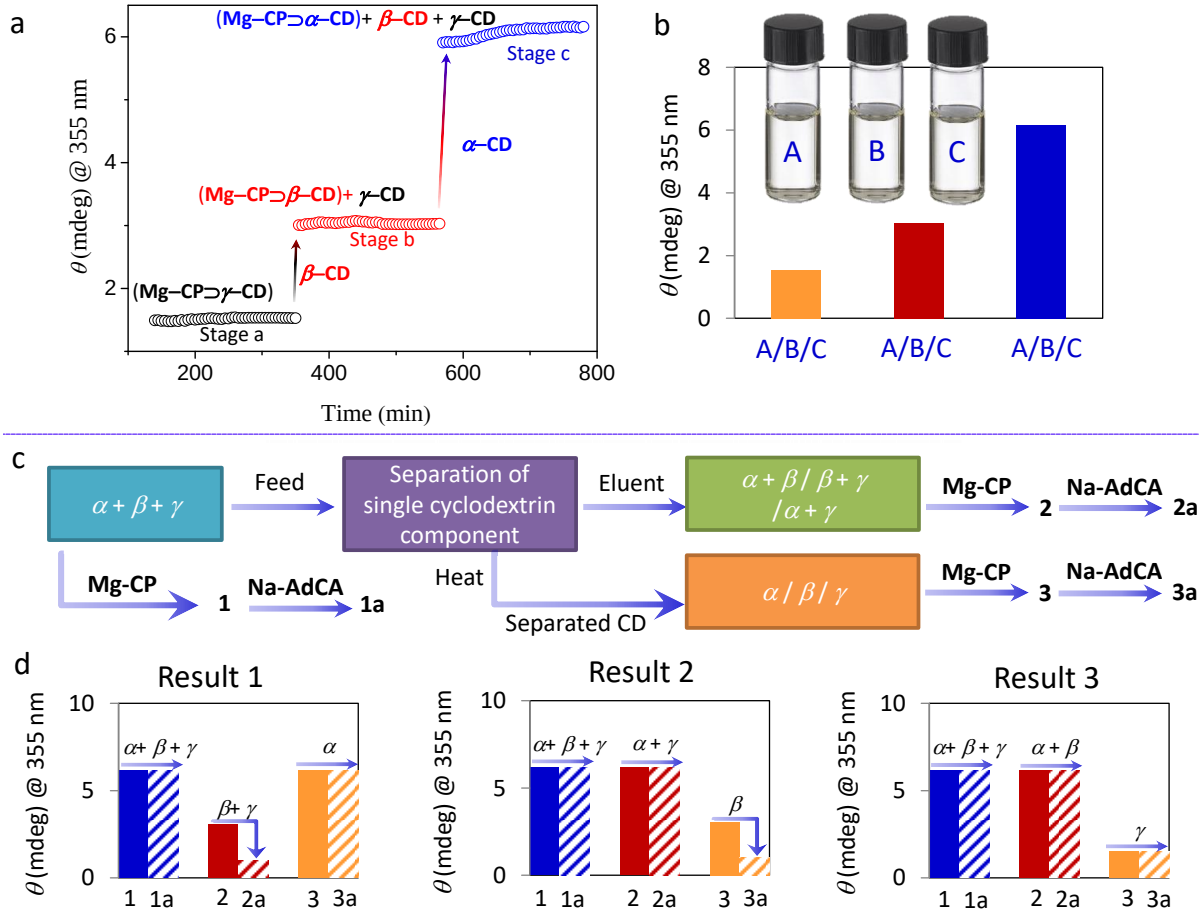

Figure 3.15. (a) Changes in the intensities of the ICD signal at 355 nm on the replacement of **γ–CD** from the **Mg-CP⊃ γ–CD** complex with **β –CD** followed by the replacement of **β –CD** with **α–CD**. (b) Decoding of unknown solutions (c = 1 x 10^{-3} M) of **α–, β–**and **γ–CD** kept in indistinguishable vials A, B and C. (c) Schematic representation of a proposed single component separation from a mixture of three cyclodextrins and experiments carried out with the feed solution (**1**, **1a**), the eluent bicomponent mixture (**2**, **2a**) and the adsorbed cyclodextrin obtained by heating the separation column (**3**, **3a**). (d) Results of ICD measurements corresponding to experiments described in (c). Results 1, 2 and 3 represent the separation of **α–, β–** and **γ–CD** respectively.

The enhanced affinity of **Mg-CP** towards **α-CD** can be attributed to the difference in thermal stability of the two complexes, where the **α-CD** complex of **Mg-CP** was found to be thermally more stable as compared to its **β-CD** analogue (Figure 3.14b). The **Mg-CP** solution, gave a rather poor ICD signal (stage a, Figure 3.15a) in the presence of **γ-CD**. The signal intensity remained constant with time but an enhancement was observed (stage b, Figure 3.15a) upon addition of **β-CD**. On subsequent addition of **α-CD** to the **Mg-CP** solution, the ICD signal further increased to a higher intensity (stage c, Figure 3.15a). The selectivity in the binding of different CDs to **Mg-CP** in presence of other CDs was confirmed by heating and cooling the corresponding solutions at stages b and c. We observed that heating the above solutions to 90 °C and cooling back to room temperature (25 °C), individually at stages b and c did not change the corresponding ICD signal, confirming the selective binding process leading to the formation of **Mg-CP$\supset\beta$-CD** (stage b, Figure 3.15a) and **Mg-CP$\supset\alpha$-CD** (stage c, Figure 3.15a), even in the presence of other CDs in solution. Stage b can be clearly distinguished from stage c via the changes in the ICD spectra, by the addition of **Na-AdCA** (Figure 3.13b). A system which can differentiate two or more structurally similar chemicals by rendering distinct readout signals is termed a molecular decoder.[29] Selective affinity as in the aforementioned case can, therefore, be exploited for the molecular level decoding of individual CDs from their unknown solutions. **Mg-CP** interacts with **α-**, **β-** and **γ-CD** showing

distinct differences in the intensity of the ICD signal at 355 nm. The intensity (I) varies in the order $I_{\alpha} > I_{\beta} > I_{\gamma}$. Therefore, to equimolar solutions of the three CDs, in three indistinguishable vials, small aliquots of **Mg-CP** were added and the corresponding the ICD spectra were obtained. Following the intensity of the ICD signal at 355 nm, the constituent CD in each vial could be identified. (Figure 3.15b). Similarly, a mixture of ***β*-CD** and ***γ*-CD** can be distinguished from all other possible bicomponent and tricomponent mixtures of CDs, by adding **Na-AdCA**. Addition of the competitive guest **Na-AdCA**, replaces the azobenzene side chain of **Mg-CP** from the ***β*-CD** cavity, leading to a corresponding reduction in the ICD signal intensity. In the other combinations of the CDs, although formation of ***β*-CD⊃Na-AdCA** complex occurs, it remains undetected. **Na-AdCA** does not replace **Mg-CP** from the ***α*-CD** cavity and hence the ICD signal remains unperturbed. This behavior could further be exploited to monitor the chemical separation of a tricomponent mixture of CDs. We hypothesized the possible outcomes of a similar separation process (Figure 3.15c) and a series of typical experiments of this sort were carried out with the plausible feed solution (1 and 1a, Figure 3.15c), permeate solution (2 and 2a, Figure 3.15c) and a separated CD solution (3 and 3a, Figure 3.15c). Results 1, 2 and 3 (Figure 3.15d) corresponds to the separation of ***α*-CD**, ***β*-CD** and ***γ*-CD** respectively.

3.3.6. Temperature Controlled Release of α–CD by Mg-CP in Quasi–Solid State: A Drug Delivery Perspective

For practical applications, say the administration of CD as a drug inside a patient via mediports, it is mandatory for the system to be controlled in its solid state.[28] The Mg-CP based host-guest system, demonstrated in the previous sections, represent a prototype for the controlled release of drug molecules at a specific location and in response to an applied temperature. For instance, **α-CD** can be incorporated into a portable implant and a tuneable drug delivery device can therefore be fabricated. Thus, temperature-dependent changes in the ICD spectrum of **Mg-CP⊃α-CD** was investigated in the solid state by preparing a film from an aqueous solution of **Mg-CP⊃α-CD** over a quartz substrate. The positive and negative ICD signals were found to be red shifted, respectively to 392 nm and 470 nm, due to the aggregation of **Mg-CP⊃α-CD** in its solid state. No detectable changes were observed in the ICD spectrum upon heating or cooling this sample (Figure 3.16a), confirming that water is a vital component in maintaining the dynamics of the self-assembly process.

Mg-CP⊃α-CD was therefore incorporated into a polyacrylamide hydrogel (Figure 3.16b) that traps a large amount of water in its quasi-solid state.[30] The yellow color of the obtained soft material confirmed the incorporation of **Mg-CP⊃α-CD** within the gel matrix. The hybrid gel was found to be highly mouldable, flexible and transparent (Figure 3.16c) and possessed an inherent chirality. Changes in CD signals

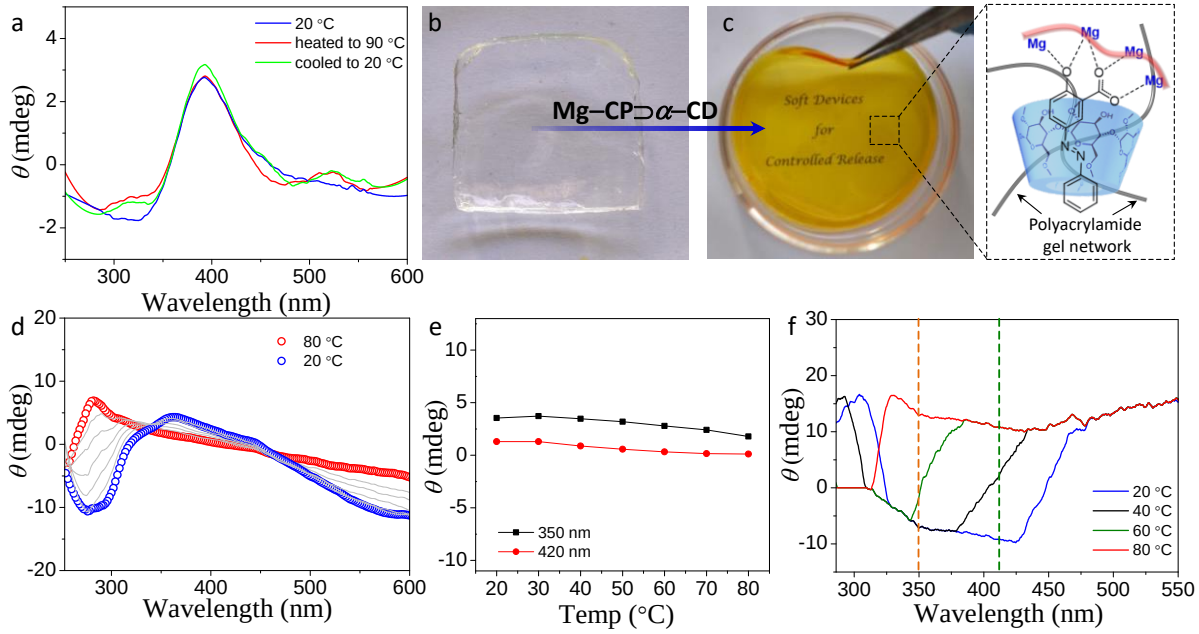

Figure 3.16. (a) Temperature-dependent changes in the ICD spectra of **Mg-CP⊃α–CD** in the film state. (b) Photograph of the polyacrylamide hydrogel. (c) Photograph of **Mg-CP⊃α–CD** incorporated inside the polyacrylamide hydrogel (a schematic representation of the gel components is shown). The resulting material is soft, flexible and transparent. (d) Temperature-dependent changes in the ICD spectra of the polyacrylamide hydrogel. (e) Temperature dependent changes in the intensity of the CD band at 350 nm and 420 nm for the polyacrylamide hydrogel showing a consistent behavior. (f) Temperature-dependent changes in the ICD spectra of the **Mg-CP⊃α–CD** entrapped polyacrylamide hydrogel. Changes in the ICD spectrum at 350 nm and 420 nm are represented by orange and green lines respectively.

were observed upon heating and cooling the hydrogel between 20 and 80 °C (Figure 3.16d). However, temperature dependent changes in the CD spectrum at wavelengths corresponding to **Mg-CP⊃α-CD** (350 nm and 420 nm), was negligible (Figure 3.16e). The ICD spectrum of **Mg-CP⊃α-CD** incorporated inside the hydrogel matrix (Figure 3.16f), recorded at different temperatures was different from that of the

complex in solution (Figure 3.11a). The changes may be attributed to the positioning of the **Mg-CP⊃α-CD** polymer strands close to one another as opposed to the larger inter-strand distance in solution, where electronic interactions are minimal. The inherent chirality of the polymer strand may also be responsible for perturbing the electronic environment of the **Mg-CP⊃α-CD** complex (Figure 3.16d) and influence its ICD spectrum in the quasi-solid state. Temperature dependent ICD spectrum of **Mg-CP⊃α-CD** trapped inside the hydrogel matrix was monitored at 350 nm (Figure 3.17a) and 420 nm (Figure 3.17b), corresponding to the major ICP bands of **Mg-CP** in solution. Contrary to the solution state ICD spectrum (Figure 3.11b), a clear hysteresis was observed between the heating and cooling cycles (Figure 3.17a and 3.17b) of **Mg-CP⊃α-CD** when incorporated into the polymer hydrogel. This observation indicates that although **α-CD** molecules were released from the **Mg-CP** on heating, they were not readily available to rebind the free azobenzene sites on cooling. The temperature-dependent swelling and deswelling of the polymer hydrogel promotes a lag phase between these binding and release processes leading to the observed hysteresis, similar to the hysteresis loop in the gas adsorption profile of soft porous crystals.[31] Akin to the solution state, the ICD signal could be consistently modulated by maintaining the hydrogel at a particular temperature. A stepwise release profile of **α-CD** from the **Mg-CP** could also be demonstrated (Figure 3.17c) as in solution.

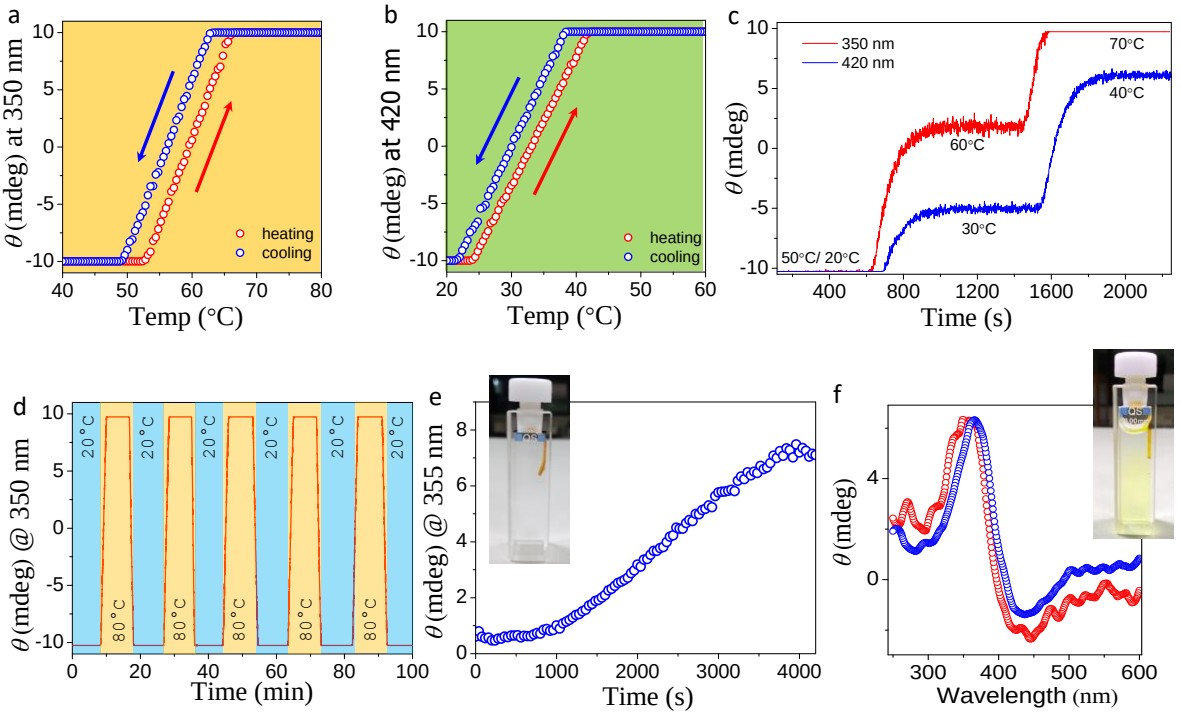

Figure 3.17. (a) Temperature-dependent changes in the ICD spectra of **Mg-CP⊃α–CD** entrapped in a hydrogel, recorded at (a) 350 nm and (b) 420 nm. Red and blue arrows represent heating and cooling cycles respectively. (c) Stepwise release profile of **α–CD** from **Mg-CP** monitored at 350 nm and 420 nm in the hydrogel at different temperature. (d) Reversible binding (blue) and release (yellow) of **α–CD** from **Mg-CP** incorporated in the hydrogel. (e) Changes in the ICD signal at 355 nm corresponding to the gradual release of **Mg-CP⊃α–CD** from hydrogel to water. Inset shows the photograph of the hydrogel strip fixed inside a quartz cuvette before the leaching experiment. (f) ICD spectra of the released **Mg-CP⊃α–CD** complex in water (red). ICD spectrum of an aqueous solution of **Mg-CP⊃α–CD** (blue) is provided for reference. Inset shows the photograph of the **Mg-CP⊃α–CD** released into solution after the leaching experiment.

The temperature dependent ICD spectrum of the polymer hydrogel, monitored at 350 nm and 420 nm (Figure 3.16e), where no perceptible changes was observed, substantiates that the differences observed above originate solely from the host-guest

interactions involving **α-CD** and **Mg-CP**. The system was also found to maintain its high reversibility for several heating cooling cycles in the quasi-solid state (Figure 3.17d). In order to prove the stability of **Mg-CP⊃α-CD** inside the polymer hydrogel matrix, leaching of the complex into water from a xerogel strip at room temperature was monitored at 355 nm (Figure 3.17e). The ICD spectrum of the aqueous phase obtained exactly matched that of **Mg-CP⊃α-CD** complex in solution (Figure 3.17f).

3.4. Conclusions

In conclusion, we have designed and synthesized a water soluble coordination polymer (**Mg-CP**) having CD binding azobenzene-based side appendages. **Mg-CP** was found to possess a greater affinity and high selectivity towards various CDs as compared to its organic precursor. The **Mg-CP** based system was utilized to demonstrate precise control over host-guest interactions using various physical and chemical stimuli, both in solution as well as in the quasi-solid state. The highly selective host-guest interactions have been further utilized for the molecular level decoding of different CDs and CD mixtures. The chemistry discussed herein reaps the thermodynamic benefits of a system in chemical equilibrium and can have potential impact in designing systems for controlled delivery of stealth drug molecules such as CDs.

3.5. Experimental Section

3.5.1. Materials and Methods

Unless otherwise stated, all starting materials, reagents and dry solvents were purchased from commercial suppliers and used as received. Solvothermal reactions were carried out in a programmable Nabertherm air oven (TR-60). The water used in all the experiments was Millipore Milli Q grade (18 MΩ.cm). (*E*)-2-hydroxy-5-(phenyldiazenyl)benzoic acid (**AzSA**) was synthesized according to Scheme 2, using a reported procedure.[32] ^{1}H and ^{13}C NMR spectra were measured on a 500 MHz Bruker Advance DPX spectrometer using TMS and $CDCl_3$ as internal standards. Melting point was measured on a MEL-Temp-II melting point apparatus and is uncorrected. Electrospray Ionization Mass Spectroscopy (ESI-MS) was performed on a Thermo Scientific Q Exactive Hybrid Quadrupole-Orbitrap electrospray ionization mass spectrometer. IR spectra were collected on a Perkin-Elmer Spectrum One FT-IR spectrometer using KBr (neat). Thermogravimetric analysis was carried out using TA instruments Q 50, all samples were heated at 10 °C/min under N_2 atmosphere.

3.5.2. Preparation of (*E*)-2-hydroxy-5-(phenyldiazenyl)benzoic Acid (AzSA)

Concentrated hydrochloric acid (20 mL) was added to an ice cold solution of aniline (6.12 g, 65.7 mmol) and cooled to 0 °C. A cold (0–5 °C) solution of $NaNO_2$ (4.55 g,

65.7 mmol) was slowly added to the above solution. The resulting benzene diazonium chloride was then added dropwise to an alkaline solution of salicylic acid (9.15 g, 65.7 mmol) at pH 8-9 (7.0 g of NaOH, 175 mmol), to yield the corresponding hydroxy azobenzene carboxylic acid. The compound was filtered and recrystallized from 50% (v/v) ethanol-water mixture. The bright orange crystals obtained were collected by filtration, washed with water and dried in a vacuum oven. Yield: 11.93 g, 75%; m.p. 218 ^{o}C; FT-IR (KBr): ν_{max} = 2850 (b), 1667(s), 1615(m), 1447(m), 1484(s) cm^{-1}; ^{1}H NMR (500 MHz, $CDCl_3$, TMS, 25 ^{o}C) δ: 10.92 (d, 4H, Ar-OH), 8.55 (d, 4H, Ar-H), 8.16 (d, 4H, Ar-H), 7.91 (d, 2H, Ar-H), 7.53 (t, 2H, Ar-H), 7.49 (d, 1H, Ar-H), 7.14 (d, 1H, Ar-H) ppm; ^{13}C NMR (125 MHz, $CDCl_3$, 25^{o}C) δ: 172.4, 164.4, 152.5, 145.5, 137.6, 130.9, 129.5, 129.1, 127.8, 122.8, 118.7 ppm; ESI-MS: m/z: calculated: 242.07: Found: 265 $[M+Na]^+$ (13%)

3.5.3. Preparation of Mg–CP

Mg-CP was prepared by modifying a reported procedure.[33] **AzSA** (1.0 g, 4.13 mmol) and magnesium nitrate hexahydrate (1.75 g, 6.82 mmol) in diethylformamide (DEF, 50 mL) by sonication. The resulting orange solution was kept in a programmable air-oven and heated to 115 °C at a rate of 0.2 °C/min, and after 24 hours, the temperature was slowly decreased (over a day) to 30° C. The orange gel formed was purified by Soxhlet extraction using chloroform. A yellowish-orange xerogel powder was

obtained after drying overnight in an air-oven at 80° C and was used without any further purification. The formation of **Mg-CP** was confirmed by FT-IR, XRD and NMR analyses and the coordination of **AzSA** with Mg^{2+} was confirmed by the absence of phenolic –OH peak as well as the shifts in the signals corresponding to the aromatic protons along with broadening of the ^{1}H NMR spectrum.

3.5.4. Preparation of Polyacrylamide Hydrogel

A 40% stock solution of acrylamide/bisacrylamide was prepared by adding 63 mL of deionized water to the commercially available acrylamide/bisacrylamide (19:1) powder mixture, dissolved the contents, filtered and stored at 4 °C. A 10% solution (100 mg/mL) of ammonium persulphate (APS) was prepared in deionized water and stored at -20°C. Tetramethylethylenediamine (TEMED) was used as obtained commercially. For preparation of the hydrogel, 1.5 mL of the 40% stock solution of the monomer was diluted with 1.5 mL of deionized water and 300 μL of 10% APS solution was added. The resulting solution was vigorously whisked to prevent the formation of air bubbles. Subsequently 30 μL of TEMED solution was added to control the rate of polymerization process. The solution was left undisturbed for ~ 1h in a glass petri dish or in a quartz cuvette to obtain a transparent hydrogel.

3.5.5. Preparation of Mg-CP⊃α-CD Trapped Polyacrylamide Hydrogel

750 μL of an aqueous solution of **Mg-CP** (2 mg mL^{-1}) was added to 750 μL of an aqueous solution of **α-CD** (58 mg mL^{-1}). To the resulting solution, 1.5 mL of 40% stock solution of acrylamide/bisacrylamide was added followed by 300 μL of 10% APS solution. The resulting mixture was vigorously whisked to prevent the formation of air bubbles. Subsequently 50 μL of TEMED solution was added to control the rate of the polymerization process. The solution was left undisturbed for ~1h in a glass petri dish or in a quartz cuvette to obtain a transparent yellow hydrogel.

3.5.6. Experimental Techniques

3.5.6.1. Morphological Analysis

Scanning Electron Microscopy (SEM) images were obtained using a Zeiss EVO 18 cryo SEM Special Edn with variable pressure detector working at 20-30 kV. **Mg-CP** gel was dismantled by ultra-sonication for 15 min and then SEM samples were prepared by drop casting the sol on freshly cleaved mica substrates. All the samples were coated with gold prior to examination. Transmission electron microscopy (TEM) and high resolution TEM (HRTEM) with selected area electron diffraction (SAED) were performed on a FEI, TECNAI 30 G2 S-TWIN microscope with an accelerating voltage of 100 and 300 kV respectively. TEM samples were prepared by dispersing 1 mg of the xerogel samples of **Mg-CP** in 5 mL methanol or water via ultra-sonication

for 15 min and then dropcasting the solution on carbon coated copper grids. Images were obtained without staining.

3.5.6.2. Rheology Experiments

Rheological measurements were carried out in an Anton Paar Physical Modulated Compact Rheometre-150 Physica (Germany). A parallel plate sensor having a diameter 50 mm and a gap size of 0.05 mm was used. Measurements were carried out in amplitude sweep mode, varying the amplitude gamma from 0.01-100 % log and keeping the angular frequency omega at 10 Hz.

3.5.6.3. X-ray Diffraction Measurements

X-ray diffraction measurements on **Mg-CP** powder were carried out on a XEUSS 2D SAXS/WAXS system using a Genix microsource from Xenocs operated at 50 kV and 0.3 mA. The Cu Kα radiation (λ = 1.54 Å) was collimated with a FOX2D mirror and two pairs of scatterless slits from Xenocs.

3.5.6.4. Optical Measurements

Solution state electronic absorption spectra were recorded on a Shimadzu UV-3600 scanning spectrophotometer equipped with a temperature-control system, using a 1 cm path length quartz cuvette. CD spectroscopy was performed on a JASCO-J-810 spectropolarimeter that was equipped with a JASCO PTC-423S Peltier-type

temperature-control system. The studies were performed either on an aqueous solution or on a hydrogel in a quartz cuvette of 1 cm path length.

*(a) Host-guest interaction studies of **AzSA** and **Mg-CP** with different CDs:* For the titration of **AzSA**, addition of an ethanolic solution of **AzSA** to an aqueous solution of CDs was avoided to prevent precipitation of the CDs, where as in case of **Mg-CP**, a specific initial concentration of the different CDs was used. CD Binding studies were conducted by either adding increasing amounts of different cyclodextrins (c = 1.5 x 10^{-2} M) in water to a fixed concentration of **AzSA** (3 mL, c = 3.3 x 10^{-4} M) (Figure 3.9c) or by adding successive aliquots of **Mg-CP** (2 mg mL^{-1}) to a fixed concentration (3 mL, 1 x 10^{-3} M) of different CD solutions (Figure 3.9d).

*(b) Chemically stimulated CD capture and release by **Mg-CP**:* Replacement of ***β*-CD** from **Mg-CP** (Figure 3.13b) by the addition of **Na-AdCA**, was performed in presence of an excess of **Mg-CP** (saturation point ~90 μL, Figure 3.8f). 30 μL of a solution of the competing guest, **Na-AdCA** (c = 0.1 M) was added to the total volume of the ***β*-CD** solution in cuvette (3 mL) to maintain a concentration equal to that of ***β*-CD** (c = 1 x 10^{-3} M). The ICD spectrum was recorded to confirm the release of ***β*-CD**. Subsequently, the addition of 60 μL of a solution of ***α*-CD** (c = 0.05 M) leads to the formation of the corresponding ***α*-CD** complex and makes the system chemically irreversible. Uptake and release of ***β*-CD** from **Mg-CP** (Figure 3.13c) was performed by successive addition of 20 μL **Na-AdCA** (c = 0.15 M) followed by ***β*-CD** (3.4 mg)

to 3 mL of **Mg-CP s**olution for each release-uptake cycle. The effective final concentration of every competing guest was maintained at 1 x 10^{-3} M maintaining a total volume of 3 mL. The condition where ***β*-CD** was present in excess than **Mg-CP** (Point B, Figure 3.14a) was maintained by the addition of 40 μL of **Mg-CP** (*c* = 2 mg mL^{-1}) to a solution of ***β*-CD** (3 mL, *c* = 1 x 10^{-3} M), assuming ~90 μL of **Mg-CP** (*c* = 2 mg mL^{-1}) was required for the complete saturation of the ICD signal (Figure 3.9d).

(c) Chemical decoding of different CDs: Molecular level decoding experiments were performed by adding a 40 μL aliquot of **Mg-CP** (*c* = 2 mg mL^{-1}) to three unlabelled glass vials having ***α*-CD**, ***β*-CD** and ***γ*-CD** solutions (*c* = 1 x 10^{-3} M) followed by recording their ICD spectra.

3.6. References

1. D. E. Koshland, *Angew. Chem. Int. Ed.*, 1995, **33**, 2375.
2. B. Alberts, *Molecular Biology of the Cell* (Garland Science, New York, 2002)
3. S. Mura, J. Nicolas and P. Couvreur, *Nat. Mater.*, 2013, **12**, 991.
4. A. Y. Rwei, W. Wang and D. S. Kohane, *Nano Today*, 2015, **10**, 451.
5. C. S. Linsley and B. M. Wu, *Ther. Deliv.*, 2017, **8**, 89.
6. C. Alvarez-Lorenzo, L. Bromberg and A. Concheiro, *Photochem. Photobiol.*, 2009, **85**, 848.
7. K. Khaletskaya, J. Reboul, M. Meilikhov, M. Nakahama, S. Diring, M. Tsujimoto, S. Isoda, F. Kim, K. Kamei, R. A. Fischer, S. Kitagawa and S. Furukawa, *J. Am. Chem. Soc.*, 2013, **135**, 10998.
8. J. F. Mano, *Adv. Eng. Mater.*, 2008, **10**, 515.
9. K. A. Connors, *Chem. Rev.*, 1997, **97**, 1325.

10. C. Bohne, *Chem. Soc. Rev.*, 2014, **43**, 4037.
11. S. Nagata, K. Kokado and K. Sada, *Chem. Commun.*, 2015, **51**, 8614.
12. X. Meng, B. Gui, D. Yuan, M. Zeller and C. Wang, *Sci. Adv.*, 2016, **2**, e1600480.
13. S. Diring, A. Carne-Sanchez, J. Zhang, S. Ikemura, C. Kim, H. Inaba, S. Kitagawa and S. Furukawa, *Chem. Sci.*, 2017, **8**, 2381.
14. J. S. Kahn, L. Freage, N. Enkin, M. A. Garcia and I. Willner, *Adv. Mater.*, 2017, **29**, 1602782.
15. G. Crini, *Chem. Rev.*, 2014, **114**, 10940.
16. A. Harada, *Acc. Chem. Res.*, 2001, **34**, 456.
17. G. Chen and M. Jiang, *Chem. Soc. Rev.*, 2011, **40**, 2254.
18. L. Abi-Mosleh, R. E. Infante, A. Radhakrishnan, J. L. Goldstein and M. S. Brown, *Proc. Natl. Acad. Sci. U. S. A.*, 2009, **106**, 19316.
19. J. D. Artiss, K. Brogan, M. Brucal, M. Moghaddam and K. L. Jen, *Metabolism*, 2006, **55**, 195.
20. M. Miyauchi, Y. Takashima, H. Yamaguchi and A. Harada, *J. Am. Chem. Soc.*, 2005, **127**, 2984.
21. X. Liao, G. Chen, X. Liu, W. Chen, F. Chen and M. Jiang, *Angew. Chem. Int. Ed.*, 2010, **49**, 4409.
22. H. Deng, S. Grunder, K. E. Cordova, C. Valente, H. Furukawa, M. Hmadeh, F. Gandara, A. C. Whalley, Z. Liu, S. Asahina, H. Kazumori, M. O'keeffe, O. Terasaki, J. F. Stoddart and O. M. Yaghi, *Science*, 2012, **336**, 1018.
23. N. L. Rosi, J. Kim, M. Eddaoudi, B. Chen, M. O'keeffe and O. M. Yaghi, *J. Am. Chem. Soc.*, 2005, **127**, 1504.
24. G. B. Deacon and R. J. Phillips, *Coord. Chem. Rev.*, 1980, **33**, 227.
25. M. A. Kline, X. Wei, I. J. Horner, R. Liu, S. Chen, S. Chen, K. Y. Yung, K. Yamato, Z. Cai, F. V. Bright, X. C. Zeng and B. Gong, *Chem. Sci.*, 2015, **6**, 152.

26. D. J. Levine, T. Runcevski, M. T. Kapelewski, B. K. Keitz, J. Oktawiec, D. A. Reed, J. A. Mason, H. Z. Jiang, K. A. Colwell, C. M. Legendre, S. A. Fitzgerald and J. R. Long, *J. Am. Chem. Soc.*, 2016, **138**, 10143.
27. B. Balan, D. L. Sivadas and K. R. Gopidas, *Org. Lett.*, 2007, **9**, 2709.
28. S. Mitragotri, P. A. Burke and R. Langer, *Nat. Rev. Drug Discov.*, 2014, **13**, 655.
29. Y. Takashima, V. M. Martinez, S. Furukawa, M. Kondo, S. Shimomura, H. Uehara, M. Nakahama, K. Sugimoto and S. Kitagawa, *Nat. Commun.*, 2011, **2**, 168.
30. Q. Wang, J. L. Mynar, M. Yoshida, E. Lee, M. Lee, K. Okuro, K. Kinbara and T. Aida, *Nature*, 2010, **463**, 339.
31. S. Horike, S. Shimomura and S. Kitagawa, *Nat. Chem.*, 2009, **1**, 695.
32. I. A. Banerjee, L. Yu and H. Matsui, *J. Am. Chem. Soc.*, 2003, **125**, 9542.
33. J. W. Brown, B. L. Henderson, M. D. Kiesz, A. C. Whalley, W. Morris, S. Grunder, H. Deng, H. Furukawa, J. I. Zink, J. F. Stoddart and O. M. Yaghi, *Chem. Sci.*, 2013, **4**, 2858.

Chapter 4

Rose Petal and Lotus Leaf Inspired Two-in-One Approach to Energy-Efficient Mechanical Motion

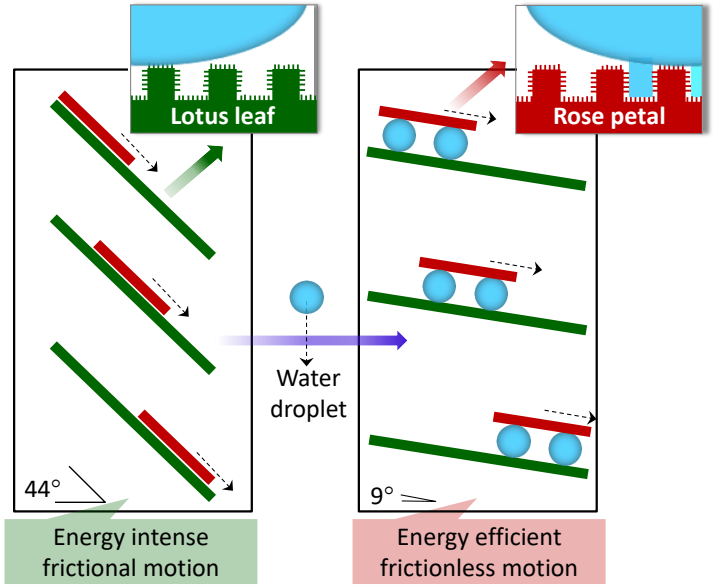

4.1. Abstract

*Inventions such as the wheel, pulley, lever, lubricants, etc. for efficient mechanical motion of objects continue to inspire mankind. Depletion of fossil fuels and concern for the environmental issues compel scientists to explore innovative ideas on energy efficiency. By combining artificially created rose petal like sticky hydrophobicity of an organic ligand and the lotus leaf like slippery hydrophobicity of a zinc based coordination polymer (**Zn-CP**), we demonstrate that water droplets can be used as a lubricant for energy-efficient sliding motion of objects. The ligand surface helps*

*pinning of the water droplets and the **Zn-CP** surface facilitates slippery motion of objects. Detailed experimental data revealed a 6–fold reduction in the coefficient of static friction (μ_s) with a 4.4–fold less force required for the mechanical movement. An extension of this concept may help creating artificial indoor skating arenas without ice layer, which can save huge amount of energy required for creating and maintaining the slippery ice surface.*

4.2. Introduction

The invention of fire and the wheel can be considered as two historical events that mark the nucleation of the technological growth of the human race.[1] While the former is related to the search for finding a suitable energy source for survival, the latter addresses the ways of reduced energy usage for movement. In the modern world, we look for alternate sources of clean and renewable energy such as solar radiation and hydrogen on one side[2,3] and machines, computers and robots on the other side to help reducing human effort in daily life. In this endeavors, energy efficient mechanical motion of objects has been one of the main challenges that originated with the Greek philosopher Archimedes, who believed that the principle of fulcrum could achieve force amplification with no limit, which led to his celebrated statement, "Give me a place to stand on, and I will move the Earth". Mankind has used this idea in the dislocation of heavy objects using fulcrum, pulley, and rollers before inventing

mechanical machines.[1] Efficient mechanical motion can also be achieved by reducing friction[4] using lubricants such as oil and grease.[5] Nature uses aqueous medium as a lubricant in biological machines like the human body especially around diarthroidal joints, the gastrointestinal tract, inside the pleural cavity as well as on the surface of the eyes.[6,7] However, water as a lubricant in artificial machines[8-10] remains elusive, due to its unfavorable phase transition temperatures, viscosity index and corrosive nature to metallic parts. Still water can be considered as the cheapest and the most environmentally benign lubricant,[11] if there is an efficient way for its utilization.

A thin layer of water behaves as a lubricant in ice-skating and related sports that involve the slippery motion of metallic skates on a hard ice surface.[12,13] While outdoor skiing and skating are possible in cold countries, indoor ice-skating is the only choice in tropical regions, however, this requires huge amount of energy for maintaining the required conditions. According to a survey in Quebec, the energy consumption in maintaining a standard indoor ice skating arena is around 1,500,000 kWh/year. This value ranges from 800,000 kWh/year for the most energy-efficient arenas to 2,400,000 kWh/year for the least efficient ones.[14] In an artificial skating arena, more than half of the total energy is consumed in refrigeration and heating of the indoor space. The energy usage for maintaining such arenas in tropical countries should in principle, exceed the above mentioned figures. In a world with growing energy demands and depleting natural resources, conservation of energy is of paramount significance. Therefore, if a suitable alternative to ice surface that can

maintain its slippery nature at an ambient temperature is available, a large amount of electricity can be saved which, in turn, reduces the emission of CO_2, and related environmental issues.

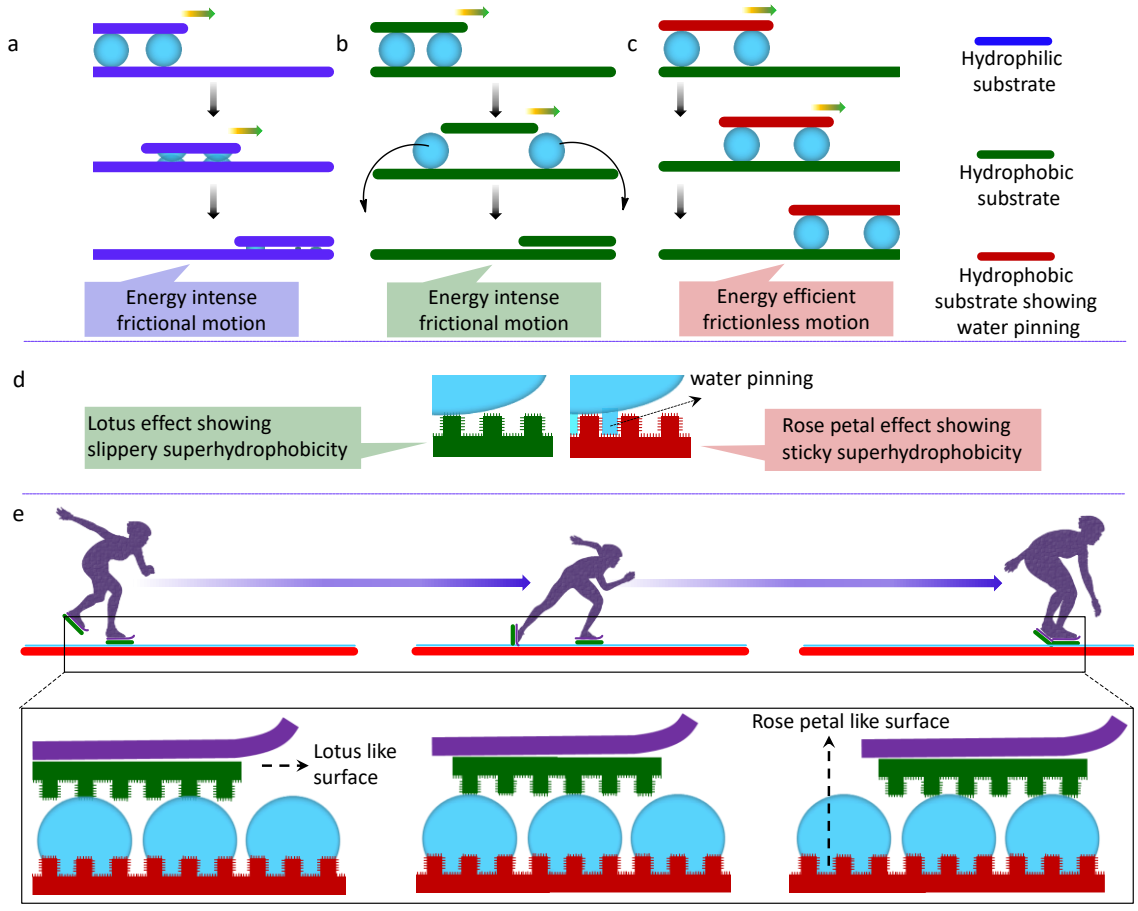

Figure 4.1. (a-c) Schematic representation of the nature of the interaction of water with different types of substrates. Hydrophilic and superhydrophobic surfaces are shown in blue and green respectively. Red surface is superhydrophobic, yet has the ability to stick to water droplets. The red substrate can move over the green one using water as a lubricant. (d) Different wetting scenarios in a lotus leaf (green) and rose petal (red). (e) Ideal situation in a skating arena, where water can be sprayed over the rose petal rink and skates with a lotus leaf like material for energy efficient self-propelled slippery motion.

4.2.1. Concept of an Artificial Iceless Skating Surface

In the context of energy conservation in indoor leisure activities, an important question to be addressed is whether an energy-efficient artificial surface for iceless skating can be realized. At this point, Michael Faraday's observation that ice is covered by a thin film of water even under ambient conditions becomes relevant.[12] An amorphous arrangement of water molecules at the surface of ice is responsible for this pre-melting phenomenon which makes ice surface slippery. The need is, therefore, a thin film of water sandwiched between the skates and the skating surface. To achieve this objective, the behavior of water molecules between the two interacting surfaces needs to be considered (Supplementary Video 1). If the surfaces are hydrophilic, water will be absorbed by both surfaces leading to direct surface contact and associated friction for the sliding action (Figure 4.1a). If both are superhydrophobic, once in contact, both surfaces should reject water, and a solid-solid frictional contact may eventually result thereby arresting the motion (Figure 4.1b). Therefore, we thought of having two differently behaving superhydrophobic surfaces, one of them helping water molecules to stick to the surface while maintaining a constant contact angle as in the case of rose petals and the other facilitating rolling of the water droplets as in the case of lotus leaves (Figure 4.1c).[15-24] When water droplets are placed in between the sticky rose petal mimicking and the slippery lotus mimicking surfaces (Figure 4.1d), the latter can slip over the former with a minimal frictional force. Moreover, we hypothesized that by using this idea, it may, in principle, be able

to achieve highly efficient self-propelled motion on an iceless surface as in ice skating (Figure 4.1e). As a proof-of-concept, we herein demonstrate, such a slippery motion using artificial rose petal and lotus leaf like superhydrophobic surfaces constructed using the metal-organic frameworks (MOFs) chemistry.[25-32]

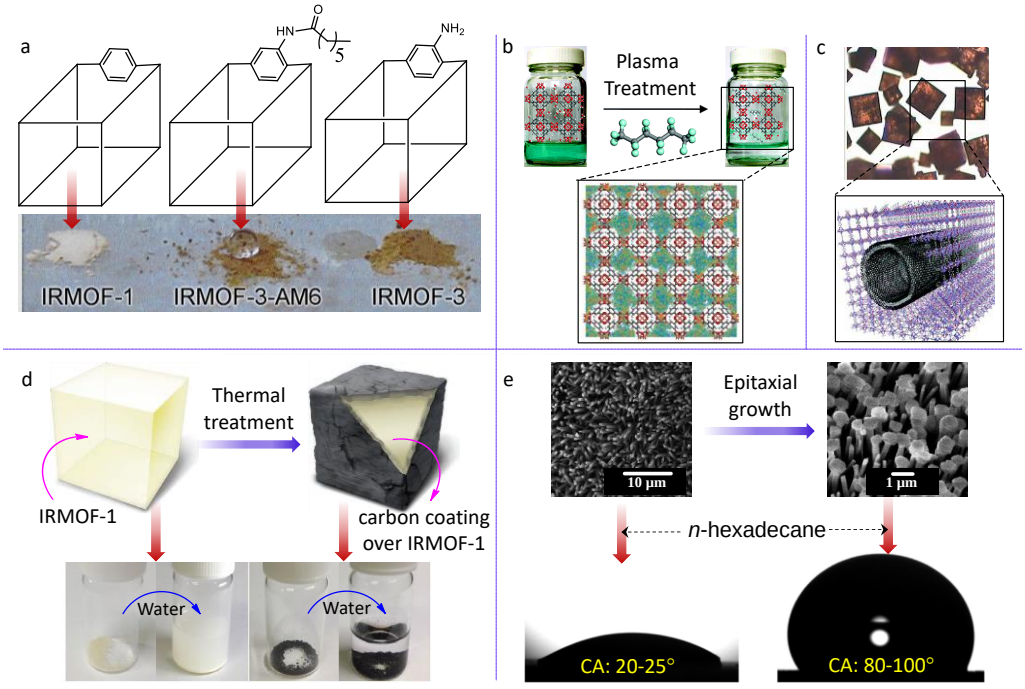

Figure 4.2. (a) Post-synthetic covalent modification of MOFs. Schematic representation of the partial chemical structure of the MOFs and the corresponding photographs of their interaction with water are provided. (b) Introduction of perfluorohexane within the pores of a MOF by plasma treatment. Grand canonical Monte Carlo (GCMC) simulations showing the accumulation of perfluorohexane (greenish blue region, crystal viewed along [100] plane) within MOF pores. (c) Optical micrograph and schematic representation of a multi-walled carbon nano tube incorporated MOF. (d) Moisture-resistant black colored MOF prepared by thermal treatment. Photographs show untreated and treated MOFs after immediate addition of water. (e) SEM images of aligned micro needles and mushroom like morphological features of a MOF. Contact angle of n-hexadecane on omniphobic surfaces having the corresponding morphology.

In order to create superhydrophobic MOFs, Cohen and co-workers have reported a post-synthetic modification strategy, wherein the MOF crystals were covalently modified with hydrophobic alkyl chains (Figure 4.2a).[26] Very recently, a similar post-synthetic modification reported by Ma and co-workers imparted omniphobicity in a different family of MOFs (zeolitic imidazolate frameworks).[27] In another strategy, Decoste and co-workers obtained water stable MOFs by introducing hydrophobic molecules (perfluorohexane) within its pores by plasma induced chemical vapor deposition (Figure 4.2b).[28] Concurrently, Park and co-workers have reported pre-synthetic modifications via the incorporation of carbon nano-materials to construct water stable MOFs with enhanced hydrogen storage capacity (Figure 4.2c).[29] An alternate approach is to protect the exterior surface of the MOF with a hydrophobic coating. Park and co-workers have developed black colored moisture resistant MOFs obtained by a controlled thermal treatment that covered the external surface of the MOF with an amorphous, hydrophobic carbon coating (Figure 4.2d).[30] Hydrophobicity can also be rendered to these materials by tuning their morphologies in the nano-mesoscale size domain. Chin and co-workers have reported microstructured omniphobic surfaces via the epitaxial growth of MOFs (Figure 4.2e).[31] In a recent development, Maji and co-workers have prepared superhydrophobic, nanoscale MOFs from organic ligands functionalized with long alky chains.[32] Kitagawa and co-workers have introduced molecular level roughness in the surface of MOF crystals to design superhydrophobic MOFs.[33] By virtue of their

tunable nanoscale morphologies, metal-organic frameworks (MOFs) and coordination polymers (CPs) can thus be considered as potential candidates for the creation of superhydrophobic surfaces.[34-36] We have therefore exploited the chemistry of metal-organic frameworks (MOFs) or the coordination polymers (CPs) for the design of superhydrophobic surfaces. We firmly believe that, these unprecedented materials developed independently by Yaghi and Kitagawa, though have many promising applications, are still awaiting a break through development.[25]

4.3. Results and Discussion

4.3.1. Synthesis of Organic Linker AzPBA

Aromatic dicarboxylic acids are one of the widely exploited building blocks for the preparation of a variety of metal-organic materials. Incorporation of additional functional group such as azobenzene moiety can impart additional property to the resultant framework. Thinking in this direction, we have designed an organic linker (*E*)-4,4'-(diazene-1,2-diyl)bis(4,1-phenylene))bis(oxy)dibutanoic acid (**AzPBA**). The linker was prepared via a reported procedure in an overall 33% yield (Scheme 3).[37] *p*-Nitrophenol upon fusing with potassium hydroxide at 220°C, followed by work up in dilute hydrochloric acid resulted in the formation of the azo compound **1** in 47% yield, which on subsequent alkylation at the phenyl hydroxy groups in presence of a mild base (activated K_2CO_3) and ethyl 4-bromo butanoate, afforded the intermediate **2** in 77% yield. **AzPBA** was synthesized via alkaline hydrolysis of azo compound **2** in

92 % yield. The conversion of intermediate **2** to **AzPBA** was confirmed from the presence of the broad band (~2500-3300 cm^{-1}) corresponding to the to the O-H stretching frequency of the carboxylic acid and the shifting of the carbonyl stretching frequency from 1728 cm^{-1} in the ester (intermediate **1**) to 1703 cm^{-1} in the acid (**AzPBA**) (Figure 4.3a-b). AzPBA was further characterized using other anlytical techniques like NMR, ESI-MS and elemental analysis. The formation of the azo chromophore was further confirmed when **AzPBA** showed UV light induced changes in its UV-Vis absorption spectrum in solution. At the photostationary state ~70% **AzPBA** molecules were photoisomerized from the *trans* to the *cis* state (Figure 4.3c).

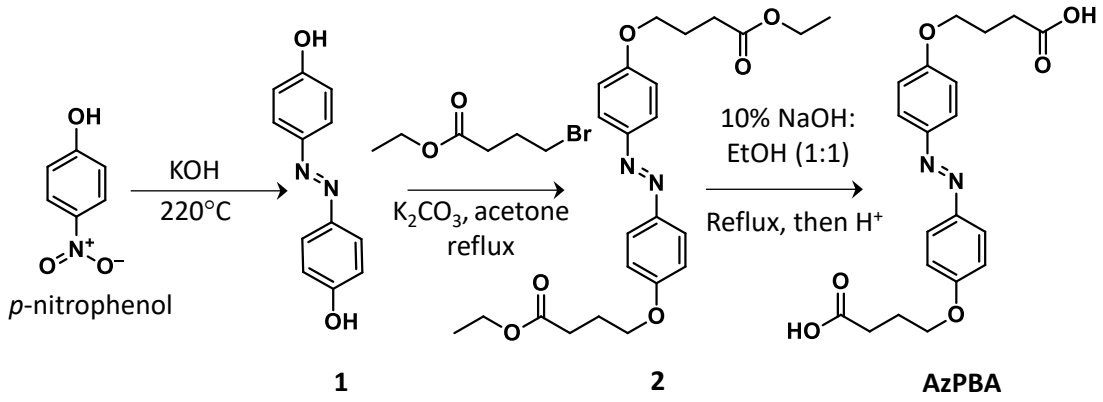

Scheme 3. Reagents and conditions for the synthesis of **AzPBA**.

4.3.2. Synthesis and Characterization of the AzPBA based Coordination Polymer (Zn-CP)

A coordination polymer **Zn-CP**, was prepared from **AzPBA** using standard solvothermal synthesis. Fourier transform infrared (FT-IR) studies on **AzPBA** and

Zn-CP showed that the broad band (~2500-3300 cm^{-1}) corresponding to the O-H stretching frequency of the carboxylic acid (**AzPBA**) was absent in **Zn-CP**, indicating the coordination of the acid groups to the Zn-based inorganic cluster (Figure 4.3a). Moreover, a decrease in the intensity of the carbonyl stretching frequency ($\nu_{assymetric}$)

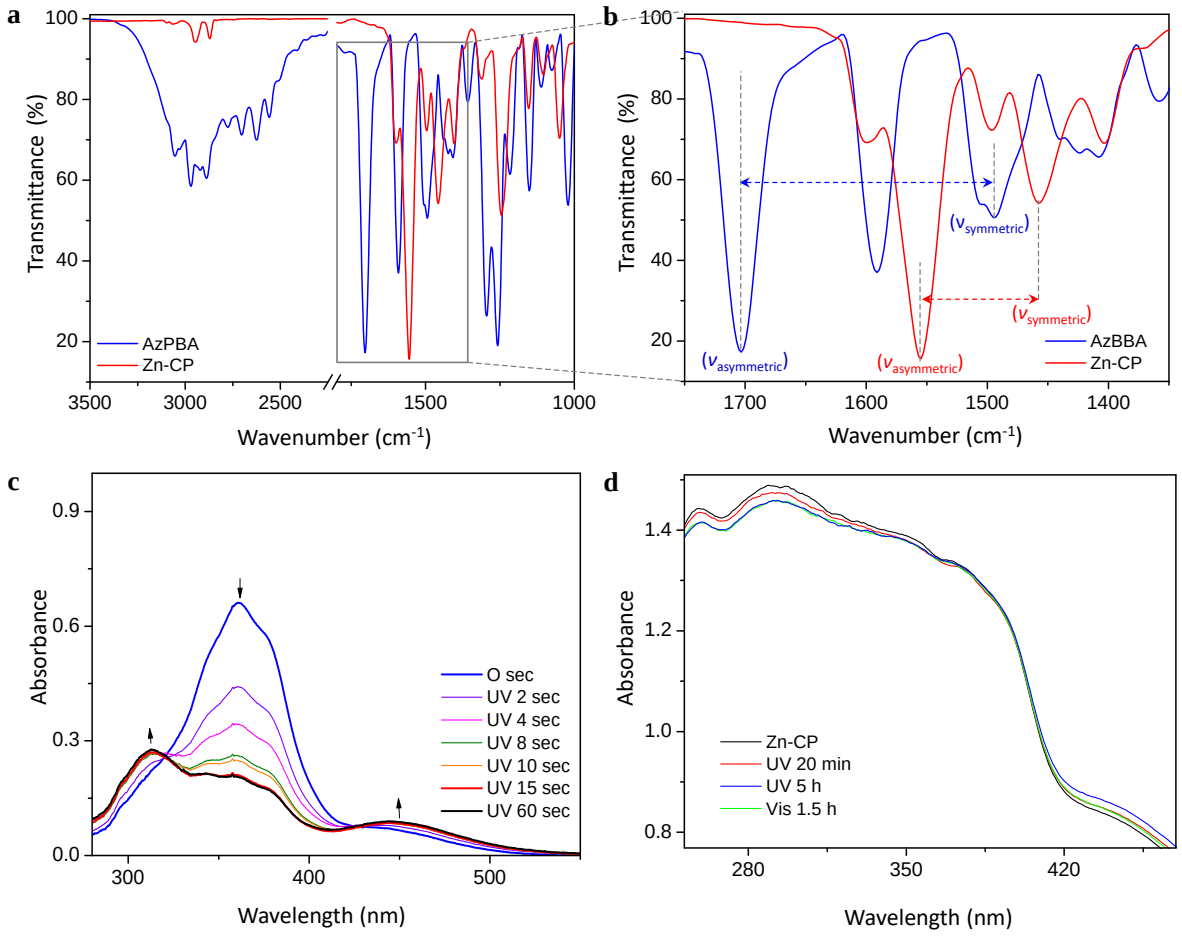

Figure 4.3. (a) FT-IR spectra of the organic ligand **AzPBA** and the coordination polymer **Zn-CP** showing changes in the region corresponding to O–H stretching frequency. (b) Expanded portion of the region (1750–1350 cm^{-1}), showing changes corresponding to the asymmetric and symmetric stretching frequencies of the carbonyl bond. (c) UV absorption spectra exhibiting *trans* to *cis* photoisomerization of **AzPBA** in DMF (c = 3 x 10^{-5} M). (d) Solid state UV absorption spectra showing the insignificant photoisomerization in **Zn-CP**.

at 1599 cm^{-1} and an increase in the intensity of the band at 1423 cm^{-1} ($\nu_{symetric}$). The mode of coordination (bidentate bridging) was further confirmed by the difference between $\nu_{assymetric}$ and $\nu_{symetric}$ stretching bands, that decreased from 280 cm^{-1} in **AzPBA** to 142 cm^{-1} in **Zn-CP** (Figure 4.3b).[38] On irradiation of the **Zn-CP** with ultraviolet light (365 nm) in its solid state, negligible photoresponse (2.4 % *trans-cis* photoconversion, monitored at 440 nm) was observed (Figure 4.3d). Elemental analysis of **Zn-CP** matched closely with the simplest repeating unit (molecular formula) of $(Zn_4O)(C_{20}H_{20}N_2O_6)_3$ (Figure 4.4a).

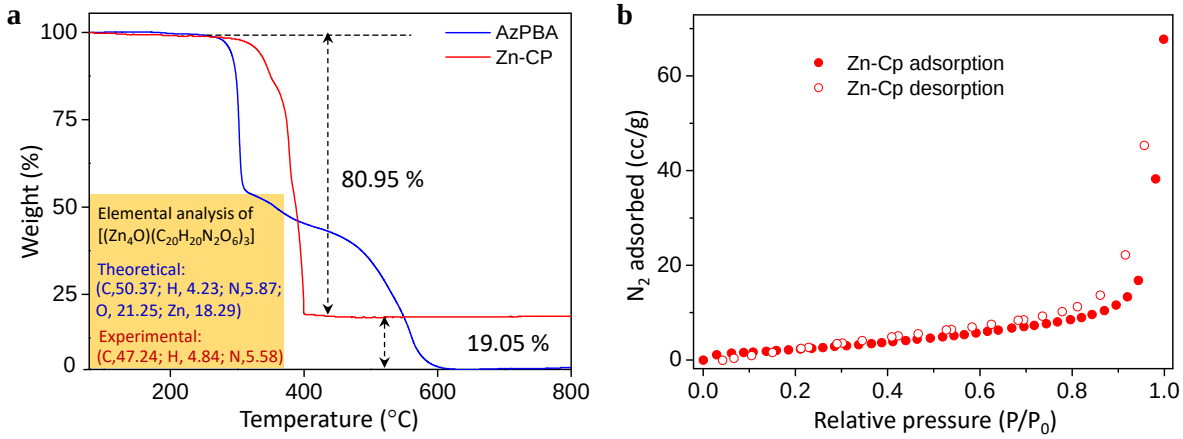

Figure 4.4. (a) TGA of **Zn-CP** and **AzPBA**, inset shows the results obtained from the elemental analysis of **Zn-CP**. (b) N_2 adsorption and desorption isotherm (Type II, nonporous behavior) of **Zn-CP** recorded at 77 K.

In thermogravimetric analysis (TGA), we observed a single weight loss step of 81% starting at ~300°C, corresponding to the decomposition of the organic ligand (estimated loss 80.9%). Afterwards, a plateau was reached at 19.05% weight, corresponding to the weight of the residual Zn_4O cluster (estimated loss 19.07%). A

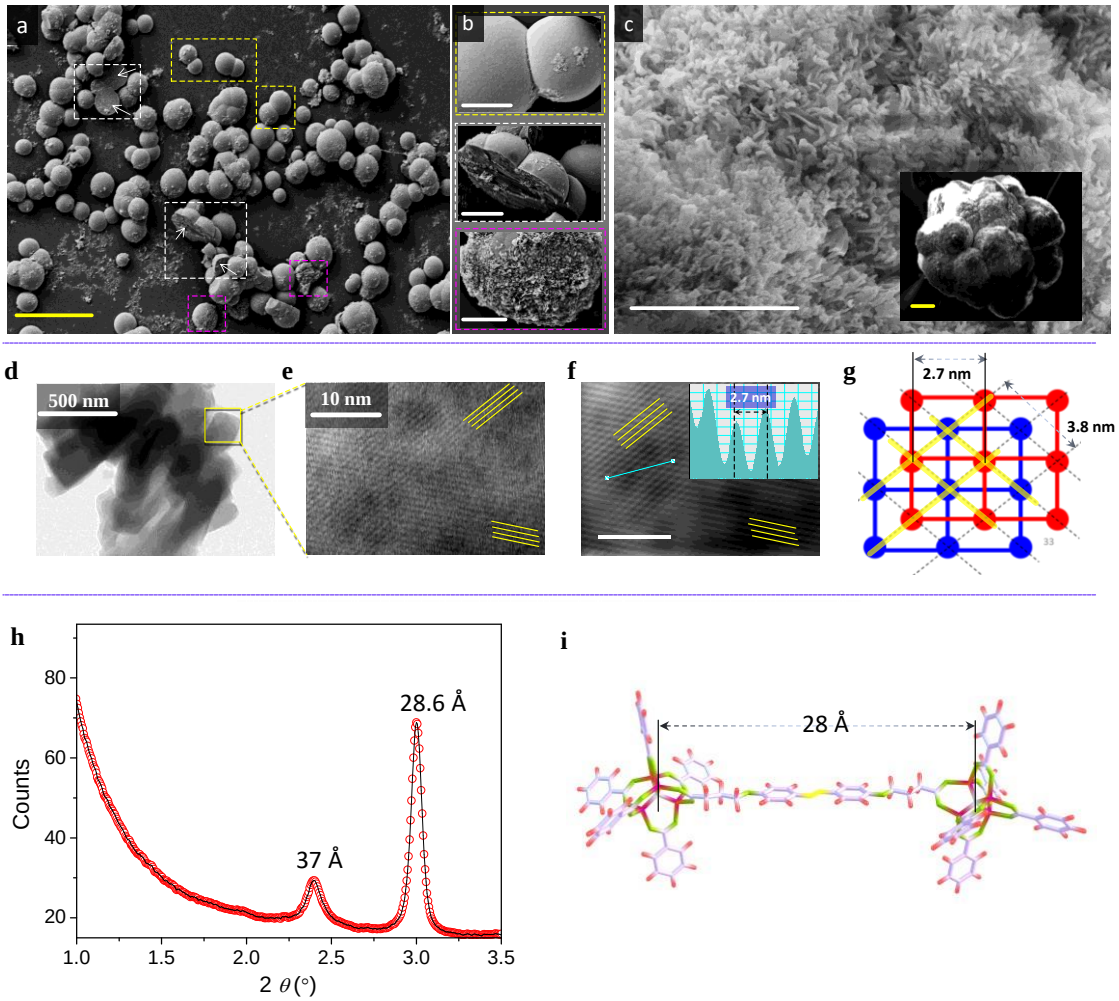

Figure 4.5. (a) SEM image of **Zn-CP**, prepared by solvothermal method. (b) Magnified view of portions marked by boxes of similar colour in (a). (c) SEM image of **Zn-CP** nanoscale rough surface prepared by time controlled solvothermal reaction (after 12 h). Inset shows the macroscopic rough surface of **Zn-CP**. Scale bars, 50 µm (yellow) and 10 µm (white). (d) TEM image and (e) HRTEM image of nanoscale **Zn-CP** asperities. (f) Reconstructed HRTEM image of (e), clearly showing a doubly interpenetrated lattice planes (marked in yellow), inset shows the line profile corresponding to the distance between the metal clusters. (g) Schematic representation of a doubly interpenetrated structure. (h) Small angle X-ray scattering (SAXS) profile of **Zn-CP**. (i) Energy minimised simplest structure (optimized using semiemperical PM6 level calculations)[40] showing the theoretically predicted distance between the tetrahedral Zn_4O clusters in **Zn-CP**, the ancillary ligands are chosen as benzoic acid based on the crystal structure of MOF-5.

negligible weight loss (3%) was observed until 240 °C, indicating that very less solvent molecules got trapped within the MOF network during the synthesis of the material (Figure 4.4a). This may be associated with the decrease in porosity, due to a more interpenetrated structure, owing to the longer length of the ligand.[39] This is indeed evident from the N_2 gas adsorption isotherm (Figure 4.4b). This interpenetrated nature of the framework may also be responsible for the negligible photoresponse in its solid state (Figure 4.3d).

Scanning Electron Microscopic (SEM) analysis of the **Zn-CP** revealed the formation of micrometer sized spherical particles that were fused together at several places (Figure 4.5a). SEM analysis also revealed the formation of nanoscale finger like structures in some regions (Figure 4.5b). By controlling the reaction time, the growth of **Zn-CP** was restricted to a stage where it forms nanoscale finger like structures on a fused spherical morphology thereby creating a dual scale roughness (Figure 4.5c).[34-36] These nano fingers were about 1 μm in length and about 200 nm in width. Transmission Electron Microscopic (TEM) analyses of these structures revealed doubly interpenetrated crystalline domains (Figure 4.5d-g) with the distance between the lattice planes matching the distance calculated from the small angle X-ray scattering (SAXS) measurements (Figure 4.5h) and the energy minimized simplest repeating unit of **Zn-CP** (Figure 4.5i).

It is interesting to note that the morphology obtained under restricted conditions (Figure 4.5c) matches well with the dual topographical features of lotus

leaves, where micrometer–sized hills and valleys are adorned by nanometer–sized coating of wax crystals. For practical applications of superhydrophobic surfaces, it is

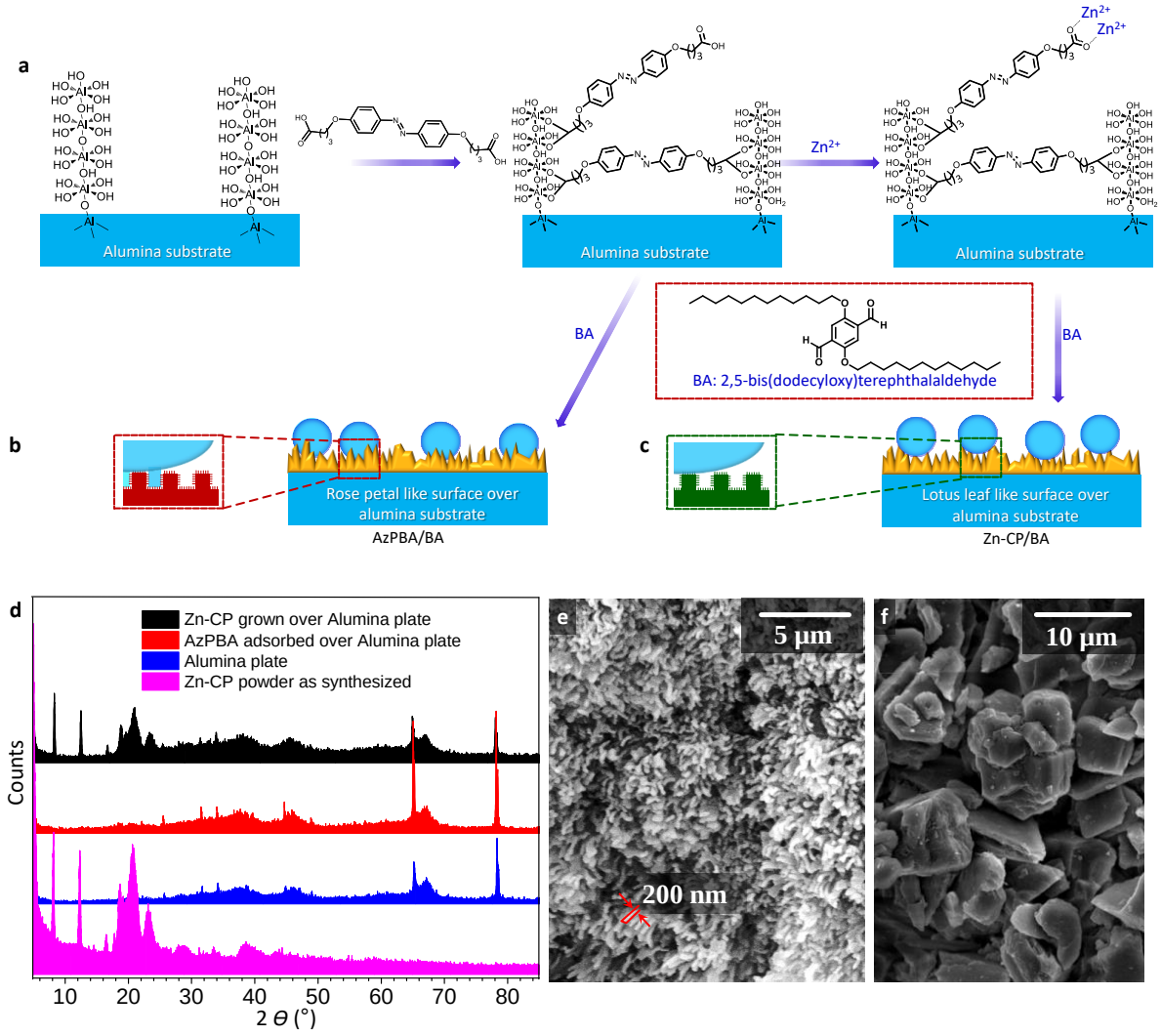

Figure 4.6. (a) Schematic representation of the chemical processes occurring during the growth of **Zn-CP/BA** and **AzPBA/BA** film over alumina plate. Inset shows the chemical structure of **BA**. (b) Cartoon representation of the sticky water droplets on **AzPBA/BA**. (c) Cartoon representation of the slippery water droplets on **Zn-CP/BA**. (d) XRD characterization of the formation of **Zn-CP** phase over alumina surface. (e) SEM image of **Zn-CP** film over alumina substrate marked with the nanoscopic dimensions of the morphological features. (f) SEM image of **AzPBA** film over alumina substrate.

important that the required morphological features are homogeneously distributed over a large area in a dense and oriented fashion. For this purpose, we adopted, the direct growth/deposition method[41] of the MOF crystals over an alumina substrate dipped into a mother liquor during a controlled solvothermal synthesis (Figure 4.6a).[31,42]

4.3.3. Lotus Leaf and Rose Petal like Superhydrophobicity

We found that both **AzPBA** and **Zn-CP** functionalized surfaces exhibited moderate to high superhydrophobicity, wherein **AzPBA** behaved like a rose petal, while **Zn-CP** exhibited the lotus leaf effect (Figure 4.6b-c). X-ray diffraction (XRD) analysis of the **Zn-CP** film over the alumina plate exhibited diffraction peaks corresponding to **Zn-CP** and the alumina surface (Figure 4.6d). SEM analysis of the alumina plates after solvothermal treatment, confirmed the complete coverage of the nano and micro scale morphological features of **Zn-CP** over the alumina surface (Figure 4.6e). The growth of **Zn-CP** over the alumina plate was followed by time dependent SEM analysis (Figure 4.7).

When the **Zn-CP** film is grown on the alumina surface, the water contact angle (CA) is significantly improved from a near zero value to an initial contact angle of 156 ± 2° which slowly reduces to 80 ± 2°. Nevertheless, we could improve and maintain the contact angle of the **Zn-CP** film by coating with an organic molecule **BA**, thereby achieving a lotus leaf like superhydrophobic material (**Zn-CP/BA**)

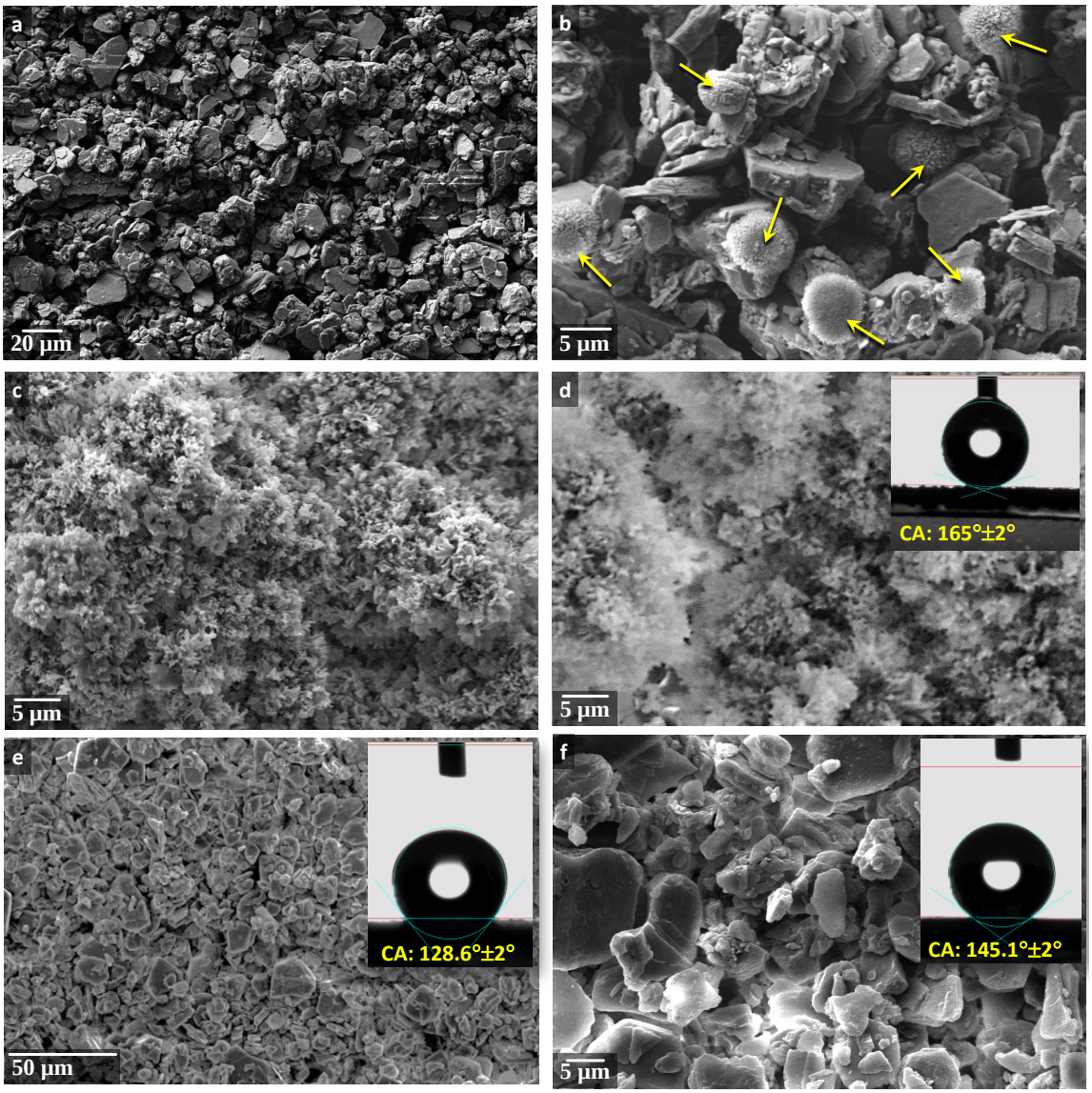

Figure 4.7. Time dependent SEM analysis of formation of **Zn-CP** coating over alumina substrate recorded after (a) 0 h and (b) 4 h. Yow arrows mark the growth of the **Zn-CP** phase. (c) Complete coverage of alumina substrate with **Zn-CP** layer after 12 h. (d) SEM image of lotus leaf like surface obtained after coating of **BA**. Inset shows the water contact angle over **Zn-CP/BA** surface. (e) SEM image of **AzPBA** coating over alumina substrate obtained after 12 h of solvothermal treatment. Inset shows the water contact angle over **AzPBA** surface. (f) SEM image of rose petal like surface obtained after coating of **BA**. Inset shows the contact angle over **AzPBA/BA** surface

having a water contact angle of 165 ± 2° (Figure 4.7d).[43] Both **Zn-CP** alone and **Zn-CP/BA** composite possessed enhanced stability in presence of moisture due to the hydrophobic propyl chains around the zinc clusters that minimized the interaction with water molecules. In order to establish the stability of the materials under air and moisture, we performed two experiments (Figure 4.8a-b). Alumina plates coated with pristine **Zn-CP** and **Zn-CP/BA** were separately kept in contact with water taken in a petri dish. The **Zn-CP/BA** coated plate did not adhere a single water droplet even after 30 h of exposure. The alumina plate containing only the **Zn-CP** showed water stranded over it. Subsequently, we did the WAXD measurements on both the plates at different time intervals; that clearly showed the retention of the crystalline order of the **Zn-CP** even after 30 h of water exposure (Figure 4.8c). In order to study the effect of water on the crystalline nature of **Zn-CP**, a pellet of the **Zn-CP** was prepared and submerged in a beaker of water and its WAXD pattern was measured at different time intervals. Wide-angle X-ray diffraction (WAXD) analysis of the synthesized **Zn-CP** showed the presence of intense diffraction peaks that correspond to a highly crystalline lamellar structure with *d*-spacing ratio of *d*, *d*/2, *d*/3, *d*/4 (Figure 4.8c-d). It was seen that the WAXD pattern of **Zn-CP** did not change even after 45 days (Figure 4.8d).[30] The WAXD data after 60 days of water exposure revealed that the lamellar structure of **Zn-CP** almost remains intact. However, the emergence of a few new peaks was observed which is attributed to the formation of a new crystalline phase of **Zn-CP** and not due to decomposition of the framework, as these peaks did not match

with the WAXD data of the thermally decomposed **Zn-CP** (Figure 4.9a) and that of a **Zn-CP** framework leached under five cycles of acidic and basic treatment (Figure 4.9b). The alkyl chains attached to the aromatic moiety also play an important role in generating a dual scale morphological feature as it is evident by a coordination polymer synthesized from a similar molecule **HqPBA** without the azobenzene core (Figure 4.10).

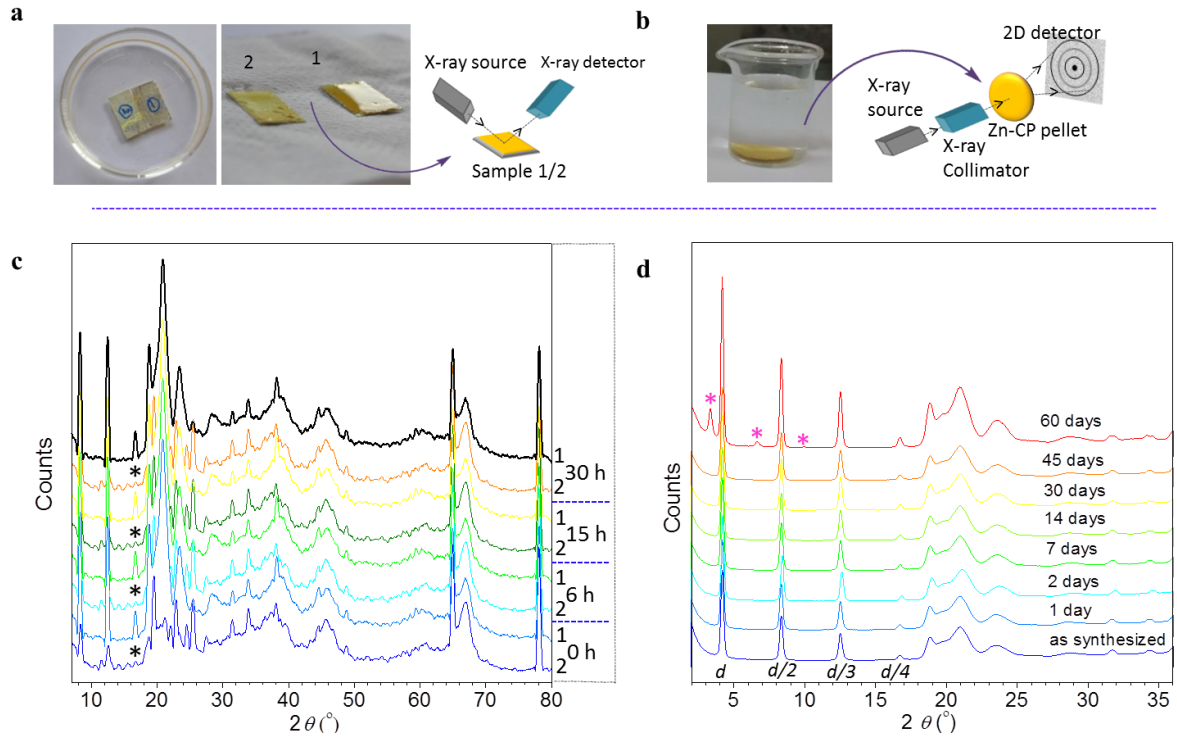

Figure 4.8. (a) Photographs of **Zn-CP** (sample 1) and **Zn-CP/BA** (sample 2) during moisture stability experiment and after being kept in contact with water for 30 h. Schematic representation XRD set up in reflection mode. (b) Photograph of **Zn-CP** pellet immersed in a 5 mL beaker containing distilled water for 60 days. Schematic representation of WAXD set up in transmission mode is shown along with. (c) The stability of the prepared alumina substrates coated with **Zn-CP** (1) and **Zn-CP/BA** (2) layers towards water was monitored via WAXD studies. Black asterisk marks the position of *d*/4 peak in sample 2. (d) The stability of the prepared **Zn-CP** pellet towards water was monitored via WAXD studies. Peaks that are newly observed after 60 days are marked by red asterisk.

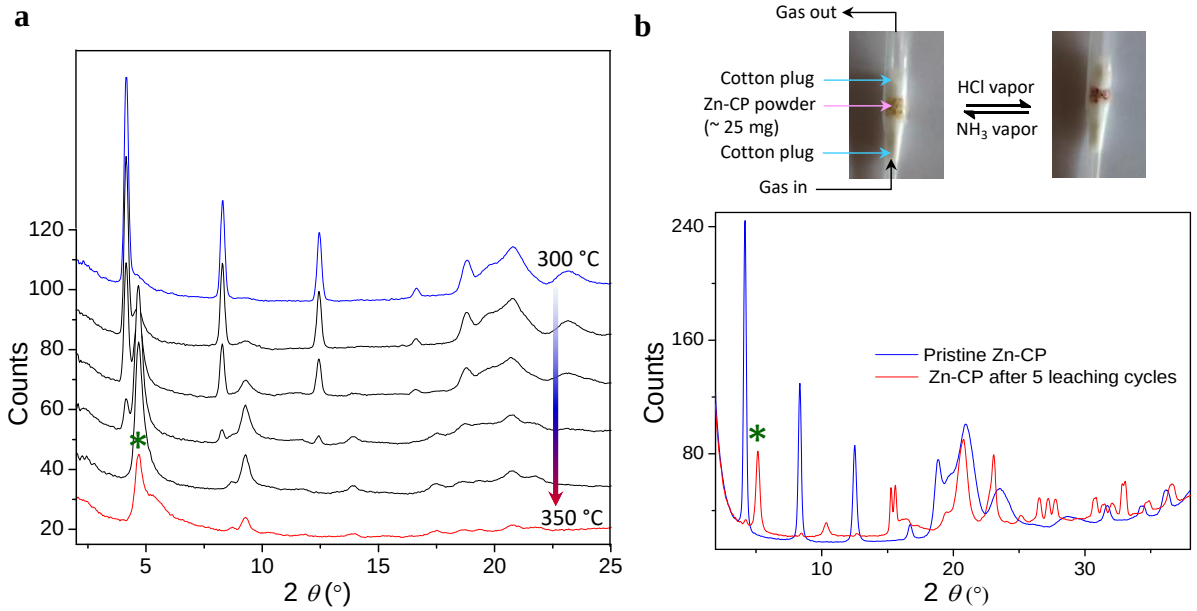

Figure 4.9. (a) Temperature dependant WAXD recorded from 300 °C to 350 °C (where the thermal decomposition of **Zn-CP** phase is observed in TGA). (b) Experimental setup for the leaching of **Zn-CP** using HCl and NH_3 vapors, WAXD of **Zn-CP** recorded after 5 leaching cycles compared to that of pristine **Zn-CP**. Green asterisk marks the position of the same diffraction peak in samples decomposed by heating or by chemical leaching of the polymer framework. This peak was absent in the **Zn-CP** pellet immersed in water for 60 days, instead a new diffraction peak in the lower 2Θ region was observed.

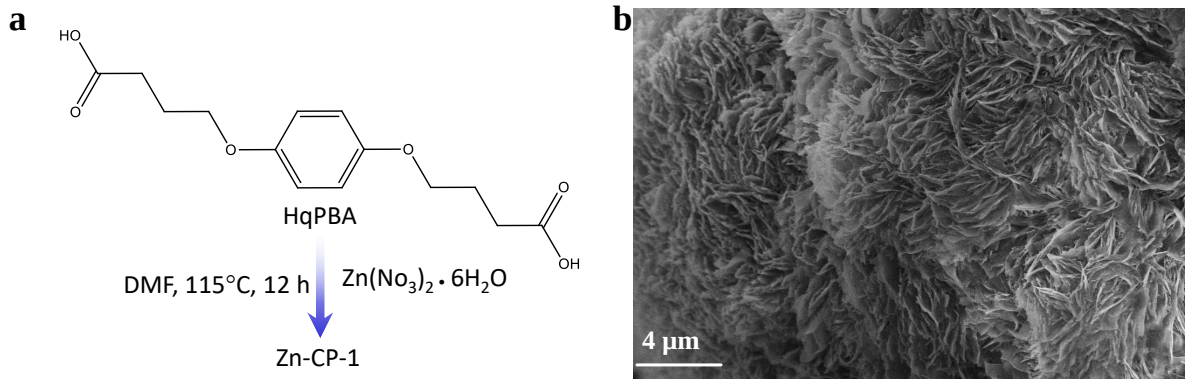

Figure 4.10. (a) Synthesis of **Zn-CP-1** from organic ligand **HqPBA** (without the azobenzene chromophore). (b) SEM image of **Zn-CP-1**.

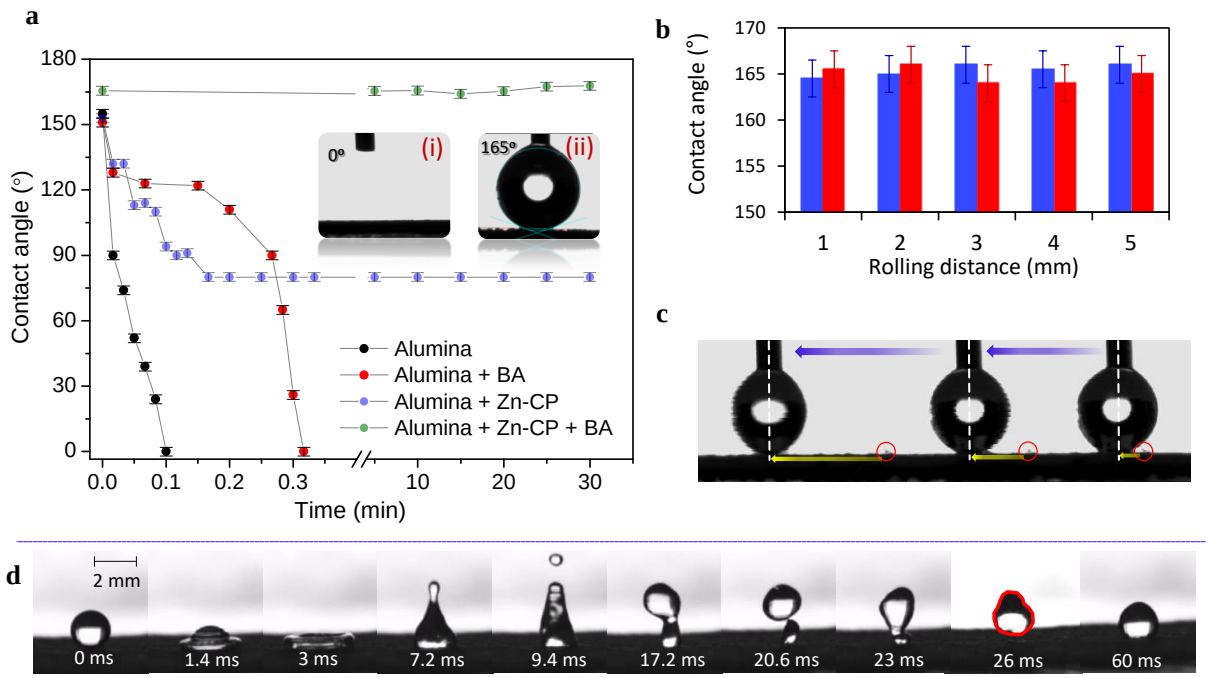

Figure 4.11. (a) Variation of CA with time for differently functionalized substrates. Inset shows the photographs of a water droplet on alumina (i) and **Zn-CP/BA** coated over alumina (ii) surfaces. (b) Results of CAH experiments based on rolling method. The advancing and receding contact angles are represented in blue and red colour respectively. (c) Snapshots of a water droplet rolling over a **Zn-CP/BA** substrate. Blue and yellow arrows show the direction of movement and the extent of displacement of the needle from the position marked with a red circle. White dashed line marks the position of the syringe needle. All CA measurements are within an error limit of ± 2°. (d) High-speed camera images of bouncing of a water droplet over a **Zn-CP/BA** surface. Snapshots of the water droplet completely detached from the surface is shown with a red outline (droplet radius R = ~1 mm; impact velocity U = 0.8 ms^{-1}).

While the contact angle of a water droplet over the surface of **Zn-CP** decreased to 80 ± 2° from the initial 157 ± 2° within 10 sec, the contact angle over **Zn-CP/BA** film remained constant at ~165° (measured upto 30 min), which is one of the required characteristics of an ideal superhydrophobic surface (Figure 4.11a).

Contact angle hysteresis (CAH) is another important parameter to determine the nature of surface wettability.[24] When a liquid droplet moves on the substrate, under the influence of an external force, the difference between the observed advancing and receding CAs is defined as CAH. It is a measure of the net force of adhesion of a droplet with a substrate and also the amount of energy dissipated during the movement of the droplet. The **Zn-CP/BA** surface is seen to possess negligible CAH (Figure 4.11b-c and Supplementary Video 2) and as a result, the water droplets move freely on the surface even at sliding angles lower than 2°.

In order to prepare the rose petal like surface, alumina plates were dipped into a solution of **AzPBA** in dry DMF and heated under solvothermal conditions for 12 h (Figure 4.6b). No extra diffraction peaks (2θ = 5–30°), corresponding to **Al-CP** was observed in the WAXD data. Therefore, formation of **Al-CP** phase was ruled out by WAXD (Figure 4.6d) and from SEM analyses (Figure 4.6f), where the morphology of the alumina plate remained unaltered. Contact angle measurements on **AzPBA** treated alumina plate revealed the hydrophobic nature of the surface (128.6º ± 2°) (Figure 4.7e). The contact angle was further improved to 145.1º ± 2°, almost reaching the superhydrophobic domain, via treatment with **BA** (Figure 4.7f). Interestingly, unlike in the **Zn-CP/BA** coated alumina plate, the **AzPBA/BA** exhibited very high CAH indicating a sticky nature of the surface (Figure 4.12a-b and Supplementary Video 2). A stranded water droplet was too sticky to be rolled even by applying force with the needle of a syringe (Figure 4.12a). The ability to pin the water droplet was further

illustrated as the water droplets did not roll on tilting the surface even at a tilt angle of 180 º (Figure 4.12c).

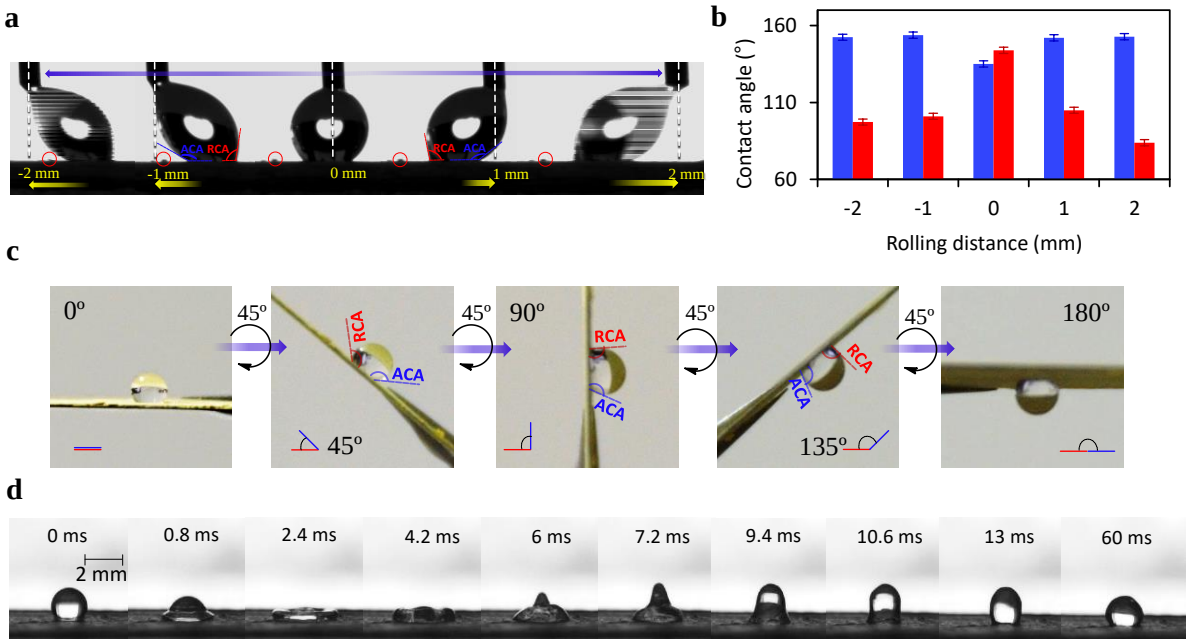

Figure 4.12. (a) Snapshots of a water droplet rolling over a **AzPBA/BA** substrate. Blue and yellow arrows show the direction of movement and the extent of displacement of the needle from the position marked with a red circle. White dashed lines mark the position of the syringe needle. (b) Results of CAH experiments based on rolling method. The advancing and receding contact angles are represented in blue and red colour respectively. (c) Photographs of a water droplet (15 µL) anchored on to an **AzPBA/BA** substrate kept at different sliding angles (0°-180°). All CA measurements are within an error limit of ± 2°. (d) High-speed images of bouncing of a water droplet over a **AzPBA/BA** surface (droplet radius R = ~1 mm; impact velocity U = 0.8 m s^{-1}).

4.3.4. Water Droplet Bouncing Dynamics on Zn-CP/BA and AzPBA/BA Surfaces

The dynamics of sticky and slippery superhydrophobicity was studied by water droplets bouncing experiment (Figure 4.13a). The bouncing dynamics of a water

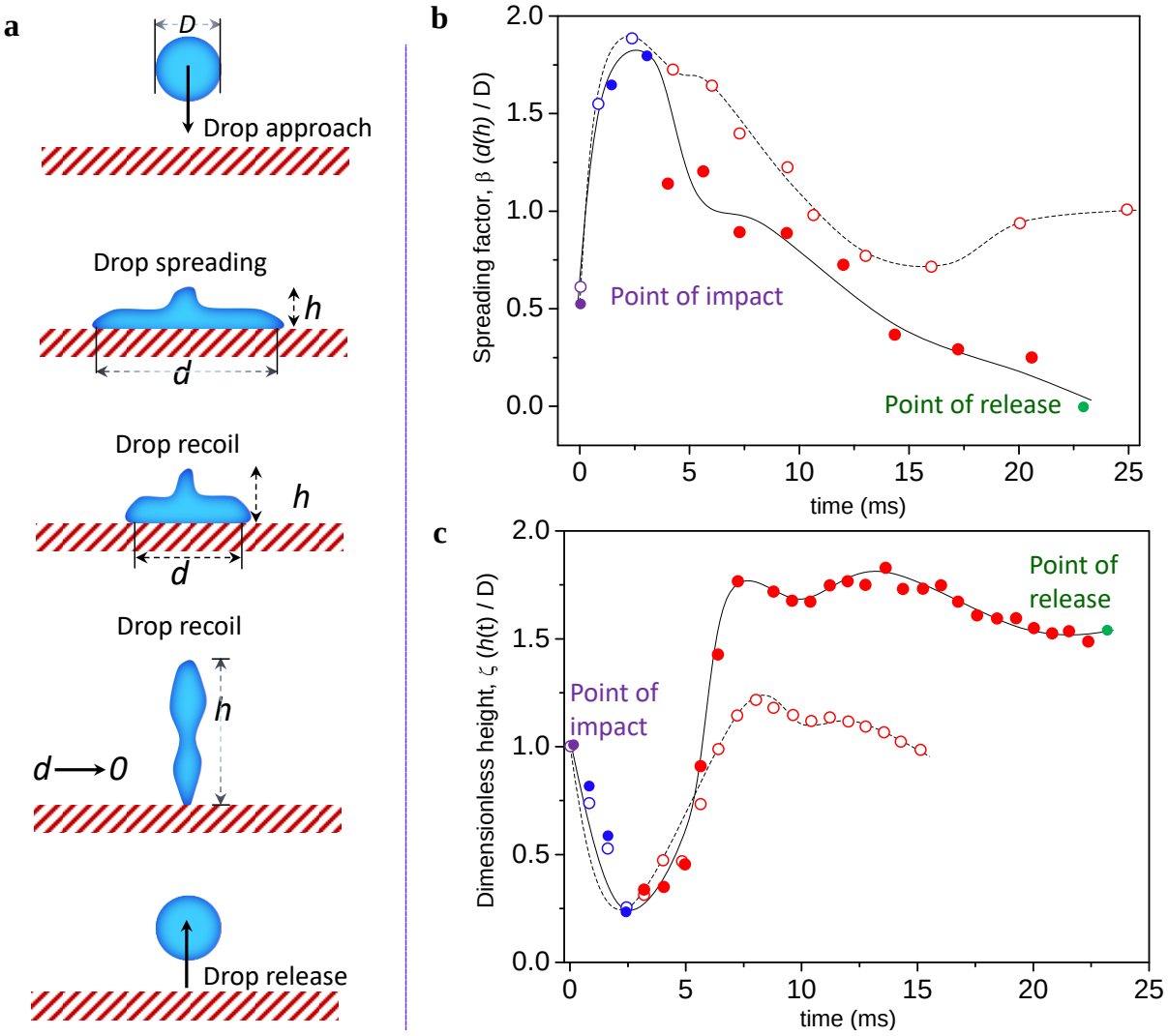

Figure 4.13. (a) Schematic representation of different stages after the impact of a water droplet on a superhydrophobic substrate. (b) Plot of spreading factor (β) with respect to time. (c) Plot of dimensionless height factor (ζ) with respect to time. Filled circles represent data for the **Zn-CP/BA** (lotus leaf) and empty circles represent data for the **AzPBA/BA** (rose petal) like surfaces. Point of droplet impact, spreading regime, recoil regime and droplet release are represented in violet, blue, red and green colors respectively.

droplet on the superhydrophobic surfaces was recorded with a high-speed camera (Figure 4.11d, 4.12d and Supplementary Video 3). The maximum spreading factor

(β_{max}) observed in the case of the **Zn-CP/BA** surface was 1.8, whereas that in the case of **AzPBA/BA** was 1.9. Similarly, the maximum dimensionless height factor (ζ_{max}) was observed to be 1.76 and 1.22 for the **Zn-CP/BA** and **AzPBA/BA** surfaces respectively (Figure 4.13b-c).[44] These values indicate that the water droplet spreads more over the **AzPBA/BA** surface and retracts to a greater height in the case of the **Zn-CP/BA** surface. After the retraction stage, the droplet completely detaches from the **Zn-CP/BA** surface (contact time ~23 ms) while it sticks on to the **AzPBA/BA** surface with a β and ζ value ~1 (corresponding to a spherical shape). The droplets remain as spheres over both the surfaces after 60 ms (Figure 4.11d and 4.12d). These observations support an enhanced pinning effect in the case of the rose petal like **AzPBA/BA** surface, which can also be understood by calculating the fraction of liquid-vapor interface in the two substrates.

4.3.5. Comparative Wetting Scenario in Rose Petal and Lotus Leaf Substrates

According to the modified Cassie equation, CA on a hydrophobic surface (θ_R) can be expressed in terms of the contact angle on a smoother surface (θ) [Eq. (1)].[24]

$$\mathrm{Cos}\,\theta_R = f_{sl}\,\mathrm{Cos}\,\theta - f_{lv} \quad \ldots\ldots\ldots\ldots \quad \text{(Eq. 1)}$$

$$\text{where, } f_{sl} + f_{lv} = 1 \quad \ldots\ldots\ldots\ldots\ldots\ldots \quad \text{(Eq. 2)}$$

The individual ratio of flat projection of solid-liquid interface area and that of the liquid-vapor interface area to the composite substrate's total flat geometrical area under the liquid droplet is f_{sl} and f_{lv} respectively. Since these two fractions comprise of the total area under the droplet, their sum can be considered as unity [Eq. (2)]. According to Cassie-Baxter model, in a surface with very high roughness factor, the liquid droplet is not able to penetrate through the asperities of the solid substrate. The droplet simply rest on the tip of asperities, balanced by a cushion of the air pockets underneath (Figure 4.1d). This trapping of air, under a liquid droplet, therefore greatly contributes to the increase in hydrophobicity of the surface. Considering $\theta = 0°$ for the alumina surface and utilizing equation (1 and 2), the f_{lv} value of the **AzPBA/BA** and **Zn-CP/BA** substrates were estimated to be 0.91 and 0.98 respectively. These values indicate that the fraction of air trapped in the surface for **Zn-CP/BA** is rather high and exceeds the amount of air trapped by **AzPBA/BA** substrate by ~8%. This can be attributed to the presence of dual phase asperities in **Zn-CP/BA** substrate which is absent in **AzPBA/BA** substrate. Not only the presence of asperities but also the presence of the hydrophobic **BA** coating is significant and is evident from the low f_{lv} (0.41) obtained for **Zn-CP** substrate alone. This can be attributed to the seepage of water through the mesoporous asperities of the **Zn-CP** substrate due to capillary forces. Upon addition of a **BA** coating, the f_{lv} increases by about 139% in case of **Zn-CP/BA** while only ~12% increase is observed in case of **AzPBA/BA**.

4.3.6. Force of Water Droplet Adhesion in Zn-CP/BA and AzPBA/BA Films

The force (F) needed to move a water droplet along any inclined surface under the influence of gravity has earlier been derived by Furmidge.[45] The same principle can be applied for estimating the force (F) needed to move the droplet along any horizontal surface as per the equation [Eq. (3)] (Supplementary Video 2). At the same time, the force of adhesion [Eq. (4)] or the threshold force required for the detachment of a water droplet from different substrates can be calculated using the equation reported by Brochard-Wyart and de Gennes (Supplementary Video 4).[46]

$$F = W \gamma_{sl} (\text{Cos } \theta_r - \text{Cos } \theta_a) \quad \ldots\ldots\ldots\ldots \quad \text{(Eq. 3)}$$

$$F_d = \pi R \gamma_{sl} (1 + \text{Cos } \theta_e) \quad \ldots\ldots\ldots\ldots\ldots\ldots \quad \text{(Eq. 4)}$$

where, W and R are the width and radius of the droplet respectively, θ_a and θ_r refers to the advancing and receding contact angles respectively, θ_e is the corresponding contact angle and γ_{sl} is the surface tension along the liquid-vapor interface.

Deformation of a water droplet may occur, when it is under the influence of two unequal adhesive forces, one towards the end of the needle and the other offered by the sticky superhydrophobic substrate. As the force towards the syringe end is increased, the water droplet is deformed to the maximum extent till a point of detachment is achieved and the force of attachment of the droplet with the surface wins. In case of the slippery superhydrophobic substrate, the water droplet

experiences almost two equal and opposite forces and therefore can be easily rolled over the substrate with minimum droplet deformation. A similar droplet deformation may be observed when a droplet is placed between a syringe needle and a sticky superhydrophobic substrate and a force is applied at either end. Deformation of the water droplet (*D*), a dimensionless quantity, was calculated from the water sliding experiments (Figure 4.11c and 4.12a) by using [Eq. (5)].[47]

$$D = (d_1-d_2)/(d_1+d_2) \quad \ldots\ldots\ldots\ldots\ldots \quad \text{(Eq. 5)}$$

where d_1 and d_2 are the major and minor axes of the droplet respectively.

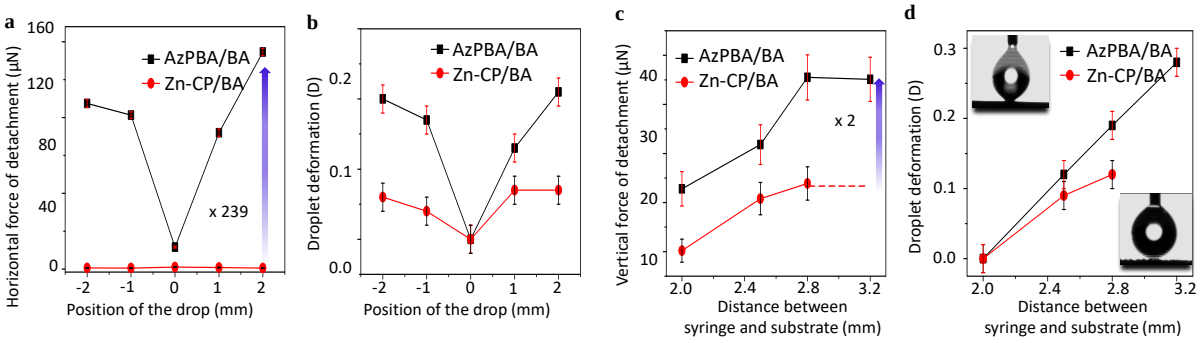

Figure 4.14. (a) Plot of force required to roll a water droplet along a **Zn-CP/BA** and **AzPBA/BA** substrates. (b) Droplet deformation as a result of rolling along the two substrates. (c) Plot of force required to detach a water droplet from a **Zn-CP/BA** and **AzPBA/BA** substrate. (d) Droplet deformation as a result of the adhesive force. All CA measurements are within an error limit of ± 2°.

A spherical water droplet will have equal minor and major axes and drop deformation should be zero. From Figure 4.14a, it is evident that the force required for the movement of a water droplet over **Zn-CP/BA** surface is about 239–fold lesser than that on **AzPBA/BA** surface. This is corroborated by the extent of droplet

deformation occurring in the case of the **AzPBA/BA** surface (D_{max}: 0.21) and the negligible deformation occurring in the case of **Zn-CP/BA** surface (D_{max}: 0.07) (Figure 4.14b). The maximum vertical force of adhesion of the water droplet towards the **AzPBA/BA** and **Zn-CP/BA** surfaces has been estimated as 45.5 μN and 23.9 μN respectively (Figure 4.14c). It was also observed that the maximum droplet deformation, observed for the vertical detachment of the water droplet is 0.28 and 0.12, respectively for **AzPBA/BA** and **Zn-CP/BA** surfaces (Figure 4.14d). These data confirmed that **AzPBA/BA** surface, although hydrophobic, shows strong adhesion towards water droplets, thereby mimicking the rose petal effect and can therefore be utilized for anchoring water droplets over it. The lotus-leaf like **Zn-CP/BA** surface, on the other hand, shows negligible affinity towards water droplets (Supplementary Video 2 and 4) and hence can easily slip over them.

4.3.7. Energy-Efficient Mechanical Motion of the Lotus Leaf Surface over the Rose Petal Surface

Having the rose petal like **AzPBA/BA** and the lotus leaf like **Zn-CP/BA** surfaces, we thought of combining these two surfaces for achieving energy efficient slippery motion of objects. In order to demonstrate this concept, we mounted a cargo with a magnetic bead over the **AzPBA/BA** surface. Water droplets were then anchored over the **AzPBA/BA** surface. Subsequently, the lotus leaf like **Zn-CP/BA** surface was placed over a magnetic stirrer which provided the necessary external force for the

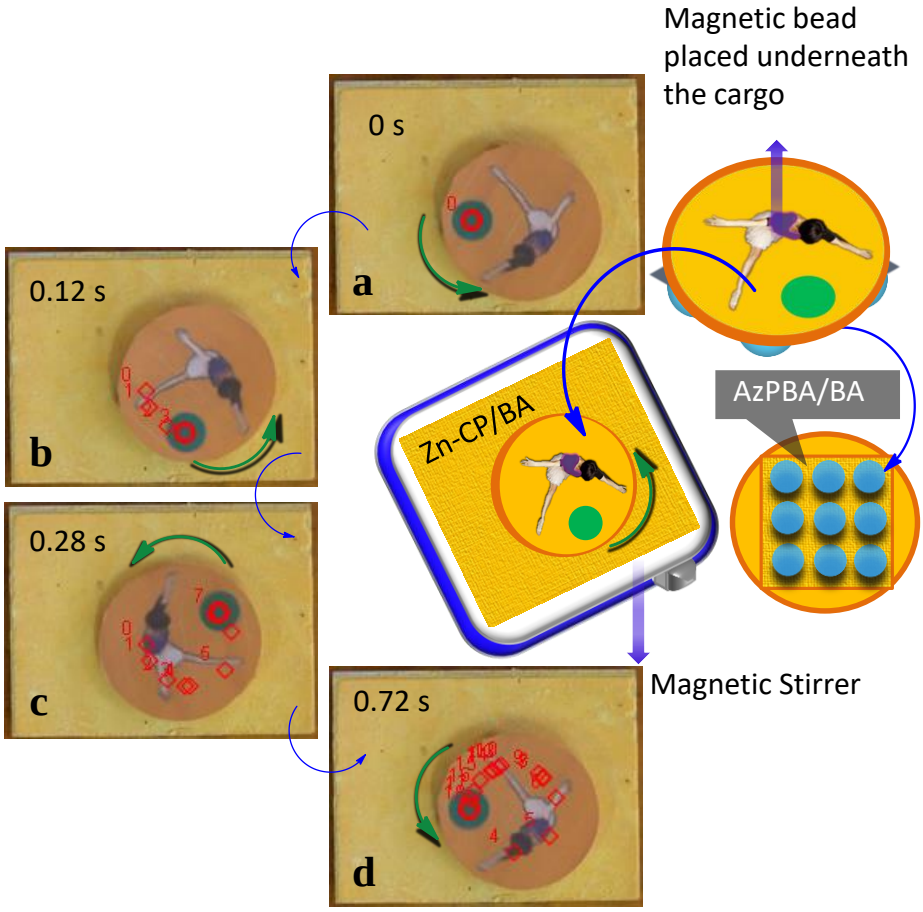

Figure 4.15. Schematic representation of a water skating experimental set up. Photographs (a–d) show the snapshots showing the position of the object (a skating girl, marked with green circle) at different time intervals. Green curved arrows show the direction of rotation.

rotation of the cargo (Figure 4.15). The same experimental set up without water droplets was made for comparison (Supplementary Video 5). The 360° movement of the cargo was tracked using Tracker Video Analysis and Modeling Tool.[48] When the stirrer operation was fixed at 80 rpm, no movement was observed for the cargo in the absence of water droplets. In this case, further increase of the motor speed to 170 rpm resulted in a twitching movement of the cargo over the **Zn-CP/BA** surface. Whereas,

in presence of water droplets in between the two surfaces, the cargo undergoes ~7 rotations in ~5 s (Figure 4.16), even when the stirrer was fixed at 80 rpm. The rotational movement of the cargo has been recorded up to 300 complete rotations.

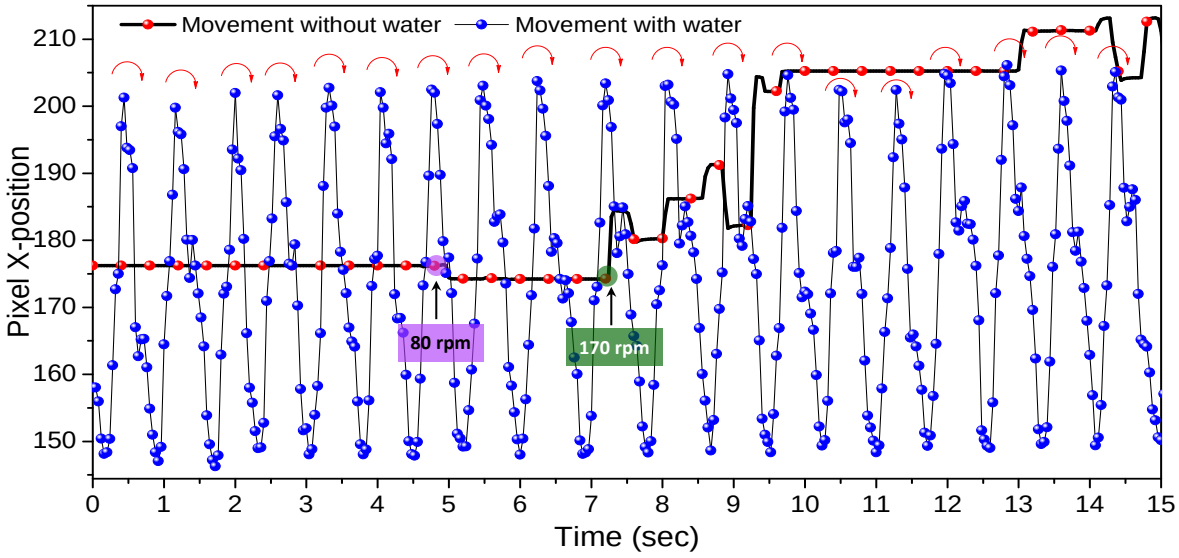

Figure 4.16. Tracking the pixel x-position of the cargo during rotational motion with and without water. Rotation of the cargo was observed at a motor speed of 80 rpm with water. Red curved arrow indicates individual 360° motion. Without water, no motion was observed at a motor speed of 80 rpm, however when increased to 170 rpm, a twitching motion is observed.

In order to quantify the frictionless motion of the lotus leaf surface on the rose petal surface in presence of water droplets, the minimum amount of force required for their relative movement was recorded on an inclined plane (Figure 4.17a). According to a standard free body diagram, for an object kept over an inclined plane, the component of weight of the object (mg) causing it to slide over the inclined plane surface due to the gravitational pull is mg sin (SA), where 'm' and 'g' correspond to mass of the object (148 mg) and acceleration due to gravity (9.8 m s^{-2}) respectively.

SA represents the sliding angle of the inclined plane. The frictional force acting against the sliding motion of the body is $\mu_s$mg cos (SA) where μ_s represents the coefficient of static friction for the two surfaces in contact. At the point of sliding motion, both these forces are equal and opposite to each other and therefore μ_s can be calculated as tan (SA). If the slope or SA is smaller, larger will be the mechanical advantage of the ramp and hence lesser amount of force will be required for the object to slide over the surface (Figure 4.17a, top). Sliding of the **AzPBA/BA** surface over the **Zn-CP/BA** surface occurs at different sliding angles (α and α'), in the absence and presence of water droplets (Figure 4.17a, bottom).

In the absence of water droplets, the sliding angle for the **AzPBA/BA** surface to slip over the **Zn-CP/BA** surface is 44°, which decreases ~5–fold, to an angle of 9° in presence of anchored water droplets (Figure 4.17b and Supplementary Video 6). The sliding movement in presence of water droplets therefore occurs with a force of 226.89 μN which is ~4.4–fold lesser than the force required to slide the cargo in the absence of water droplets (1007.53 μN) (Figure 4.17c). A 6–fold reduction of the coefficient of static friction (μ_s) was observed in the case of experiment 2 (μ_s=0.16) when compared to that in experiment 1 (μ_s = 0.97). This decrease in μ_s is quite significant when compared to the μ_s observed for other standard substrates with greasy lubricants (Figure 4.17d).[49]

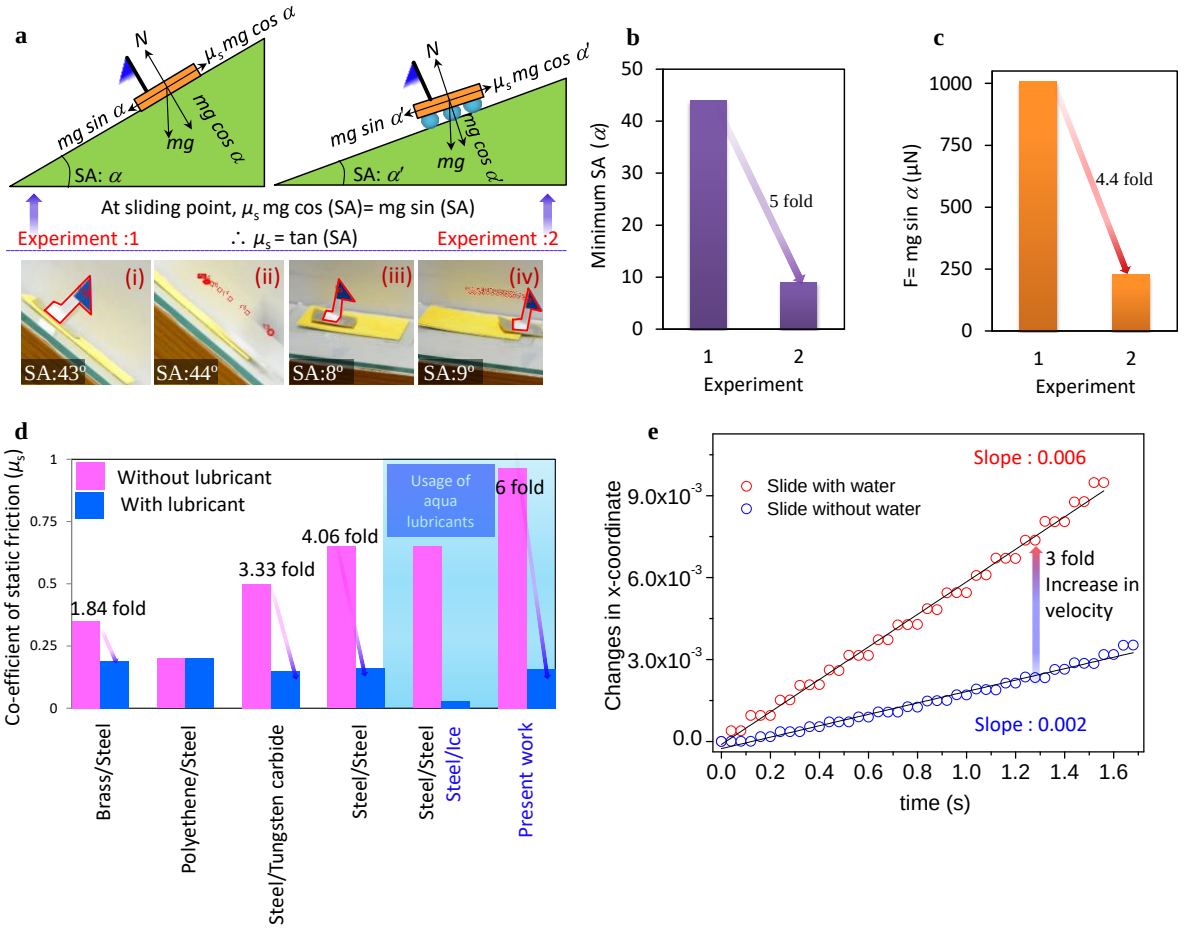

Figure 4.17. (a) Top panel shows the schematic representation and free body diagram of a cargo placed over an inclined plane without (Experiment: 1) and with (Experiment: 2) water droplets between the cargo and the inclined plane surfaces. Bottom panel shows the snapshots of the tracking of the cargo movement at different sliding angles without (i, ii) and with (iii, iv) water droplets. (b) Comparison of the minimum sliding angles obtained from experiments 1 and 2. (c) Minimum sliding force required in experiments 1 and 2. (d) A comparative plot of the reduction in the coefficient of static friction (μ_s) using oil and water based lubricants in various standard systems.[49] (e) Position of the cargo at a particular SA (45°), with and without water, monitored along x-axis with respect to time, using a video tracker. Black line corresponds to the linear fit obtained. All SA measurements are within an error limit of ± 1°.

The position of the cargo along the x-axis was tracked using a video tracker and plotted against time (t) at a sliding angle of 45°. The component of weight (mg

$\sin\alpha$) acting along the hypotenuse of the inclined plane was constant in both experiments in this case (Figure 4.17e). The velocity of the lotus leaf surface was estimated from the slope of the plot. It was observed that the movement of the cargo is 3 times faster in presence of water droplets, justifying the role played by water as a lubricant (Supplementary Video 7). The cargo in presence of water droplets therefore moves 3–fold greater distance utilizing the same amount of gravitational force (mg sin45), manifesting the energy efficiency of the process.

4.4. Conclusions

The combination of an organic ligand having the sticky superhydrophobicity of a rose petal and a coordination polymer having the slippery superhydrophobicity of a lotus leaf, to achieve frictionless movement of objects, is a new concept. This idea can be extended to the creation of indoor ice-skating surfaces without the use of ice, thereby saving a significant amount of energy. We have demonstrated the role of MOF chemistry to achieve the synthesis of the superhydrophobic materials. At this point of time, even though it appears far from a practical implementation, design of new artificial materials with stable, sticky and slippery superhydrophobic properties for large area applications may lead this concept into a technical reality. The proof-of-concept described here may facilitate the search for new generation superhydrophobic materials for achieving such ‘ever thought of challenging’ applications.

4.5. Experimental Section

4.5.1. Materials and Methods

^{1}H and ^{13}C NMR spectra were measured on a 300 MHz or 500 MHz Bruker Advance DPX spectrometer using TMS and $CDCl_3$ as internal standards. Melting point was measured on a MEL-Temp-II melting point apparatus and is uncorrected. Fast Atom Bombardment Mass Spectroscopy (FAB-MS) was performed on JEOL JM AX 505 HA instrument and Electrospray Ionization Mass Spectroscopy (ESI-MS) was performed on a Thermo Scientific Q Exactive Hybrid Quadrupole-Orbitrap electrospray ionization mass spectrometer. Elemental analyses were obtained using a Perkin-Elmer Series 2 Elemental Analyzer 2400. IR spectra were collected on a Perkin-Elmer Spectrum One FT-IR spectrometer using KBr (neat). Thermogravimetric analysis was carried out using TA instruments Q 50, all samples were heated at 10 K/min under N_2 atmosphere. N_2 gas adsorption studies were carried out at 77 K on a Quantachrome Quadrasorb automatic volumetric instrument. About 70 mg of the **Zn-CP** sample was activated at 140°C for 6h for gas adsorption experiments.

4.5.2. Preparation of Compound 1

A mixture of KOH (60.0 g, 1.07 mol), *p*-nitrophenol (10.0 g, 72 mmol) and water (10 mL) was heated to 120°C for 4 h with constant stirring to allow the mixture to fuse. Then temperature is slowly allowed to rise to 220°C. A brown liquid

was formed with vigorous effervescence. Heating was continued till the effervescence ceased. The reaction mixture formed a sticky liquid and was slowly cooled down. The mixture thus obtained was then dissolved in water and acidified with con. HCl (~5 mL). A dense chocolate colored precipitate was formed, which was extracted with diethyl ether. The organic extract was then washed with brine, dried over anhydrous Na_2SO_4 and concentrated under atmospheric pressure to yield a dark red residue. Recrystallization from 50% (v/v) EtOH-Water mixture yielded azo compound **1** in 47% yield. m.p: 207°C. FT-IR (KBr, cm^{-1}) 3460 (m), 3205 (broad), 1664 (w), 1591 (s). ^{1}H NMR (500 MHz, DMSO-d_6) δ: 10.14 (s, 2H, Ar OH), 7.72 (d, 4H, Ar H), 6.91 (d, 4H, Ar H). ^{13}C NMR (DMSO-d_6, 125 MHz) δ: 164.3, 141.7, 126.9, 116.5. Elemental analysis calculated for $C_{12}H_{10}N_2O_2$; C, 67.28; H, 4.71; N, 13.08. Found. C, 68.45; H, 5.20; N, 13.36. FAB-MS: m/z: calculated: 214.07: Found: 214.41

4.5.3. Preparation of Compound 2

Compound **1** (5.0 g, 23.33 mmol) and activated K_2CO_3 (10.0 g, 73.99 mmol) in distilled acetone (50 mL) was stirred until complete dissolution (~1 h). To the solution, ethyl 4-bromo butanoate (20.0 mL, 72 mmol) was added and the reaction mixture was refluxed for 24 h under inert atmosphere. The reaction mixture was then evaporated to dryness, the residue was dissolved in water and extracted with chloroform (500 mL). The organic layer was separated, dried over Na_2SO_4 and concentrated under reduced pressure. The crude product was purified by column

chromatography (Silica gel, chloroform as eluent). The product was obtained as orange-yellow crystals. Yield of the reaction was 77%. m.p: 96°C. FT-IR (KBr cm^{-1}) 2974 (m), 1728 (s), 1593 (s). ^{1}H NMR (500 MHz, DMSO-d_6,) δ: 7.86 (d, 4H, Ar H), 6.98 (d, 4H, Ar H), 4.16 (qt, 4H, ester -OCH_2-), 4.09 (t, 4H, ether -OCH_2-), 2.54 (t, 4H, -(C=O)-CH_2-), 2.15 (m, 4H, -CH_2-), 1.26 (t, 6H, -CH_3). ^{13}C NMR (DMSO-d_6, 125 MHz) δ: 173.2, 160.9, 125.9, 124.9, 114.4, 67.6, 60.5, 29.3, 24.6, 14.2. Elemental analysis calculated for $C_{24}H_{30}N_2O_6$; C, 65.14; H, 6.83; N, 6.33.Found C, 65.57; H, 7.0; N, 6.7. FAB-MS: m/z: calculated: 442.21: Found: 443.17 $[M+H]^+$

4.5.4. Preparation of AzPBA

Compound **2** (3.32 g, 7.5 mmol), was dissolved in 10% NaOH solution and EtOH (1:1, v/v, 80 mL) and refluxed for 24 h. The reaction mixture was cooled in ice and acidified with drop wise addition of conc. HCl. The bright yellow precipitate obtained, was filtered and washed with water (50 mL) and then dried in a vacuum oven. Yield of the reaction was 92 %. m.p: 246°C. FT-IR (KBr, cm^{-1}) 2892 (broad), 1703 (s), 1591 (s). ^{1}H NMR (500 MHz, DMSO-d_6) δ: 12.13 (s, 2H, -COOH), 7.74 (d, 4H, Ar H), 4.0 (t, 4H, ether -OCH_2-), 2.33 (t, 4H, -CH_2-), 1.89 (m, 4H, -CH_2-). ^{13}C NMR (DMSO-d_6, 125 MHz) δ: 174.0, 160.7, 146.1, 124.1, 114.9, 67.0, 30.0, 24.1. Elemental analysis calculated for $C_{20}H_{22}N_2O$; C, 62.17; H, 5.74; N, 7.25. Found. C, 62.45; H, 5.42; N, 7.56. ESI-MS: m/z: calculated: 386.15: Found: 387.15 $[M+H]^+$

4.5.5. Preparation of HqPBA

The organic ligand 4,4'-(1,4-phenylenebis(oxy))dibutanoic acid (**HqPBA**) was prepared by following the same procedure as that for **AzPBA,** but using hydroquinone as the starting material instead of compound **1**. **HqPBA** was obtained as a pale pink powder in 60 % yield. m.p: 181°C. FT-IR (KBr, cm^{-1}) 2934 (broad), 1693 (s), 1508 (s).^{1}H NMR (500 MHz, DMSO-d_6,) δ: 12.13 (s, 2H, -COOH), 6.8 (d, 4H, Ar H), 3.37 (t, 4H, ether -OCH_2-), 2.37 (t, 4H, -CH_2-), 1.89 (m, 4H, -CH_2-). ^{13}C NMR (DMSO-d_6, 125 MHz) δ: 174.0, 115.8, 67.4, 30.6, 24.8. Elemental analysis calculated for $C_{14}H_{18}O_6$; C, 59.57; H, 6.43. Found. C, 60.45; H, 5.99. ESI-MS: m/z: calculated: 282.11: Found: 281.1 $[M–H]^+$

4.5.6. Preparation of Zn-CP and Zn-CP-1.

In a typical experiment, **AzPBA** (0.077 g, 0.2 mmol) and zinc nitrate hexahydrate, $Zn(NO_3)_3{\cdot}6H_2O$ (0.178 g, 0.60 mmol) were dissolved in dimethylformamide (DMF, 5 mL) and the mixture was placed in a Teflon lined stainless steel pressure vessel. The vessel was slowly heated to 115°C and kept for 48 h in a programmable oven and then slowly cooled over a period of 6h to room temperature. Yellow colored aggregates of **Zn-CP** adhered to the walls of the pressure vessel was collected and purified via repeated cycles of centrifugation (at 2500 rpm) and washing with DMF (50 mL) and methanol (20 mL) followed by drying in an air oven at 60°C for 6 h. Controlled synthesis of **Zn-CP** was carried out by reducing the reaction time to 12 h.

For the synthesis of **Zn-CP-1**, **HqPBA** was used instead of **AzPBA** and the same procedure was followed maintaining the reaction time at 12 h. A white powder was obtained which was purified by repeated centrifugation and washing with DMF and methanol to remove the starting materials and dried in an air oven at 60°C for 6 h.

4.5.7. Preparation of Rose Petal like (AzPBA/BA) and Lotus Leaf like (Zn-CP/BA) Surfaces

Alumina plates (TLC Aluminium oxide 60 F_{254}, neutral) were cut into small strips (4 cm x 3 cm) and dipped into the mother liquor containing **AzPBA** (50 mg, 0.13 mmol) for the rose petal surface and to a mixture of **AzPBA** (50 mg, 0.13 mmol) and $Zn(NO_3)_3{\cdot}6H_2O$ (116 mg, 0.39 mmol) in dry DMF (35 mL). The vessel was sealed and was heated at 115°C for 12 h. After completion of the reaction, the alumina plates were washed with dry DMF (50 mL) and dried in an air oven at 60°C for 2 h. A solution of 2,5-bis(dodecycloxy)terephthalaldehyde[50] (**BA**, 2 mg/mL) in dichloromenthane was prepared. The plates were then dipped into the aforesaid solution and dried in air for about 30 min. The treatment of **BA** solution was repeated 5-6 times to get a superhydrophobic surface. **BA** has a sticky nature which acts as wax like coating over the **AzPBA** and the **Zn-CP** surfaces, maintaining a dual scale surface topology. The cyan fluorescence of **BA** also helped in monitoring the proper coating of the alumina substrates.

4.5.8. Experimental Techniques

4.5.8.1. Optical Measurements and Photoirradiation

Electronic absorption spectra were recorded on a Shimadzu UV-3600 scanning spectrophotometer using a 1 cm path length quartz cuvette. Solid-state absorption or reflection spectra were obtained using $BaSO_4$ as a standard. Photoirradiation was carried out by LOT-Oriel 200 W high pressure Hg Lamp using $\lambda_{band\ pass}$ = 350 and 420 nm.

4.5.8.2. Morphological Analyses

SEM images were obtained using a Zeiss EVO 18 cryo SEM Special Edn with variable pressure detector working at 20-30 kV. Time dependent SEM analysis was carried out by taking the alumina substrate from the solvothermal vessel at different time intervals and pasting the substrate over a SEM stub using a two side carbon tape. The samples were coated with gold prior to examination. Transmission electron microscopy (TEM) and high resolution TEM (HRTEM) were performed on a FEI, TECNAI 30 G2 S-TWIN microscope with an accelerating voltage of 100 and 300 kV, respectively. The TEM samples were prepared by dispersing 1 mg of **Zn-CP** or **Zn-CP-1** (both purified and dried) in 5 mL methanol by ultra-sonication for 15 min and then drop casting the dispersions on to carbon coated copper grids. Images were obtained without staining. IFFT reconstruction of the HR-TEM images was done using Digital MicrographTM (GATAN Inc.) following a reported procedure.[51]

Initially, a fast Fourier transform (FFT) of the experimentally obtained image was taken, which was followed by appropriate mask filtering to remove the spatial frequency of the diffractogram. Finally, the Inverse FFT led to a reconstructed HR-TEM image.

4.5.8.3. X-ray Diffraction Measurements

WAXD and SAXS measurements on **Zn-CP** pellet or powder were carried out on a XEUSS 2D SAXS/WAXS system using a Genix microsource from Xenocs operated at 50 kV and 0.3 mA. The Cu Kα radiation (λ = 1.54 Å) was collimated with a FOX2D mirror and two pairs of scatter less slits from Xenocs. Measurements on the **Zn-CP** film were performed on a Phillips diffractometer using Ni filtered Cu Kα radiation.

4.5.8.4. Contact Angle Measurements

CAs were measured on a CA goniometer Kernco Instrument Inc. at ambient temperature. Water droplets (~4 µL) were placed on appropriate substrates and measurements were done by sessile drop method. The average static contact angle was obtained by measuring CA at five different positions of each sample. CAH was measured by rolling the droplet horizontally along the superhydrophobic surfaces and monitoring the advancing and receding water contact angles.

4.5.8.5. Droplet Bouncing Dynamics and Imaging

Impact of water droplets with different surfaces was captured with a high-speed camera (*HiSpec* 2), recording at a minimum of 5,000 frames per second. The droplets were released from a burette at a fixed height (3 cm) above the surface. The diameter of the droplet (2 mm), the impact velocity (0.8 m/s), the contact time, spreading factor (β) and dimensionless height factor (ζ) were calculated directly from the high speed images for each experiment.

4.5.8.6. Coefficient of Static Friction Measurement

Sliding angle experiments were conducted with a cardboard made cargo, specially fabricated for the purpose and pasted over the rose petal like **AzPBA/BA** surface (total weight, 148 mg). Water droplets were anchored over the **AzPBA/BA** surface. The lotus leaf like **Zn-CP/BA** surface was pasted with two-side tape over an inclined plane with a glass surface and adjustable ramp angle (0 to 47°). Experiments were conducted by placing the cargo with anchored water droplets over the **Zn-CP/BA** surface attached over the inclined plane and changing the ramp angle manually at a rate of ~1°sec^{-1}. An average of five measurements was taken for each experiment.

4.5.8.7. Video Analysis and Editing

Videos of all the experiments were recorded on a Sony Handycam (HDR-PJ410). Tracking the rotational or sliding motion of cargo has been performed using Tracker

Video Analysis and Modelling Tool. All videos were calibrated using a known distance (e.g. the length of the TLC strip). The motion of the cargo was tracked by fixing the origin pixel position at the created point mass (blue flag in case of the sliding experiment and green circle in case of the rotational motion) and thereby using the autotracker option. All supporting videos were edited using Corel Video Studio ProX3 software.

4.6. References

1. E. B. Paz, M. Ceccarelli, J. E. Otero and J. L. M. Sanz, A Brief Illustrated History of Machines and Mechanisms, Ch. 1 (Springer, 2010).
2. S. Chu, and A. Majumdar, *Nature*, 2012, **488**, 294.
3. C. Wilson, A. Grubler, K.S. Gallagher and G.F. Nemet, *Nat. Clim. Change*, 2012, **2**, 780.
4. K. Holmberg, P. Andersson and A. Erdemir, *Tribol. Int.*, 2012, **47**, 221.
5. A. Dorinson and K. C. Ludema, Mechanics and Chemistry in Lubrication, Ch. 1 (Elsevier, 1985).
6. L. Ma, A. Gaisinskaya-Kipnis, N. Kampf and J. Klein, *Nat. Commun.*, 2015, **6**, 6060.
7. A. Singh, M. Corvelli, S.A. Unterman, K.A. Wepasnick, P. McDonnell and J.H. Elisseeff, *Nat. Mater.*, 2014, **13**, 988.
8. M. R. Panman, B. H. Bakker, B. d. Uyl, E. R. Kay, D. A. Leigh, W. J. Buma, A. M. Brouwer, J. A. J. Geenevasen and S. Woutersen, *Nat. Chem.*, 2013, **5**, 929.
9. Y. Suzuki, K. Okuro, T. Takeuchi and T. Aida, *J. Am. Chem. Soc.*, 2012, **134**, 15273.
10. M. Yanagisawa, K. Tashiro, M. Yamasaki and T. Aida, *J. Am. Chem. Soc.*, 2007, **129**, 11912.

11. L. D. Barron, L. Hecht and G. Wilson, *Biochemistry*, 1997, **36**, 13143.
12. R. Rosenberg, *Phys. Today*, 2005, **58**, 50.
13. F. Formenti and A.E. Minetti, *Biol. J. Linnean Soc.*, 2008, **93**, 1.
14. P. E. Laurier Nichols, *ASHRAE J.*, 2009, June, 16.
15. A. Lafuma and D. Quere, *Nat. Mater.*, 2003, **2**, 457.
16. R. Blossey, *Nat. Mater.*, 2003, **2**, 301.
17. C. Sanchez, H. Arribart and M. M. Giraud Guille, *Nat. Mater.*, 2005, **4**, 277.
18. A. Tuteja, W. Choi, M. Ma, J.M. Mabry, S.A. Mazzella, G. C. Rutledge, G. H. McKinley and R. E. Cohen, *Science*, 2007, **318**, 1618.
19. S. Srinivasan, V. K. Praveen, R. Philip and A. Ajayaghosh, *Angew. Chem. Int. Ed.*, 2008, **47**, 5750.
20. K. Koch and W. Barthlott, *Philos. Trans. A Math Phys. Eng. Sci.*, 2009, **367**, 1487.
21. T.S. Wong, S. H. Kang, S. K. Y. Tang, E. J. Smythe, B. D. Hatton, A. Grinthal and J. Aizenberg, *Nature*, 2011, **477**, 443.
22. L. Bocquet and E. Lauga, *Nat. Mater.*, 2011, **10**, 334.
23. E. Ueda and P. A. Levkin, *Adv. Mater.*, 2013, **25**, 1234.
24. M. Nosonovsky and B. Bhushan, Green Tribology, Green Energy and Technology. Ch. 2 (Springer, 2012).
25. H. Furukawa, K. E. Cordova, M. O'Keeffe and O.M. Yaghi, *Science*, 2013, **341**, 1230444.
26. J. G. Nguyen and S. M. Cohen, *J. Am. Chem. Soc.*, 2010, **132**, 4560.
27. Q. Sun, H. He, W. –Y. Gao, B. Aguila, L. Wojtas, Z. Dai, J. Li, Y. –S. Chen, F. –S. Xiao and S. Ma, *Nat. Commun.*, 2016, **7**, 13300.
28. J. B. Decoste, G. W. Peterson, M. W. Smith, C. A. Stone and C. R. Willis, *J. Am. Chem. Soc.*, 2012, **134**, 1486.

29. S. J. Yang, J. Y. Choi, H. K. Chae, J. H. Cho, K. S. Nahm and C. R. Park, *Chem. Mater.*, 2009, **21**, 1893.
30. S. J. Yang and C. R. Park, *Adv. Mater.*, 2012, **24**, 4010.
31. T. T. Y. Tan, M. R. Reithofer, E. Y. Chen, A. G. Menon, T. S. A. Hor, J. Xu and J. M. Chin, *J. Am. Chem. Soc.*, 2013, **135**, 16272.
32. S. Roy, V. M. Suresh and T. K. Maji, *Chem. Sci.*, 2016, **7**, 2251.
33. K. P. Rao, M. Higuchi, K. Sumida, S. Furukawa, J. Duan and S. Kitagawa, *Angew. Chem. Int. Ed.*, 2014, **53**, 8225.
34. N. Stock and S. Biswas, *Chem. Rev.*, 2012, **112**, 933.
35. S. Jung and M. Oh, *Angew. Chem. Int. Ed.*, 2008, **47**, 2049.
36. R. D. Mukhopadhyay, V. K. Praveen, A. Hazra, T. K. Maji and A. Ajayaghosh, *Chem. Sci.*, 2015, **6**, 6583.
37. A. K. Mahapatra, P. Sahoo, S. Goswami, H. –K. Fun and C. S. Yeap, *J. Incl. Phenom. Macrocycl.Chem.*, 2009, **67**, 99.
38. G. B. Deacon and R. J. Phillips, *Coord. Chem. Rev.*, 1980, **33**, 227.
39. H. Deng, S. Grunder, K. E. Cordova, C. Valente, H. Furukawa, M. Hmadeh, F. Gándara, A. C. Whalley, Z. Liu, S. Asahina, H. Kazumori, M. O´Keeffe, O. Terasaki, J. F. Stoddart and O. M. Yaghi, *Science*, 2012, **336**, 1018.
40. J. J. P. Stewart, *J. Mol. Model.*, 2007, **13**, 1173.
41. P. Falcaro, K. Okada, T. Hara, K. Ikigaki, Y. Tokudome, A. W. Thornton, A. J. Hill, T. Williams, C. Doonan and M. Takahashi, *Nat. Mater.*, 2017, **16**, 342.
42. J. Reboul, S. Furukawa, N. Horike, M. Tsotsalas, K. Hirai, H. Uehara, M. Kondo, N. Louvain, O. Sakata and S. Kitagawa, *Nat. Mater.*, 2012, **11**, 717.
43. I.A. Larmour, S.E. Bell and G.C. Saunders, *Angew. Chem. Int. Ed.*, 2007, **46**, 1710.
44. S. Chandra and C. T. Avedisian, *Proc. R. Soc. Lond. A*, 1991, **432**, 13.
45. C. G. L. Furmidge, *J. Colloid Sci.*, 1962, **17**, 309.
46. F. Brochard-Wyart and P.-G. de Gennes, *C. R. Physique*, 2003, **4**, 281.

47. M. M. Cui, T. Emrick and T. P. Russell, *Science*, 2013, **342**, 460.
48. D. Brown, Tracker Video Analysis and Modeling Tool, http://www.opensourcephysics.org/items/detail.cfm?ID=7365 (2008) (Accessed on November 11, 2016)
49. Friction and Friction Coefficients, http://www.engineeringtoolbox.com/friction-coefficients-d_778.html (Accessed on November 11, 2016)
50. A. Ajayaghosh and S. J. George, *J. Am. Chem. Soc.*, 2001, **123**, 5148.
51. Y.-M. Kim, J.-M. Jeong, J.-G. Kim, Y.-J. Kim and Y. S. Lim, *J. Korean Phys. Soc.*, 2006, **48**, 250.

Papers Presented at Conferences (Posters/Oral)

1. **R. D. Mukhopadhyay** and A. Ajayaghosh, Azobenzene Derived Photochromic MOF-gels. 8th JNC Research Conference on Chemistry of Materials, September 30 – October 2, 2012, Trivandrum, Kerala, India. (*Poster and Oral*)

2. **R. D. Mukhopadhyay** and A. Ajayaghosh, Tweaking the Morphology of Porous Coordination Polymers at the Mesoscale by Light Induced Pre-Synthetic Modification. Nano India-2013, February 19–20, 2013, Trivandrum, Kerala, India.

3. R. Thirumalai, **R. D. Mukhopadhyay** and A. Ajayaghosh, Fluorescent π–Assembles for Security Applications. ACS on Campus event, November 29, 2013, Trivandrum, Kerala, India.

4. **R. D. Mukhopadhyay** and A. Ajayaghosh, Modulation of Mesoscale Self-Assembly in a Coordination Polymeric Gel by Light. 8th Asian Photochemistry Conference ‘‘APC-2014’’, November 10–13, 2014, Trivandrum, Kerala, India.

5. **R. D. Mukhopadhyay** and A. Ajayaghosh, A. Light Induced Modulation of Mesoscale Self-Assembly in a Coordination Polymeric Gel. 2014 RIKEN Center for Emergent Matter Science International Symposium on Supramolecular Chemistry & Functional Materials (CEMSupra 2014), December 13–26, 2014, Tsumagoi, Gunma, Japan. (*Invited*)

6. **R. D. Mukhopadhyay** and A. Ajayaghosh, Tuning the Properties of Coordination Polymeric Gels. HEAM Scientist 2012 (A national level meet of young scientists of **H**ydrogen **E**nergy and **A**dvanced **M**aterials), December 14, 2012, University of Kerala, Trivandrum, Kerala, India. (*Oral*)

7. **R. D. Mukhopadhyay** and A. Ajayaghosh, Mesoscale Self-Assembly of Photoresponsive Co-ordination Polymers. Polymer Conference for Young Researchers (PCYR-2014), October 18, 2012, Trivandrum, Kerala, India. (*Invited Talk*)

8. **R. D. Mukhopadhyay** and A. Ajayaghosh, Tuning of Mesoscale Self-Assembly in Supramolecular Polymers. Saturday Symposium for Students (S^3), January 16, 2016, Trivandrum, Kerala, India. (*Invited Talk*)

9. **R. D. Mukhopadhyay** and A. Ajayaghosh, Self-Assembly of Metal-Organic Materials: Futuristic Applications. National Seminar on Recent Advances in Chemical Sciences (RACS-17), March 13, 2017, University College, Trivandrum, Kerala, India. (*Invited Talk*)

List of Publications from the Thesis

1. Photoresponsive Metal-Organic Materials: Exploiting the Azobenzene Switch. **R. D. Mukhopadhyay**, V. K. Praveen and A. Ajayaghosh,

   Mater. Horiz., 2014, **1**, 572.

2. Light Driven Mesoscale Assembly of a Coordination Polymeric Gelator into Flowers and Stars with Distinct Properties. **R. D. Mukhopadhyay**, V. K. Praveen, A. Hazra, T. K. Maji and A. Ajayaghosh,

   Chem. Sci., 2015, **6**, 6583.

3. Rose Petal and Lotus Leaf Inspired Two-in-One Approach to Energy-Efficient Mechanical Motion. **R. D. Mukhopadhyay**, B. Vedanarayan and A. Ajayaghosh, (*manuscript in preparation*).

4. Precise Control of Host-Guest Interactions by a Coordination Polymeric Gelator. **R. D. Mukhopadhyay**, G. Das and A. Ajayaghosh, (*manuscript in preparation*).

List of Publications from Other Related Works

1. Supramolecular Gels and Functional Materials Research in India. Kartha, Kalathil K., **R. D. Mukhopadhyay** and A. Ajayaghosh,

   Chimia, 2013, **67**, 51.

2. A Slippery Molecular Assembly allows Water as a Self-Erasable Security Marker. R. Thirumalai, **R. D. Mukhopadhyay**, V. K. Praveen and A. Ajayaghosh,

   Sci. Rep., 2015, **5**, 09842; doi: 10.1038/srep09842.

3. Living Supramolecular Polymerization. **R. D. Mukhopadhyay** and A. Ajayaghosh,

   Science, 2015, **349**, 241.

4. A π–Gel Scaffold for Assembling Fullerene to Photoconducting Supramolecular Rods.
   V. S. Nair, **R. D. Mukhopadhyay**, A. Saeki, S. Seki and A. Ajayaghosh,

   Sci. Adv., 2016, **2**, e1600142; doi: 10.1126/sciadv.1600142.

5. Development of Superhydrophobic Coatings for Energy Saving Mechanical Motion and Related Applications.
   B. Vedanarayan, **R. D. Mukhopadhyay** and A. Ajayaghosh,

   2017 (*Patent to be filed*)